MULTI-SCALE MODELING OF STEAM METHANE REFORMER HEATED BY ELECTRICAL CURRENT

by

Yi Ran Lu

A thesis submitted in partial fulfillment of the requirements for the degree of

Doctor of Philosophy

in

Chemical Engineering

Department of Chemical and Materials Engineering
University of Alberta

Abstract

The study is dedicated to investigating the possibility of a new type of fixed-bed steam methane reformer heated by electrical current flowing through the particles. The objective of the thesis is to develop a multi-scale modeling for the electrically heated reformer, consisting of two types of particles. The electrically conductive metal particles act as heating elements, providing the heat of reaction for the endothermic reactions, and the catalyst particles provide the active sites for reaction. To verify this concept, a new multi-scale 1D-3D Euler-Lagrange model has been developed and validated.

A new 0D sub-system model is developed. A single catalyst particle is simulated using 3D CFD tools. The catalyst is exposed to a stream of reacting gas using LHHW kinetics. The full thickness of the boundary layers around the particle and the diffusion inside the porous catalyst particle are resolved. The 0D submodel was developed based on the results of the 3D CFD simulation. Excellent agreement was demonstrated. The 0D submodel is contrasted against 1D solutions in a parametric study to verify its usage for various temperatures (650K-1000K), particle size (2mm-25.4mm) and boundary conditions. Good agreement was found using the 0D model comparing the 1D results. The submodel is assembled in a 1D-3D Euler-Lagrange model to simulate reactions in a steam methane reformer. The results from the new model were validated against results from particle-resolved 3D-CFD simulation published in the literature. The comparison between our DEM-based model and 3D CFD case demonstrated good agreement, comprising of a 4K (1%) difference in the temperature of the outflow gas phase and up to 3% differences in mass fraction.

The volt-ampere characteristics of a fixed bed heated by the Joule heating were calculated using node-voltage method by treating the particle centers as nodes and the contact points as resistors. An experiment was conducted to validate the method using a cylinder filled with metal spheres. Electricity was flown through the bed and the voltage and current were measured. Open-source DEM software is used to model the packing of the fixed bed. Based on the packing, the electric field distribution is calculated using a new DEM-based model, with coupled with heat transfer simulation

to account for the temperature dependency of the steel particles' electrical conductivity. The results were found to be in good agreement with experimental data.

The multi-scale model is then used to simulate a steam-methane reformer with electrically heated particles. The Joule heating term for each electrically conductive particle was calculated. The inter-particle heat conduction is calculated based on contact area, particle size and thermal conductivity. The most important feature of the multi-stage model is that it retains 3D characteristics of the system in the solid phase, such as strong radial temperature gradient in the wall-heated case, yet demands computational power significantly less than that of a 3D simulation. A cylindrical electrically insulated tube filled with 23000 particles was simulated to test the performance of the model and feasibility of the concept. The limit for maximum power and temperature and a correlation between production capacity and the conversion rate was found.

A larger SMR comprising of 1 million particle was simulated in the scale-up study. The reformer has a diameter of 0.5 m and a height of 0.88 m and is filled with metal particles and catalyst particles with diameters of 10 mm and 4 mm, respectively. The modeled results show that electric current and Joule heating is widespread and well scattered in the fixed bed. The main distinguishing feature of the reformer that temperature distribution is relatively uniform in the radial direction regardless of the diameter of the fixed bed. Parametric runs have been carried out for different flow rates from 0.04 kg/s to 0.1 kg/s and electrical power from 185 kW to 462 kW.

The multi-stage model proved to be a useful way to resolve the intricacies of the complex phenomenon inside a reactor, not only for the new electrically heated SMR, but also in other cases with a strong internal heat source and sink for energy conversion and storage. It fills the gap between the continuum model and the particle-resolved model. Future steps towards realizing and implementation of the new reformer have been laid out in this study.

Preface

This thesis is an original work by Yi Ran Lu ("the author"). The mathematical formulations of all Chapters are derived by myself, with the assistance of Prof. P.A. Nikrityuk. Moreover, the experimental setups presented in Chapter 5 were designed by the author along with Prof. P.A. Nikrityuk, Dr. Deepak Pudasainee, Dr. Md Khan and Prof. Gupta.

Chapter 2 of this thesis has been published as ***A New Semiempirical Model for the Heat and Mass Transfer Inside a Spherical Catalyst in a Stream of Hot CH_4/H_2O gases*** by Y.R. Lu, D. Pashchenko and P.A. Nikrityuk in *Chemical Engineering Science*. The 3D CFD simulations in this publication were completed by D. Pashchenko. In Chapter 2 The author is responsible for 0D model formulation, programming and validations comprising of overall 70% of the total work in this chapter.

Chapter 3 of this thesis is based on original work accepted recently for publication in FUEL journal as ***Verification of a 0D model for the heat and mass transfer inside a moving spherical catalyst***. The author is responsible for 1D PDE model formulation, programming, calculations and verifications comprising of overall 75% of the total work in this chapter.

Chapter 4 of this thesis is an original work by the author and the supervisor, and has been published as ***DEM-based model for steam methane reforming*** in by Y.R. Lu and P.A. Nikrityuk *Chemical Engineering Science*. The author is responsible for overall 75% of the total work in this chapter.

Chapter 5 of this thesis includes materials published in ***Particle Unresolved Model for Predictions of Volt-Ampere Characteristics of a Packed Bed Heated by Joule Heating*** by Y.R. Lu, Prof. P.A. Nikrityuk, Dr. Deepak Pudasainee, Dr. Md Khan and Prof. Gupta in *Journal of Energy Resource Technology*. The experimental part of the work was done in collaboration with Dr. Deepak Pudasainee and Dr. Md Khan. The author is responsible for overall 70% of the total work in this chapter.

Chapter 6 of this thesis is an original work by the author and the supervisor, and has been published as ***Steam Methane Reforming driven by the Joule Heating*** by Y.R. Lu and P.A. Nikrityuk in *Chemical Engineering Science*. The author is responsible for overall 75% of the total work in this chapter.

Chapter 7 of this thesis has been published as ***Scale-up Studies on Electrically Driven Steam Methane Reforming*** in *Fuel* and is currently under second review. The author is responsible for overall 75% of the total work in this chapter.

In all publications mentioned above, the author is responsible for theoretical developments, programming in MATLAB and YADE, computation, data analysis, and writing. Prof. P.A. Nikrityuk was the supervisory author and was involved with concept formations and manuscript revisions.

Acknowledgements

I would like take this opportunity acknowledge the people who have helped me complete the journey through my doctoral program.

First, I would like to thank my supervisor, Dr. Petr Nikrityuk, for the inception of this project and providing me with this opportunity. This study has been a lengthy journey and a worthwhile one. I have learned many things through research, discussion, experiment and mistakes. The knowledge and skills you have taught me far exceed what this thesis can exemplify. I would also like to thank my supervising committee members Dr. Bob Hayes, Dr. Natalia Semagina for being open and accessible to the questions and concerns I had in their expert field. I would like also like to thank Dr. Rajender Gupta for his contribution and help in the experimental part of this work. I would also like to thank other professors and academic staff at the University of Alberta, whom I have inquired, consulted or challenged thoughts of. I am especially grateful towards the Faculty of Engineering's open, honest, bold and diligent academic atmosphere, qualities rare and desperately needed not only in science, engineering, but every part of the public discourse.

I will also like to express my cherishing for the friendships I have built along the way. We have perhaps faced the most challenging time during our lifetime. Our mutual supports help us maintain a clear vision and a strong will.

Last but not least, I would like to thank my family for the support they offered me. You are the reason I believe in myself and find the motivation to work towards goals in life.

Table of Contents

List of Tables

List of Figures

Chapter 1

Introduction

1.1 Background

1.1.1 Resources and Environment

Energy is the foundation of human activities and a necessity to our survival. Fossil fuel technology sparked the industrialization and greatly improved the effectiveness of human energy usage. Along with the prosperity and success that it brought, a few hundred years of industrial civilization has rapidly consumed a large part of the earth's energy reserve. IEA projects that global energy demand will continue to increase with population growth and economical development. The earth's energy reserve inevitably becomes harder to find and more expensive to extract. It is imperative that we try to extend the existing energy resources through technological innovation while searching for alternatives towards the future. In nature, solar energy is stored through photosynthesis, turning carbon dioxide in the air into organic matter. Organic matter eventually turns into hydrocarbons through degradation, decay and incomplete combustion. The natural energy storage through the carbon cycle is an inefficient and slow process. The stored energy will eventually be depleted if we do not have a way to store renewable energy. Therefore energy storage using artificial technology is the necessary for conserving and energy resources while satisfying human energy needs.

1.1.2 Hydrogen as a fuel

Hydrogen has gained interest as a fuel for energy uses from a number of countries. Currently, there are around 50 targets, mandates and policy incentives that directly support the use and research of hydrogen [1]. Hydrogen does not occur naturally on earth, so it acts as a means of energy storage and delivery rather than a natural occurring resource. Combined with technologies such as renewable power generation, carbon storage and sequestration, it has the potential to build an energy framework that is not only less dependent on hydrocarbon, but also cleaner and less carbon intensive. Currently, almost all of the existing production of hydrogen is done using steam-methane

reforming, which results in a less efficient and more carbon intensive overall process than gasoline per unit heat of combustion. The most promising use of hydrogen is in a fuel cell to generate electricity, especially in a mobile setting to power personal automobiles. The advantage of hydrogen usage is the elimination of air pollutants and carbon dioxides emissions at the site of the usage, enabling options to implement clean and efficient solutions for pollution management or carbon storage at the site of its production. With technological advancement, hydrogen fuel cell also has the potential to supersede the overall energy efficiency and cost efficiency of internal combustion engines [2]. There are several limitations. Hydrogen has a much lower volumetric energy density compared to fossil fuels such as gasoline or diesel. Even compared to the other gaseous fuels such as natural gas or propane, hydrogen is still at a disadvantage, requiring high pressure to store and pump. Up to 25% of total energy to supply hydrogen is lost through transportation and pumping[3].

1.1.3 Methane decomposition

Although hydrogen can be an emission-free source of energy through electrolysis, the existing infrastructure does not yet have excess capacity to produce hydrogen this way. Instead, hydrogen has the potential to be utilized as a medium to convert fossil fuel into usable energy, taking advantage of technologies such as carbon capture and pollution processing to reduce emissions and environmental impact. One way to use natural gas to produce hydrogen is the decomposition of methane. Methane decomposition can be separated into two categories, catalytic decomposition(CDM) and thermal conversion. CDM has been proposed as an alternative to steam methane reforming as a way to produce hydrogen with CO_2 emissions. Many transition metallic catalysts on support have been studies as candidates for industrial production.Takenaka et al. decomposed methane into Hydrogen and Carbon Nanofibers over Pd-Ni catalysts[4] and found Ni would turn into carbide with carbon deposition from the decomposed methane and alloying with Pd allows Ni to maintain its microstructure. Zein and Mohamed investigated the MnOx/NiO/TiO2 catalysts for methane decomposition[5]. Cunha et al. experimented with Raney-type Fe catalyst using La_2O_3 as a promoter[6]. Geng et al. studied the kinetics of CDM over Fe2O3 catalyst in a fluidized bed[7]. Gao et al. studied the performance of the Ni/Co catalyst on Al_2O_3 support[8]. Metallic catalysts have high activity, but the nature of carbon decomposition means the catalysts inevitably degrade after cycles of regeneration. The reliability and reproducibility suffer as a result, which become cost prohibitive for industrial applications. Lazaro et al. reported the use of carbon black as a catalyst to co-produce carbon nano-tube with hydrogen from CDM[9]. Carbon catalyst is noted for its stability, cheaper cost and ability to continue to operate in a reactor without the need to be regenerated, but its lower activity means carbon catalyst is used in high temperature applications, closer to thermal decomposition. Dahl et al. identified intrinsic kinetics of methane decomposition over carbon catalyst using a graphite aerosol flow reactor[10]. Maag et al. reported experimental and modeling studies with tubular reactor with a graphite annulus[11]. Paxman et al. used a mixed-reactor-with-bypass

(CPMR) model to model an experimental study of thermal decomposition and found better results than the traditional perfectly mixed reactor[12].

1.1.4 Syngas

Synthetic gas or syngas, is the mixture produced from steam methane reforming. Syngas consists of primarily hydrogen and carbon monoxide, but also carbon dioxide and hydrocarbons. Parameters such as temperature, pressure, composition of feed are tuned in accordance to the desired composition of the product. Thermodynamically, lower pressure is favored, as the equilibrium of Reaction 1 shifts towards the reactants with the increase in pressure. However, the most common intended use for syngas is the production of ammonia, methanol and the use as a fuel. As the post-reforming processes occur at high pressure, compressing the cold gas mixture before reforming is preferred for overall thermal efficiency. As a result, SMR is typically operated at 20-30bar and 800 to 1000 ^oC [13], to achieve a high conversion of methane. If not for pump energy considerations, lower pressure is preferred as it allows higher conversion of SMR at the same temperature. Syngas can be used to produce hydrogen-rich fuel. As gasification converts fuel into a mixture H_2 and CO_2, the hydrogen is separated from carbon dioxide. For the production of hydrogen-rich fuel, pressure swing adsorption(PSA) is used to separate syngas. In the downstream operations, water-gas shifting at low temperature in a selective catalyst reactor is used to convert CO to CO_2. While hydrogen is to be used as a fuel, CO_2 can be captured and stored so that it would no longer be emitted to the atmosphere. Since CO_2 is captured without the flue gas, gasification is considered a pre-combustion capture technology.

1.1.5 Gas fired reformers

SMR is a strongly endothermic process. Conventional gas-fired reformers are heat transfer limited. Because the combustion occurs in a different chamber from the reactor, the heat has to go through a radiant wall. Because of the limited heat transfer through the wall, the diameter of a reactor tube has to be designed to be deliberately narrow. In a large scale SMR plant, one reactor consists of a firing chamber with an array of hundreds of tubes, and the temperature distribution of the reforming tubes can differ significantly. Temperature distribution is crucial to the performance of a reactor [13] . The radial temperature gradient in the reactor means inconsistent reaction rate inside the reactor, limited effectiveness, accelerated carbon deposition and deactivation of catalysts. To avoid the risk of carbon deposition, a high steam-to-methane ratio often at 3:1 is used. However, a high steam-to-methane ratio increases the energy consumption to produce the excess steam and decreases overall efficiency.

Throughout decades of commercialization, the industrial SMR technology has fundamentally remained unchanged. Although continual efforts to optimize the process have provided significant

improvement to the efficiency, the limitations of the efficiency and effectiveness of the existing technology have prompted the development of alternatives.

1.1.6 Joule Heating

Joule heating is the dissipation of heat due to electrical resistance. Joule heating has been proposed as a means to provide the heat of reaction for endothermic processes. In fact, direct Joule heating of conductive particles is first proposed by Glaser and Thodos in their original work in 1958[14]. Rieks et al. studied the used of a Joule heated dry reformer in a series of experiment[15]. Lavoie's group studied the use of steel wires as heaters to provide heat for dry reforming [16, 17]. The original idea of using metal particles mixed in catalysts to generate heat is published in an article published by the author [18]. Most studies praised the accuracy of control that Joule heating provides that cannot be achieved by combustion. In addition to the reduction in pricing expected from renewable sources, improvement in efficiency through advanced monitoring and control techniques is also a major reason to take advantage of Joule heating.

1.1.7 Modeling

Reactor modeling can be classified by the scale of resolution. Microscale modeling ranges from direct numerical simulation (DNS), which resolves flow down to the Kolmogorov scale, to Large eddy simulations, which uses sub-grid models to handle small eddies. For a fixed bed reactor, Microscale simulation is a non-trivial task, as the complex shape inside a fixed fed requires very fine resolution of the solid-fluid boundaries. Also, the size of the fixed bed affect the packing density and geometry due to wall effect. Therefore, the phenomenon observed at a small tube-to-particle ratio can be totally different when the ratio is enlarged. For the reactor of our interest, which consists of many particles in a reforming tube of a large diameter, it becomes computationally too expensive. Nonetheless, there have been studies conducted using DNS on SMR reactors, which give insights to the internal physics of an SMR. Macroscale modeling usually uses a single-phase approach. The reaction rates and transport phenomena are calculated on a per-volume basis. Macroscale can resolve 3D spatial features, but it is more appropriate to use a series of plug flow models to simplify the flow, as spatial resolution cannot reflect the characteristics of the real flow, as the solid-fluid interface is not resolved, but considered as a continuum phase. Macroscale modeling is simple to use. However, it lacks the ability to predict details on a finer scale. Especially in the case where Joule heating is happening inside the fixed bed, it is not able to resolve the interparticle heat transfer through conduction and radiation, as conditions could differ significantly for particles in close proximity. Hence in our study, we make use of a multi-scale DEM Euler-Lagrange model. The interparticle heat transfer is handled with a thermal resistance model. The particle internal is resolved using a 0D subsystem model. The fluid phase is solved using a 1D model that has grid equal to two particle

diameters.

1.2 Scope and Objective

In this work, the possibility of using hydrogen to store renewable electrical energy is investigated. A new design of a electrically driven steam-methane reformer has been proposed in the work [18]. The new reformer consists of a fixed bed of metal and catalyst particles. Unlike conventional reactors where the heat is supplied through the sidewalls, different designs with heat source and heat storage directly embedded in the reactor among catalyst particles are explored. The goal is create a multi-scale model that has the capacity to resolve a fixed bed reactor based on a random packing. The model begins with an individual particle, which is usually simulated by solving 1D partial-differential equations. 0D sub-system model heat and mass transfer inside a catalyst particle with reactions. 1D PDE solutions are used to verify the applicability of the 0D sub-system model under different conditions. An experiment is used to verify electrical calculations in fixed bed. Compare with CFD DNS results. Presentation of concept and use the models in multi-scale simulation. Scale up the simulation to test the computational capabilities. The aim in this work is to develop a 0D model that would allow the simplification of the particle-resolved method. The model has to work with both heat transfer and reactions. The sub-system model is then used in the simulation of a bed of particles and compared to published case of a conventional steam methane reformer. With each component validated, the reformer is scaled up to test the model's computational ability. For the heat transfer in the bulk of the reformer, the fluid phase is resolved using mesoscale heat equations.

Bibliography

[1] IEA. The future of hydrogen. Technical report, G20, 2019.

[2] T. Taner. The novel and innovative design with using H_2 fuel of PEM fuel cell: Efficiency of thermodynamic analyze. *FUEL*, 302:121109, 2021. ISSN 00162361.

[3] A. Scipioni, A. Manzardo, and R. Jingzheng. *Hydrogen economy: supply chain, life cycle analysis and energy transition for sustainability.* Academic Press, 2017.

[4] S. Takenaka, Y. Shigeta, E. Tanabe, and K. Otsuka. Methane decomposition into hydrogen and carbon nanofibers over supported Pd-Ni catalysts: characterization of the catalysts during the reaction. *The Journal of Physical Chemistry B*, 108(23):7656–7664, 2004.

[5] S.H. Sharif-Zein and A.R. Mohamed. $Mn/Ni/TiO_2$ catalyst for the production of hydrogen and carbon nanotubes from methane decomposition. *Energy & Fuels*, 18:1336–1345, 2004.

[6] A. F. Cunha, N. Mahata, J. J. M. Orafo, and J. L. Figueiredo. Methane decomposition on la2o3-promoted raney-type Fe catalysts. *Energy & Fuels*, 23(8):4047–4050, aug 2009.

[7] Sulong Geng, Zhennan Han, Yan Hu, Yanbin Cui, Junrong Yue, Jian Yu, and Guangwen Xu. Methane decomposition kinetics over Fe_2O_3 catalyst in micro fluidized bed reaction analyzer. *Industrial & Engineering Chemistry Research*, 57(25):8413–8423, jun 2018.

[8] Bingying Gao, I-Wen Wang, Lili Ren, Thomas Haines, and Jianli Hu. Catalytic performance and reproducibility of Ni/Al_2O_3 and Co/Al_2O_3 mesoporous aerogel catalysts for methane decomposition. *Industrial & Engineering Chemistry Research*, 58(2):798–807, dec 2018.

[9] M. J. Lázaro, J. L. Pinilla, R. Utrilla, I. Suelves, R. Moliner, F. Moreno, and M. Muñoz. H2-CH4 mixtures produced by carbon-catalyzed methane decomposition as a fuel for internal combustion engines. *Energy & Fuels*, 24(6):3340–3345, feb 2010.

[10] Jaimee K. Dahl, Victor H. Barocas, David E. Clough, and Alan W. Weimer. Intrinsic kinetics for rapid decomposition of methane in an aerosol flow reactor. *International Journal of Hydrogen Energy*, 27(4):377–386, 2002. ISSN 0360-3199.

[11] G. Maag, S. Rodat, G. Flamant, and A. Steinfeld. Heat transfer model and scale-up of an entrained-flow solar reactor for the thermal decomposition of methane. *International Journal of Hydrogen Energy*, 35(24):13232–13241, 2010. ISSN 0360-3199. 3rd Asian Bio Hydrogen Symposium.

[12] D. Paxman, S. Trottier, M.R. Flynn, L. Kostiuk, and M. Secanell. Experimental and numerical analysis of a methane thermal decomposition reactor. *International Journal of Hydrogen Energy*, 42(40):25166–25184, 2017. ISSN 0360-3199.

[13] K. Aasberg-Petersen, J.H. Bak Hansen, T.S Christensen, I. Dybkjaer, P.S. Christensen, C. Stub Nielsen, S.E.L Winter Madsen, and J.R Rostrup-Nielsen. Technologies for large-scale gas conversion. *Applied Catalysis A: General*, 221(1-2):379–387, 2001. ISSN 0926860X.

[14] M.B. Glaser and G. Thodos. Heat and momentum transfer in the flow of gases through packed beds. *AIChE Journal*, 4(1):63–68, 1958.

[15] M. Rieks, R. Bellinghausen, L. Mleczko, and N. Kockmann. Experimental study of methane dry reforming in an electrically heated reactor. *International Journal of Hydrogen Energy*, 40 (46):15940–15951, 2015. ISSN 03603199.

[16] Raynald Labrecque and Jean Michel Lavoie. Dry reforming of methane with CO_2 on an electron-activated iron catalytic bed. *Bioresource Technology*, 102:11244–11248, 2011.

[17] J.M. Lavoie. Review on dry reforming of methane, a potentially more environmentally-friendly approach to the increasing natural gas exploitation. *Frontiers in Chemistry*, 2:81, 2014.

[18] Y.R. Lu and P. Nikrityuk. A new fixed bed reactor for electrical energy storage into chemicals: Proof of concept. *Applied Energy*, 228:593–607, 2018.

Chapter 2

A 0D Sub-system model for the Heat and Mass Transfer inside a spherical catalyst [1]

Abstract

This work is devoted to the development and validation of a new 0-D model (sub-model) for the steam reforming of methane inside a spherical catalyst particle (Ni/α-Al_2O_3) placed in a hot methane/steam atmosphere. The particle diameter is 4 mm. The submodel includes six gaseous chemical species (CH_4, CO_2, CO, H_2O, H_2, N_2) and uses experimentally defined reaction rate expressions taken from the literature. The distinguishing feature of the subgrid model is its ability to take into account the internal heat and mass transfer coupled with the heat and mass transfer on the catalyst surface influenced by convection and diffusion around the particle. The sub-model was validated against a comprehensive 3D-CFD-based model resolving the issues of bulk flow, thermal and species boundary layers around the particle and convection and diffusion processes inside the porous catalyst particle. Good agreement was achieved between the new 0-D model and the 3D CFD-based model.

[1] This chapter is based on the work: Yi Ran Lu, Dmitry Pashchenko, Petr A. Nikrityuk. *A New Semi-empirical Model for the Heat and Mass Transfer Inside a Spherical Catalyst in a Stream of Hot CH_4/H_2O gases*, Chemical Engineering Science, Vol. 238, pp. 116565, 2021. DOI: 0.1016/j.ces.2021.116565

Nomenclature

A_p	particle surface area	Sh	Sherwood number
V_p	particle volume	Re	Reynolds number
c_p	specific heat capacity	Sc	Schmidt number
D	diffusivity	Nu	Nusselt number
d	diameter	Pr	Prandtl number
K	equilibrium constant	ρ	gas density
k_1, k_2, k_3	reaction rate coefficient	ϵ_v	catalyst void fraction
α	stoichiometric coefficient	a	adsorption coefficient
k_{eff}	thermal conductivity	μ	dynamic viscosity
ε	particle porosity	τ	tortuosity
$\vec{v}$	velocity	P	Pressure
U_{in}	Inlet gas velocity	p_i	Partial pressure of species i
R_g	ideal gas constant	M	molar mass

h_{pg}	Particle-gas heat transfer coefficient
β_{pg}	Particle-gas mass transfer coefficient
$(hA)_{in}$	Particle internal heat transfer coefficient
$(\beta A)_{in}$	Particle internal mass transfer coefficient
N_p, N_r	number of particles, number of reactions
$R_{V,r}, R_{s,r}$	volume, surface based reaction rate
T_{in}	Ambient temperature and inflow temperature in 3D simulations
T_s	Temperature of the catalyst surface in 0-D model
T_p	Particle-averaged temperature inside the particle in 3D model or in 0-D model
$Y_{i,in}$	Ambient mass fraction of species i in 0-D model and inflow mass fraction in 3D model
$Y_{i,s}$	Mass fraction of species i on the catalyst surface in 0-D model
$Y_{i,p}$	Particle-averaged mass fraction of species i in 3D model or in 0-D model

2.1 Introduction

Today, the sustainable production of hydrogen is becoming extraordinarily important for the next step of industrial growth combined with a reduction of CO_2 emissions around the world [1]. One of the options for the increased production of H_2 is the storage of electricity (during overproduction peaks) in the form of chemicals [2, 3]. Steam methane reforming is and will continue to be basically considered a primary technology for the industrial production of hydrogen. For a review of technological developments in hydrogen production, we refer to a review [4] and books [1].

In the design of novel, more effective reactors for steam methane reforming, the important issue is the adequate prediction of the basic characteristics of such devices, e.g., their length and diameter

(see the book [1]. Due to the complexity of physical and chemical processes inside reformers, experimental studies are not always capable of characterizing the basic features of all related phenomena. Therefore, computer simulation models have become well-established tools for understanding and optimizing steam-methane reformers, e.g. see the work [5, 6]. It should be noted that all these models use Computational Fluid Dynamics (CFD) equations and algorithms, e.g. see the review [7]. For instance, a number of works have been recently published on the numerical modeling of lab-scale reformers, e.g. [8] and industrial-scale reactors[5, 6, 9].

In particular, an analysis of these works shows that basically five global models are used:

- an equilibrium model [10, 11],
- a CFD-based permeability model[8] (fixed bed is treated as a porous media),
- a catalyst-resolved CFD-based model [12] (transport equations and numerical grid resolve catalyst particles, but particles are treated as porous or solid)
- 1D & 2D mixture-based models [12, 9] (heat and mass transfer are modeled using mixture formulation)
- semi-empirical based models [13], which use semi-global balance heat and mass transfer equations coupled with closure relations for nondimensional numbers.

It should be critically emphasized that the distinguishing feature of all permeability- or mixture-based CFD simulations of reformers is the use of so-called computational closure relations or equations describing catalyst-gas and catalyst-wall interactions on the single-catalyst-particle level or describing axial and radial dispersion coefficients in fixed beds, respectively, e.g. see the works [12, 9].

Recently, with significant progress in multi-scale numerical simulations of dense particulate flows, e.g. see the reviews [14, 15], particle-unresolved Euler-Lagrange models in the form of coupled discrete-element models (DEM) and CFD models are becoming a well-accepted tool for simulations of large-scale particulate systems. In DEM-CFD methods, the fluid phase is treated in Euler space using CFD and the particle trajectories are modeled in Lagrangian space using DEM [14, 15]. Depending on the level of coupling, DEMs and CFD models are connected using closure relations [14]. In particular, to model the heat and mass transfer using a particle-unresolved DEM-CFD model, special closure submodels are required, e.g. see the latest review [15]. It should be emphasized that particle-unresolved DEM-CFD models showed good capabilities in modeling the heat and mass transfer in complex particulate systems [16], where permeability-based CFD models or mixture models fail to predict transport phenomena in particulate media adequately. With this in mind, so-called direct numerical simulations, e.g. see the works [17, 18], are used to verify and validate new submodels for mixture-based models or particle unresolved DEM-CFD simulations. One of the

first steps in the development and validation of submodels for chemically reacting particles is single particle-resolved CFD, e.g. see the work [19], which can be enhanced to a model for packed beds, e.g. see the work [20].

Referring to catalyst-resolved CFD studies and the development of new submodels for convective-diffusion heat and mass transfer around and inside catalyst, a number of works have been reported in the literature. The idea of using an internal mass transfer coefficient to model mass transfer, or internal Sherwood number, was first proposed by Balakotaiah et al.[21, 22]. In their study, the authors examined the performance of internal mass transfer coefficient related to the effectiveness factor and Thiele modulus. However, it should be emphasized that pioneering semi-empirical relations for the heat/mass transfer inside the catalyst particles used classical models utilizing pellet effectiveness factor via Thiele module and effective diffusion coefficient of CH_4, which were derived for steady-state intra-pellet mass/heat transfer in the case of first-order reaction, e.g. see the book [23]. With time progressing, new more complex kinetics, e.g. Langmuir-Hinshelwood-Hougen-Watson (LHHW) kinetics for SMR, were reported in the literature [24]. Thus, the use of the effectiveness factor for such kinetics, especially for the unsteady intra-pellet mass/heat transfer, is not a trivial task.

Dixon et al [25] carried out 3-D CFD-based resolved-particle simulations of a single catalyst particle placed in a stream of hot steam/methane. The commercial software ANSYS-Fluent was used. The catalyst particle was modeled as a porous region and alternatively as a solid, allowing no-slip surface flow boundary conditions on the particle surface. It was demonstrated that using a porous representation of the catalyst particle results in inaccurate temperature and species profiles due to an artifact of convective flux across the particle-fluid interface. It should be noted that this uncertainty was demonstrated for the turbulent flow regime ($Re = 10^4$) using a SST-$k - \omega$ RANS model. We assume that inaccuracies in temperature and species profiles inside the porous catalyst can be attributed to spurious flows inside the porous particle caused by the use of interior boundaries along with the co-located storage of variables. This could be minimized by refining the mesh inside the particle, which will automatically cause high computational costs. In this view, the use of "solid particle" approach proposed by the authors of [25] is more computationally reliable.

Sulaiman et al. [26] carried out a numerical investigation using 2D axisymmetric CFD into the interplay between convection, diffusion and reaction, referring to an isothermal solid spherical catalyst particle experiencing a first-order irreversible reaction. The authors additionally established a 0-D model for the mass transfer between the isothermal particle and bulk flow. No heat transfer model was presented. This model uses a mean volume species concentration to account for diffusion inside the catalyst and internal first-order chemical reactions. The authors employed the decoupled treatment of external and internal mass transfer, where the internal mass transfer coefficient was coupled with kinetics for the first-order chemical reaction. This submodel produced good agreement with isothermal 2D axisymmetric CFD results over a wide range of Reynolds numbers and Schmidt numbers.

In conclusion, it should be noted that recent publications devoted to CFD-based simulations of the heat and mass transfer inside and around a catalyst particle in a hot gas atmosphere, operate with the influence of input parameters such as the particle velocity, ambient temperature or ambient concentration for a single reaction case. However, no efforts have been made to develop and to validate a semiempirical model for multiple reactions cases, such as LHHW kinetics [24], referring to steam methane reforming (SMR), which are well-established kinetics used for CFD simulations of SMR [12, 9]. Such a semiempirical model can serve as a submodel for the heat and mass transfer inside and around a catalyst particle is of great importance in the successful modeling of large-scale reformers using Euler-Lagrange-based models. Additionally, existing isothermal submodels validated against catalyst-resolved CFD operate only with volume-averaged dependent variables, such as the temperature and species concentration, neglecting the heat and mass transfer on the catalyst surface. Motivated by this fact, in this work, we develop a sub-model for the steam reforming of the methane inside a catalyst particle placed in a stream of hot steam/methane atmosphere. This model accounts for the internal heat and mass transfer using surface-averaged and volume-averaged species concentrations instead of only mean volume concentrations. The model is validated against a comprehensive CFD-based model, where the Navier-Stokes equations coupled with the energy and species conservation equations were used to solve the problem by means of the steady state approach.

2.2 Problem and semi-empirical model formulation

Before we proceed with the formulation of a 0-D model, we next describe the computational domain and input conditions for the model. We consider a porous spherical catalyst particle with a diameter of $d_p = 4$ mm and porosity of $\varepsilon = 0.5$ placed in a hot stream of steam, methane and nitrogen. The inflow Reynolds number $Re = \frac{\rho_{in} U_{in} d_p}{\mu_{in}}$ is 100. The composition of the inflow gas is $Y_{in,CH_4} = 0.3$, $Y_{in,H_2O} = 0.6$ and rest is Y_{in,N_2}. The inflow temperature is varied between 600 K and 1000 K. The ambient pressure is one atmosphere. A diagram of the problem setup is shown in Fig. 2.1a. In this work we assume that all reactions occur inside the catalyst particle. The choice of Re and the particle size is related to a new fixed bed, see the work [3], where the electrical heating is used to drive SMR. Finally, the second reason of small Re is to avoid turbulent flow conditions, which accurate modeling is computationally expensive.

The following assumptions are made in the semi-empirical model

- Viscous heating and buoyancy effects are neglected.
- Thermal diffusion is neglected.
- The particle is not-permeable for the gas flow.
- The particle is porous and its porosity is isotropic, the particle porosity is $\varepsilon = 0.5$. This

value of porosity was used only for the verification against 3D CFD simulations and is not a necessary characteristic used for the 0D model.

2.2.1 Mass transfer

The balance of the chemical species on the particle surface takes the following form:

$$\underbrace{\beta_{pg} A_p \rho_{g,s} \left(Y_{i,in} - Y_{i,s}\right)}_{Convection\ and\ Diffusion} + \underbrace{M_i A_p \sum_{r}^{N_r} \alpha_{r,i}\ R_{s,r}}_{Surface\ reactions} = \underbrace{\left(\beta A\right)_{in} \rho_{g,p} \left(Y_{i,s} - Y_{i,p}\right)}_{Intraparticle\ Diffusion} \tag{2.1}$$

where β_{pg} is the mass transfer coefficient due to the external convection and diffusion, $(\beta A)_{in}$ is the mass transfer coefficient describing the diffusion inside the particle and $Y_{i,s}$ is the particle surface-averaged mass fraction of species $'i'$.

The balance equation for the chemical species inside the particle takes the following form:

$$V_p \epsilon_v \rho_{g,p} \frac{dY_{i,p}}{dt} = (\beta A)_{in} \rho_{g,p} (Y_{i,s} - Y_{i,p}) + \underbrace{M_i V_p \sum_{r}^{N_r} (\alpha_{r,i} R_{V,r})}_{Reactions\ inside\ Particle} \tag{2.2}$$

where $Y_{i,p}$ reflects the particle volume-averaged mass fraction of species $'i'$. Similar model equations (with different source terms) for the chemical species on the particle surface and for the chemical species inside the particle have been successfully applied for the modeling of char particles gasification in entrained-flow gasifiers. Validations of that methodology against experimental data showed very good agreement, see the work by Schulze at al. [27].

It should be noted that eq. (2.2) is written in a general unsteady form. In a steady state, eq. (2.2) and eq. (2.1) can be combined into one equation:

$$\beta_{pg} A_p \rho_{g,s} (Y_{i,in} - Y_{i,s}) + M_i A_p \sum_{r}^{N_r} \alpha_{r,i}\ R_{s,r} + M_i V_p \sum_{r}^{N_r}\ \alpha_{r,i} R_{V,r} = 0 \tag{2.3}$$

Neglecting the term describing chemical reactions on the particle surface, we have the final equation:

$$Y_{i,s} = Y_{i,in} + \frac{M_i V_p \sum_{r}^{N_r} (\alpha_{r,i} R_{V,r})}{\beta_{pg} A_p \rho_{g,s}} \tag{2.4}$$

Using that equation, we can calculate $Y_{i,s}$.

After $Y_{i,s}$ is defined, we can calculate $Y_{i,p}$:

$$Y_{i,p} = Y_{i,s} + \frac{M_i V_p \sum_{r}^{N_r} (\alpha_{r,i} R_{V,r})}{(\beta A)_{in} \rho_{g,p}} \tag{2.5}$$

Using Eqs. (2.4) and (2.5) we finally have:

$$Y_{i,p} = Y_{i,in} + M_i V_p \sum_r^{N_r} (\alpha_{r,i} R_{V,r}) \left(\frac{1}{\beta_{pg} A_p \rho_{g,s}} + \frac{1}{(\beta A)_{in} \rho_{g,p}} \right) \tag{2.6}$$

Finally, we emphasize that eq. (2.5) is fully implicit equations because terms which include $R_{V,r}$ depends nonlinearly on $Y_{i,p}$. However, the form of eq. (2.5) corresponds to the fixed-point numerical method, which was used to solve this equation for each species. To illustrate the nonlinearity of eq. (2.5) we write this equation in the full form for $Y_{CH_4,p}$:

$$Y_{CH_4,p} = Y_{CH_4,s} + \\ + \frac{M_{CH_4} V_p}{(\beta A)_{in} \rho_{g,p}} \left(- \frac{k_1 (p_{\mathrm{CH_4}} p_{\mathrm{H_2O}}^{0.5} - p_{\mathrm{H_2}}^3 p_{\mathrm{CO}} / K_1 p_{\mathrm{H_2O}}^{0.5})}{p_{\mathrm{H2}}^{1.25} \mathrm{den}^2} - \frac{k_3 (p_{\mathrm{CH_4}} p_{\mathrm{H_2O}} - {p_{\mathrm{H_2}}}^4 p_{\mathrm{CO_2}} / K_3 p_{\mathrm{H_2O}})}{{p_{\mathrm{H_2}}}^{3.5} \mathrm{den}^2} \right) \tag{2.7}$$

where $p_{CH_4} = \frac{Y_{CH_4} P M}{M_{CH_4}}$. For mathematical expressions of terms in that equation we refer to Section 2.2.3 and Section 2.2.4.

We want to emphasize that the chemical reactions on the particle surface were neglected because the ratio between the particle surface and overall particle surface participating in the reactions is $6 \cdot 10^{-3}\%$ for $d_p = 4$ mm. The surface area (BET, m^2/g) of the catalyst is 14.3 m^2/g, see the work [24].

2.2.2 Heat transfer

An equation describing the heat balance on the catalyst surface takes the following form:

$$\underbrace{(hA)_{in} (T_s - T_p)}_{Internal\ Diffusion} = \underbrace{h_{pg} A_p (T_{in} - T_s)}_{External\ Convection\ and\ Diffusion} + \underbrace{\epsilon \sigma A_p \left(T_{in}^4 - T_s^4\right)}_{Radiation} + \underbrace{A_p \sum_r^{N_r} (-\Delta H_r) R_{s,r}}_{Surface\ reactions} \tag{2.8}$$

where T_s is the particle surface-averaged temperature. The emissivity of the particle surface was set to 0.7. It should be noted that T_{in} corresponds to the inlet temperature of the gas and at the same time in the problem we solve it equals to the ambient temperature of the gas T_∞. For dense bed systems (fixed beds or fluidized beds) T_{in} will correspond to the gas phase temperature inside a control volume where the particle is placed. The following works [20, 3] show formulations of eq. (2.8) for cases with multiple particles. The radiative heat transfer between the particle surface and the bulk flow having the temperature $T = T_{in} = T_\infty$ is modeled using the Stefan-Boltzmann term $\epsilon \sigma A_p \left(T_{in}^4 - T_s^4\right)$, which is well acceptable approximation for the modeling of the radiative heat transfer between a solid surface and bulk gas flow. For an example we refer to the works by Schulze

et al. [27] (single particle case) and by Lu and Nikrityuk [3] (multiple particles case).

The particle temperature T_p can be calculated similarly to two temperature 0-D model developed for an ice-particle melted in a stream of hot water [28]:

$$m_p c_p \frac{dT_p}{dt} = (hA)_{in}(T_s - T_p) + \underbrace{V_p \sum_r^{N_r} (-\Delta H_r) R_{V,r}}_{Reactions\ inside\ Particle} \tag{2.9}$$

where T_p reflects the volume-averaged temperature of the particle. It should be noted that similar two temperature 0-D model has been validated against experimental data referring to phase change phenomena, see the works [29, 30, 31]. In a steady state, both equations can be combined into one equation:

$$h_{pg} A_p (T_{in} - T_s) + \epsilon \sigma A_p (T_{in}^4 + T_s^4) - A_p \sum_r^{N_r} (-\Delta H_r) R_{s,r} + V_p \sum_r^{N_r} (-\Delta H_r) R_{V,r} = 0 \tag{2.10}$$

Neglecting the impact which chemical reactions on the particle surface exert on the overall heat rate, we may write the final equation:

$$h_{pg} A_p (T_{in} - T_s) + \epsilon \sigma A_p \left(T_{in}^4 - T_s^4\right) + V_p \sum_r^{N_r} (-\Delta H_r) R_{V,r} = 0 \tag{2.11}$$

That equation can be easily solved using the Newton method to find T_s.

Finally, in a steady state, the particle temperature T_p can be predicted using the following equation:

$$T_p = T_s + \frac{V_p \sum_r^{N_r} (-\Delta H_r) R_{V,r}}{(hA)_{in}} \tag{2.12}$$

The system of equations comprising of Eqs. (2.4), (2.6), (2.11) and (2.12) is solved implicitly via Matlab. All equations, except Eq. (2.10), whose solution was found applying the Newton method, were calculated utilizing a fixed-point method with underrelaxation. The iterations were stopped when the estimated relative error for each dependent variable (T_s, T_p, $Y_{i,s}$, $Y_{i,p}$) was less than 10^{-6}.

2.2.3 Closure relations

The external mass transfer coefficient β_{pg} is calculated from the Sherwood number correlation.

$$Sh = \frac{\beta_{pg} \cdot 2r_p}{D_i} \tag{2.13}$$

Likewise, the heat transfer coefficient is calculated from the Nusselt number.

$$Nu = \frac{h_{pg} \cdot 2r_p}{k_g} \tag{2.14}$$

The Sherwood and Nusselt numbers are obtained using the Whitaker correlation [32]:

$$Nu = 2 + \left(0.4Re^{0.5} + 0.06Re^{0.67}\right) Pr^{0.4} \left(\frac{\mu}{\mu_s}\right)^{0.25} \tag{2.15}$$

In this work we assume that the Lewis number equals unity ($Le = 1$), which is a reasonable assumption for the chemically reacting systems particle-gase under laminar flow conditions, e.g. see the works [19, 27]. Finally, we may write the following $Nu = Sh$:

$$Sh = 2 + \left(0.4Re^{0.5} + 0.06Re^{0.67}\right) Sc^{0.4} \left(\frac{\mu}{\mu_s}\right)^{0.25} \tag{2.16}$$

This statement can be approved by the fact that if the Lewis number equals to unity then $Pr = Sc$.

The particle Reynolds number is calculated using

$$Re_p = \frac{\rho_{in} \mathbf{U}_{in} \cdot 2r_p}{\mu_{in}} \tag{2.17}$$

The diffusion coefficient D_i is obtained by using the Lewis number equals to 1.

$$Le = \frac{k_g}{D_i c_p \rho} = 1; \;\; D_i = \frac{k_g}{c_p \, \rho} \tag{2.18}$$

where transport properties k_g, c_p and μ are functions of T and are calculated utilizing polynomials taken from the data base [33].

The mass and heat transfer coefficients for the intraparticle mass and heat transfer are defined as follows [29]:

$$(\beta A)_{in} = 4\pi D_{\text{eff}} \left(\frac{1}{a_1 r_p} - \frac{1}{r_p}\right)^{-1} \tag{2.19}$$

$$(hA)_{in} = 4\pi k_{eff} \left(\frac{1}{a_1 r_p} - \frac{1}{r_p}\right)^{-1} \tag{2.20}$$

where $a_1 = 0.85$ [29]

The effective diffusion coefficient inside the porous particle D_{eff} is expressed using void volume fraction and tortuosity.

$$D_{\text{eff}} = \frac{\varepsilon}{\tau} D_i \approx \varepsilon^2 D_i \tag{2.21}$$

It should be noted that this relation corresponds to micropore-macropore model of Wakao and

Smith [34]. In this work we use this relation only for purposes of validation against 3D CFD. For comparisons with experimental data we have to use exact values of τ measured in experiments. Plus, the Knudsen diffusion should be taken into account if we want to compare our model with experiments.

2.2.4 Kinetics

Reaction rates $R_{V,r}$ for each chemical reaction are calculated from reaction kinetics [24], where the reaction kinetics for steam reforming are given in the units of [mol/m^3·s].

$$\mathrm{CH_4 + H_2O \Leftrightarrow CO + 3H_2} \tag{2.22}$$

$$R_{V,1} = \frac{k_1(p_{\mathrm{CH_4}} p_{\mathrm{H_2O}}^{0.5} - p_{\mathrm{H_2}}^3 p_{\mathrm{CO}} / K_1 p_{\mathrm{H_2O}}^{0.5})}{p_{\mathrm{H2}}^{1.25} \mathrm{den}^2} \tag{2.23}$$

$$\mathrm{CO + H_2O \Leftrightarrow CO_2 + H_2} \tag{2.24}$$

$$R_{V,2} = \frac{k_2(p_{\mathrm{CO}} p_{\mathrm{H_2O}}^{0.5} - p_{\mathrm{H_2}} p_{\mathrm{CO_2}} / K_2 p_{\mathrm{H_2O}}^{0.5})}{p_{\mathrm{H2}}^{0.5} \mathrm{den}^2} \tag{2.25}$$

$$\mathrm{CH_4 + 2H_2O \Leftrightarrow CO_2 + 4H_2} \tag{2.26}$$

$$R_{V,3} = \frac{k_3(p_{\mathrm{CH_4}} p_{\mathrm{H_2O}} - {p_{\mathrm{H_2}}}^4 p_{\mathrm{CO_2}} / K_3 p_{\mathrm{H_2O}})}{{p_{\mathrm{H_2}}}^{3.5} \mathrm{den}^2} \tag{2.27}$$

$$\mathrm{den} = 1 + K_{\mathrm{CO}} * p_{\mathrm{CO}} + K_{\mathrm{H}} * p_{\mathrm{H_2}}^{0.5} + K_{\mathrm{H_2O}} * p_{\mathrm{H_2O}} / p_{\mathrm{H_2}} \tag{2.28}$$

According to the work [24], the rate coefficients are

$$k_1 = 5.922 \cdot 10^8 \exp\left(\frac{-209200}{R_g\, T}\right) \ [\mathrm{kmol/s/kg/kPa^{0.25}}] \tag{2.29}$$

$$k_2 = 6.028 \cdot 10^{-4} \exp\left(\frac{-15400}{R_g\, T}\right) \ [\mathrm{kmol/s/kg/kPa}] \tag{2.30}$$

$$k_3 = 1.093 \cdot 10^3 \exp\left(\frac{-109400}{R_g\, T}\right) [\mathrm{kmol/s/kg/kPa^{0.25}}] \tag{2.31}$$

The adsorption coefficients take the following forms [24]:

$$K_{\mathrm{H_2O}} = 9.251 \cdot \exp\left(\frac{-15900}{R_g\, T}\right) \ ; K_{\mathrm{H}} = 5.68 \cdot 10^{-10} \exp\left(\frac{93400}{R_g\, T}\right) [\mathrm{kPa^{-0.5}}] \tag{2.32}$$

$$K_{\mathrm{CO}} = 5.127 \times 10^{-13} \exp\left(\frac{140000}{R_g\, T}\right) [\mathrm{kPa^{-1}}] \tag{2.33}$$

In this work we used the following expressions for the equilibrium coefficients:

$$K_1 = 1.198 \cdot 10^{17} \exp\left(\frac{-26830}{T}\right) [\mathrm{kPa}^2];\ \mathrm{K}_2 = 1.767 \cdot 10^{-2} \exp\left(\frac{4400}{\mathrm{T}}\right) [\mathrm{kPa}] \tag{2.34}$$

$$K_3 = 2.117 \cdot 10^{15} \exp\left(\frac{-22430}{T}\right)\ [\mathrm{kPa}^2] \tag{2.35}$$

Finally, source terms in Eq. (2.2) and the subsequent equations take the following form for each specific species:

$$CH_4 :\ \sum_r^{N_r} (\alpha_{r,i} R_{V,r}) = -\left(R_{V,1} + R_{V,3}\right) \tag{2.36}$$

$$H_2O :\ \sum_r^{N_r} (\alpha_{r,i} R_{V,r}) = -\left(R_{V,1} + R_{V,2} + 2R_{V,3}\right) \tag{2.37}$$

$$CO :\ \sum_r^{N_r} (\alpha_{r,i} R_{V,r}) = R_{V,1} - R_{V,2} \tag{2.38}$$

$$CO_2 :\ \sum_r^{N_r} (\alpha_{r,i} R_{V,r}) = R_{V,2} + R_{V,3} \tag{2.39}$$

$$H_2 :\ \sum_r^{N_r} (\alpha_{r,i} R_{V,r}) = 3R_{V,1} + R_{V,2} + 4R_{V,3} \tag{2.40}$$

The reaction enthalpy for reactions Eq. (2.22), Eq. (2.24) and Eq. (2.26) are $-\Delta H_1 = -206.1$ kJ/mol, $-\Delta H_2 = 41.2$ kJ/mol and $-\Delta H_3 = -165.0$ kJ/mol, respectively. As a reference we used the works [12, 35]. The relation between the partial pressure and mass fraction is

$$p_i = \frac{Y_i P\, M}{M_i};\ M = \frac{1}{\sum_i^N \frac{Y_i}{M_i}} \tag{2.41}$$

2.3 Validation against 3D CFD

To validate our semi-empirical model we use 3D CFD simulations as a validation tool. A diagram of the computational domain is given in Fig. 2.1b. The size of the 3D domain corresponds to $30d_p \times 12d_p \times 12d_p$ in x, y and z directions, respectively. The flow field is directly determined by the inflow, with the mean velocity having a constant value across the inflow plane. The temperature at the inflow exhibits a constant, uniform profile. Far away from the particle, in directions normal to the free stream, we assume, that no more velocity or temperature gradients are present, so all surrounding domain boundaries excluding the in- and outflow, are symmetry boundaries. The domain size, boundary conditions and computational grid (body-fitted mesh with overall $2.2 \cdot 10^6$

control volumes (CVs), where $5 \cdot 10^4$ CVs were used inside the particle) have been taken from the work by Richter & Nikrityuk [36]. The grid and domain size studies were carried out in the work [36]. It should be noted that the grid resolution inside the particle is significantly higher than in works [25, 35]. For this reason we did not conduct a separate grid study.

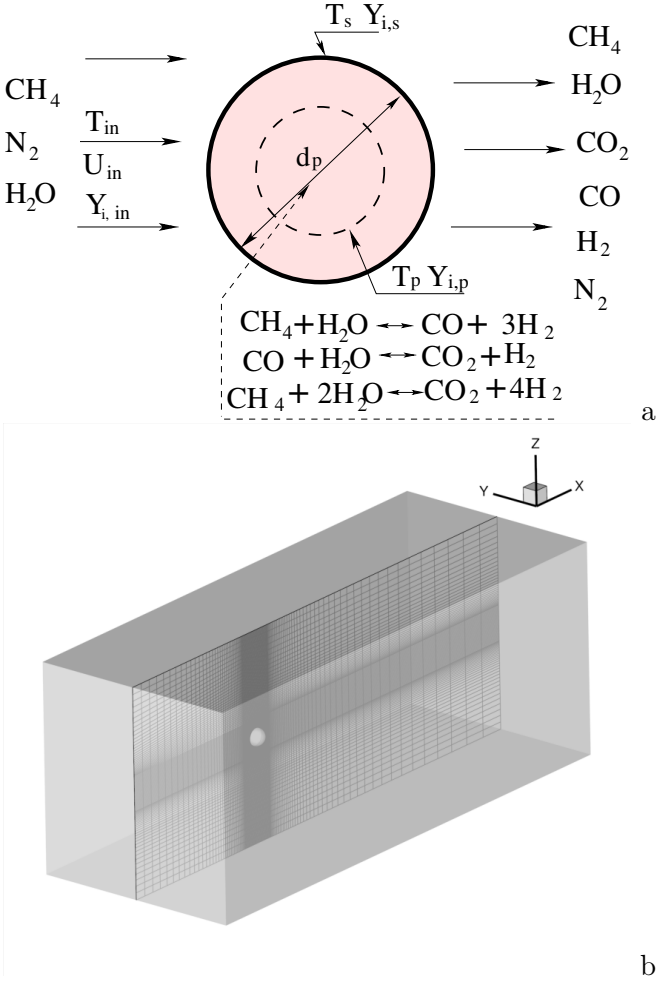

Figure 2.1: Diagram illustrating the catalyst particle places in a stream of hot gas consisting of methane and steam (a), 3D domain ($30d_p \times 12d_p \times 12d_p$) and grid ($2.2 \cdot 10^6$ CV, where $5 \cdot 10^4$ CV were used inside the sphere) for CFD simulations (b).

The set of all CFD equations and CFD software validation can be found in the recent work by Pashchenko and Eremin [35]. In this work the following assumptions were utilized:

- Due to the small velocity magnitudes compared to the local speed of sound, the fluid behaves as a nearly incompressible medium, so the fluid density is treated as an ideal incompressible gas.
- Viscous heating and buoyancy effects are neglected.

- Thermal diffusion is neglected.
- The flow is laminar and steady.
- The particle is porous and its porosity is isotropic, the particle porosity is $\varepsilon = 0.5$.
- The solid and gas phase are in thermal equilibrium inside the porous particle.
- The diffusion coefficient for each species is calculated using the kinetic theory of gases. Inside the porous particle, the diffusion coefficient is computed using eq. (2.21).

The effective thermal conductivity of the porous particle, k_{eff}, is computed as the volume average of the fluid conductivity and the solid conductivity:

$$k_p = k_{\text{eff}} = \varepsilon k_g + (1 - \varepsilon) k_s \tag{2.42}$$

where ε is the porosity of the particle, k_g is the gas phase thermal conductivity, k_s is the solid medium thermal conductivity. In this work we used $c_{p_p} = 1000$ J/kg K, $\rho_p = 1947$ kg/m^3 and $k_p = 1$ W/mK, see the work[12]. The molecular viscosity, which is calculated using the kinetic theory. This option is available in the CFD software Ansys-Fluent 19.1 which was used for CFD simulations.

The flow inside the porous particle is simulated using the Darcy-Forchheimer term added to momentum conservation equations:

$$S_i = -\left(\sum_{j=1}^{3} \frac{1}{\alpha} \mu v_j + \sum_{j=1}^{3} C_2 \frac{1}{2} \rho |v| v_j \right) \tag{2.43}$$

where S_i is the source term for the ith (x, y, or z) momentum equation; $|v|$ is the magnitude of the velocity; α is the permeability and C_2 is the inertial resistance factor. It should be noted that the use of the Darcy-Forchheimer term in the CFD simulations is explained by its default aviability in the commercial CFD-solver ANSYS Fluent. In particular, the 2nd term in Eq. (2.43) does not have any influence on the solution due to the laminar flow regime, see the discussion below.

The permeability and inertial loss coefficient in each component direction were calculated as follows:

$$\alpha = \frac{{D_{pore}}^2}{150} \frac{\varepsilon^3}{(1 - \varepsilon)^2} \tag{2.44}$$

and

$$C_2 = \frac{3.5}{D_{pore}} \frac{(1 - \varepsilon)}{\varepsilon^3} \tag{2.45}$$

where D_{pore} is the pore size; ε is the porosity of the particle. In this CFD model we used $D_{pore} = \frac{d_p}{100}$, $\varepsilon = 0.5$. It should be noted the value of D_{pore} was taken according to damp the gas flow inside the

porous particle. Its value was defined numerically to get a stable CFD solution by damping gas flow inside porous particle. This technique is used in the so-called Immersed Boundary methods. It was shown numerically that gas flow does not penetrate the porous particle with $\varepsilon = 0.5$ under laminar flow conditions [37, 38].

To implement an intrinsic reaction mechanism, the chemical kinetic model described in Section (2.2.4) was hooked to CFD software Ansys-Fluent 19.1 using UDF 'DEFINE_VR_RATE'. The parameters of the chemical model for the CFD model and for the semi-empirical model are the same. Examples of UDFs for the kinetic mechanism defined by Xu and Froment [39] can be found in the work by Pashchenko and Eremin [35]. Finally, we emphasize that the CFD software used in this work have been validated against experimental data for steam methane reforming published in the literature, see the work by Pashchenko and Eremin [35].

2.4 Results

Before we compare the predictions obtained using 0-D and 3D CFD models, we want to describe the main findings calculated utilizing the 3D particle-resolved CFD model. Referring to flow past a spherical particle in a steady-state regime, there are several flow features which should be mentioned. First, for $Re = 100$ (considered in this work) the flow past a sphere is steady laminar and axisymmetric. For this Reynolds number, the isothermal flow past a sphere features a so-called recirculating zone (vortex ring), which develops close to the rear stagnation point. This stagnation point is known as the backward stagnation point. A forward stagnation point is located on the forward side of the sphere surface, namely on the symmetry axis. The forward and backward stagnation points are characterized by the largest and lowest local temperature gradients on the sphere surface [36].

Figs. 2.2 and 2.3 show 3-D distributions of the temperature and species Y_{CH_4} and Y_{H_2} inside the catalyst particle, respectively. In particular, from Fig. 2.2 it can be seen that inside the particle the temperature drops rapidly due to endothermic reactions in the porous catalyst. The mass fraction of CH_4 decreases and the mass fraction of H_2 increases in the particle, see Fig. 2.3. The increase in the ambient temperature T_{in} enhances the drop in the temperature and in Y_{CH_4}. Comparing Figs. 2.2a and 2.2c shows that increase in T_{in} from 600 K to 1000 K causes a significant decrease in the particle temperature such that the temperature in the recirculation zone decreases significantly. It should be noted that the particle surface is not isothermal.

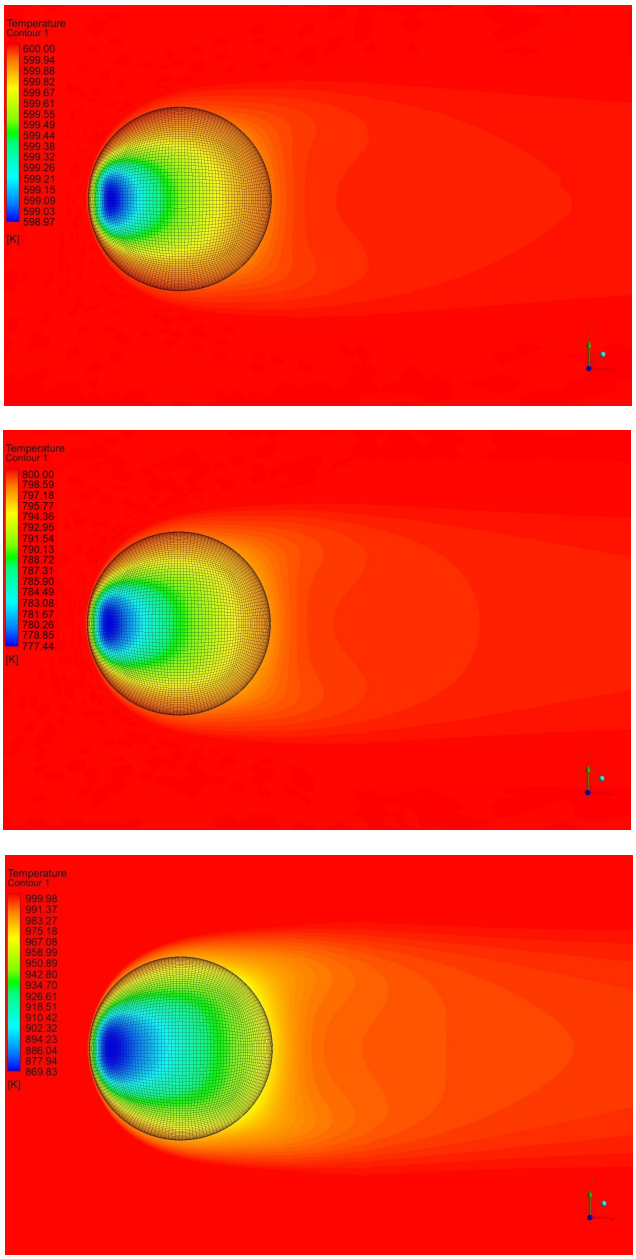

Figure 2.2: Contour plots of the temperature on a slice through the midplane of the particle (YX plane, for $z = 0$) predicted for $Re = 100$ and different ambient temperatures: a - $T_{in} = 600K$, b - $T_{in} = 800K$, c - $T_{in} = 1000K$. The flow is from left to right.

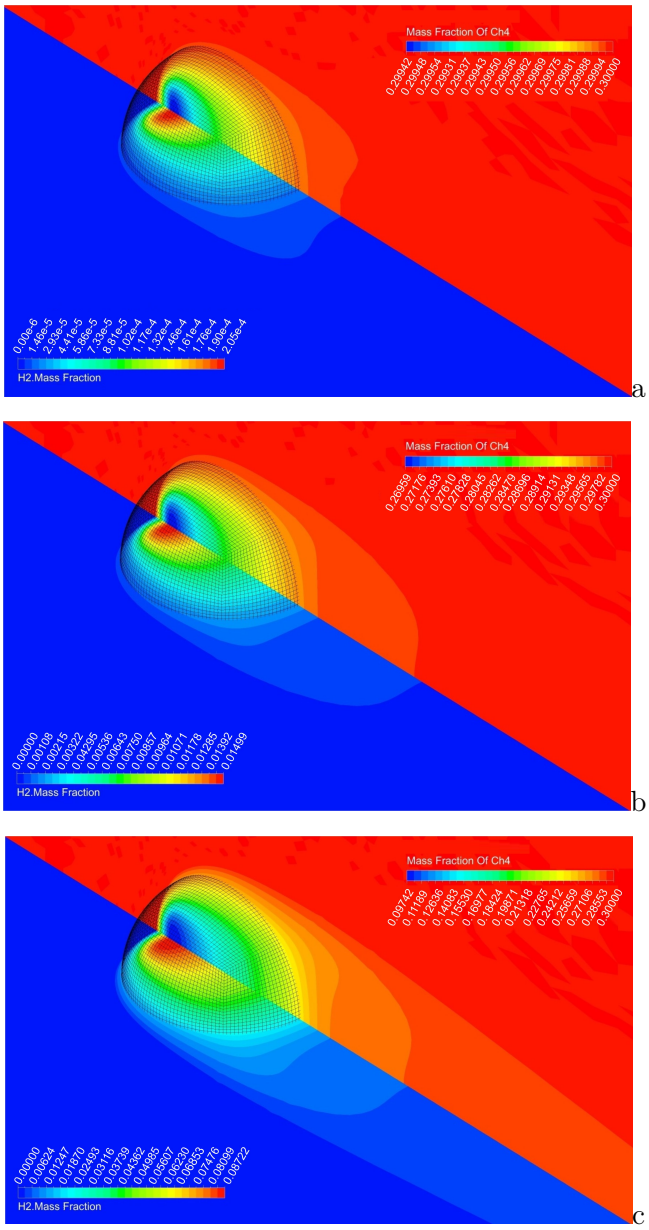

Figure 2.3: 3D distribution of CH_4 and H_2 mass fractions inside the particle predicted for $Re = 100$ and different ambient temperatures: a - $T_{in} = 600K$, b - $T_{in} = 800K$, c - $T_{in} = 1000K$.

For a qualitative illustration of changes in the species mass fractions and temperature inside the particle, Fig. 2.4 depicts axial profiles of T, the methane mass fraction, Y_{CH_4} and hydrogen mass fraction, Y_{H_2} along the particle symmetry axis at $z = 0$ and $y = 0$. Analysis of the profiles revealed strong changes in the temperature and species mass fractions inside the particle with increase in the ambient temperature from 800 K to 1000 K. The minimum temperature inside the particle was detected at $x/d_p = 0.11$ from the forward stagnation point of the sphere, $x = 0$. This distance

corresponds to the minimum values for the methane mass fraction and maximum values for the hydrogen mass fraction. The CH_4 mass fraction decreases inside the particle between $x/d_p = 0$ and $x/d_p = 0.11$, reaching a minimum at $x/d_p = 0.11$. An increase in the ambient temperature T_{in} leads to an increase in the temperature gradients and mass fractions of all species inside the particle. It should be noted, that T_{min} does not correspond to the particle-averaged temperature T_p used in Eq. (2.12). T_{min} is the minimum temperature inside the particle.

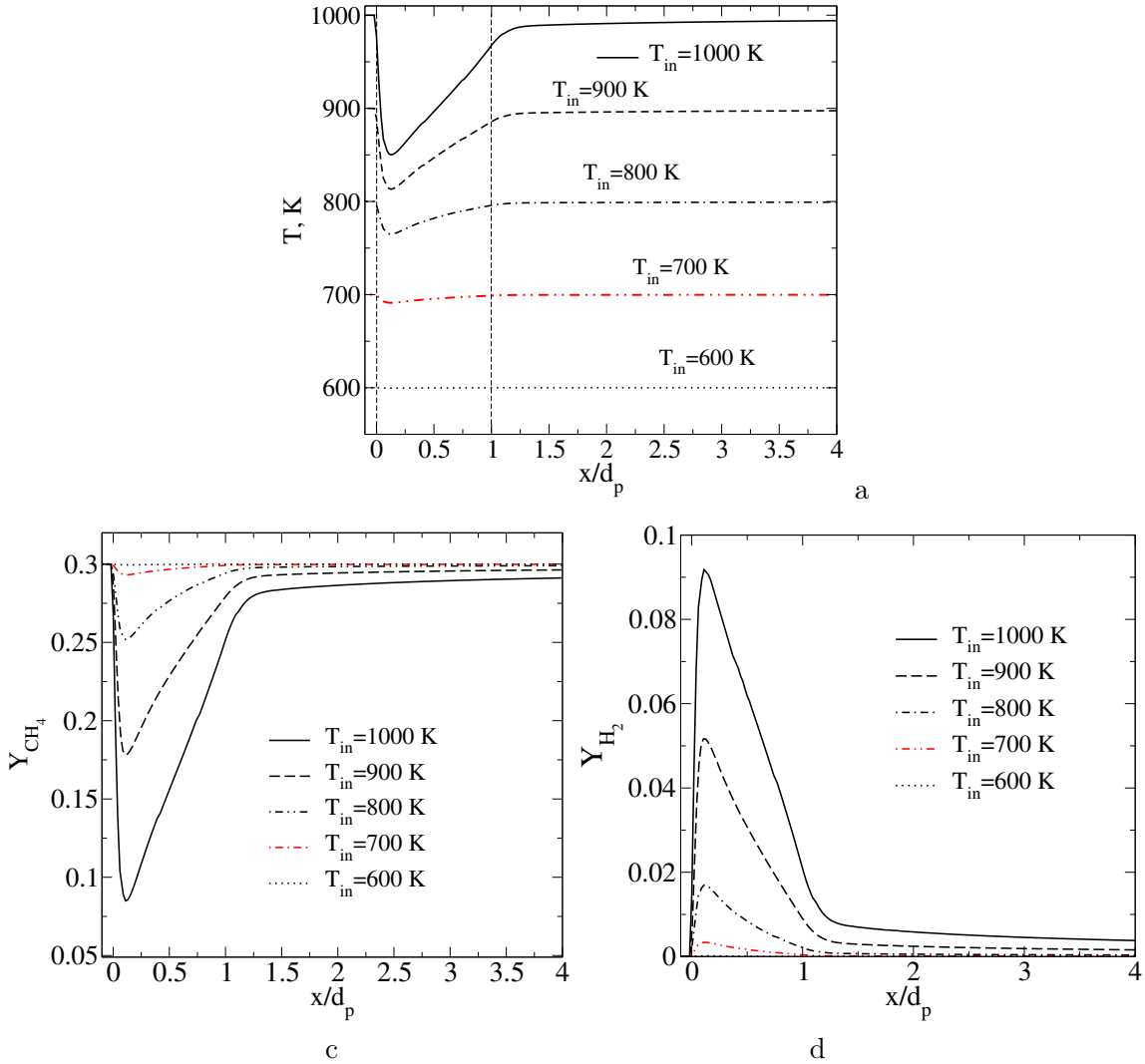

Figure 2.4: Axial profiles of the temperature, T (a), methane mass fraction, Y_{CH_4} (b) and hydrogen mass fraction, Y_{H_2} along the particle symmetry axis at $z = 0$ and $y = 0$ predicted using 3D CFD for different values of the ambient temperature T_{in} and constant $Re = 100$.

To estimate the scale of the temperature drop and change in species mass fractions inside the particle, Fig. 2.5 illustrates the T_{in}-dependence of a change in the temperature difference ($T_{in} - T_{min}$),

a change in the relative temperature difference $\frac{T_{in}-T_{min}}{T_{in}}$ and a change in the relative difference of the CH_4 mass fraction between ambient values and minimum values inside the particle. It can be seen that increase in T_{in} leads to a more significant nonlinear decrease in the CH_4 mass fraction inside the particle (up to 80%) in comparison to the temperature drop (up to 15%).

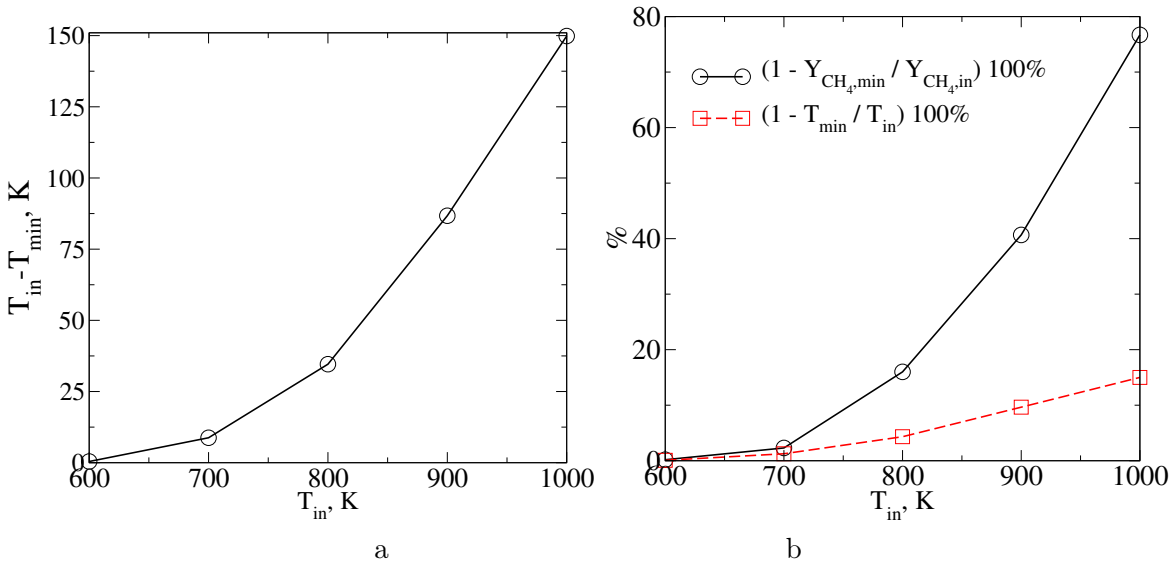

Figure 2.5: Change of temperature ($T_{in} - T_{min}$) (a) and relative differences in the temperature $\frac{T_{in}-T_{min}}{T_{in}}$ and CH_4 mass fraction (b) between ambient values and minimum values inside the particle depending on the ambient temperature T_{in}.

Finally, to compare the results of 3D CFD model against the predictions of the 0-D model, we use the volume-averaged quantities such as the particle-averaged temperature and particle-averaged mass fractions of each species, calculated as follows:

$$T_p = \frac{1}{V_p} \int_{V_p} T\,(x, y, z)\; dV_p \tag{2.46}$$

$$Y_{i,p} = \frac{1}{V_p} \int_{V_p} Y_i\,(x, y, z)\; dV_p \tag{2.47}$$

where $V_p = \frac{4}{3}\pi\, r_p^3$ is the particle volume.

Fig. 2.6 depicts a comparison of the particle-averaged temperature T_p and particle-averaged species mass fractions of species obtained from 3D CFD simulations and T_p, $Y_{i,p}$ predicted using 0-D model for $Re = 100$. Excellent agreement between the two models can be observed. In particular, the 0-D model precisely predicts all the trends relating to the change in the particle temperature and species mass fractions with the increase in the ambient temperature T_{in}. Namely, an increase in

T_{in} from 800 K to 1000 K leads to a significant decrease in the CH_4 and H_2O mass fractions inside the particle and a substantial increase in the H_2, CO and CO_2 mass fractions.

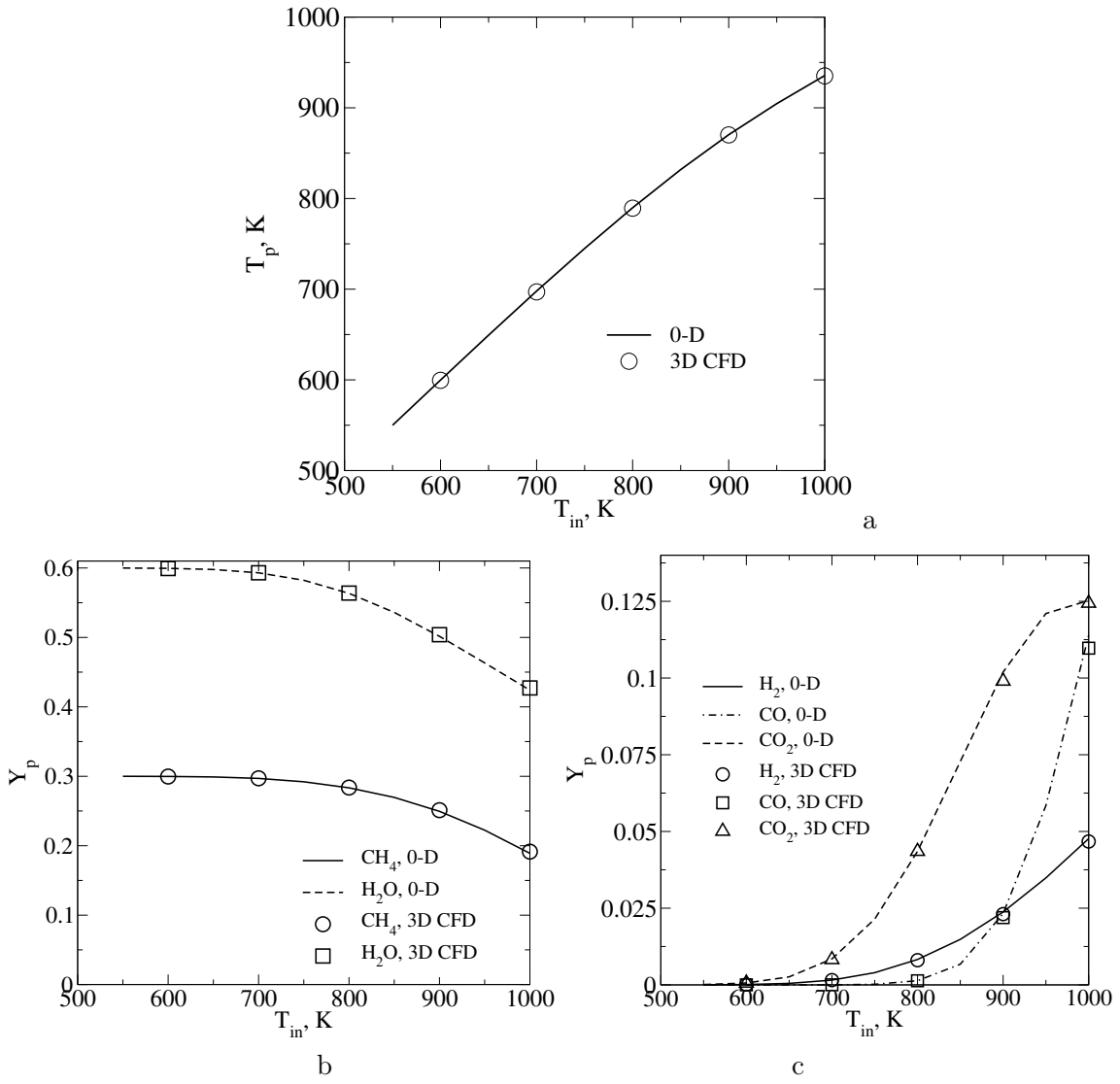

Figure 2.6: 3D CFD vs 0-D: comparison of the particle-averaged temperature (Eq. 2.46) against T_p calculated using Eq. (2.12) (a) and particle-averaged mass fractions of species (Eq. 2.47) (b), (c) obtained from 3D CFD simulations and T_p, $Y_{i,p}$ predicted using the 0-D model (Eq, 2.6) for $Re = 100$.

To estimate the role of the particle surface-averaged temperature, T_s and species mass fractions $Y_{s,i}$ in the heat and mass transfer between the bulk flow and particle, Fig. 2.7 plots the difference between T_s, T_p and T_{in}, and $Y_{i,s}$, $Y_{i,p}$ and $Y_{i,in}$ predicted using the 0-D model for different ambient temperatures and $Re = 100$. Analysis of this figure revealed that, firstly, the particle surface-averaged values of the temperature and mass fractions, T_s, $Y_{s,i}$, deviate substantially from T_p and

$Y_{p,i}$, which characterize the particle internal temperature and mass fractions of the species. The difference between the particle surface-averaged mass fractions of species CH_4 and H_2 and of the same particle-averaged quantities, $(Y_s - Y_p)$. The relative error in mass fraction is larger in comparison to the temperature.

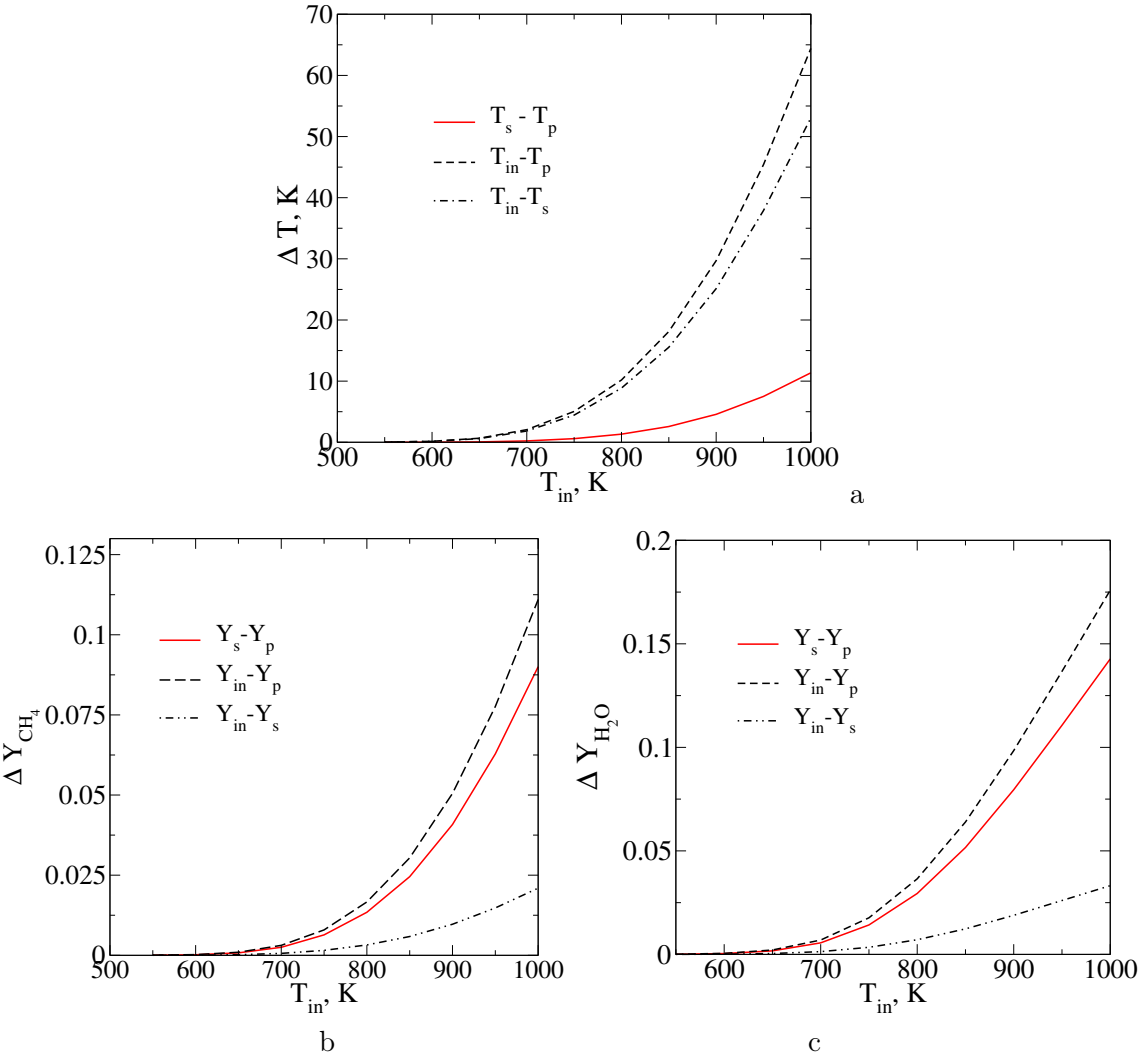

Figure 2.7: 0-D model: change in the difference between T_s, T_p and T_{in} (a) and $Y_{i,s}$, $Y_{i,p}$ and $Y_{i,in}$ of CH_4 (b) and H_2O (c) depending on the ambient temperature T_{in} for $Re = 100$.

2.5 Conclusions

This work presents the development and validations of a new 0-D model for the steam reforming of methane inside a spherical catalyst particle (Ni/α-Al_2O_3) placed in a hot methane/steam atmosphere. The 0-D model includes six gaseous chemical species (CH_4, CO_2, CO, H_2O, H_2, N_2) using a global mechanism of LHHW kinetics taken from the literature. This new model predicts the particle surface-averaged temperature and species mass fractions, and intraparticle values of the temperature and species mass fractions. Introducing surface- and interparticle-relevant variables enables calculations of the particle internal heat and mass transfer coupled with the heat and mass transfer on the catalyst surface influenced by convection and diffusion around the particle. The 0-D model has been validated against a comprehensive 3D-CFD-based model resolving the issues of bulk flow, thermal and species boundary layers around the particle and convection-diffusion processes inside the porous catalyst particle. Excellent agreement was achieved between the results of the new 0-D model and the 3D particle-resolved CFD model. The results of CFD simulations revealed a considerable change in the temperature and species mass fractions inside the particle as the ambient temperature increased from 800 K to 1000 K. The minimum temperature inside the particle was detected at $x/d_p = 0.11$ from the forward stagnation point of the sphere. This distance corresponds to the minimum values for the methane mass fraction and maximum values for the hydrogen mass fraction.

2.6 Acknowledgment

Yi Ran Lu and Petr A. Nikrityuk acknowledge the financial support by the Natural Sciences and Engineering Research Council (NSERC) Canada under the Discovery Grant 'Energy to Chemicals (E2C) using direct electrical current flowing through dense beds'.

Bibliography

[1] Ibrahim Dincer and Calin Zamfirescu. *Sustainable Hydrogen Production.* Elsevier Inc, Amsterdam, Netherlands, 2016.

[2] M. Aneke and M. Wang. Energy storage technologies and real life applications – a state of the art review. *Applied Energy*, 179:350–377, 2016.

[3] Yi Ran Lu and Petr Nikrityuk. A new fixed bed reactor for electrical energy storage into chemicals: Proof of concept. *Applied Energy*, 228:593–607, 2018.

[4] T.L. LeValley, A.R. Richard, and M. Fan. The progress in water gas shift and steam reforming hydrogen production technologies - A review. *Int. J. Hydrogen Energy*, 39:16983–17000, 2014.

[5] A.Tran, A. Aguirre, H. Durand, M. Crose, and P.D. Christofides. CFD modeling of a industrial-scale steam methane reforming furnace. *Chemical Engineering Science*, 171:576–589, 2017.

[6] Son Ich Ngo, Young-Il Lim, Woohyun Kim, Dong Joo Seo, and Wang Lai Yoon. Computational fluid dynamics and experimental validation of a compact steam methane reformer for hydrogen production from natural gas. *Applied Energy*, 236:340–353, 2019.

[7] A.G. Dixon, M. Nijemeisland, and Stitt E.H. Packed tubular reactor modeling and catalyst design using computational fluid dynamics. *Advances in Chemical Engineering*, 31:307–389, 2006.

[8] Dmitry Pashchenko. Effect of the geometric dimensionality of computational domain on the results of CFD-modeling of steam methane reforming. *International Journal of Hydrogen Energy*, 43(18):8662–8673, 2018.

[9] Bhanu Vardhan Reddy Kuncharam and Anthony G. Dixon. Multi-scale two-dimensional packed bed reactor model for industrial steam methane reforming. *Fuel Processing Technology*, 200: 106314, 2020.

[10] Dmitry Pashchenko. Combined methane reforming with a mixture of methane combustion products and steam over a Ni-based catalyst: An experimental and thermodynamic study. *Energy*, 185:573–584, 2019.

[11] Dmitry Pashchenko. Thermodynamic equilibrium analysis of steam methane reforming based on a conjugate solution of material balance and law action mass equations with the detailed energy balance. *International Journal of Energy Research*, 44(1):438–447, 2020.

[12] Dixon A.G. Local transport and reaction rates in a fixed bed reactor tube: Endothermic steam methane reforming. *Chemical Engineering Science*, 168:156–177, 2017.

[13] Alexey Shigarov. Modeling of low temperature steam reforming of flare gas to methane-rich fuel gas on Ni catalyst in different types of reactors. *Chemical Engineering Journal*, 397:125313, 2020.

[14] Martin Anton van der Hoef, M. van Sint Annaland, N.G. Deen, and J.A.M. Kuipers. Numerical simulation of dense gas-solid fluidized beds: a multiscale modeling strategy. *Annu. Rev. Fluid Mech.*, 40:47–70, 2008.

[15] Z. Peng, E. Doroodchi, and B. Moghtaderi. Heat transfer modelling in Discrete Element Method (DEM)-based simulations of thermal processes: Theory and model development. *Progress in Energy and Combustion Science*, 79:100847, 2020.

[16] T. Bluhm-Drenhaus, E. Simsek, S. Wirtz, and V. Scherer. A coupled fluid dynamic-discrete element simulation of heat and mass transfer in a lime shaft kiln. *Chemical Engineering Science*, 65:2821–2834, 2010.

[17] N.G. Deen, E.A.J.F. Peters, J.T. Padding, and J.A.M.Kuipers. Review of direct numerical simulation of fluid-particle mass, momentum and heat transfer in dense gas-solid flows. *Chem. Eng. Sci.*, 116:710–724, 2014.

[18] V. Chandra, E.A.J.F. Peters, and J.A.M. Kuipers. Direct numerical simulation of a non-isothermal non-adiabatic packed bed reactor. *Chem. Eng. Journal*, 385:123641, 2020.

[19] S. Schulze, M. Kestel, Safronov. D., and P. Nikrityuk. From detailed description of chemical reacting coal particles to subgrid models for CFD: model development and validation. *Oil & Gas Science and Technology*, 68:1007–1026, 2013.

[20] S. Schulze and P. Nikrityuk. A new subgrid model for the heat and mass transfer between a hot gas and char particles in dense-bed reactors. *J. Energy Resources Technology (ASME)*, 138: 042206–1/7, 2016.

[21] V. Balakotaiah. On the relationship between aris and sherwood numbers and friction and effectiveness factors. *Chemical Engineering Science*, 63:5802 – 5812, 2008.

[22] S.Y. Joshi, M.P. Harold, and V. Balakotaiah. On the use of internal mass transfer coefficients in modeling of diffusion and reaction in catalytic monoliths. *Chemical Engineering Science*, 64: 4976–4991, 2009.

[23] N. Lapidus and N.R. Amundson. *Chemical reactor theory: A Review.* Prentice-Hall, Inc. Englewood Cliffs, New Jersey, USA, 1977.

[24] K. Hou and R. Hughes. The kinetics of methane steam reforming over a Ni/α-Al_2O catalyst. *Chem. Eng. J.*, 82:311–328, 2001.

[25] Anthony G. Dixon, M. Ertan Taskin, Michiel Nijemeisland, and E. Hugh Stitt. CFD method to couple three-dimensional transport and reaction inside catalyst particles to the fixed bed flow field. *Ind. Eng. Chem. Res.*, 49:9012–9025, 2010.

[26] Mostafa Sulaiman, Eric Climent, Abdelkader Hammouti, and Anthony Wachs. Mass transfer towards a reactive particle in a fluid flow: Numerical simulations and modeling. *Chemical Engineering Science*, 199:496–507, 2019.

[27] S. Schulze, A. Richter, M. Vascellari, A. Gupta, B. Meyer, and P. Nikrityuk. Novel intrinsic-based submodel for char particle gasification in entrained-flow gasifiers: Model development, validation and illustration. *Applied Energy*, 164:805–814, 2016.

[28] H. Bansal and P.A. Nikrityuk. A submodel for spherical particles undergoing phase change under the influence of convection. *Can. J. Chem. Eng.*, 95:150–156, 2017.

[29] R. Schmidt, K. Wittig, and P. Nikrityuk. Single particle heating and drying. In P. Nikrityuk and B. Meyer, editors, *Gasification Processes: Modeling and Simulation*, pages 105–142. Willey-VCH Verlag GmbH & Co, Weinheim, Germany, 2014.

[30] H. Bansal and P.A. Nikrityuk. Arbitrary shaped ice particle melting under the influence of natural convection. *AIChE J.*, 63:3158–3176, 2017.

[31] H. Bansal, S. Ghaemi, and P.A. Nikrityuk. A scale-bridging model for ice particles melting in air. *Chem. Eng. Sci.*, 172:66–78, 2017.

[32] S. Whitaker. Forced convection heat transfer correlations for flow in pipes, past flat plates, single cylinders, single spheres, and flow in packed beds and tube bundles. *American Institute of Chemical Engineers Journal*, 18:361, 1972.

[33] B.J. Bride, S. Gordon, and M.A. Reno. Coefficients for calculating thermodynamic and transport properties of individual species. *Technical report, NASA*, 1993.

[34] N. Wakao and J.M. Smith. Diffusion in catalyst pellets. *Chem. Eng. Sci.*, 17:825–834, 1962.

[35] D. Pashchenko and A. Eremin. Heat flow inside a catalyst particle for steam methane reforming: CFD-modeling and analytical solution. *International Journal of Heat and Mass Transfer*, 165: 120617, 2021.

[36] A. Richter and P. Nikrityuk. Drag forces and heat transfer coefficients for spherical, cuboidal and ellipsoidal particles in cross flow at sub-critical reynolds numbers. *Int. J. Heat Mass Transfer*, 55:1343–1354, 2012.

[37] K. Wittig, A. Golia, and P.A. Nikrityuk. 3D numerical study of the influence of particle porosity on the heat and fluid flow. *Progress in Computational Fluid Dynamics*, 12:207–219, 2012.

[38] K. Wittig, , P.A. Nikrityuk, and A. Richter. Drag coeffcient and nusselt number for porous particles under laminar flow conditions. *Int. J. Heat Mass Transfer*, 112:1005–1016, 2017.

[39] Jianguo Xu and Gilbert F. Froment. Methane steam reforming, methanation and water-gas shift: 1. intrinsic kinetics. *AIChE Journal*, 35:88–96, 1989.

Chapter 3

Verification of a 0D model for the heat and mass transfer inside a moving spherical catalyst[1]

Abstract

This work is devoted to the verification of a new 0D model for the steam reforming of methane inside a spherical catalyst particle (Ni/α-Al_2O_3) moving in a hot methane/steam atmosphere. The submodel includes six gaseous chemical species (CH4, CO2 , CO, H2O, H2, N2) and uses experimentally defined reaction rate expressions taken from the literature. The distinguishing feature of the subgrid model is its ability to take into account the internal heat and mass transfer coupled with the heat and mass transfer on the catalyst surface influenced by convection and diffusion around the particle. The sub-model was verified against a comprehensive 1D-based model resolving diffusion and conduction processes inside the porous catalyst particle using 1D differential equations for the temperature and chemical species written in spherical coordinates. Comparisons between the 0D model and 1D model have been made for the particle diameters, d, 2 mm, 1 cm and 2.54 cm. The ambient temperature was varied between 650 K and 1000 K, respectively. Good agreement (less than 1-2%) was achieved between predictions obtained using the new 0D model and results calculated using the 1D-based model for all particle diameter ranges for the ambient gas temperatures below 900K. The increase in the ambient temperature and in the particle diameter leads to the deviations of up to 5-10% between the 0D model and 1D model predictions up to 5-10%.

[1]This chapter is based on the work: Yi Ran Lu, Petr A. Nikrityuk. *Verification of 0D model for the heat and mass transfer inside a moving catalyst particle*, accepted by publication by FUEL, 2022.

Nomenclature

A_p	particle surface area	Sh	Sherwood number
V_p	particle volume	Re	Reynolds number
c_p	specific heat capacity	Sc	Schmidt number
D	diffusivity	Nu	Nusselt number
d	diameter	Pr	Prandtl number
K	equilibrium constant	ρ	gas density
k_1, k_2, k_3	reaction rate coefficient		
α	stoichiometric coefficient	a	adsorption coefficient
k_{eff}	thermal conductivity	μ	dynamic viscosity
ε	particle porosity	τ	tortuosity
$\vec{v}$	velocity	P	pressure
U_{in}	inlet gas velocity	p_i	partial pressure of species i
R_g	ideal gas constant	M	molar mass

h	particle-gas heat transfer coefficient
β	particle-gas mass transfer coefficient
$(hA)_{in}$	particle internal heat transfer coefficient
$(\beta A)_{in}$	particle internal mass transfer coefficient
N_p, N_r	number of particles, number of reactions
$R_{V,r}, R_{s,r}$	volume, surface based reaction rate
T_∞	ambient temperature
T_s	temperature of the catalyst surface
T	temperature
T_p	particle volume-averaged temperature
$Y_{i,in}$	ambient mass fraction of species i
$Y_{i,s}$	mass fraction of species i on the catalyst surface
$Y_{i,p}$	particle volume-averaged mass fraction of species i

3.1 Introduction

Recent developments in the energy transition from the use of fossil fuels to that of renewable energy have made chemical engineering one of the driving forces in the this field due to the huge demand for novel conversion processes enabling CO_2 utilization and conversion, and H_2 production using renewable or atomic energy. The developments of such new technologies is only feasible with the use of multi-scale modeling of prototypical processes, as preliminary tools to determine various design parameters for a prototype, identify the limits and find the potential optimum. For a thorough review of recent developments in multi-scale modeling in chemical engineering, bioenergy and catalysts,

please refer to the works [1, 2]. In both reviews, exceptional attention is paid to the multi-scale modeling of fixed-bed reactors. Both catalytic fixed beds and high-temperature pyrolytic fixed beds should attract great research interests.

Fixed-bed reactors are one of the widely used systems in chemical engineering. For example, most steam methane reformers (SMRs) are fixed beds consisting of solid catalyst particles [3, 4]. An industrial-scale steam methane reformer consists of several tubes filled with porous catalyst. The typical tube length is of about 10 m and the internal diameter is typically 10 cm[5, 4]. One of the main challenges in modeling fixed-bed catalytic reformers is a coupling transport equations describing reactor-scale processes with the heat and mass transfer occurring inside each catalysts. The catalysts particles are porous, and intraparticle diffusion and intrinsic reactions play a governing role in performances of catalytic packed beds. Thus, one of the main strategies for taking into account multi-scale effects caused by different scales of transport processes inside a catalyst and in the gas phase inside fixed beds is to use so-called scale model bridges, which are simultaneously coupled with reactor-scale transport equations and sub-system models (submodels) for intraparticle transport during numerical calculations of the whole reactor. It must be emphasized that direct modeling of an industrial-scale catalytic fixed bed by resolving each particle is computationally expensive. Particle-resolved CFD-based simulations are basically used as a benchmark tool to understand the transport process in small lab-scale fixed beds [6].

The first submodels for intraparticle processes were based on semi-empirical relations for the heat/mass transfer inside the catalyst particles. Classical models of this kind calculated the pellet effectiveness factor using the Thiele modulus and the effective diffusion coefficient, which are derived for steady-state intra-pellet mass/heat transfer. [7]. The model works well for simple reaction mechanism, such as first order rate law, where the formula can be easily derived. For more complex kinetics, e.g. Langmuir-Hinshelwood-Hougen-Watson (LHHW) kinetics for SMR, reported in the literature [8], it can difficult to get an accurate approximation. Thus, the derivation of the effectiveness factor for such kinetics, especially for the unsteady intra-pellet mass/heat transfer, is not a trivial task. Recently, Kuncharam and Dixon [5] reported a multi-scale two-dimensional packed-bed reactor model for industrial steam methane reforming. The model was implemented into the commercial solver COMSOL. The distinguishing feature of this model is that it couples the 1D intraparticle diffusion equation for each species and 1D heat conduction equation with the heat and mass transfer equations describing the process throughout the reactor. In this model, each finite element of the grid had a representative particle for which a system of 1D transport equations was solved. Lu and Nikrityuk [9] used data from the work [5] to validate a new 3D discrete element model (DEM) coupled with a 1D computational fluid dynamics (CFD) model for the steam methane reforming. The main idea of this new particle-unresolved DEM-CFD-based model lies in the calculation of the volume-averaged and surface-averaged species mass fraction and temperatures in the catalyst for each catalyst particle via 0D submodels coupled with the transport equations for the gas phase.

This model is in some ways similar to multi-layer models described below.

In regard to DEM-based models coupled with CFD, which are used to model high-temperature conversion processes such as biomass gasification or reforming, there are three major classes of submodels. The most commonly used class formulates one-dimensional (1D) transport equations based on spherical symmetry. The 1D submodel solves the partial differential equations describing transport phenomena inside catalyst particles or solid-phase reactants. The processes inside the particle include conduction, diffusion, heterogeneous reaction, etc. This class of models has been excellently illustrated by Peters et al. in the works [10, 11]. In particular, the authors developed an extended discrete element method (XDEM) multi-physics and multi-scale simulation platform for DEM-CFD simulations of engineering applications. In this XDEM model, fluid phase transport equations are written in Eulerian space and governing equations for each particle are written in Lagrangian space in the form of 1D PDE. The two systems are coupled through the source terms and boundary conditions on the particle surface. Excellent agreement was demonstrated with experimental data published in the literature. One of disadvantage of 1D PDE based models is the computational time needed to solve finely discretized 1D PDE equations for each particle. When there are millions of particles, the overall time required to solve millions of PDEs is too high to be used in the design of reactors.

So-called lumped capacity models (LCMs) relate to the 2nd class of submodels which are represented by 1st-order nonlinear ordinary differential equations (ODEs) for initial value problems (IVPs) or just non-linear equations for steady state applications[12]. In particular, the work [12] presented a LCM-based submodel for biomass fast pyrolysis, where the particle temperature was tracked using the 1st-order ordinary differential equation initial value problem (ODE-IVP). The model was calibrated against particle-resolved CFD-based simulations. Good agreement was observed. 3D simulations of a fluidized bed with developed submodels and calibrated coefficients were used to illustrate the submodel's performance. It should be emphasized that LCM-based models assume homogeneous distribution of species and temperature inside the porous catalyst, leading to the condition $T_s = T_p$ and $Y_s = Y_p$. This condition is satisfied when the Biot number is significantly less than unity. However, in the pore-diffusion and diffusion regimes, this condition is not applicable. Thus, a numerical solution of the 1D conduction/diffusion equation is required. Alternatively, the so-called effectiveness factor based semi-analytical model can be used, see the comparative analysis of the two models [13]. This model only works for simple 1st-order kinetics. In cases involving more complex kinetics, the easiest method is to couple 1D equations on the particle scale with reactor-scale equations.

One alternative to both LCM and 1D PDE is a model which splits a particle into multiple homogeneous shell-like volume elements [14, 15, 16, 17]. In particular, Ström and Thunman [14] presented a computationally efficient particle submodel for CFD simulations of fixed-bed conversion, e.g. drying and devolatilization. A heat balance and a mass balance are formulated for each particle

shell leading to a system of 1st-order ODEs. It was shown that the proposed model was able to predict the correct drying and devolatilization behavior using a small number of variables and a relatively coarse resolution of the particle interior. Nikrityuk and coworkers [15, 18] presented a two-layer submodel for intraparticle heat and species mass transfer for a particle undergoing drying, devolatilization, combustion and gasification. The particle temperature and species mass fractions inside the particle and on the particle surface are calculated using a coupled system of ODE-IVPs. This model has been further developed and validated for entrained-flow [16] and dense-bed systems [19]. Gimez et al. [17] presented a multilayer submodel for biomass particles, which takes into account intraparticle gradients, interactions with other particles and the gas phase using an Euler-Euler CFD framework. Four dynamic layers were introduced by particle subgrid modeling, which calculates the evolution of the layer volumes and temperatures in an unsteady process. This model has been successfully applied for CFD simulations of fixed-bed burners. Schwarz et al. [13] presented a new one-dimensional particle submodel for char structure evolution for numerical simulations of fixed bed gasifiers. In this model, char particles are subdivided into multiple homogeneous shell-like volume elements. This approach is similar to a control-volume-based discretization of a 1D PDE representing unsteady diffusion equation. The submodel has been implemented into the two-dimensional CFD simulation of a lab-scale fixed-bed reactor. Very good agreement with experiments has been demonstrated.

Recently, in a series of works[9, 20], the authors have developed a 0D submodel for spherical catalyst particles in a classical SMR fixed bed reactor and in a new electrically heated SMR fixed bed, respectively. Validation against particle-resolved 3D CFD simulations showed very good agreement for small sized catalysts [21, 9]. However, this model has yet to be verified comprehensively for different particle sizes and bulk conditions. Motivated by this fact, this work compares the new 0D model against the 1D-based model for the steam reforming of the methane inside a catalyst particle placed in a stream of hot steam/methane atmosphere. Both models account for the internal heat and mass transfer using surface-averaged and volume-averaged species concentrations instead of only mean volume concentrations. A comprehensive 1D-based model includes PDE equations for the energy and species conservation equations used to solve the problem by means of the steady state approach.

3.2 Model Formulation

The model is formulated to simulate the reaction of steam and methane inside a particle. Before the formulation is presented, the input conditions for the model are first described in the following section. A porous spherical catalyst particle with a diameter of d and porosity of ε is placed in a hot stream of steam, methane and nitrogen. The inflow Reynolds number is defined as $Re = \frac{\rho_{in} U_{in} d}{\mu_{in}}$.

To verify the proposed model, we have designed a series of parametric studies under different

conditions. The input parameters for the verification cases are listed in Table. 3.1. Two sets of gas composition are used, Y_i where the CH_4:H_2O:inert gas ratio is 3:6:1 by mass to simulate the inlet conditions; and Y_d to represent a mid-reactor composition. The exact mass fraction is found in Table 3.2.

Study	T_∞, K	$Y_{i,\infty}$	Re	d, m	radiation	Figures
2	650-1000	Y_i	100	0.002-0.0254	No	3.6,3.7
3	650-1000	Y_i	100	0.002-0.0254	Yes	3.8,3.9
1	1000	Y_i/Y_d	100	0.002-0.04	Yes/No	3.10,3.11
4	650-1000	Y_d	500-10000	0.0254	No	3.12

Table 3.1: List of conditions used in the studies

Y	$Y_{CH4,\infty}$	$Y_{H2O,\infty}$	$Y_{H2,\infty}$	$Y_{CO,\infty}$	$Y_{CO2,\infty}$	$Y_{N2,\infty}$
Y_i	0.3	0.6	0	0	0	0.1
Y_d	0.0926	0.4680	0.0442	0.1181	0.2771	0

Table 3.2: List of mass fraction used in this study

The ambient pressure is 1 atm. A diagram of the problem setup is shown in Fig. 3.1. In this work we assume that all reactions occur inside the catalyst particle.

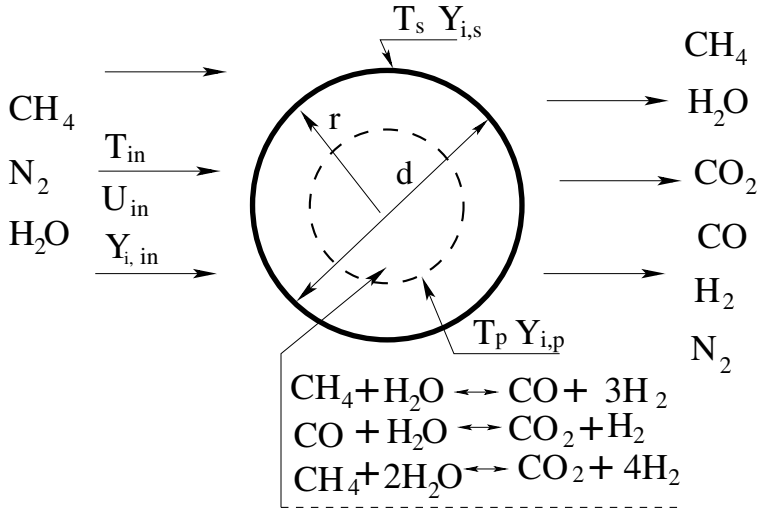

Figure 3.1: Diagram illustrating the catalyst particle placed in a stream of hot gas consisting of methane and steam.

3.2.1 1D Model

The following assumptions are applied to the model for the set of all equations,

- Viscous heating and buoyancy effects are neglected.
- Thermal diffusion is neglected.
- The particle is non-permeable for the gas flow. It is reasonable assumption for the laminar flow regime and particle porosity below 0.5, e.g. see the work [22].
- The particle is porous and its porosity is isotropic; the particle porosity is $\varepsilon = 0.44$.

In the work [22] it was shown that under laminar flow conditions the gas flow does not penetrate into porous particles with a porosity below 0.6. Thus, the Nusselt number relations for a solid sphere can be used to calculate the convective heat and mass transfer coefficients for the heat/mass transfer between the gas and the catalyst particle.

Following this assumption, a system of 1D equations written in spherical coordinates takes the form:

- Heat conservation equation:

$$\rho_p c_p \frac{\partial T}{\partial t} = \frac{1}{r^2}\frac{\partial}{\partial r}\left(r^2\, k_p \frac{\partial T}{\partial r}\right) + \sum_r^{N_r}(-\Delta H_r R_{V,r}) \tag{3.1}$$

Boundary conditions:

$$\left.\frac{\partial T}{\partial r}\right|_{r=0} = 0 \tag{3.2}$$

$$\left.-k\frac{\partial T}{\partial r}\right|_{r=R_p} = h\,(T_s - T_\infty) + \varepsilon_\sigma \sigma\left(T_s^4 - T_\infty^4\right) - \sum_r^{N_r}(-\Delta H_r R_{S,r}) \tag{3.3}$$

It should be noted that the last term on the right hand side of this equation describes the impact of chemical reactions on the catalyst surface.

The convective heat transfer coefficient, h, between the catalyst and gas phase is calculated using simplified Whitaker correlation [23]:

$$h = \frac{Nu\, k_\infty}{d} \tag{3.4}$$

$$Nu = 2 + \left(0.4\, Re^{0.5} + 0.06\, Re^{0.667}\right) Pr^{0.4} \tag{3.5}$$

- Species conservation equation for the mass fraction of i species:

$$\rho_p \frac{\partial Y_i}{\partial t} = \frac{1}{r^2}\frac{\partial}{\partial r}\left(r^2\left(\rho_g D_{\text{eff}}\right)\frac{\partial Y_i}{\partial r}\right) + M_i \sum_r^{N_r}(a_{r,i} R_{V,r}) \tag{3.6}$$

Boundary conditions:

$$\frac{\partial Y_i}{\partial r}\Big|_{r=0} = 0 \tag{3.7}$$

$$\rho_g D_{\text{eff}} \frac{\partial Y_i}{\partial r}\Big|_{r=R_p} = \rho_g \beta (Y_{s,i} - Y_{\infty,i}) - M_i \sum_{r}^{N_r} (a_{r,i} R_{S,r}) \tag{3.8}$$

where the surface based reaction rate, $R_{S,r}$, is calculated as follows:

$$R_{S,r} = \frac{R_{V,r}}{A_V} \tag{3.9}$$

where according to the data [8], A_V can be calculated as follows:

$$A_V = 2.56 \cdot 10^7 \, m^2/m^3$$

It should be noted that the last term on the right side of Eq. (3.7) describes the chemical reactions on the catalyst surface.

The convective mass transfer coefficient, β, is calculated using the same correlation as heat transfer:

$$\beta = \frac{Sh \, D_\infty}{d} \tag{3.10}$$

$$Sh = 2 + \left(0.4 \, Re^{0.5} + 0.06 \, Re^{0.667}\right) Sc^{0.4} \tag{3.11}$$

In this work, the following parameters are used for the catalyst in Eq. (3.12): $r_{pore} = 10^{-7}$m, $\varepsilon = 0.44$ and $\tau = 3.54$ according to the works [8, 6]. As the mean pore diameter is in the same order of magnitude as the mean free path of the reacting gas, Knudsen diffusion can have an impact on the effective diffusivity of the gas mixture. However, the scope of this study is focused on validating 0D model versus 1D model, and having identical values for both models should yield consistent results. The bulk diffusivity D_∞ is simplified based on Le=1. The effective diffusion inside the catalyst particle D_{eff} is calculated as follows [9]:

$$D_{\text{eff}} = \frac{\epsilon}{\tau} D_\infty \tag{3.12}$$

Kinetics

The reaction rates $R_{V,r}$ and the chemical reactions are given in Table 3.3, where reaction kinetics for steam reforming are given in the units of $[mol/m^3 s]$ according to the work [8].

N_r	Reaction	$R_{V,r}$, $[mol/m^3 s]$
1	$CH_4 + H_2O \Leftrightarrow CO + 3H_2$	$R_{V,1} = \frac{k_1 \left(p_{CH_4} p_{H_2O}^{0.5} - \frac{p_{H_2}^3 \, p_{CO}}{K_1 \, p_{H_2O}^{0.5}} \right)}{p_{H2}^{1.25} \, \xi^2}$
2	$CO + H_2O \Leftrightarrow CO_2 + H_2$	$R_{V,2} = \frac{k_2 \left(p_{CO} \, p_{H_2O}^{0.5} - \frac{p_{H_2} \, p_{CO_2}}{K_2 \, p_{H_2O}^{0.5}} \right)}{p_{H2}^{0.5} \, \xi^2}$
3	$CH_4 + 2H_2O \Leftrightarrow CO_2 + 4H_2$	$R_{V,3} = \frac{k_3 \left(p_{CH_4} \, p_{H_2O} - \frac{{p_{H_2}}^4 \, p_{CO_2}}{K_3 \, p_{H_2O}} \right)}{{p_{H_2}}^{3.5} \, \xi^2}$
-	-	$\xi = 1 + K_{CO} \, p_{CO} + K_H \, p_{H_2}^{0.5} + K_{H_2O} \, \frac{p_{H_2O}}{p_{H_2}}$

Table 3.3: List of chemical reactions and expressions for volumetric reaction rates according to the work [8], where $k_{V,r} = k_r \rho$, $\rho = 1790$ [kg/m^3].

According to the work [8], the rate coefficients are

$$k_1 = 5.922 \cdot 10^8 \exp\left(\frac{-209200}{R_g \, T}\right) \text{ [kmol/s/kg/kPa}^{0.25}\text{]} \tag{3.13}$$

$$k_2 = 6.028 \cdot 10^{-4} \exp\left(\frac{-15400}{R_g \, T}\right) \text{ [kmol/s/kg/kPa]} \tag{3.14}$$

$$k_3 = 1.093 \cdot 10^3 \exp\left(\frac{-109400}{R_g \, T}\right) \text{ [kmol/s/kg/kPa}^{0.25}\text{]} \tag{3.15}$$

The adsorption coefficients take the following forms [8]:

$$K_{H_2O} = 9.251 \cdot \exp\left(\frac{-15900}{R_g \, T}\right) \; ; K_H = 5.68 \cdot 10^{-10} \exp\left(\frac{93400}{R_g \, T}\right) \text{ [kPa}^{-0.5}\text{]} \tag{3.16}$$

$$K_{CO} = 5.127 \times 10^{-13} \exp\left(\frac{140000}{R_g \, T}\right) \text{ [kPa}^{-1}\text{]} \tag{3.17}$$

In this work, we used the following expressions for the equilibrium coefficients:

$$K_1 = 1.198 \cdot 10^{17} \exp\left(\frac{-26830}{T}\right) \text{ [kPa}^2\text{]; } \mathrm{K_2} = 1.767 \cdot 10^{-2} \exp\left(\frac{4400}{\mathrm{T}}\right) \text{ [kPa]} \tag{3.18}$$

$$K_3 = 2.117 \cdot 10^{15} \exp\left(\frac{-22430}{T}\right) \text{ [kPa}^2\text{]} \tag{3.19}$$

Species	Source term $M_i \sum_r^{N_r}(a_{r,i}R_{V,r})$
CH_4	$\sum_r^{N_r}(\alpha_{r,i}R_{V,r}) = -(R_{V,1} + R_{V,3})$
H_2O	$\sum_r^{N_r}(\alpha_{r,i}R_{V,r}) = -(R_{V,1} + R_{V,2} + 2R_{V,3})$
CO:	$\sum_r^{N_r}(\alpha_{r,i}R_{V,r}) = R_{V,1} - R_{V,2}$
CO_2	$\sum_r^{N_r}(\alpha_{r,i}R_{V,r}) = R_{V,2} + R_{V,3}$
H_2	$\sum_r^{N_r}(\alpha_{r,i}R_{V,r}) = 3R_{V,1} + R_{V,2} + 4R_{V,3}$

Table 3.4: List of source terms in Eq. 3.6 for each Y_i.

The source terms in Eq. 3.6 for each specific Y_i are given in Table 3.4. The reaction enthalpy for reactions given in Table 3.3 are $-\Delta H_1 = -206.1$ kJ/mol, $-\Delta H_2 = 41.2$ kJ/mol and $-\Delta H_3 = -165.0$ kJ/mol, respectively. For reference, the values are taken the same as in the work [6]. The relation between the partial pressure and mass fraction is

$$p_i = \frac{Y_i P\, M}{M_i};\; M = \frac{1}{\sum_i^N \frac{Y_i}{M_i}} \tag{3.20}$$

The particle's radius is discretized into a 120-grid mesh. The second derivative was approximated using the central difference scheme. The grid points are evenly spaced along the radius of the particle. At the center of the particle, the no-flux Neumann boundary condition is applied because of axisymmetric geometry. At the surface of the particle, the Robin boundary condition is applied and the 1st-order backward difference scheme is used to approximate the temperature and species gradient. A 120-row tridiagonal matrix is formed as a result of the FD formulation. A direct solver based on Gaussian elimination is used to solve the matrix. The matrix has to be solved iteratively due to the dependence on temperature and mass fraction for the properties in the coefficients and the source term. A relaxation factor of 10^{-12} is used to initialize the solution and exponentially increased to 0.001. The iterations are stopped when the estimated relative errors for both the mass fraction and temperature are below 10^{-6}.

3.2.2 0D Model

The 0D model presented in this section was developed and presented in the previous chapter [21]. The main idea of this model is that instead of resolving the particle internal conditions using grid points, the 0D model operates with two dependent variables for the temperature and species mass fraction for specific i: the first variable is the volume-averaged quantity, T_p and $Y_{p,i}$ and the second is the surface-averaged quantity T_s and $Y_{s,i}$ see Fig. 3.1. It should be noted that T_p and $Y_{p,i}$ relates to the specific radius that splits the volume of the particles in half. However, the radius can be a tuning parameter that should be optimized to suit the specific operating conditions of the reactor. According to Chapter 3, the system of equations for the 0D model takes the form:

The balance of the chemical species on the particle surface takes the following form:

$$\underbrace{\beta A_p \rho_{g,s} \left(Y_{i,in} - Y_{i,s}\right)}_{Convection\ and\ Diffusion} + \underbrace{M_i A_p \sum_r^{N_r} \alpha_{r,i}\ R_{s,r}}_{Surface\ reactions} = \underbrace{(\beta A)_{in} \rho_{g,p} \left(Y_{i,s} - Y_{i,p}\right)}_{Intraparticle\ Diffusion} \tag{3.21}$$

where β is the mass transfer coefficient due to the external convection and diffusion, $(\beta A)_{in}$ is the mass transfer coefficient describing the diffusion inside the particle and $Y_{i,s}$ is the particle surface-averaged mass fraction of species $'i'$.

The balance equation for the chemical species inside the particle takes the following form:

$$V_p \epsilon_v \rho_{g,p} \frac{dY_{i,p}}{dt} = (\beta A)_{in} \rho_{g,p} (Y_{i,s} - Y_{i,p}) + \underbrace{M_i V_p \sum_r^{N_r} (\alpha_{r,i} R_{V,r})}_{Reactions\ inside\ Particle} \tag{3.22}$$

where $Y_{i,p}$ reflects the particle volume-averaged mass fraction of species $'i'$. Similar model equations (with different source terms) for the chemical species on the particle surface and for the chemical species inside the particle have been successfully applied to model char particles gasification in entrained-flow gasifiers.

An equation describing the heat balance on the catalyst surface takes the following form:

$$\underbrace{(hA)_{in} \left(T_s - T_p\right)}_{Internal\ Diffusion} = \underbrace{h_{pg} A_p \left(T_{in} - T_s\right)}_{External\ Convection\ and\ Diffusion} + \underbrace{\epsilon \sigma A_p \left(T_{in}^4 - T_s^4\right)}_{Radiation} + \underbrace{A_p \sum_r^{N_r} (-\Delta H_r) R_{s,r}}_{Surface\ reactions} \tag{3.23}$$

where T_s is the particle surface-averaged temperature. The emissivity of the particle surface was set to 0.7. It should be noted that T_{in} corresponds to the inlet temperature of the gas while in the problem we solve, it equals to the ambient temperature of the gas T_∞.

The particle temperature T_p can be calculated as follows:

$$m_p c_p \frac{dT_p}{dt} = (hA)_{in} (T_s - T_p) + \underbrace{V_p \sum_r^{N_r} (-\Delta H_r) R_{V,r}}_{Reactions\ inside\ Particle} \tag{3.24}$$

where T_p reflects the volume-averaged temperature of the particle.

The intraparticle mass and heat transfer coefficients are defined as follows [21]:

$$(\beta A)_{in} = 4\pi D_{\text{eff}} \left(\frac{1}{a_1 r_p} - \frac{1}{r_p}\right)^{-1} \tag{3.25}$$

$$(hA)_{in} = 4\pi k_{eff} \left(\frac{1}{a_1 r_p} - \frac{1}{r_p} \right)^{-1} \tag{3.26}$$

where $a_1 = 0.85$ [21]

a_1 is a tuning parameter based on the radius, and represents the average distance from the surface where the reacting volume of the particle is. The impact of a_1 is studied and the results are listed in the next chapter.

The diffusion coefficient D_i is obtained by using a Lewis number equals to 1.

$$Le = \frac{k_g}{D_i c_p \rho} = 1; \;\; D_i = \frac{k_g}{c_p \, \rho} \tag{3.27}$$

where the transport properties k_g, c_p and μ are functions of T and are calculated utilizing polynomials taken from the NIST database.

The system of equations comprising of Eqs. (3.21), (3.22), (3.23) and (3.24) is solved implicitly via Matlab. All equations, except Eq. (3.23), whose solution was found applying the Newton method, were calculated utilizing a fixed-point method with underrelaxation. The iterations were stopped when the estimated relative error for each dependent variable (T_s, T_p, $Y_{i,s}$, $Y_{i,p}$) was less than 10^{-6}.

3.3 Verification Results

In this study, a series of simulations were carried out to test the capabilities and limitations of the particle-based 0D model. The 0D model is compared against a particle-resolved 1D finite-difference model. To compare the two model predictions, we use the particle volume-averaged quantities such as the particle-averaged temperature T_p and the particle -averaged mass fraction of species Y_p calculated using profiles of T and Y_i from 1D model:

$$T_p = \frac{3}{\left(\frac{d}{2}\right)^3} \int_0^{d/2} r^2 \, T \, dr \tag{3.28}$$

$$Y_{i,p} = \frac{3}{\left(\frac{d}{2}\right)^3} \int_0^{d/2} r^2 \, Y_{i,p} \, dr \tag{3.29}$$

where i refers to chemical species H_2, CH_4, CO, CO_2, H_2O.

Firstly, we compare the results of the 1D model against 3D CFD simulations for $d = 4$ mm and $Re = 100$ reported in the work [21] using the same operating parameters. Fig. 3.2 plots the particle volume-averaged temperature T_p and the particle volume-averaged species mass fractions

$Y_{i,p}$ for CH_4, H_2 and CO_2, which were calculated using the 1D model and Eqs. (3.28) and (3.29) for different values of the ambient temperature, T_∞. It can be seen that the results of the 1D FD model proved to be very close. The relative error in temperature is less than 0.005%, and the maximum relative error for CO_2 is less than 2%. The main source of error comes from the external heat and mass transfer, as the 1D model uses an average surface condition obtained using the Whitaker correlation in this study. It was concluded that the difference was within reasonable limits and the 1D results were validated.

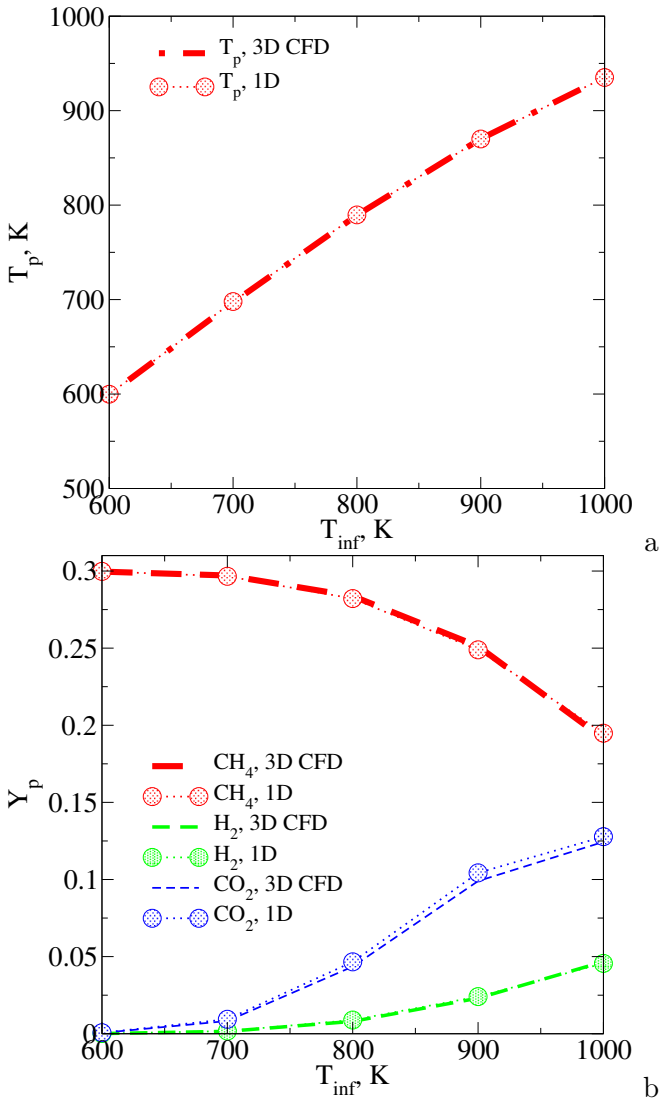

Figure 3.2: Validation of the 1D model against 3D CFD simulations [21] for $d = 4$ mm: a - the particle volume-averaged temperature T_p, b - the particle volume-averaged species mass fractions $Y_{i,p}$.

Secondly, a grid study was conducted to find a sufficient number of points to resolve the particle.

All of the grid points in this study are equally spaced in a radial position. The cases using 30, 60, 120, 1000 points are compared in Fig. 3.3 for different sizes of particles, $d = 2mm$ and $d = 2cm$. More accurate results can be obtained using more grid points. Compared to the 1000-point case, the relative errors for the cases with 30, 60, 120 points are 1.2%, 0.51%, and 0.18%. A minimum of 120 points should be used for the results to be considered grid-independent. We chose the 120-grid mesh as the standard 1D particle resolution for a good balance between computational time and accuracy.

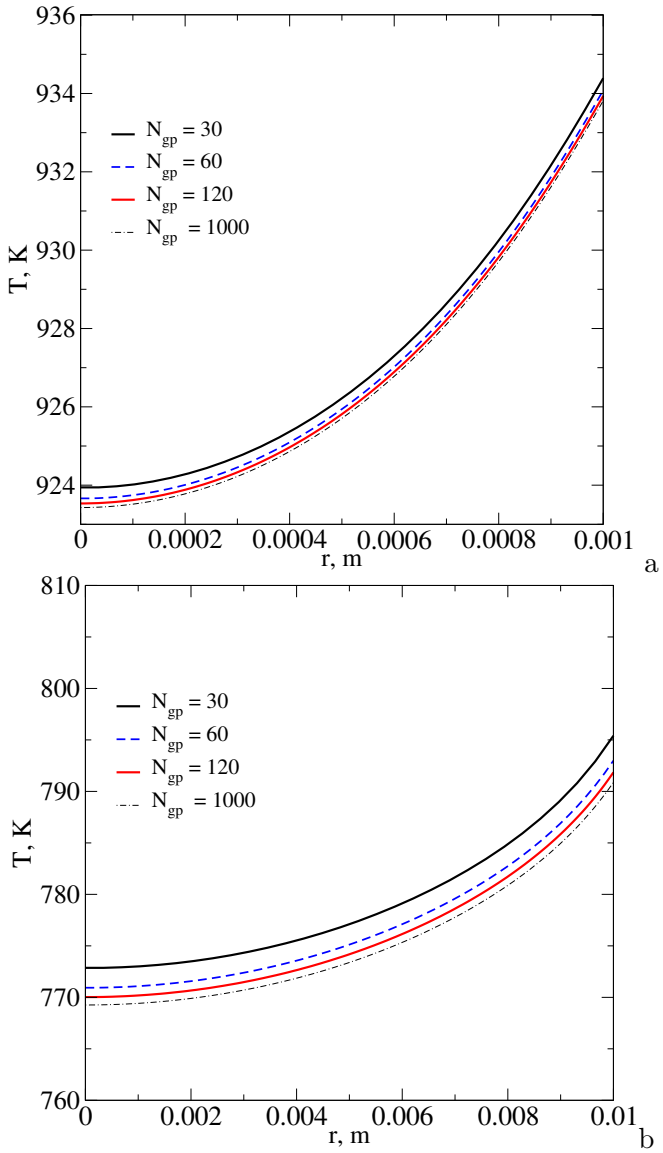

Figure 3.3: Comparison of temperature profile over radial position using different number of grid points. a - d=0.002m, b - 0.02 m T_∞=1000K. Re=100

Before we explore the deviations between the 1D model and the 0D model, we illustrate the influence of particle size on the radial profiles of T and Y_i inside the catalyst particles for different T_∞ at $Re = 100$. One of the most important factors affecting the catalytic reaction rate is the particle size. To illustrate the effect of mass transfer limitation due to particle size, the non-dimensional profiles of 3 cases are plotted in Fig. 3.4, with the particle diameter being 2mm, 10mm, and 25.4mm. It is observed that the smaller particles have almost the entirety of their reactions occurring close to surface conditions. The surface temperature is only 10K lower than in the bulk conditions. In the 2mm range, the reaction rate is kinetically limited at 800K. The internal conditions of the larger particles feature a much lower temperature and higher conversion. In the 25mm range, the internal temperature is much lower than the surface and bulk temperature due to higher heat transfer limitations. For the 10mm particle, the temperature profile is relatively flat. However, the species profiles exhibit significant difference between the surface and the interior conditions. The CH_4, H_2 and CO_2 curves show the reactions to be internally mass-transfer-limited. As seen from the results, even in identical bulk conditions, particle size can critically limit the reaction rate due to both internal diffusion and heat conduction. Therefore, to validate the 0D submodel, it is important to conduct comprehensive verifications to ascertain that the model encompasses different conditions and regimes.

Since the 0D model does not resolve the particle internal condition, the profiles inside the particles cannot be directly compared. The particle temperature and mass fractions calculated with the 0D model are compared to the 1D model's volume-averaged values. The 0D surface temperature and mass fractions are compared to the 1D surface values, shown by the difference between surface and volume-averaged conditions. For each case, the temperature, CH_4, H_2 and CO_2 are plotted to show the difference between two models. To start the verification of the 0D model, we test the sensitivity of the non-dimensional radius value, a_1, on the 0D model results, Fig. 3.5 compares T_p, T_s and $Y_{i,p}$ calculated from the 1D model and 0D model. The 0D model uses a parameter a_1, which is the artificial non-dimensional radius, to model the internal heat and mass transfer, see Eqs. (3.26) and (3.25). The artificial radius is based on the distance where the reaction rate is split in half calculated at base conditions. The artificial radius used for all cases, but it can be adjusted to improve the accuracy of the model. It can be seen that the curves of the 1D results do not match perfectly with any of the 0D results. The rates of diffusion are different for the species and heat. Therefore, the 0D model is limited in terms of its accuracy and range of application. Considering both the volume-averaged values and surface values for temperature and all mass fractions, we find that when $a_1 = 0.85$, the results of the 1D and 0D models match within reasonably well across all values compared. The finding agrees with previously published results[15, 21], in which the model and the parameter were proposed. Although a_1 is a tuning parameter that is not universal to all reactions, the fact that it agrees well in both coal gasification and steam reforming shows good potential for the model.

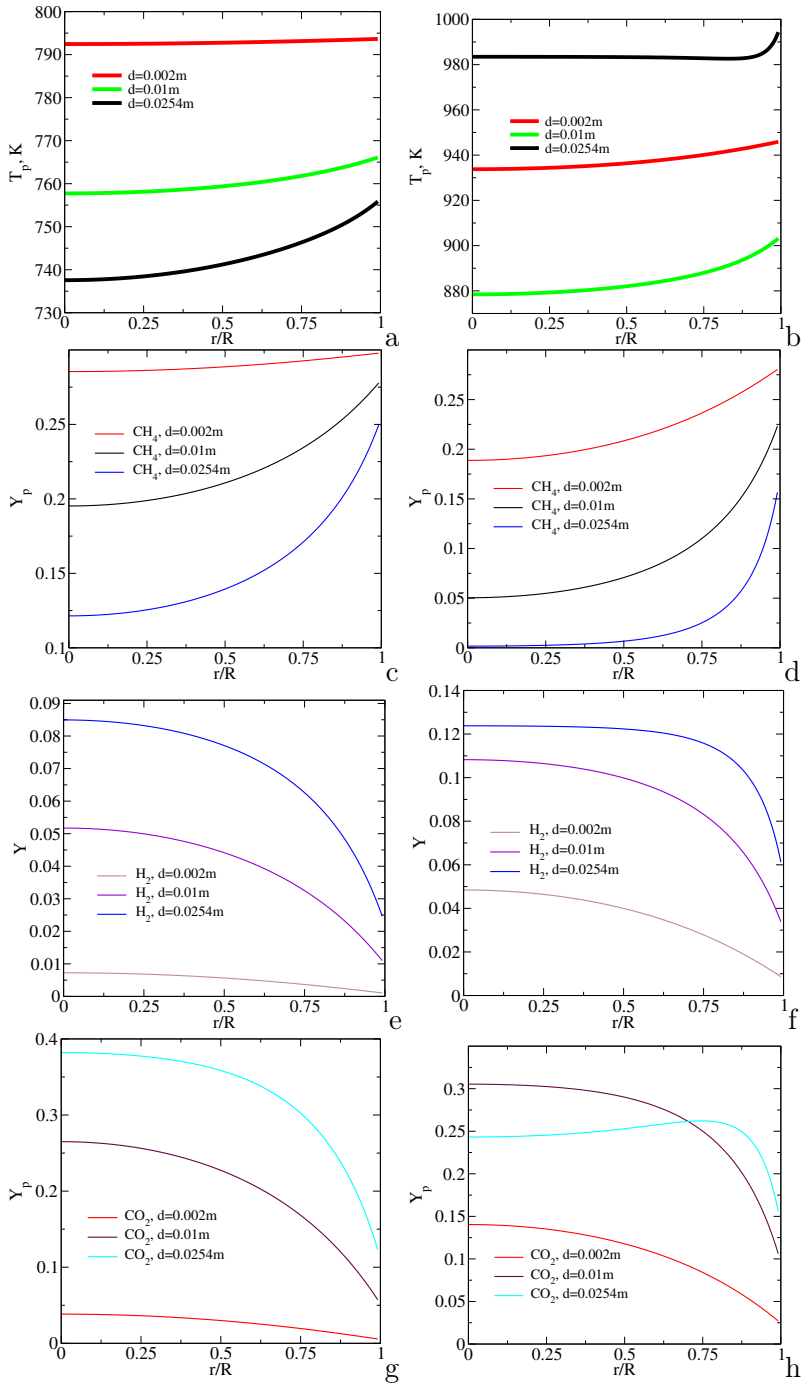

Figure 3.4: Radial profiles of the temperature and species mass fractions calculated using 1D model for different sizes of particles and two different ambient temperatures $T_\infty = 800$ K (left column) and $T_\infty = 1000$ K (right column): a, b - T; c,d - CH_4; e,f - H_2; g,h - CO_2. Here $Re = 100$, $N_{gp} = 120$.

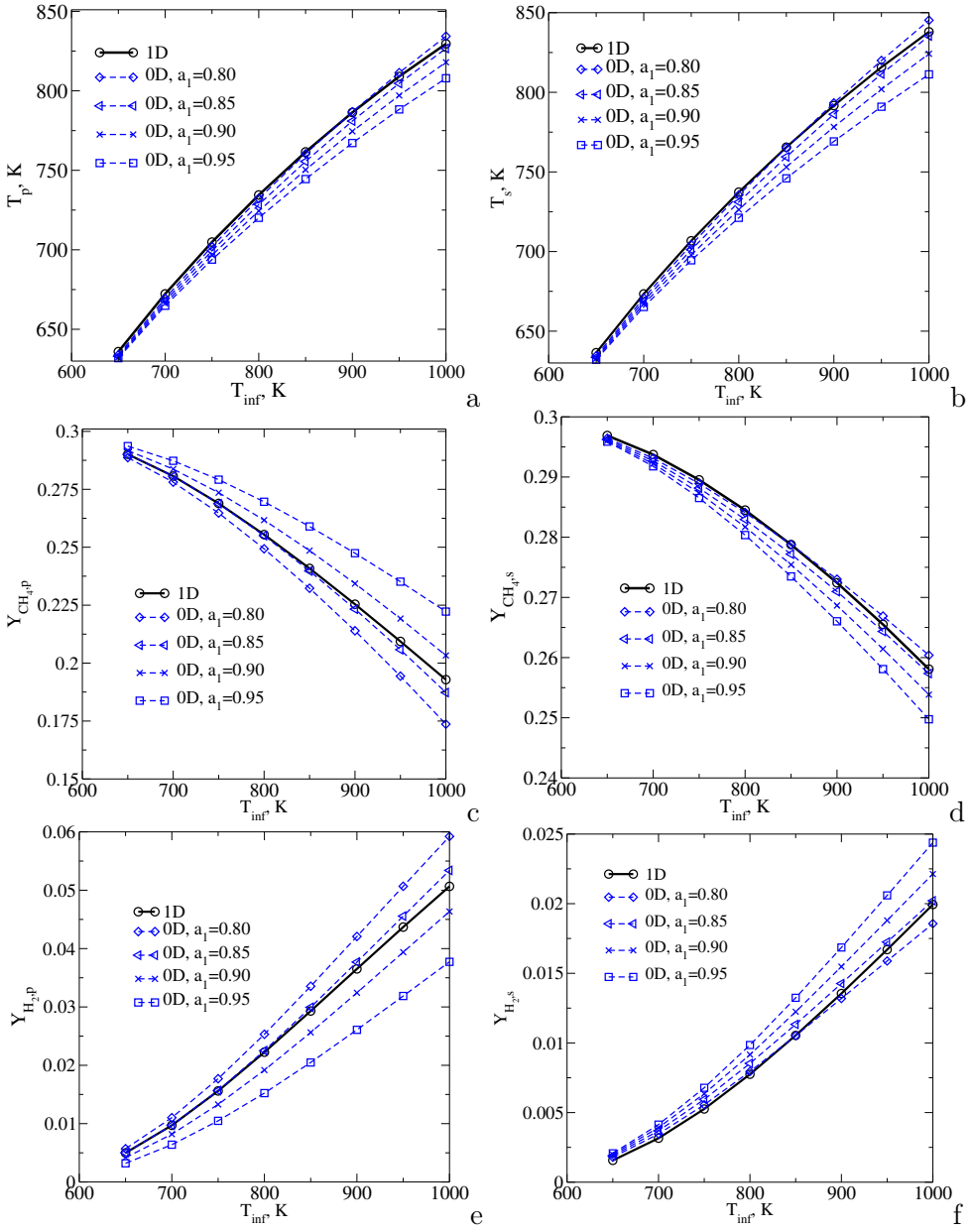

Figure 3.5: Comparison between 1D model predictions (using 120-grid) and 0D model results obtained using different values of the non-dimensional radius a_1 for the particle diameter $d = 1$ cm, $Re = 100$ and no radiation: a - the particle volume-averaged temperature T_p, b - the particle surface temperature T_s, c - the particle volume-averaged $Y_{CH_4,p}$, d - the particle surface $Y_{CH_4,s}$, e - the particle volume-averaged $Y_{H_2,p}$, f - the particle surface $Y_{H_2,s}$.

In Fig. 3.6, the comparisons between the 0D and 1D models are plotted against the bulk temperature for three separate particle diameters without surface radiation. In all three cases, the temperature profiles are very close comparing the two models. The maximum temperature difference of about 10 K is observed for the particle with d=2.54 mm. The discrepancy agrees with our prediction, since the largest particle is very diffusion-limited and the majority of the reaction occurs much closer to the surface of the particle. The results for species CH_4, H_2 and CO_2 also show general good agreement, with the discrepancy most significant for the largest particle, with the maximum error being about 5%. Moreover, the difference grows slightly as the temperature rises, since the reaction rate is low at the lower end of the temperature curve. In Fig. 3.7, the temperature and CH_4 difference between surface and volume average are plotted. The maximum temperature difference between the two curves can again be seen for the 25.4mm particle, with the difference increasing for higher bulk temperature. The maximum temperature difference is about 5K and the maximum CH_4 difference is about 0.02. Overall, both surface and volume-averaged conditions show consistent results. There is considerable error in the extreme cases for large particle sizes and high temperatures.

In Figs. 3.8 and 3.9, the results plotted are for the 0D model and 1D model with radiation under otherwise the same conditions as in Figs. 3.6 and 3.7. The surface emissivity is assumed to be 0.7. At lower temperatures, the error of the 0D model is less than the previous cases without radiation in terms of in both temperature and CH_4 conversion and H_2 formation. The same trend is observed that the error is larger for the larger particles. The temperature difference between the surface and volume average is slightly larger. With radiation, the external heat transfer is greatly amplified. Therefore, internal conductivity becomes even more rate limiting. As a result, at elevated temperature, the reaction is more concentrated towards the surfaces of the catalyst and the disparity of the 0D model becomes more significant.

Since particle size proves to be one of the significant factors affecting the accuracy of the 0D model, a series of studies were carried out to test the behavior of the 0D, with the results plotted in Figs. 3.10 and 3.11. Three conditions are used, with the bulk temperature equal at 1000K but different heat transfer conditions and bulk mass fractions, following the conditions shown in Table 3.2. General good fitting is found between the 1D curve and the 0D curve. As expected, almost identical results are observed at the lower end of the particle size range. In the centimeter range, the maximum relative errors are 2% and 10% for the temperature and species mass fraction, respectively. With diameters up to 40mm, the 0D model holds up well in all of the cases tested. As for $T_s - T_p$ and $Y_s - Y_p$, the temperature difference is within 5K and the mass fraction difference is within 0.03. As the particle size is increased to the higher end, the 0D model actually predicts a higher conversion and lower temperature inside the particle. This phenomenon is not observed with radiation enabled. This change can be attributed to heat transfer limitations playing a larger role in larger particles. The majority of the reactions happen very close to the surface and external heat transfer becomes

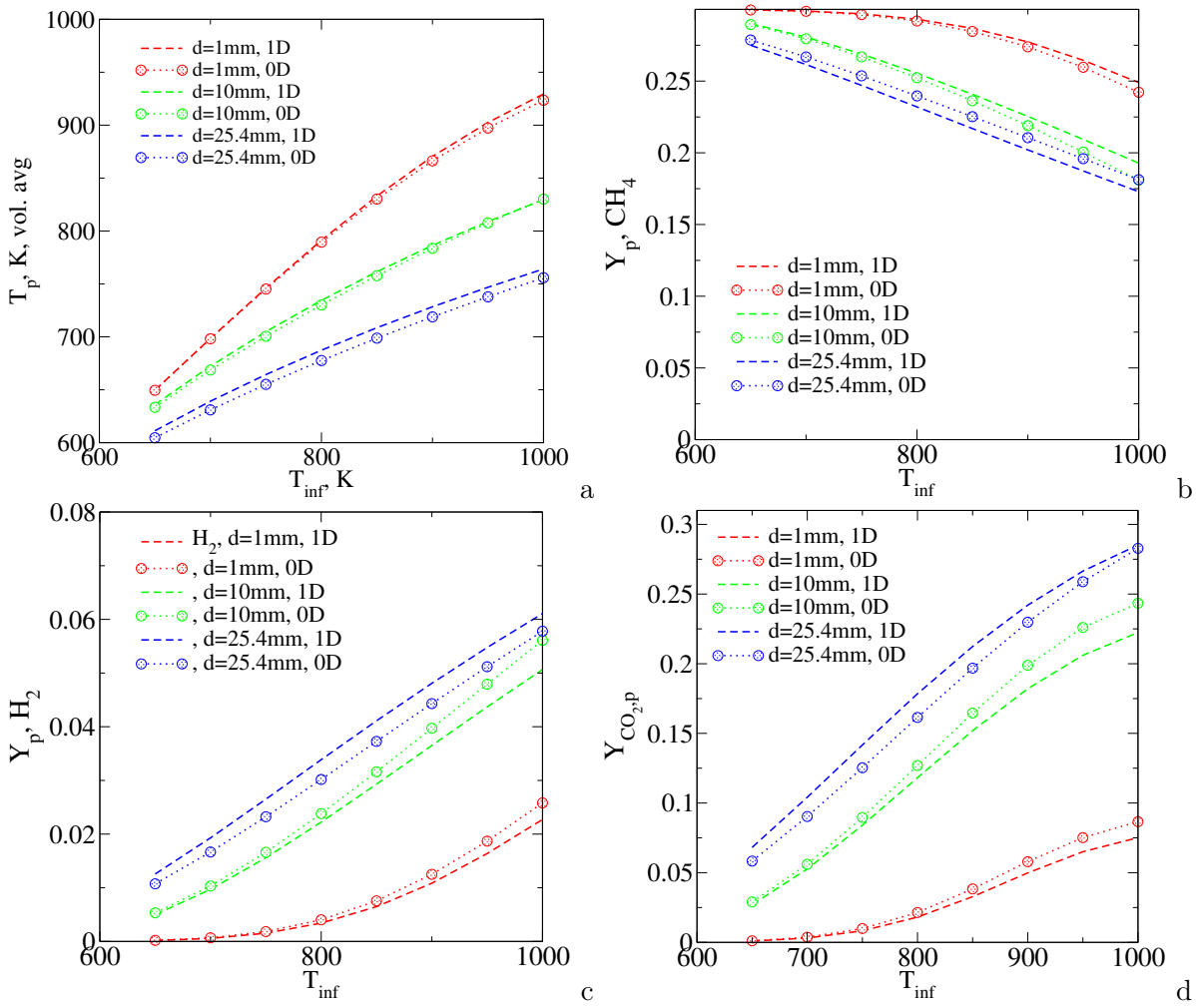

Figure 3.6: Comparison of the particle volume-averaged temperature (a) and mass fractions of CH_4 (b), H_2 (c), CO_2 (d) predicted using 1D model ($N_{gp} = 120$) and using 0D model for different ambient temperatures. Here $Re = 100$ and no radiation.

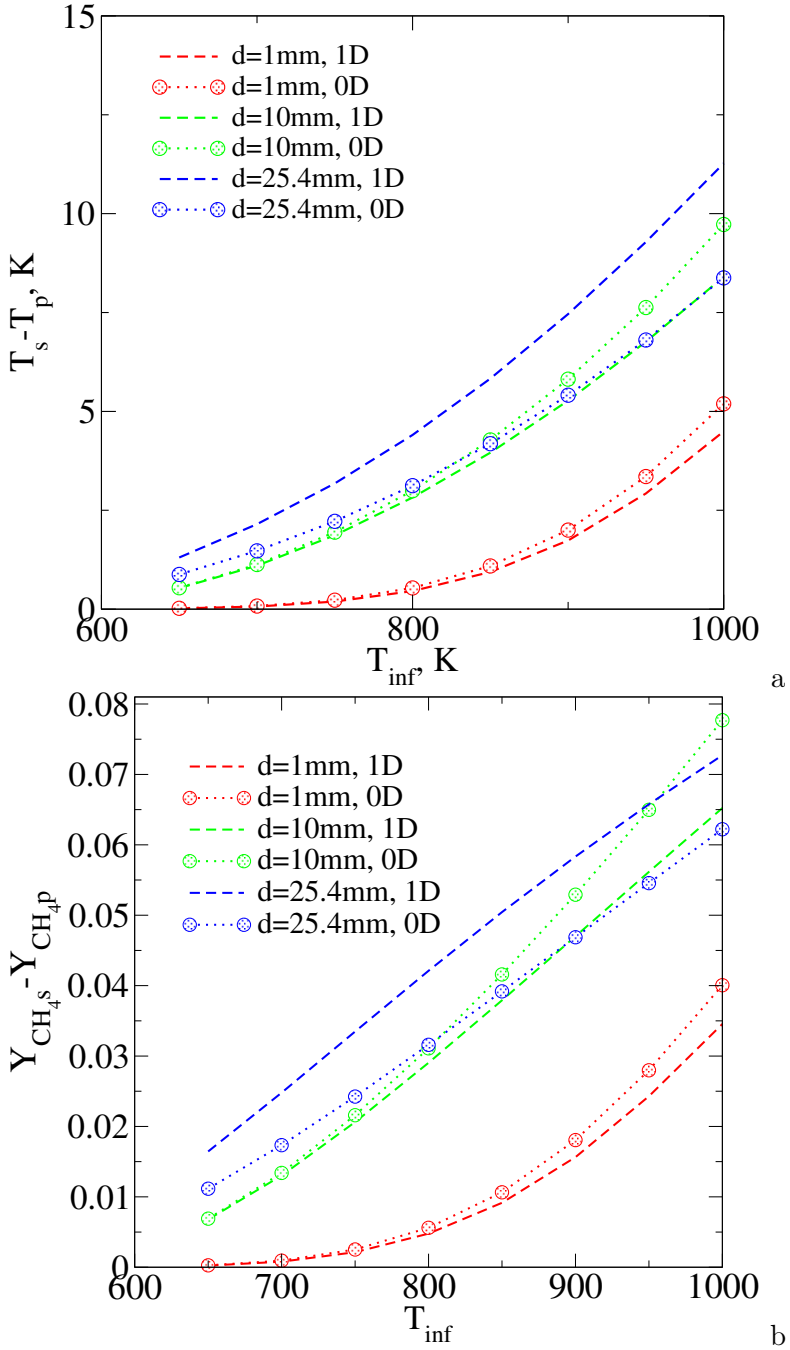

Figure 3.7: Difference between surface and volume-averaged temperatures (a) and mass fractions (b) compared for 1D model vs 0D submodel for different free stream temperatures. Here $Re = 100$ and no radiation.

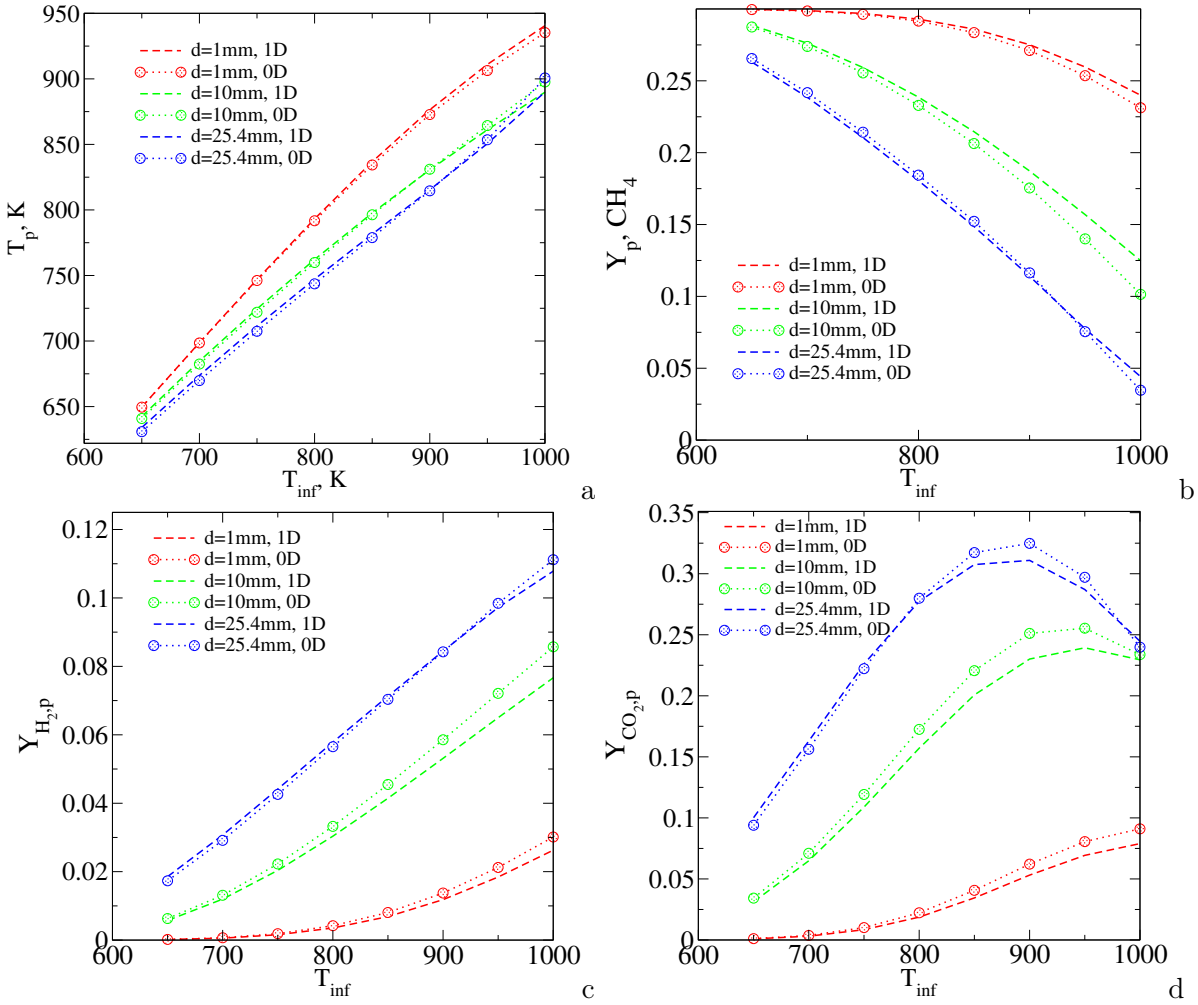

Figure 3.8: Comparison of the particle volume-averaged temperature (a) and mass fractions of CH_4 (b), H_2 (c), CO_2(d) predicted using 1D model ($N_{gp} = 120$) and using 0D model for different ambient temperatures. Here $Re = 100$ and with radiation.

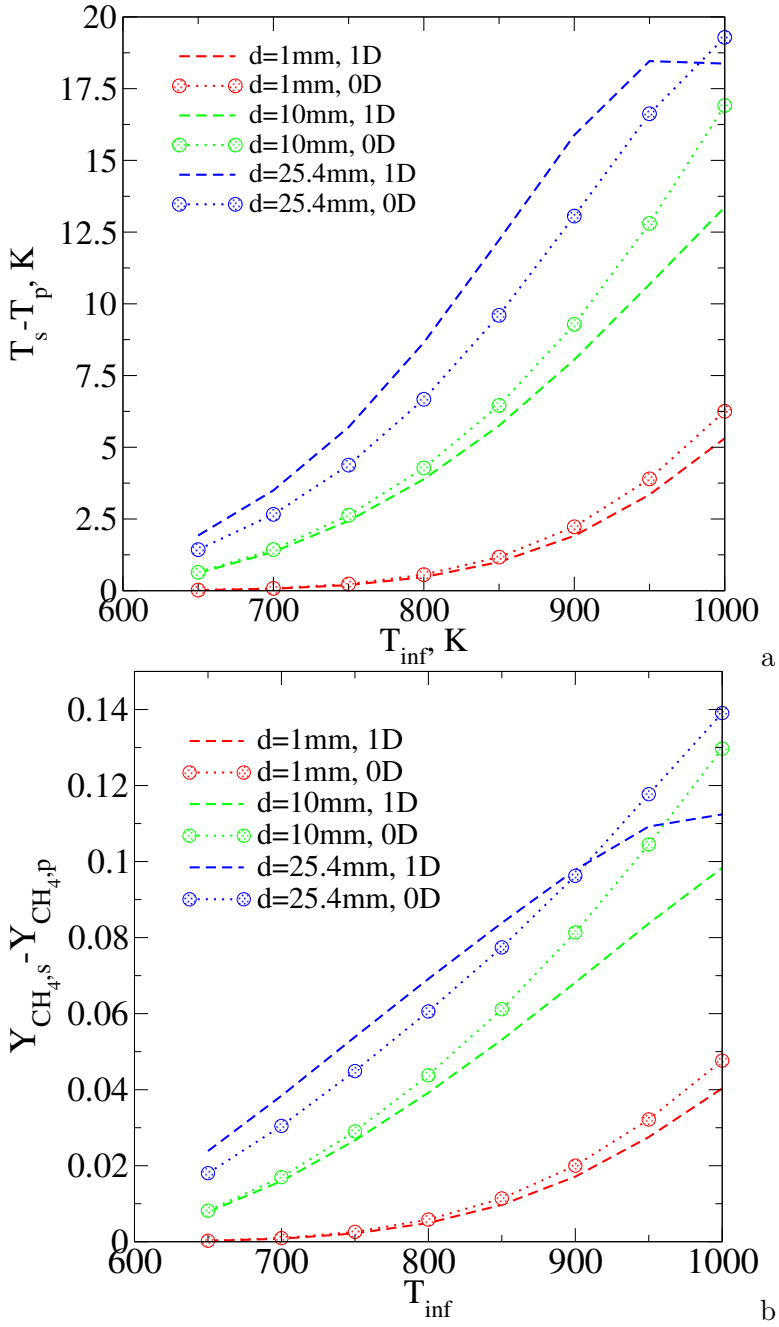

Figure 3.9: Difference between surface and volume-averaged temperatures, $(T_s - T_p)$, (a) and mass fractions for CH_4, $(Y_{CH_4,s} - Y_{CH_4,p})$, compared for 1D model vs 0D submodel for different ambient temperatures. Here $Re = 100$ and with radiation.

rate limiting, since all particles are subject to low-Reynolds conditions. The 0D model underpredicts the heat transfer rate and results in a profile with higher conversion than the 1D model.

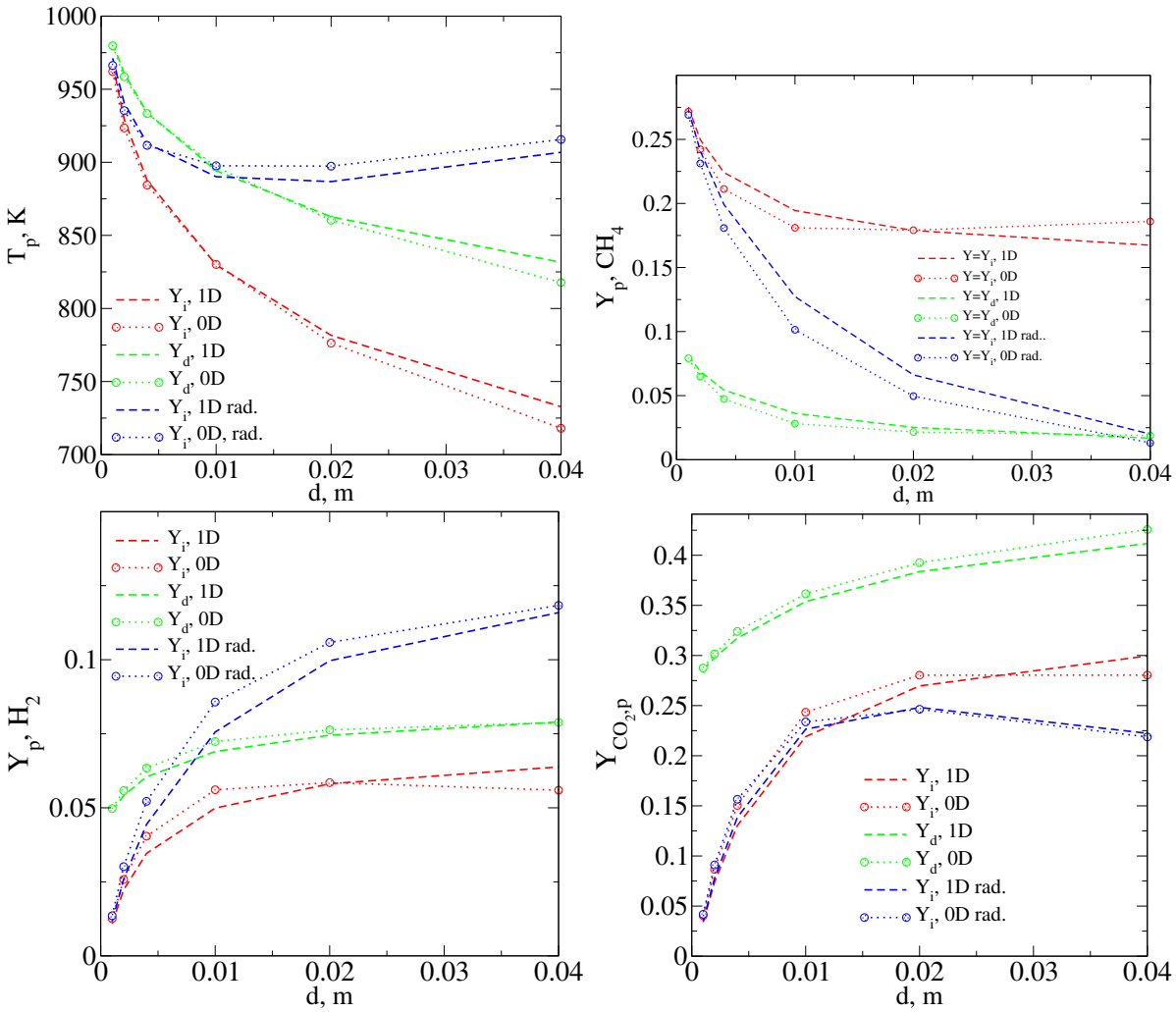

Figure 3.10: Comparison of the particle volume-averaged temperature and mass fractions of CH_4, H_2, CO_2 predicted using 1D model ($N_{gp} = 120$) and using 0D model for different diameters of the catalyst particle and different compositions of the ambient gas, see Table 3.2. Here $Re = 100$ and $T_\infty = 1000$ K.

To understand the influence of the Reynolds number on the accuracy of the 0D model, the results from 3 separate cases were plotted against the bulk temperature in Fig. 3.12. The diameter used here is 25.4mm. With Reynolds numbers ranging from 500 to 10000, the 0D and 1D models show almost identical results in terms of both the particle temperature and mass fractions. In fact, the Reynolds number or external transport conditions appears not to have a significant effect on the volume-averaged values in the given conditions. The Reynolds number has an effect on the surface values. In terms of the difference between surface and internal conditions, both the temperature

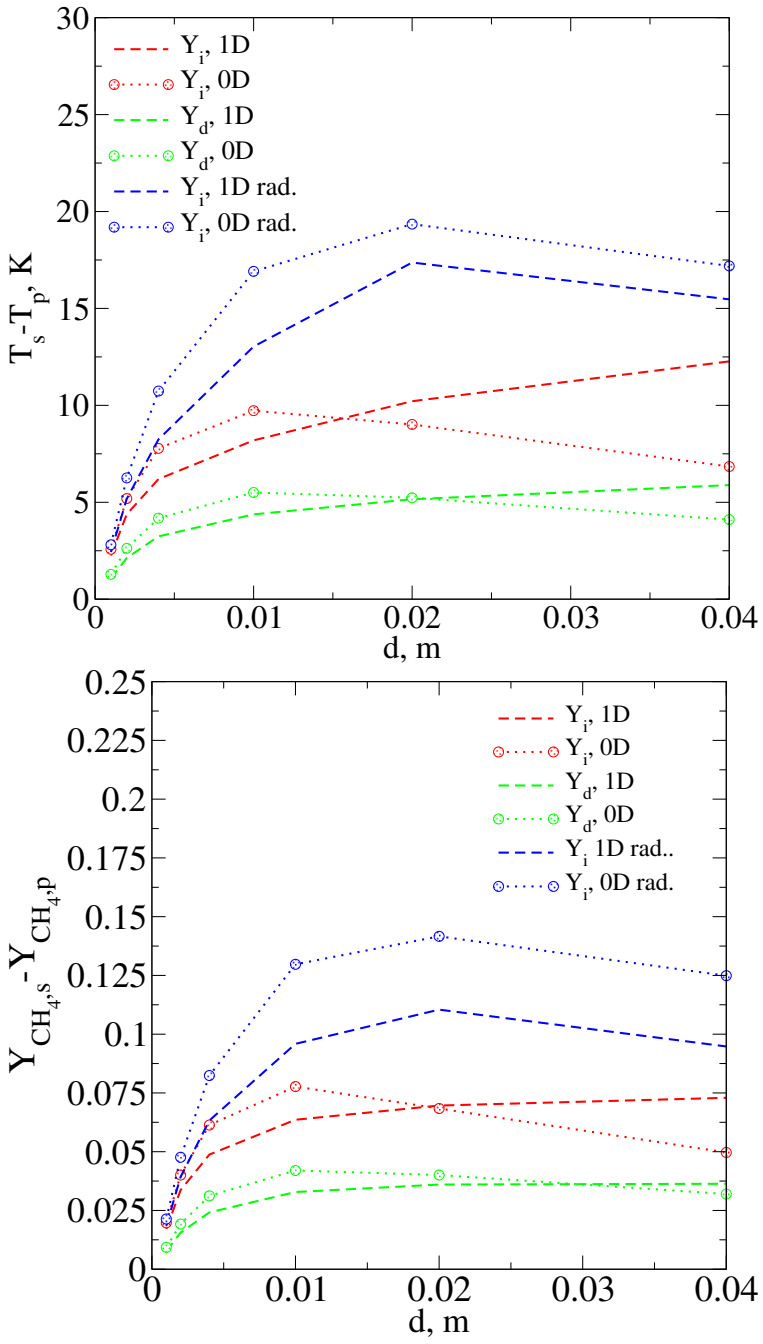

Figure 3.11: Difference between surface and volume-averaged temperatures and mass fractions compared for 1D model vs 0D submodel for different different diameters of the catalyst particle and different compositions of the ambient gas, see Table 3.2. Here $Re = 100$ and $T_\infty = 1000$ K

.

and mass fractions showed good agreement while comparing the 0D and 1D models, the maximum error being within 5K and 0.007, respectively.

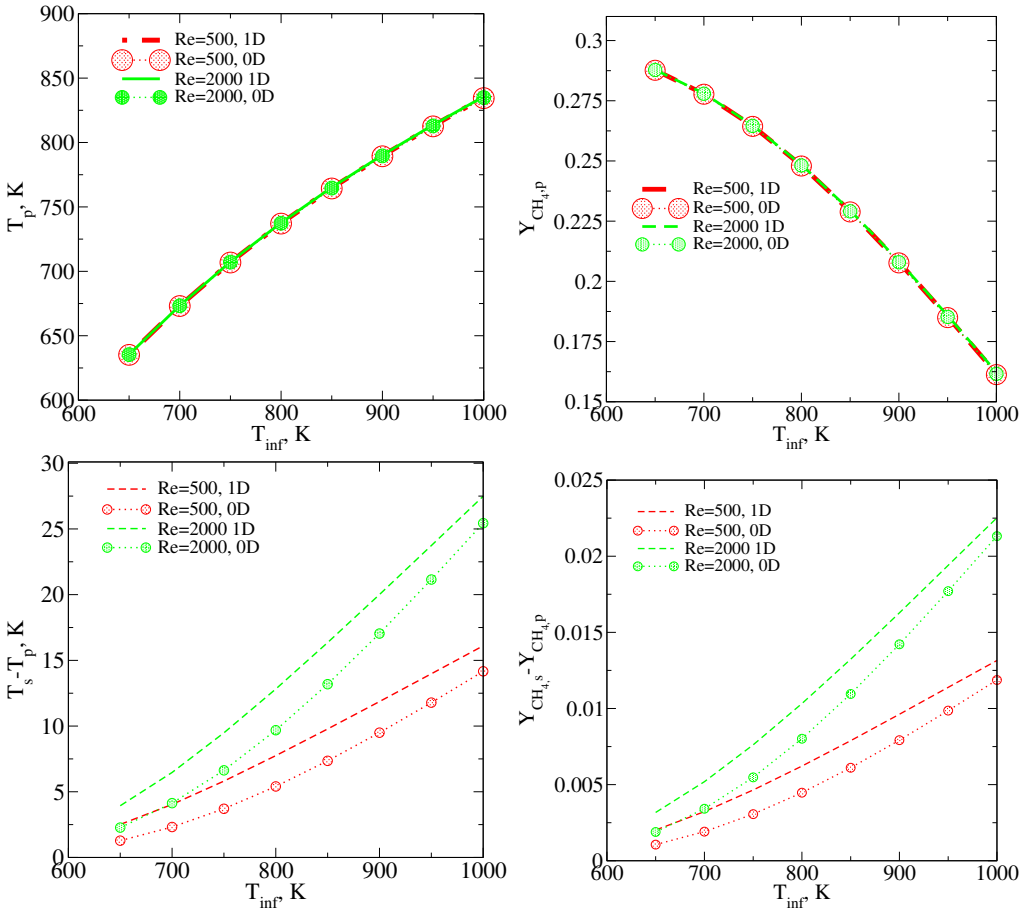

Figure 3.12: Comparison of the particle volume-averaged temperature and mass fractions of CH_4, H_2, CO_2 predicted using 1D model ($N_{gp} = 120$) for different ambient temperatures and Re. Here $d = 25.4$ mm.

3.4 Conclusions

In this work, a new 0D model for the steam reforming of methane inside a spherical catalyst particle (Ni/α-Al_2O_3) moving in a hot methane/steam atmosphere has been verified against a comprehensive 1D model that takes into account the internal heat and mass transfer coupled with the heat and mass transfer on the catalyst surface influenced by convection and diffusion around the particle. Good agreement (less than 1-2%) was achieved between predictions obtained using the new 0D model and results calculated using the 1D-based model for all particle diameter ranges for ambient gas temperatures below 900K. The increase in the ambient temperature and in the particle diameter

leads to deviations up to 5-10% between the 0D model and 1D model predictions.

Acknowledgment

The financial support by the Natural Sciences and Engineering Research Council (NSERC) Canada under Discovery Grant is appreciated.

Bibliography

[1] Shahab Golshan, Rahmat Sotudeh-Gharebagh, Reza Zarghami, Navid Mostoufi, Bruno Blais, and J.A.M. Kuipers. Review and implementation of CFD-DEM applied to chemical process systems. *Chemical Engineering Science*, 221:115646, 2020.

[2] P.N. Ciesielski, M.B. Pecha, N.E. Thornburg, M.F. Crowley, X. Gao, O. Oyedeji, H. Sitaraman, and N. Brunhart-Lupo. Bridging scales in bioenergy and catalysis: A review of mesoscale modeling applications, methods, and future directions. *Energy and Fuels*, 35:14382–14400, 2021.

[3] A.G. Dixon, M. Nijemeisland, and E.H. Stitt. Packed tubular reactor modeling and catalyst design using computational fluid dynamics. *Advances in Chemical Engineering*, 31:307–389, 2006.

[4] Jingyu Wang, Shangshang Wei, Qiuwang Wang, and Bengt Sunden. Transient numerical modeling and model predictive control of an industrial-scale steam methane reforming reactor. *International Journal of Hydrogen Energy*, 46:15241–15256, 2021.

[5] Bhanu Vardhan Reddy Kuncharam and Anthony G. Dixon. Multi-scale two-dimensional packed bed reactor model for industrial steam methane reforming. *Fuel Processing Technology*, 200: 106314, 2020.

[6] Dixon A.G. Local transport and reaction rates in a fixed bed reactor tube: Endothermic steam methane reforming. *Chemical Engineering Science*, 168:156–177, 2017.

[7] R. B. Bird, W. E. Stewart, and E. N. Lightfoot. *Transport Phenomena*. John Wiley & Sons, 2007.

[8] K. Hou and R. Hughes. The kinetics of methane steam reforming over a Ni/α-Al_2O catalyst. *Chem. Eng. J.*, 82:311–328, 2001.

[9] Yi Ran Lu and Petr A. Nikrityuk. DEM-based model for steam methane reforming. *Chemical Engineering Science*, 247:116903, 2022.

[10] B. Peters, M. Baniasadi, M. Baniasadi, X. Besseron, A.E. Donoso, M. Mohseni, and G. Pozzetti. XDEM multi-physics and multi0scale simulation technology: Review of DEM-CFD coupling, methodology and engineering applications. *Particuology J*, 44:176–193, 2019.

[11] A. Mahmoudi, P.A.J. Donkers, K. Walayat, B. Peters, and M. Shahi. A thorough investigation of thermochemical heat storage system from particle to bed scale. *Chemical Engineering Science*, 246:116877, 2021.

[12] L. Lu ad X. Gao, M. Shahnam, and W.A. Rogers. Bridging particle and reactor scales in the simulation of biomass fast pyrolysis by coupling particle resolved simulation and coarse grained cfd-dem. *Chemical Engineering Science*, 216:115471, 2020.

[13] R. Schwarz, S. DeYoung, and H. Spliethoff. Numerical simulation of gasification with a one-dimensional particle submodel for char structure evolution. *Fuel*, 293:120492, 2021.

[14] H. Ström and H. Thunman. A computationally efficient particle submodel for cfd-simulations of fixed-bed conversion. *Applied Energy*, 112:808–817, 2013.

[15] R. Schmidt, K. Wittig, and P. Nikrityuk. Single particle heating and drying. In P. Nikrityuk and B. Meyer, editors, *Gasification Processes: Modeling and Simulation*, pages 105–142. Willey-VCH Verlag GmbH & Co, Weinheim, Germany, 2014.

[16] S. Schulze, A. Richter, M. Vascellari, A. Gupta, B. Meyer, and P. Nikrityuk. Novel intrinsic-based submodel for char particle gasification in entrained-flow gasifiers: Model development, validation and illustration. *Applied Energy*, 164:805–814, 2016.

[17] M.A. Gimez, J. Porteiro, D. Patino, and J.L. Miguez. Fast-solving thermally thick model of biomass particles embedded in a cfd code for the simulation of fixed-bed burners. *Energy Conversion and Management*, 105:30–44, 2015.

[18] S. Schulze, R. Schmidt, and P. Nikrityuk. Subgrid models for particle devolatilization-combustion-gasification. In P. Nikrityuk and B. Meyer, editors, *Gasification Processes: Modeling and Simulation*, pages 271–304. Willey-VCH Verlag GmbH & Co, Weinheim, Germany, 2014.

[19] S. Schulze and P. Nikrityuk. A new subgrid model for the heat and mass transfer between a hot gas and char particles in dense-bed reactors. *Journal of Energy Resources Technology*, 138: 042206, 2016.

[20] Y.R. Lu and P.A. Nikrityuk. Steam methane reforming driven by the joule heating. *Chemical Engineering Science*, page submitted, 2021.

[21] Y.R. Lu, D. Pashchenko, and P.A. Nikrityuk. A new semiempirical model for the heat and mass transfer inside a spherical catalyst in a stream of hot CH_4/H_2O gases. *Chem. Eng. Sci.*, 238:116565, 2021.

[22] K. Wittig, A. Golia, and P.Nikrityuk. 3D numerical study of the influence of particle porosity on the heat and fluid flow. *Progress in Computational Fluid Dynamics*, 12:207–219, 2012.

[23] S. Whitaker. Forced convection heat transfer correlations for flow in pipes, past flat plates, single cylinders, single spheres, and flow in packed beds and tube bundles. *American Institute of Chemical Engineers Journal*, 18:361, 1972.

Chapter 4

DEM-based Model for Steam Methane Reforming [1]

4.1 Abstract

This work is devoted to the development and validation of a new 3D DEM-based (Euler-Lagrange) model for the steam reforming of methane in a tube filled with spherical catalyst particles (Ni/α-Al_2O). The new model includes five gaseous chemical species (CH_4, CO_2, CO, H_2O, H_2). The model uses reaction rate expressions taken from the literature (Langmuir-Hinshelwood-Hougen-Watson (LHHW) kinetics). The main novelty of the model is its ability to account for the intraparticle heat and mass transfer for each individual particle coupled with the heat and mass transfer between the particles and the bulk flow. The model is validated against results from a comprehensive particle-resolved 3D-CFD-based model published in the literature. This 3D benchmark case corresponds to a 0.7 m length of packed tube, that consists of 807 spherical catalyst particles at a tube-to-particle diameter ratio of $N = 5.96$. The comparison between our DEM-based model and 3D benchmark results demonstrates a good agreement comprising of 4 K (1%) difference in the temperature of outflow gas phase and up to 3% differences in the composition of outflow gas. Additionally, this new model is compared with a partial equilibrium model, which uses chemical equilibrium inside the catalyst particles and mass transfer rates between the particle surface and gas flow to calculate the reaction rate expressions. The performances of these new models are illustrated using additional simulations for the same packed bed taking into account thermal radiation. Finally, we validate our model against 2D simulations of an industrial scale reformer-tube published in the literature. Good agreements were demonstrated.

[1] This chapter is based on the work: Yi Ran Lu, Petr A. Nikrityuk. *DEM-based model for steam methane reforming.* Chemical Engineering Science, Vol. 247, pp. 116903, 2022. DOI: 10.1016/j.ces.2021.116903

4.2 Introduction

The main objective of this work is the development and validation of the new simple heat and mass transfer models for steam methane reforming (SMR) in fixed beds. The distinguishing feature of new models is their ability to calculate SMR taking into account intraparticle transport processes inside each catalyst particle in a fixed bed using a minimal computational time and a minimal number of closure relations. Three models are considered: the first two models are based on a coupling of one-dimensional computational fluid dynamics model (1D-CFD) for the gas phase written in the Euler space and three-dimensional discrete element model (3D-DEM) formulated in the Lagrange space for the solid phase. The models are coupled via source terms characterizing the heat and mass transfer exchange between gas and solid phases. The third model is based on the assumption of chemical equilibrium in the gas and solid phases.

In the design of effective reactors for steam methane reforming, the important issue is the adequate prediction of the optimal characteristics of such devices, e.g., their length and diameter, and preferably homogeneous radial temperature distribution, determined by the thermal power available for SMR. Due to the complexity of transport and chemical processes inside reformers, not all experiments are capable to deliver fundamental features of all related phenomena. In this view, mathematical and numerical models have become viable alternatives and effective tools for understanding and optimizing steam-methane reformers[1, 2]. It should be emphasized that all these models use Computational Fluid Dynamics (CFD). For example, a number of works have recently been published on the numerical modeling of lab-scale reformers, e.g. [3, 4], and industrial-scale reactors[1, 2, 5]. The main majority of models utilizes 1D mixture models [6] or 2D & 3D CFD based model where fixed beds are treated as porous media[4]. In spite of the simplicity of permeability and mixture models, they demonstrate a good agreement with experiments [4]. But, one of the disadvantages of 2D and 3D mixture based CFD simulations that both models require closure relations for the dispersion coefficients and spatial distribution of the volume fraction of the solid phase in tubes. Such profiles can be predicted utilizing particle-resolved (PR) CFD coupled with the discrete element method (DEM) [7]. The coupled PR CFD-DEM approach enables modeling transport processes inside the bed, similarly to experiments. Such simulations require significant computing time and power [3]. This is why PR CFD calculations, resolving chemical reactions inside catalyst particles, are now limited by small-scale lab-reactors or to tubes.

With significant progress in multi-scale numerical simulations of dense particulate flows, e.g. see the reviews [8, 9], particle-unresolved Euler-Lagrange models in the form of coupled discrete-element models (DEM) and CFD models are becoming well-accepted tools for simulations of large-scale particulate systems.

Although there are studies on SMR using particle-resolved CFD, see the review [7], numerical models utilizing particle-unresolved CFD-DEM are rare. Due to this fact, in this work, we develop

two new particle-unresolved CFD-DEM-based models for the steam reforming of the methane inside a cylindrical packed bed filled with catalyst particles heated from the sidewall. Both models account for the internal heat and mass transfer using surface-averaged and volume-averaged temperature and species concentrations predicted for each individual particle. These models are validated against a comprehensive particle-resolved 3D CFD-based model[3], where the steady-state Navier-Stokes equations and the energy and species conservation equations were utilized to model the heat and mass transfer inside a tube for SMR.

4.3 Problem description

To validate our models, we calculate Dixon's benchmark case published in the literature [3]. A random packed bed consists of 807 spherical catalyst particles packed randomly in tube with $N = \frac{D_r}{d_p} = 5.96$. The constant heat flux is supplied to the tube wall. Semi-global chemical reactions have the form:

$$CH_4 + H_2O \Leftrightarrow CO + 3H_2 \tag{4.1}$$

$$CO + H_2O \Leftrightarrow CO_2 + H_2 \tag{4.2}$$

$$CH_4 + 2H_2O \Leftrightarrow CO_2 + 4H_2 \tag{4.3}$$

A simplified computational domain is shown in Fig 4.1a, where the tube length and diameter were $L = 0.6858$ m and $D_r = 0.1514$ m. The tube was packed with spheres, whose diameter was $d_p = 0.0254$ m. According to the work [3], the first three particle layers ($Li = 0.0762$ m) comprising 85 spheres were inert. This distance is shown in Fig. 4.1a as L_i. It should be noted that the original geometry considered by Dixon [3] included the first 0.0254 m and the last 0.0508 m of the tube as empty and insulated, for reason related to the inflow and outflow. In this work we exclude both parts from consideration.

The flow conditions are taken from the work [3], see Table 4.1. It can be seen that the inflow particle Reynolds number is $Re_p \approx 3 \cdot 10^3$. The properties of the gas phase and catalyst particles were assumed to be constant, see Table 4.2. The fluid was approximated as an ideal gas with inflow composition given in Table 4.3. For comparison, we show equilibrium values of mass fractions $Y_{g,i}$ predicted for $T = 1019$ K and $P = 2140000$ Pa.

The tube wall thickness was taken as $\delta_w = 0.01$ m. According to the work [3] the wall properties are:

- wall density $\rho_w = 8000$ kg/m^3
- specific heat $c_{pw} = 680$ J/kg K
- thermal conductivity $k_w = 25.0$ W/m K

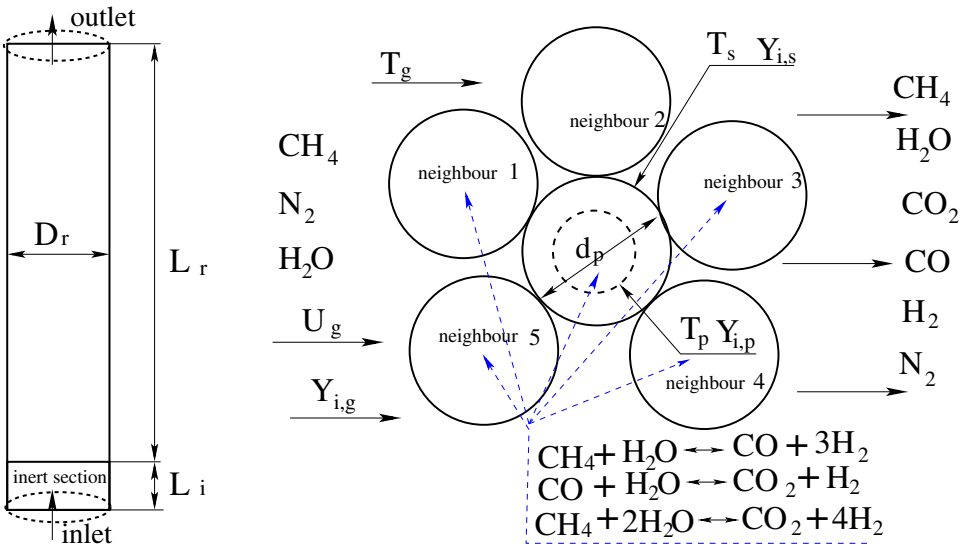

Figure 4.1: Diagram of benchmark geometry and diagram of catalyst particle with its neighbors in a fixed bed to illustrate arrangement in the system of equations

Inflow velocity U_{in}	Inlet temperature T_{in}	Outlet pressure P_{out}	Wall heat flux q''_w	Inlet Re_p
2.626 m/s	1019.05 K	2110 kPa	117.3 kW/m^2	$3 \cdot 10^3$

Table 4.1: Flow conditions as in the work [3].

Property	Gas	Catalyst
heat capacity	$c_{pg} = 2658.6$ J/kg K	$c_{pp} = 1000$ J/kg K
thermal conductivity	$k_g = 0.1685$ W/m K	$k_p = 1.0$ W/m K
viscosity	$\mu_g = 3.78 \cdot 10^{-5}$ Pa s	$- - -$
density	ideal gas	$\rho_p = 1947$ kg/m^3

Table 4.2: Material properties as in the work [3].

4.4 Kinetics-based model - KM

In this section, we describe the kinetic-based model to predict numerically the heat and mass transfer in a packed tube heated from the sidewall. The model includes conservation equations for the gas phase written in 1D form. Heat and species balance equations are written in 0D form for each particle using Lagrangian space. A 0D heat and mass transfer model for a single catalyst particle was derived and validated in the work [10]. Because our model treats each particle separately, the model is capable to calculate the 3D distribution of the solid phase temperature and species concentration inside the tube. To solve numerically 1D transport equations for the gas phase, the

	Y_{CH_4}	Y_{H_2O}	Y_{H_2}	Y_{CO}	Y_{CO_2}
inlet	0.0926	0.4680	0.0442	0.1181	0.2771
equilibrium	0.0902	0.4617	0.0455	0.1165	0.2861
$\left\|\frac{Y_{in,i}-Y_{eq,i}}{Y_{eq,i}}\right\| \cdot 100\%$	2.6608%	1.3645%	2.8571%	1.3734%	3.1458%

Table 4.3: Inflow gas composition as in the work [3].

tube is divided into segments in the axial direction. The fluid phase and the particle phase are coupled using empirical relations for the Nusselt and Sherwood numbers. The particle surface and particle interior are treated using 0D balance models to take into account the effects of internal diffusion.

Before the mathematical model is described, we introduce the following assumptions:

1. the system is at steady-state with unsteady forms of original balance equations shown to illustrate the derivation of the final equations,
2. the catalyst particle porosity does not influence the overall pressure drop in the tube,
3. the gas flow is treated as an ideal gas,
4. due to 1D character of the model describing the heat and mass transfer in the gas phase the influence of turbulence on the heat and mass transfer is not considered,
5. buoyancy effects are neglected,
6. due to 1D character of the model describing the heat and mass transfer in the gas phase the influence of the wall channeling effect on the heat and mass transfer near the wall is not considered. The 'near-wall channeling' effect is attributed to a sinusoidal radial profile of the void fraction close to the wall within several particle diameters, for details we refer to the review[7],
7. radiative heat transfer is neglected in the base case as in the work [3], however, considered in this work in a separate case.

Using the assumptions, the final governing equations take the following form:

- Mass conservation equation:

$$\frac{d}{dz}\left(\rho_g\, u_z\right) = 0; \qquad \rho_g = \frac{P}{R_g\, T_g} \tag{4.4}$$

The Ergun equation [11] is used to calculate P:

$$\frac{\Delta P}{L} = \frac{150\mu_g}{d_p^2}\frac{(1-\varepsilon)^2}{\varepsilon^3}v + \frac{1.75\rho_g}{d_p}\frac{(1-\varepsilon)}{\varepsilon^3}v^2 \tag{4.5}$$

It should be emphasized that instead of the Ergun's relation, the Eisfeld-Schnitzelin equation [12] could be used to take into account the wall channeling effect on the pressure drop. However, Kuncharam and Dixon [5] showed that both models produce almost the same results in terms of the heat and mass transfer predictions.

- The heat balance equation for the gas phase, written for a segment with the control volume of $A_c\Delta z$:

$$\cancelto{0}{c_{pg}\rho_g(\varepsilon A_c\Delta z)\frac{\partial T_g}{\partial t}} + \dot{m}c_{pg}\Delta z\frac{\partial T_g}{\partial z} = k_g\cdot\varepsilon A_c\Delta z\frac{\partial^2 T_g}{\partial z^2} + h_{wg}\pi D_i\Delta z(T_w - T_g) + \\ + \sum_{j=1}^{N_p}\left(h_{pg}A_p\left(T_{s,j} - T_g\right)\right) + \cancelto{0}{\sum_{j=1}^{N_p}\left(\epsilon_p\sigma A_p\left(T_s^4 - T_g^4\right)\right)} \tag{4.6}$$

where $A_c = \pi\frac{D_r^2}{4}$, N_p is the number of particles inside the control volume $A_c\Delta z$, $D_i = D_r - 2\delta_w$ is the internal diameter of the tube.

- The heat balance equation for the tube wall:

$$\cancelto{0}{c_{pw}\rho_w A_w\Delta z\frac{\partial T_w}{\partial t}} = k_w\cdot A_w\Delta z\frac{\partial^2 T_w}{\partial z^2} + \sum_{j=1}^{N_w}\left[\frac{T_{p,j} - T_w}{R_{th,w}}\right] + h_{wg}\pi D_i\Delta z(T_g - T_w) - \\ - \cancelto{0}{\sum_{j=1}^{N_w}\left(\epsilon_p\sigma\frac{A_p}{2}(T_w^4 - T_s^4)\right)} + q_w''A_w\Delta z \tag{4.7}$$

where $A_w = \frac{\pi}{4}(D_r^2 - D_i^2)$, and N_w is the number of particles in contact with the wall inside a control volume $A_w\Delta z$. In this equation the radiative heat transfer between the tube internal surface and the gas close to the wall is neglected.

- The heat balance equation for the catalyst particle surface:

$$(hA)_{in}(T_s - T_p) = h_{pg}\cdot A_p(T_g - T_s) + \cancelto{0}{A_p\sum_r^{N_r}(-\Delta H_r)R_{r,s}} + \cancelto{0}{\epsilon_p\sigma A_p\left(T_g^4 - T_s^4\right)} \tag{4.8}$$

- The heat balance equation for the catalyst particle:

$$\cancelto{0}{m_p c_p\frac{dT_p}{dt}} = (hA)_{in}(T_s - T_p) + V_p\sum_r^{N_r}(-\Delta H_r)R_{r,V} + \sum_{j=1}^{N_p}\left(\frac{T_{p,j} - T_p}{R_{th}}\right) + \delta_{pw}\left(\frac{T_w - T_p}{R_{th,w}}\right) \tag{4.9}$$

where δ_{pw} is the Dirac delta function, which equals zero for all particles except the particles in contact with the wall: for such particles $\delta_{pw} = 1$. Here, we neglect the impact of reactions

on the particle surface. N_{nb} is the number of neighbors for each particle. N_p is the number of particles inside the control volume $A_c\Delta z$.

- The species conservation equation for i species CH_4, CO_2, CO, H_2O and H_2 in the gas phase:

$$\cancelto{0}{\varepsilon\rho_g A_c\Delta z\frac{\partial Y_{i,g}}{\partial t}} + \dot{m}\Delta z\frac{\partial Y_{i,g}}{\partial z} = \varepsilon D_{gas}\cdot\rho_g A_c\Delta z\frac{\partial^2 Y_{i,g}}{\partial z^2} + \sum_{j=1}^{N_{nb}}\left[\beta_{pg}\cdot\rho_g A_p\left(Y_{i,s,j}-Y_{i,g}\right)\right] \quad (4.10)$$

- The species balance equation for i species CH_4, CO_2, CO, H_2O and H_2 on the catalyst particle surface:

$$\beta_{pg}A_p\rho_{g,s}(Y_{i,g}-Y_{i,s}) + \cancelto{0}{M_i A_p\sum_r^{N_r}\alpha_{r,i}\,R_{r,s}} = (\beta A)_{in}\rho_{g,p}(Y_{i,s}-Y_{i,p}) \quad (4.11)$$

  The chemical reactions on the particle surface in Eq. (4.11) and Eq. (4.8) were neglected because the ratio between the particle surface and overall particle surface participating in the reactions is approximetaly $10^{-2}\%$ for d_p considered in this work. The surface area (BET, m^2/g) of the catalyst used is 14.3 m^2/g, see the work [13].

- The species conservation equation for i species CH_4, CO_2, CO, H_2O and H_2 inside the particle:

$$\cancelto{0}{V_p\varepsilon_V\rho_{g,p}\frac{dY_{i,p}}{dt}} = (\beta A)_{in}\rho_{g,p}(Y_{i,s}-Y_{i,p}) + M_i V_p\sum_r^{N_r}\alpha_{r,i}R_{r,V} \quad (4.12)$$

  In this equation, we neglect the diffusive mass transfer between connected catalyst particles.

The reaction rates $R_{V,r}$ for each chemical reaction are calculated from reaction kinetics [13], where the reaction kinetics for steam reforming are given in units of [mol/m^3·s].

$$R_{V,1} = \frac{k_1(p_{CH_4}p_{H_2O}^{0.5} - p_{H_2}^3 p_{CO}/K_1 p_{H_2O}^{0.5})}{p_{H2}^{1.25}\mathrm{den}^2};\ R_{V,2} = \frac{k_2(p_{CO}p_{H_2O}^{0.5} - p_{H_2}p_{CO_2}/K_2 p_{H_2O}^{0.5})}{p_{H2}^{0.5}\mathrm{den}^2} \quad (4.13)$$

$$R_{V,3} = \frac{k_3(p_{CH_4}p_{H_2O} - {p_{H_2}}^4 p_{CO_2}/K_3 p_{H_2O})}{{p_{H_2}}^{3.5}\mathrm{den}^2} \quad (4.14)$$

where

$$\mathrm{den} = 1 + K_{CO}p_{CO} + K_H p_{H_2}^{0.5} + K_{H_2O}p_{H_2O}/p_{H_2} \quad (4.15)$$

According to the work [13], the rate coefficients are

$$k_1 = 5.922 \cdot 10^8 \exp\left(\frac{-209200}{R_g\, T}\right)\ [\text{kmol/s/kg/kPa}^{0.25}] \tag{4.16}$$

$$k_2 = 6.028 \cdot 10^{-4} \exp\left(\frac{-15400}{R_g\, T}\right)\ [\text{kmol/s/kg/kPa}] \tag{4.17}$$

$$k_3 = 1.093 \cdot 10^3 \exp\left(\frac{-109400}{R_g\, T}\right) [\text{kmol/s/kg/kPa}^{0.25}] \tag{4.18}$$

The adsorption coefficients take the following forms [13]:

$$K_{\text{H}_2\text{O}} = 9.251 \cdot \exp\left(\frac{-15900}{R_g\, T}\right)\ ; K_{\text{H}} = 5.68 \cdot 10^{-10} \exp\left(\frac{93400}{R_g\, T}\right) [\text{kPa}^{-0.5}] \tag{4.19}$$

$$K_{\text{CO}} = 5.127 \times 10^{-13} \exp\left(\frac{140000}{R_g\, T}\right) [\text{kPa}^{-1}] \tag{4.20}$$

In this work, we used the following expressions for the equilibrium coefficients:

$$K_1 = 1.198 \cdot 10^{17} \exp\left(\frac{-26830}{T}\right) [\text{kPa}^2];\ \text{K}_2 = 1.767 \cdot 10^{-2} \exp\left(\frac{4400}{\text{T}}\right) [\text{kPa}] \tag{4.21}$$

$$K_3 = 2.117 \cdot 10^{15} \exp\left(\frac{-22430}{T}\right)\ [\text{kPa}^2] \tag{4.22}$$

Finally, source terms in Eq. (4.12) and the subsequent equations take the following form for each specific species:

$$CH_4 :\ \sum_r^{N_r} (\alpha_{r,i} R_{V,r}) = -\left(R_{V,1} + R_{V,3}\right) \tag{4.23}$$

$$H_2O :\ \sum_r^{N_r} (\alpha_{r,i} R_{V,r}) = -\left(R_{V,1} + R_{V,2} + 2R_{V,3}\right) \tag{4.24}$$

$$CO :\ \sum_r^{N_r} (\alpha_{r,i} R_{V,r}) = R_{V,1} - R_{V,2};\ CO_2 :\ \sum_r^{N_r} (\alpha_{r,i} R_{V,r}) = R_{V,2} + R_{V,3} \tag{4.25}$$

$$H_2 :\ \sum_r^{N_r} (\alpha_{r,i} R_{V,r}) = 3R_{V,1} + R_{V,2} + 4R_{V,3} \tag{4.26}$$

The reaction enthalpy for reactions Eq. (4.1), Eq. (4.2) and Eq. (4.3) are $-\Delta H_1 = -206.1$ kJ/mol, $-\Delta H_2 = 41.2$ kJ/mol and $-\Delta H_3 = -165.0$ kJ/mol, respectively according to the work [3]. The

relation between the partial pressure and mass fraction is

$$p_i = \frac{Y_i P\, M}{M_i};\; M = \frac{1}{\sum_i^N \frac{Y_i}{M_i}} \tag{4.27}$$

The system of equations comprising Eqs. (4.6) - (4.12) is solved implicitly via MATLAB. The convective and diffusion terms in Eqs. (4.6) and (4.10) were discretized using the 2nd order upwind scheme and finite central difference scheme, respectively. The size of Δz was taken to be approximately $2r_p$. It should be noted that we utilized the minimum possible value of Δz. If we decrease Δz then we must calculate ε (bed porosity) values for each $\Delta z < d_p$. However, in this case the use of Gunn's relations is questionable. If we increase Δz such that $\Delta z \gg d_p$, then overall accuracy will be decreased. That is why we used $\Delta z \approx d_p$, which is the compromise between model reliability and accuracy of calculations. For the same reason, we had to use 2nd order Upwind scheme for discretization of convective terms. Due to the fact that $\Delta z \approx d_p$ the use of 1st order Upwind scheme would introduce a significant truncation error in calculations. The discretized Eqs. (4.6) and (4.10) were solved using a Gauss-Seidel matrix solver with the overrelaxation technique.

The coordinates of the catalyst particles were calculated using the open-source discrete element model (DEM) software YADE [14, 15], which uses DEM with the soft-sphere collision model to describe collisions between particles. The coordinates generated from YADE were imported into MATLAB with coordinates used to calculate resistances between particles. The validation of that software was reported in the work [16]. The system of non-linear equations was solved utilizing a fixed-point method with underrelaxation. The iterations were stopped when the estimated relative error for each dependent variable (T_s, T_p, $Y_{i,s}$, $Y_{i,p}$) was less than 10^{-6}. The simulation took less than 30 minutes to finish on a i7-5820HK 3.6Ghz computer. The MATLAB code of the developed model including input files with 3D coordinates of each particle can be found in supplementary materials of this article.

4.4.1 Closure relations and contact area

The mass transfer coefficient β_{pg} between the particle and gas phase is calculated from the Sherwood number correlation.

$$Sh = \frac{\beta_{pg} \cdot 2r_p}{D_i} \tag{4.28}$$

Likewise, the heat transfer coefficient is calculated from the Nusselt number.

$$Nu = \frac{h_{pg} \cdot 2r_p}{\lambda_g} \tag{4.29}$$

The Sherwood and Nusselt numbers are obtained using the Gunn relation [17]:

$$Nu = (7 - 10\varepsilon + 5\varepsilon^2)(1 + 0.7Re^{0.2}Pr^{0.33}) + (1.33 - 2.4\varepsilon + 1.2\varepsilon^2)Re^{0.7}Pr^{0.33} \tag{4.30}$$

$$Sh = (7 - 10\varepsilon + 5\varepsilon^2)(1 + 0.7Re^{0.2}Sc^{0.33}) + (1.33 - 2.4\varepsilon + 1.2\varepsilon^2)Re^{0.7}Sc^{0.33} \tag{4.31}$$

Both equations were chosen to be used in this work due to their verification against 3D DNS [18] (for lower Re_p values). In this work, we assume that the Lewis number equals unity ($Le = 1$), which is a reasonable assumption for hot gases [19, 20], thus, $Nu = Sh$. In Eq. (4.30), ε is the void fraction of the bed, which is calculated as follows:

$$\varepsilon = \frac{\frac{16}{3}\sum_{i=1}^{N_p} \pi r_{p,i}^3}{\pi D_r^2 L} \tag{4.32}$$

where $L = L_i + L_r$ is the height of the tube.

The particle Reynolds number is calculated using

$$Re_p = \frac{\rho_g u_z \cdot 2r_p}{\mu_g} \tag{4.33}$$

The diffusion coefficient of the gas D_{gas} is obtained by using Lewis number $Le = 1$:

$$Le = \frac{k_g}{D_{gas} c_p \rho} = 1; \;\; D_{gas} = \frac{k_g}{c_p \, \rho} \tag{4.34}$$

The mass and heat transfer coefficients for the intraparticle mass and heat transfer are defined as follows [21]:

$$(\beta A)_{in} = 4\pi D_{\text{eff}} \left(\frac{1}{a_1 r_p} - \frac{1}{r_p} \right)^{-1} \tag{4.35}$$

$$(hA)_{in} = 4\pi k_{\text{eff}} \left(\frac{1}{a_1 r_p} - \frac{1}{r_p} \right)^{-1} \tag{4.36}$$

where $a_1 = 0.85$ [21]

The effective diffusion inside the porous particle D_{eff} can be calculated combining two diffusion mechanisms: Knudsen diffusion and pore in porous media [22]:

$$D_{\text{pore}} = \frac{1}{\frac{1}{D_{gas}} + \frac{1}{D_{\text{Kn}}}} \tag{4.37}$$

The pore diffusion coefficient can be calculated using the molecular diffusion and the porosity of the

particle:

$$D_{\text{eff}} = \frac{\varepsilon_p}{\tau_p} D_{\text{pore}} \tag{4.38}$$

where $\varepsilon_p = 0.44$ is the catalyst particle porosity and $\tau_p = 3.54$ is the particle tortuosity [3].

The Knudsen diffusion coefficient is calculated as

$$D_{\text{Kn}} = \frac{2}{3} r_{pore} \sqrt{\frac{8 R_g T}{\pi M}} \tag{4.39}$$

where M is the molar mass of the mixture, r_{pore} is the pore radius. In this work, we used $r_{pore} = 10^{-7}$m according to the works [13, 3].

The wall-to-bed heat transfer coefficient h_w is calculated using the Yagi and Wakao wall-to-bed Nusselt number [23], which was recently verified numerically [24]:

$$Nu_w = 0.6 Re^{0.5} \; (Re < 40); \;\; Nu_w = 0.2 Re^{0.8} \; (Re > 40) \tag{4.40}$$

where $Nu_w = \frac{h_w 2 r_p}{k_g}$.

The heat rate between the two particles due to their static contact is calculated as follows:

$$Q_{cond} = \frac{T_i - T_j}{R_{th}} \tag{4.41}$$

where the thermal resistance due to the inter-particle conduction R_{th} takes the form (see the review [9]):

$$\frac{1}{R_{th}} = \frac{4 r_c}{\frac{1}{k_{p,i}} + \frac{1}{k_{p,j}}} \tag{4.42}$$

where r_c is the contact radius, and $k_{p,j}$ and $k_{p,i}$ are the thermal conductivities of particles j and i, respectively. If $k_{p,j} = k_{p,i}$, the thermal resistance R_{th} takes the form [25]:

$$R_{th} = \frac{1}{2\, r_c\, k_p} \tag{4.43}$$

The thermal resistance due to the particle-wall conductance $R_{th,w}$ takes the form:

$$\frac{1}{R_{th,w}} = \frac{4 r_c}{\frac{1}{k_w} + \frac{1}{k_{p,j}}} \tag{4.44}$$

The contact radius r_c between two touching elastic particles i and j which are locally spherical with radii r_i and r_j can be calculated according to Hertz theory[25, 26]. Since the fixed bed is modeled using DEM with a soft-sphere collision model (see Yade[15]), each particle reaches its state of the rest when the force balance for each particle is satisfied within a given numerical accuracy:

$$\left| \sum_{i=1}^{N_p} \vec{F}_{pn,i} + \delta_w \vec{F}_w + \vec{F}_g \right| \leq \delta_F \tag{4.45}$$

where $\vec{F}_{pn,i}$ and $\vec{F}_w$ are the compression forces acting on a particle normal to the common tangent plane at the point of contact with another particle or with the tube wall, respectively. $\vec{F}_g$ is the gravity force. In this work, we set $\delta_F = 10^{-2}$.

The force acting on the particle at position P_i from the particle at P_j is expressed as follows [26]:

$$\vec{F}_{pn} = \frac{4}{3} K R_m^{1/2} d^{3/2} \vec{n}; \text{ or } \vec{F}_{pn} = \frac{4}{3} \frac{K}{R_m} r_c^3 \vec{n} \tag{4.46}$$

where $\vec{n}$ is the unit vector indicating the direction of force.

$$\vec{n} = \frac{\vec{P}_i - \vec{P}_j}{|\vec{P}_i - \vec{P}_j|} \tag{4.47}$$

The constant K is the effective stiffness and it represents the elastic properties of the particle:

$$\frac{1}{K} = \frac{1 - \nu_i^2}{E_i} + \frac{1 - \nu_j^2}{E_j} \tag{4.48}$$

where E_i, E_j are the Young's moduli and ν_i, ν_j are the Poisson's ratios of particles i and j, respectively. The effective radius of curvature R_m of the particles i and j is given as follows:

$$\frac{1}{R_m} = \frac{1}{r_{p,i}} + \frac{1}{r_{p,j}} \tag{4.49}$$

Finally, the depth of indentation can be calculated using the following equation:

$$d = r_{p,i} + r_{p,j} - \left| \vec{P}_i - \vec{P}_j \right| \tag{4.50}$$

At the same time, d can be defined using the contact radius[26]:

$$d = \frac{r_c^2}{R_m}; \text{ or } r_c = \sqrt{R_m \, d} \tag{4.51}$$

To calculate $\vec{F}_w$ the same methodology can be used, just using a radius of curvature for the wall of $1/r_w = 0$, leading to $R_m = r_p$. Due to the fact that the E of the wall is higher than that of the particle in contact with the wall, thus $K = \frac{1-\nu_i}{E_i}$. The mechanical properties of the solid particles were set to those of alumina. For the purpose of simulation of packing, Young's modulus $E = 300GPa$ and Poisson's ratio $\nu = 0.21$ were used.

After Eq. (4.45) is satisfied, Eq. (4.51) is used to calculated r_c. Fig. 4.2 shows the contact area calculated between catalyst particles packed in the tube considered in this work. It can be seen that

the averaged contact radius is in the range from 1% to 0.1% of r_p.

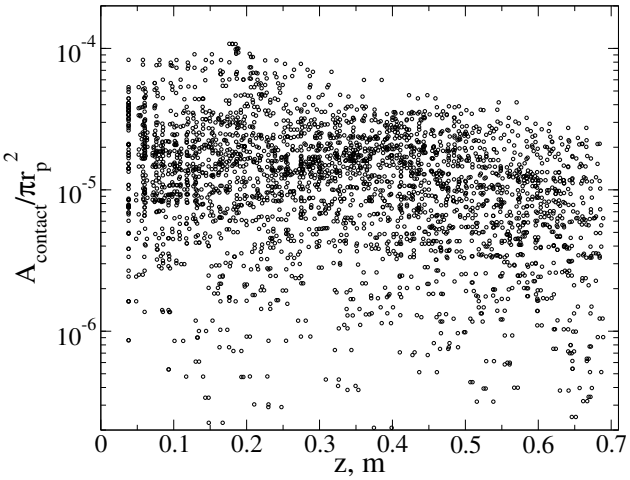

Figure 4.2: Contact area between particles predicted numerically

4.5 Partial equilibrium model - PEM

The distinguishing feature of the partial equilibrium model is the assumption that the gas composition inside the catalyst particle has reached equilibrium. The rate of reaction is equated to the rate of mass transfer and the heat rate of reaction is equated to the rate of heat transfer. The species concentration on the particle surface and in the gas phase are calculated from transport equations. This assumption is valid when the reaction is highly transport -limited. Under this assumption, the complete set of governing equations for the heat and mass transfer takes the following form:

- The heat transfer equation for the gas phase is given by Eq. (4.6).
- The heat transfer equation for the tube wall is given by Eq. (4.7).
- The heat transfer balance equation for the catalyst particle surface is given by Eq. (4.8).
- The heat transfer equation for the catalyst particle is given by Eq. (4.9)
- The species conservation equation for i species CH_4, CO_2, CO, H_2O and H_2 in the gas phase is the same as Eq. (4.10)
- The species balance equation for i species CH_4, CO_2, CO, H_2O and H_2 on the catalyst particle surface takes the form of Eq. (4.11).

- There is no species conservation equation for species CH_4, CO_2, CO, H_2O and H_2 inside the particle. Instead we calculate $Y_{i,p}$ using equilibrium values utilizing T_p and pressure values:

$$Y_{i,p} = f(T_p, P, Y_{g,i}) \tag{4.52}$$

The equilibrium system has 5 species and 3 atom balances. We only need two equations to find equilibrium. Eq. (4.1) and Eq. (4.2) are the two independent chemical reactions that are used to find the chemical composition inside the catalyst particle. Eq. (4.12) can be used to derive the source term in mass transfer equations:

$$M_i V_p \sum_{r}^{N_r} \alpha_{r,i} R_{r,V} = -(\beta A)_{in} \rho_{g,p} (Y_{i,s} - Y_{i,p}) \tag{4.53}$$

Since the species CH_4 and CO_2 only appears in one of the equations, the reaction rate can be expressed as the rate of mass transfer for CH_4 and CO_2.

$$-M_{CH_4} V_p R_{1,V} = -(\beta A)_{in} \rho_{g,p} (Y_{CH_4,s} - Y_{CH_4,p}) = -\beta_{pg} \rho_g A_p (Y_{\mathrm{CH_4,g}} - Y_{\mathrm{CH_4,s}}) \tag{4.54}$$

$$M_{CO_2} V_p R_{2,V} = -(\beta A)_{in} \rho_{g,p} (Y_{CO_2,s} - Y_{CO_2,p}) = -\beta_{pg} \rho_g A_p (Y_{\mathrm{CO_2,g}} - Y_{\mathrm{CO_2,s}}) \tag{4.55}$$

- Finally, the source term in the heat transfer equation in Eq. (4.9) takes the form:

$$\begin{aligned} V_p \sum_{r}^{N_r} (-\Delta H_r) R_{r,V} = {} & \frac{(-\Delta H_1)}{M_{CH_4}} (\beta A)_{in} \rho_{g,p} (Y_{CH_4,s} - Y_{CH_4,p}) - \\ & - \frac{(-\Delta H_2)}{M_{CO_2}} (\beta A)_{in} \rho_{g,p} (Y_{CO_2,s} - Y_{CO_2,p}) \end{aligned} \tag{4.56}$$

In summary, the partial equilibrium model can be used in diffusion-limited regimes since the rate of reaction is determined by diffusion. Instead of using kinetic models to find reaction rates, the partial equilibrium model equates the rate of reaction to the rate of mass transfer. Combined with the heat balance equation, the gas composition inside the particle is solved using equilibrium conditions.

4.6 Full equilibrium model - EM

The full equilibrium model is a homogeneous model that calculates the gas composition at equilibrium based on a given temperature and pressure. The equations for equilibrium constants take the

form in Eq. 4.57 and Eq. 4.58. The equilibrium constants were approximated based on Gibbs free energy from 1000K to 1100K, taken from NIST WebBook [27].

To validate the goodness of fit for Eq. (4.57) and Eq. (4.58), we numerically predicted the conversion of CH_4 depending on the gas temperature for different initial gas compositions, seen in Fig. 4.3. The results of simulations are compared with the data published by Sheu et al [28]. Excellent agreement has been found.

$$K_1 = 1.198 \cdot 10^{17} \exp\left(\frac{-26830}{T}\right) [\mathrm{kPa}^2]; \tag{4.57}$$

$$K_2 = 1.767 \cdot 10^{-2} \exp\left(\frac{4400}{T}\right) \tag{4.58}$$

The equations to be solved for equilibrium composition are:

$$X_{\mathrm{CO,g}} X_{\mathrm{H2,g}}^3 - \frac{K_1}{P^2} X_{\mathrm{CH_4,g}} X_{\mathrm{H_2O,g}} = 0 \tag{4.59}$$

$$X_{\mathrm{CO_2,g}} X_{\mathrm{H2,g}} - K_2 X_{\mathrm{CO,g}} X_{\mathrm{H_2O,g}} = 0 \tag{4.60}$$

The fluid phase heat balance equation is:

$$\varepsilon c_{p,g} \rho_g A_c \Delta z \frac{\partial T_g}{\partial t} + \dot{m} c_{p,g} \Delta z \frac{\partial T_g}{\partial z} = k_g \varepsilon A_c \Delta z \frac{\partial^2 T_g}{\partial z^2} + h_{wg} \pi d_i \Delta z (T_w - T_g) + Q_{chem} \tag{4.61}$$

where Q_{chem} is

$$Q_{chem} = \dot{m} \Delta z \left[\frac{(-\Delta H_1)}{M_{\mathrm{CH_4}}} \frac{\partial Y_{g,\mathrm{CH4}}}{\partial z} + \frac{(-\Delta H_2)}{M_{\mathrm{CO_2}}} \frac{\partial Y_{g,\mathrm{CO2}}}{\partial z} \right] + \tag{4.62}$$

$$+ \varepsilon D_{gas} \rho_g A_c \Delta z \left[\frac{(-\Delta H_1)}{M_{\mathrm{CH_4}}} \frac{\partial^2 Y_{g,\mathrm{CH4}}}{\partial z^2} + \frac{(-\Delta H_2)}{M_{\mathrm{CO_2}}} \frac{\partial^2 Y_{g,\mathrm{CO2}}}{\partial z^2} \right] \tag{4.63}$$

The term Q_{chem} is calculated from the simplified species mass transfer equation:

$$\dot{m} \Delta z \frac{\partial Y_{i,g}}{\partial z} - \varepsilon D_{gas} \cdot \rho_g A_c \Delta z \frac{\partial^2 Y_{i,g}}{\partial z^2} = M_i V_p \sum_r^{N_r} \alpha_{r,i} R_{r,V} \tag{4.64}$$

Finally,

$$X_{g,i} = \frac{Y_{g,i}}{M_i \sum_{i=1}^{N_s} \frac{Y_{g,i}}{M_i}} \tag{4.65}$$

where N_s is the number of chemical species.

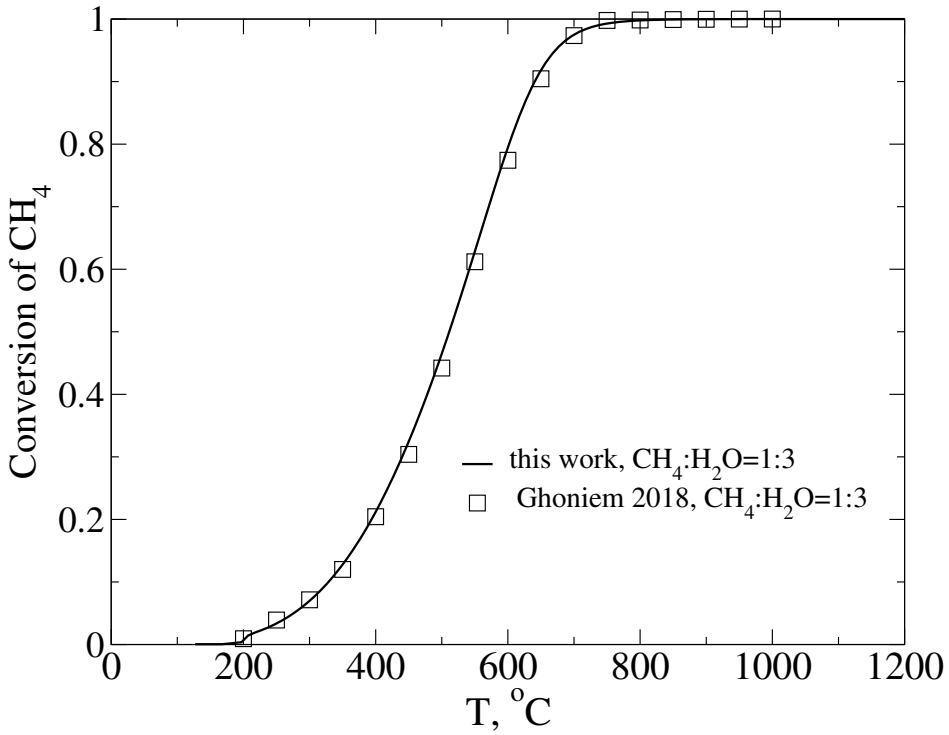

Figure 4.3: Temperature dependence of methane conversion at equilibrium for steam reforming for $P = 1$ amt. Here 'Ghoniem 2018' refers to the work [28].

4.7 Validation against Dixon's benchmark cases

The distinguishing feature of the models presented in this work is the absence of 3D computational meshes, the design of which is a non-trivial task due to the problem of the particle-particle contact point problem [3]. The KM and PEM models utilize a 1D mesh in the axial direction to solve all transport equations for the gas phase. The heat and species mass transfer between the catalyst particles and gas phase is modeled using 0D models via semi-empirical closure relations. 0D models bridge Eulerian space, where gas-phase equations are solved, and the Lagrangian space, where heat and species mass transfer is numerically calculated for every single particle. In this work, all the results predicted using the models are validated against Dixon's benchmark case, where comprehensive 3D CFD simulations were carried out to define the local transport and reaction rates in an endothermic steam methane reformer. This section presents comparisons of the results obtained using our three models: KM, PEM and EM with 3D CFD results predicted in the work[3].

It should additionally be emphasized that the analysis of reaction rates inside every particle was not carried out in detail. Since the description of transport processes gas phase and particle are identical to the benchmark case which this work is based on, for a detailed analysis of local transport processes inside the fixed bed and catalyst particles, please refer to the original work [3].

Axial profiles of the gas velocity, the gas temperature and particle temperature, and chemical species were compared to show the validity of the models in this work. In particular, Fig. 4.4 compares the axial profile of the superficial velocity predicted using the KM model with that obtained in 3D CFD simulations[3], where particles were connected with bridges to simplify the design of a computational mesh[3].

An excellent agreement is found though we use the 1D model for the gas phase equations, which do not allow us to take possible effects of turbulence on the transport processes in the gas phase into account. More valuable data are shown in Fig. 4.5 which presents a comparison of the axial profiles of particle temperature T_p and gas-phase temperature T_g. The results were obtained using three different models(the kinetic model (KM), the partial equilibrium model (PEM) and the full equilibrium model (EM)) and compared against Dixon's data [3] obtained from 3D CFD and 1D models, respectively. The 3D CFD results used bridges and the 1D results were without corrections. It can be seen that the full equilibrium model does not adequately predict the axial temperature profile, as the system does not reach equilibrium throughout the length of the tube. At the same time, it is evident that the KM and PEM models produced T_p and T_g values close to Dixon's data. It should be noted that the KM and PEM curves for both temperatures are almost identical. This similarity is explained by the fact that, firstly, the inflow composition of the gas phase is close to equilibrium values, shown in Table 4.3. Secondly, for the given temperature and particle size, the intraparticle reaction rate is in a diffusion-controlled regime, which results in near-equilibrium conditions inside the particle. The logic for using partial equilibrium model is for the simplicity of

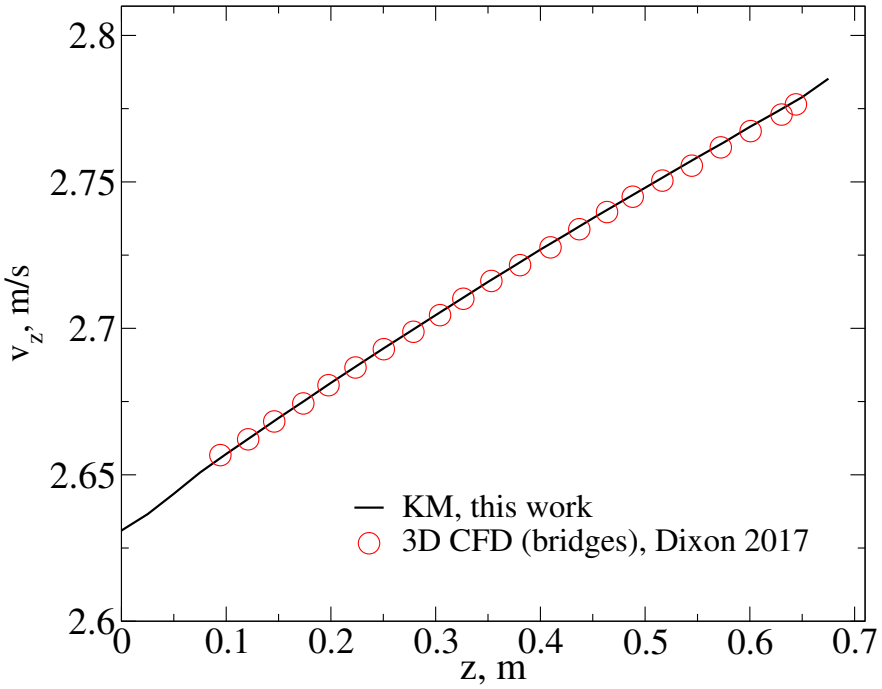

Figure 4.4: Axial profile of the superficial velocity predicted numerically using KM model. Here '3D CFD, Dixon 2017' reffers to the work [3].

computation. When the reaction rates are diffusion limited, as they are in this case, the kinetic model results in a system of equations that are very stiff. PEM makes the equation much easier to solve, thus greatly reducing the computational cost require to run the simulation.

Fig. 4.6 shows the axial profiles of species mole fractions predicted using the KM, PEM and EM models. For comparison, the results of 3D CFD and 1D simulations by Dixon [3] are also given in the figure. Again, it can be seen that the full equilibrium model (EM) does not produce close results along the tube axis. The KM and PEM models show results close to 3D CFD data, except the methane conversion, see Fig. 4.6f. Both KM and PEM data over predict 3D CFD by 3%. This discrepancy can be attributed to the different diffusion models used in the two works. In this work, mixture diffusion is used with the assumption of Le=1. In the benchmark case, Dixon used Fickian diffusion derived from the dusty gas model. The resultant effective diffusivity in the pellets would be different, causing the reaction rates to differ.

For the next part of the work, the influence of radiation on the heat and species mass transfer inside the tube is investigated. Equations describing the KM model, including Eqs. (4.6), (4.7) and (4.8), were solved with activated terms describing the radiative heat transfer. The exterior heat flux q''_w is maintained at the same level as the base case so the overall heat going into the system remains constant. The results of simulations are shown in Fig. 4.7 and Fig. 4.8. Fig. 4.7 depicts 3D plots of the particle temperature T_p and mole fractions of CH_4 and H_2 inside each particle inside the packed

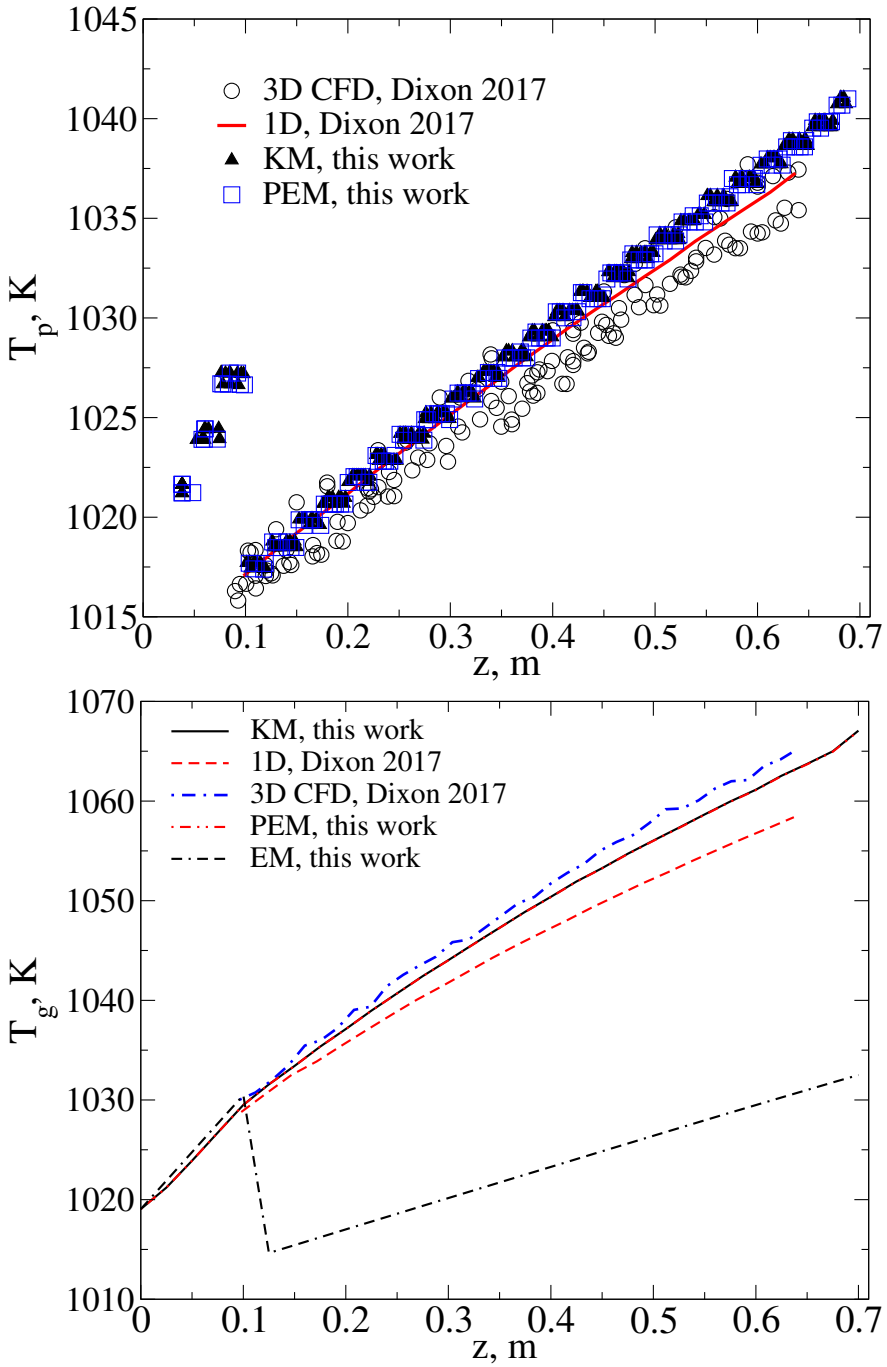

Figure 4.5: Comparison of axial profiles of the particle temperature T_p and gas phase temperature T_g predicted KM, PEM and full equilibrium model with Dixon's data [3] obtained from 3D CFD and 1D models, respectively.

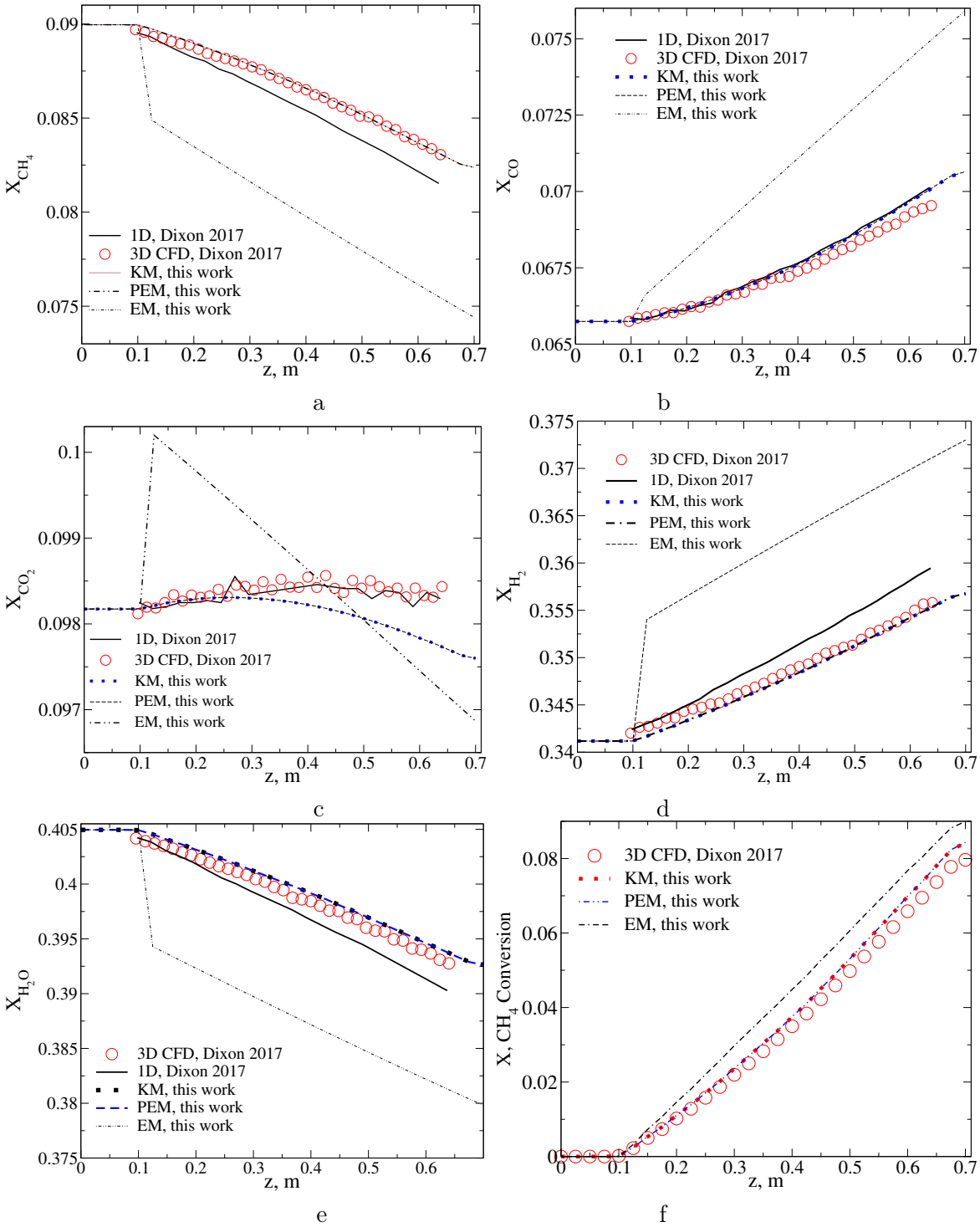

Figure 4.6: Comparison of axial profiles of species mole fractions predicted using KM, PEM and full equilibrium model with Dixon's data [3] obtained from 3D CFD and 1D models, respectively.

tube calculated using KM model. Due to the radiative heat transfer between the wall and particles, the particles in contact with the wall are at a higher temperature. The temperature increase in the near-wall particles due to radiation is quite significant in the case presented.

Fig. 4.8 shows the comparison of axial profiles of the particle temperature T_p and species mole fractions $X_{p,i}$ predicted using the KM without radiation and with radiation. The influence of radiation on the overall reaction rate is mixed, as shown in Fig. 4.8b and Fig. 4.8c. When radiation is included, strong radial variation in particle temperature is observed. Near-wall particles are most affected, with a significant increase in particle temperature. This effect leads to the acceleration of reactions in those particles. As a result, the outlet values of the methane mole fraction are less than values calculated without thermal radiation, see Fig.4.8b, and finally, the methane conversion values are higher than values predicted without radiative heat transfer, see Fig. 4.8c.

Since the heat flux is kept constant, the internal particles have a lower temperature and subsequently lower reaction rates. Because of the strong radial variation in the particle temperature, a significant temperature gradient is also expected in the fluid phase in the near-wall region. Thus, it can be seen that when radiation is strongly present, the accuracy of the model could be improved using 2D conservation equations for the heat and mass transfer in the gas phase [3].

To illustrate the deviation between our model results and Dixon's 2D effective medium model [3] predictions, Fig. 4.9 depicts the axial temperature profiles of the particles T_p and gas phase T_g predicted using KM model and Dixon's 2D model. The 2D-based model includes 2D the heat and chemical species conservation equations for the gas-phase and 1D diffusion equations for the spherical pellets. The axial velocity of the gas flow was calculated similarly to 1D model. From Fig. 4.9 it can be seen that our model produced results for the gas temperature closer to 3D data in comparison to 2D-base data. However, Dixon's 2D model with the inclusion of a radially-varying superficial averaged axial velocity $v_z(r)$ and the void fraction profile from (taken from 3D CFD) showed a fairly good agreement with 3D CFD simulations for T_g and T_p. In our KM model, we do not have 2D distribution of the axial velocity, that is why we cannot repeat the exact flow conditions with our model. Moreover, adding diffusion terms in the radial direction to Eqs. (4.6) and (4.10) will significantly increase the time of simulations.

Finally, to investigate our model performances referring to a large-scale steam methane reformer we compare our simulations with predictions of a multi-scale 2D simulations published in the literature [5]. Input parameters and inlet gas composition are given in Tab. 4.4. In our simulations we used $N_p = 9055$ and grid size $\Delta z = 2d_p$. Iterations were stopped when the estimated relative error for T_p, T_g and chemical species was less than 10^{-7}. The simulation took approximately 300 minutes using i7-5820HK 3.6Ghz computer.

Fig. 4.10 and Fig. 4.11 show the results of simulations. Both figures show that the gas temperature increases nonlinearly while the methane mass fraction decreases correspondingly. The deviation between the outlet gas temperatures predicted using our KM model and values calculated in the

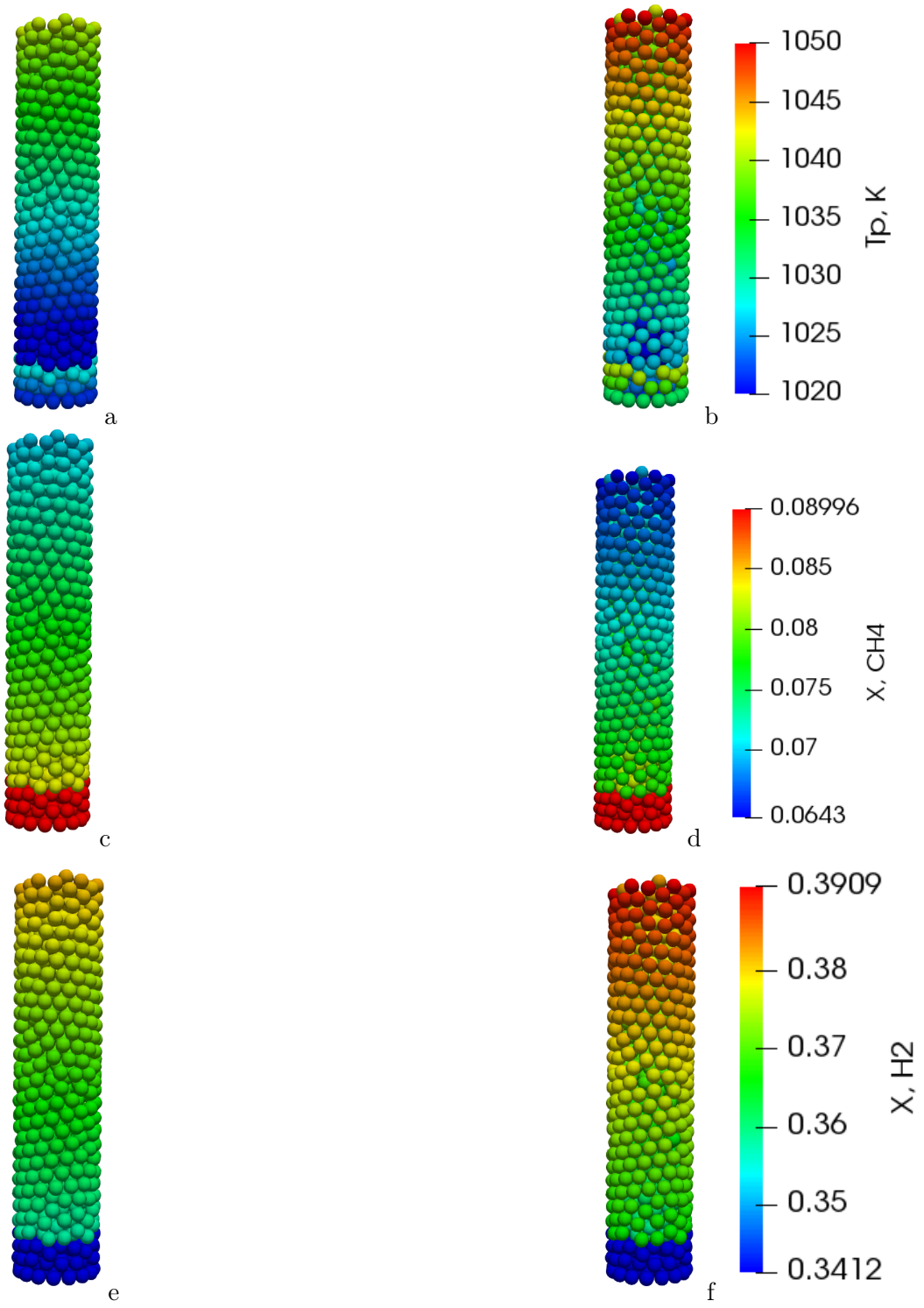

Figure 4.7: 3D plots of the particle temperature T_p and mole fractions of CH_4 and H_2 predicted using KM model without radiation a), c), e): and with radiation b), d), f).

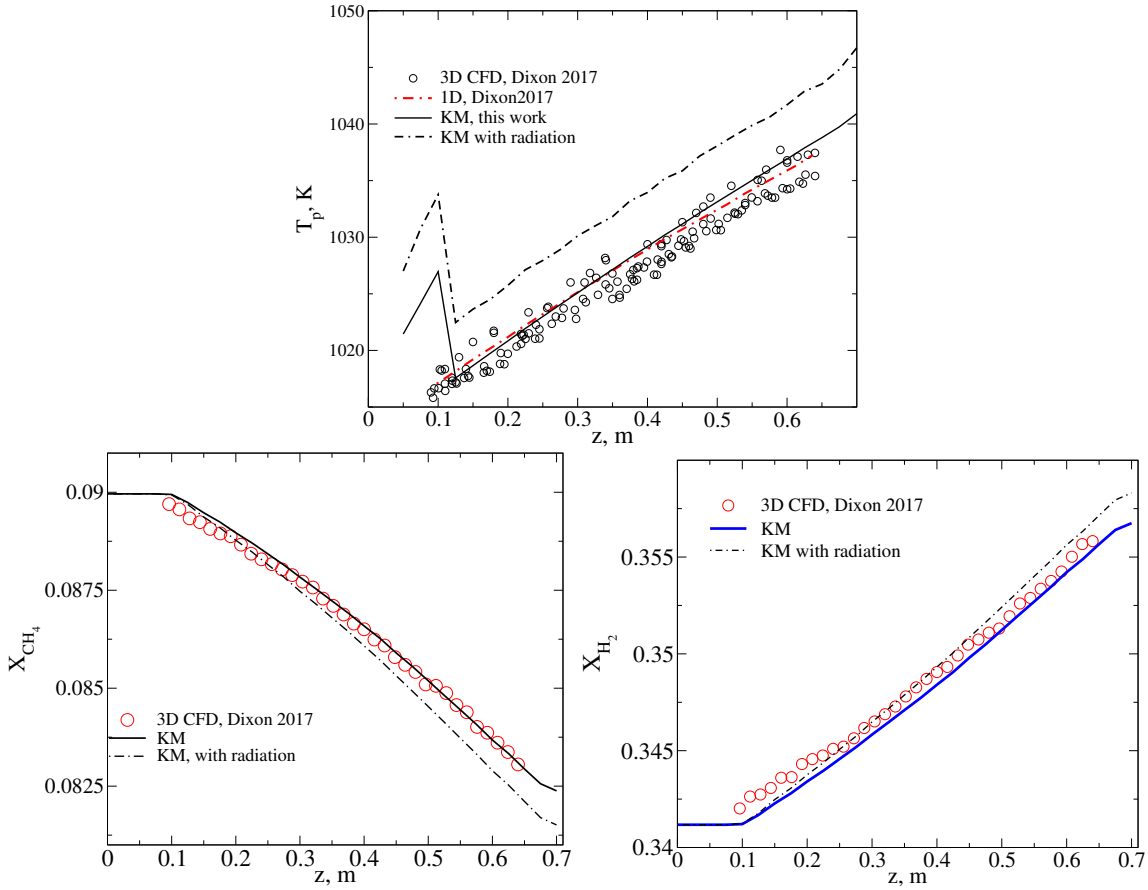

Figure 4.8: Comparison of axial profiles of the average particle temperature T_p (a) and axial profiles of species mole fractions predicted using KM without radiation and with radiation. Here Dixon 2017 refers to the work [3]

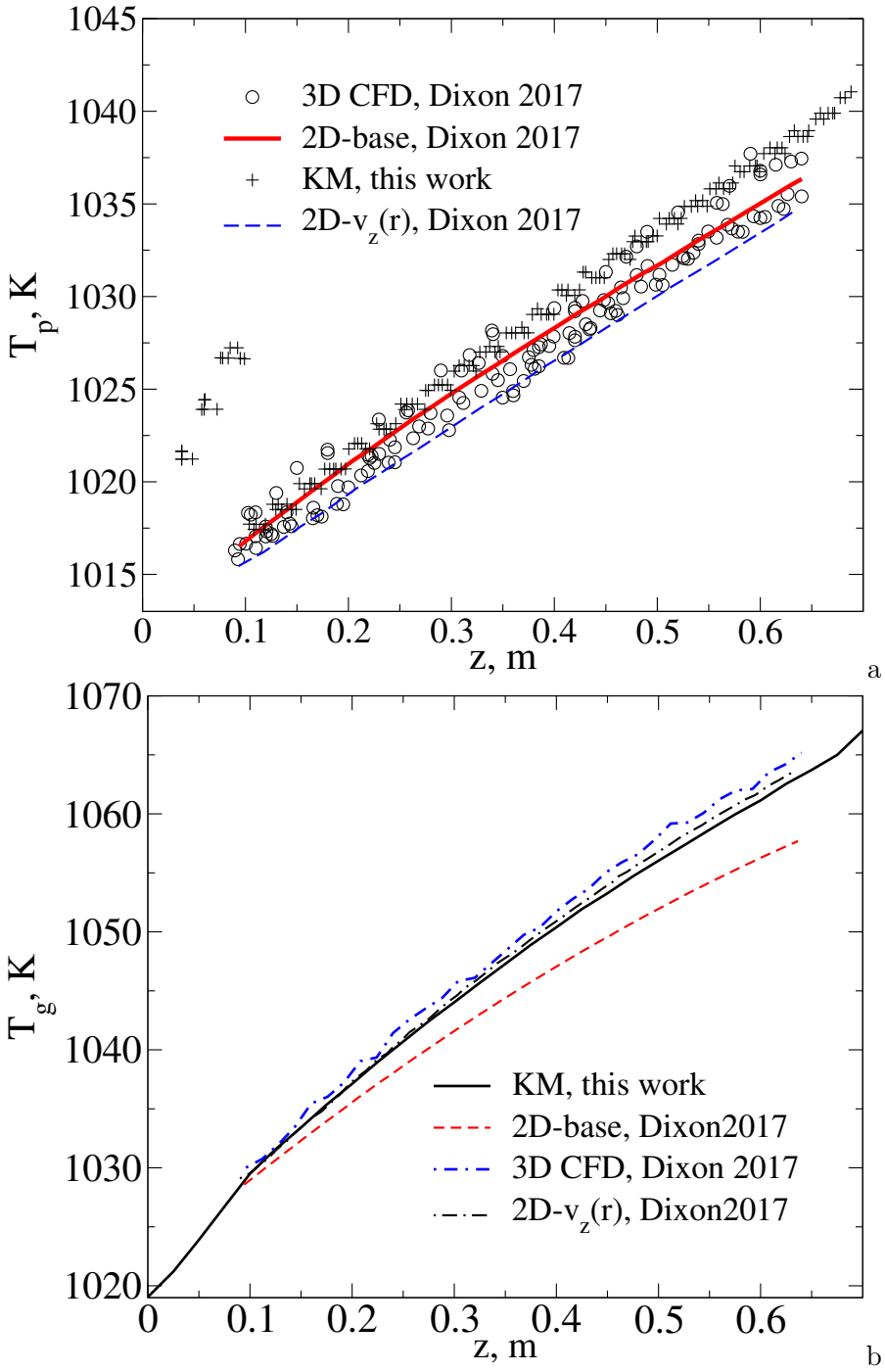

Figure 4.9: Comparison of axial profiles of the particles temperature T_p (a) and gas phase temperature T_g (b) predicted using KM model against 2D Dixon's data [3].

work [5] is 20 K comprising of 2% from the outlet value from 2D work. Referring to the mass fractions of chemical species CH_4 and H_2 in the gas outflow the difference between the 2D model and our KM model is 4%.

Parameters	
Inlet temperature (K)	824.15
Inlet pressure (bar)	21.59
Inlet velocity (m/s)	1.6237
Reactor tube diameter (m)	0.127
Reactor tube length (m)	10.6
Catalyst pellet diameter (m)	0.0254
Catalyst pellet density (kg/m^3)	1947
Porosity of packed bed	0.42
Density of packed bed (kg/m^3)	1130
Gas therm conductivity (W/m K)	0.1635
Pellet thermal conductivity (W/m K)	1.0
Inlet gas composition (mol %)	
CH_4	23.92
CO	0.05
CO_2	7.76
H_2	0.5
H_2O	67.77

Table 4.4: Input parameters and inlet gas composition [5].

4.8 Conclusions

In this work, we develop two new models: the kinetic model (KM) and the partial equilibrium model (PEM) for the steam reforming of methane inside a cylindrical packed bed filled with catalyst particles heated from the sidewall. Both models account for the intra-particle heat and mass transfer using surface-averaged and volume-averaged temperature and species concentrations predicted for each individual particle. The models incorporate interparticle heat transfer using the resistance model and particle-gas heat and mass transfer using convection correlations. The models have been validated against a comprehensive particle-resolved 3D CFD-based model in the published literature. Despite of the lack of resolution of the transport processes in the radial direction, the model was able to reproduce axial profiles with good agreement. In particular, the deviation between our DEM-based model and 3D benchmark results comprised of 1% difference in the temperature of outflow gas phase and up to 3% differences in the composition of outflow gas. The basis for this agreement is the

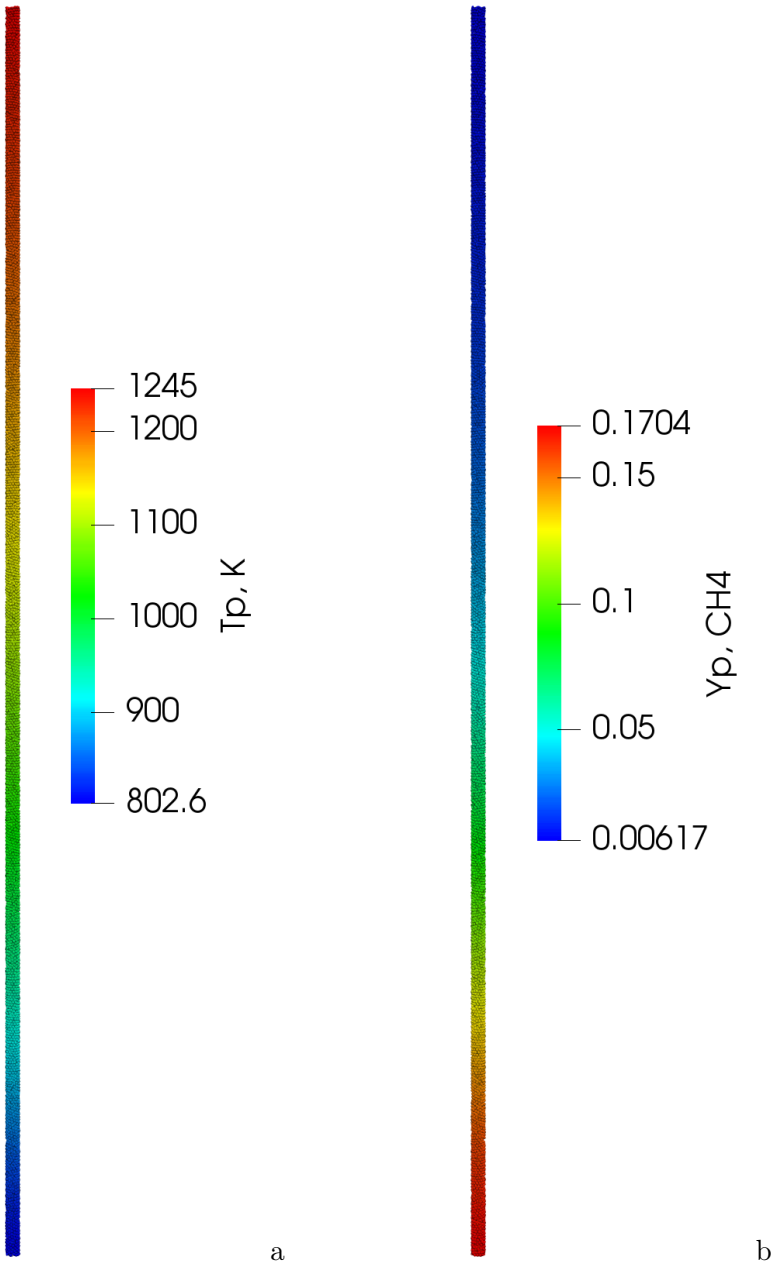

Figure 4.10: 3D plots of the particle temperature T_p and mass fraction of CH_4 inside pellets predicted using KM model according to the conditions from the work [5]

.

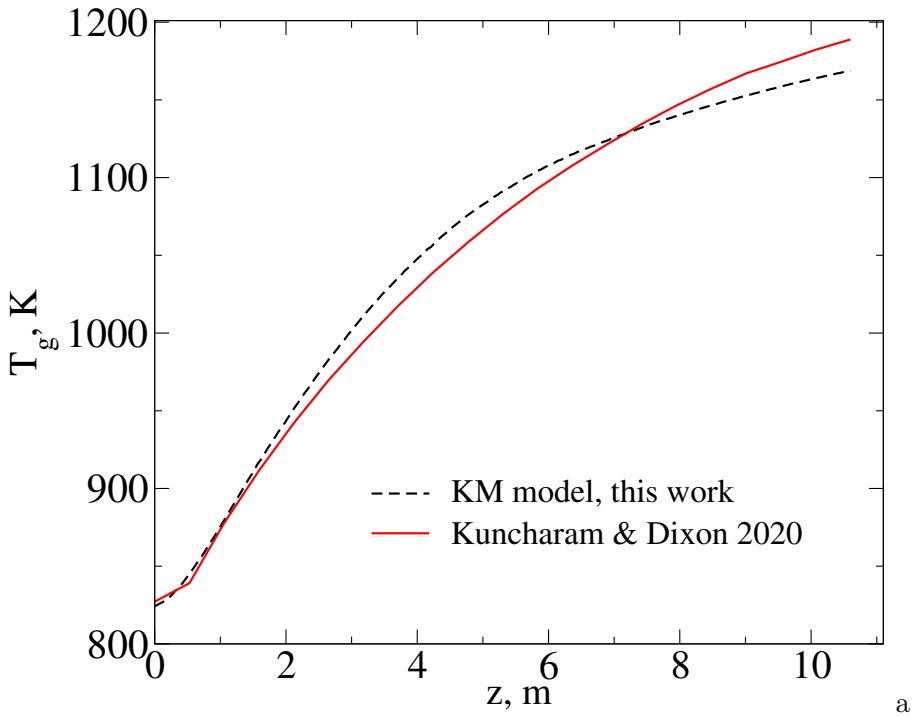

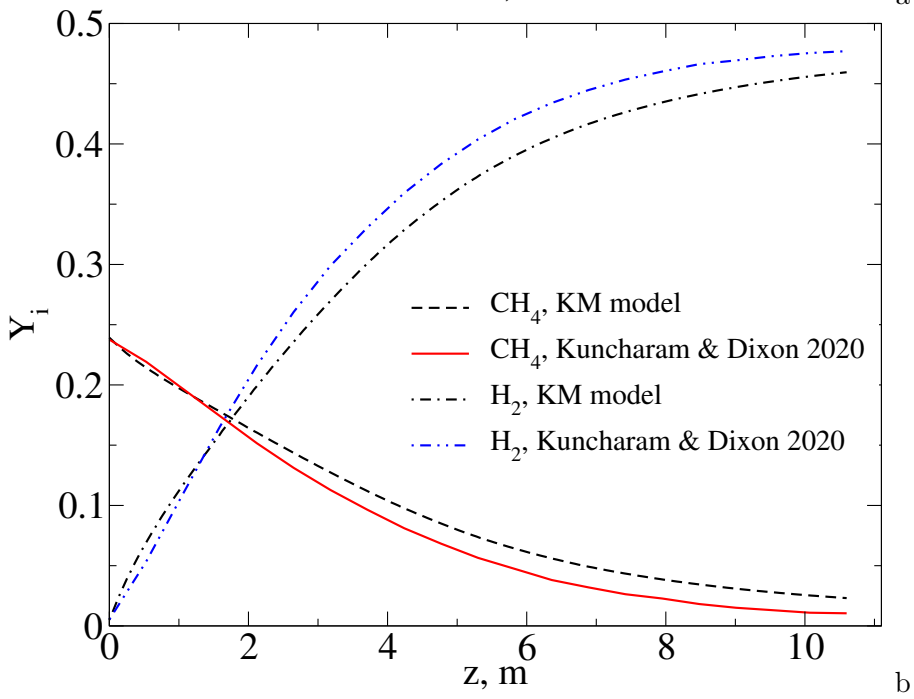

Figure 4.11: Comparison of axial profiles of the gas flow temperature T_g (a) and chemical species in the gas phase predicted using KM model against 2D Dixon's data [5].

local variations in the temperature and mass fractions from particle to particle, as observed in CFD simulations but unaccounted for in traditional 1D and 2D effective medium models. Additionally, we found out that for the given inlet flow conditions, the reaction is strongly diffusion-limited and the inlet gas compositions is close to equilibrium values. No significant deviation between the KM and PEM results was observed. There is observable deviation when the reaction kinetics play a role in determining the reaction rate.

4.9 Acknowledgments

The authors acknowledge the financial support by the Natural Sciences and Engineering Research Council (NSERC) Canada under the Discovery Grant 'Energy to Chemicals (E2C) using direct electrical current flowing through dense beds'.

Bibliography

[1] A.Tran, A. Aguirre, H. Durand, M. Crose, and P.D. Christofides. CFD modeling of a industrial-scale steam methane reforming furnace. *Chemical Engineering Science*, 171:576–589, 2017.

[2] Son Ich Ngo, Young-Il Lim, Woohyun Kim, Dong Joo Seo, and Wang Lai Yoon. Computational fluid dynamics and experimental validation of a compact steam methane reformer for hydrogen production from natural gas. *Applied Energy*, 236:340–353, 2019.

[3] Dixon A.G. Local transport and reaction rates in a fixed bed reactor tube: Endothermic steam methane reforming. *Chemical Engineering Science*, 168:156–177, 2017.

[4] Dmitry Pashchenko. Effect of the geometric dimensionality of computational domain on the results of CFD-modeling of steam methane reforming. *International Journal of Hydrogen Energy*, 43(18):8662–8673, 2018.

[5] Bhanu Vardhan Reddy Kuncharam and Anthony G. Dixon. Multi-scale two-dimensional packed bed reactor model for industrial steam methane reforming. *Fuel Processing Technology*, 200: 106314, 2020.

[6] S.Z. Abbas, V. Dupont, and T. Mahmud. Kinetics study and modelling of steam methane reforming process over a NiO/Al_2O_3 catalyst in an adiabatic packed bed reactor. *Int. J. Hydrogen Energy*, 42:2889– 2903, 2017.

[7] N. Jurtz, M. Kraume, and G.D. Wehinger. Advances in fixed-bed reactor modeling using particle-resolved computational fluid dynamics (CFD). *Reviews in Chemical Engineering*, 35: 139–190, 2019.

[8] Martin Anton van der Hoef, M van Sint Annaland, NG Deen, and JAM Kuipers. Numerical simulation of dense gas-solid fluidized beds: a multiscale modeling strategy. *Annu. Rev. Fluid Mech.*, 40:47–70, 2008.

[9] Z. Peng, E. Doroodchi, and B. Moghtaderi. Heat transfer modelling in Discrete Element Method (DEM)-based simulations of thermal processes: Theory and model development. *Progress in Energy and Combustion Science*, 79:100847, 2020.

[10] Y.R. Lu, D. Pashchenko, and P.A. Nikrityuk. A new semiempirical model for the heat and mass transfer inside a spherical catalyst in a stream of hot CH_4/H_2O gases. *Chem. Eng. Sci.*, 238:116565, 2021.

[11] S. Ergun. Fluid flow through packed columns. *Chem. Eng. Prog.*, 48:89–94, 1952.

[12] B. Eisfeld and K. Schnitzlein. The influence of confining walls on the pressure drop in packed beds. *Chem. Eng. Sci.*, 56:4321–4329, 2001.

[13] K. Hou and R. Hughes. The kinetics of methane steam reforming over a Ni/α-Al_2O catalyst. *Chem. Eng. J.*, 82:311–328, 2001.

[14] J. Kozicki and F. Donzé. Yade-open DEM: an open-source software using a discrete element method to simulate granular material. *Engineering Computations*, 26(7):786–805, 2009.

[15] Yade - Open source software for DEM. https://yade-dem.org/doc/, 2009.

[16] Yi Ran Lu and Petr Nikrityuk. A new fixed bed reactor for electrical energy storage into chemicals: Proof of concept. *Applied Energy*, 228:593–607, 2018.

[17] D. J. Gunn. Transfer of heat or mass to particles in fixed and fluidized beds. *International Journal of Heat and Mass Transfer*, 21(467-476), 1978.

[18] M.W. Baltussen, K.A. Buist, E.A.J.F. Peters, and J.A.M. Kuipers. Multiscale modelling of dense gas-particle flows. *Advances in Chemical Engineering*, 53:1–52, 2018.

[19] S. Schulze, M. Kestel, Safronov. D., and P. Nikrityuk. From detailed description of chemical reacting coal particles to subgrid models for CFD: model development and validation. *Oil & Gas Science and Technology*, 68:1007–1026, 2013.

[20] S. Schulze, A. Richter, M. Vascellari, A. Gupta, B. Meyer, and P. Nikrityuk. Novel intrinsic-based submodel for char particle gasification in entrained-flow gasifiers: Model development, validation and illustration. *Applied Energy*, 164:805–814, 2016.

[21] R. Schmidt, K. Wittig, and P. Nikrityuk. Single particle heating and drying. In P. Nikrityuk and B. Meyer, editors, *Gasification Processes: Modeling and Simulation*, pages 105–142. Willey-VCH Verlag GmbH & Co, Weinheim, Germany, 2014.

[22] R. E. Hayes and J. P. Mmbaga. *Introduction to chemical reactor analysis.* CRC Press Taylor and Francis Group, 2012. ISBN 9781466580534.

[23] S. Yagi and N. Wakao. Heat and mass transfer from wall to fluid in packed beds. *AIChE J*, 1: 79–85, 1959.

[24] V. Chandra, E.A.J.F. Peters, and J.A.M. Kuipers. Direct numerical simulation of a non-isothermal non-adiabatic packed bed reactor. *Chem. Eng. Journal*, 385:123641, 2020.

[25] G.K. Batchelor and R.W. Brien. Thermal or electrical conduction through a granular material. *Pro. Roy. Soc. Lond. A Math. Phys. Sci.*, 355:313–333, 1977.

[26] E. Dintwa, E. Tijskens, and H. Ramon. On the accuracy of the hertz model to describe the normal contact of soft elastic spheres. *Granular Matter*, 10:209–221, 2008.

[27] National Institute of Standarts and Technology, Chemistry WebBook, USA. https://webbook.nist.gov/chemistry, 2018.

[28] E.J. Sheu, E.M.A. Mokheimer, and A.F. Ghoniem. A review of solar methane reforming systems. *Int. J. Hydrogen Energy*, 40:12929–12955, 2015.

Chapter 5

Particle Unresolved Model for Predictions of Volt-Ampere Characteristics of a Packed Bed Heated by Joule Heating [1]

Abstract

This work is devoted to the development and experimental validation of a new model based on the Discrete Element Method (DEM) making it possible to calculate of volt-ampere characteristics of a fixed bed heated by the Joule heating. Joule heating is employed to provide the heat for chemically reacting gases flowing through the bed reactor. To validate our model against experimental data, we use a simple experimental setup, involving a cylindrical packed bed is considered with a height of 11 cm and an internal diameter of 4.8 cm. This bed is filled with 86 steel balls made of carbon steel with a diameter of 1/2 inches (1.27 cm). For the modeling, open-source DEM software is used to generate the cylindrical packed bed. Electric field distribution is calculated using a new particle-unresolved DEM-based model coupled with a simple heat transfer model to account for the temperature dependency of the steel particles' electrical conductivity. The results of the simulation were found to be in good agreement with experimental data. The new model can be used to design and optimize reactors heat source in the fixed bed reactors for energy conversion and storage.

[1] This chapter is based on the work: Y. R. Lu, D. Pudasainee, Md Khan, R. Gupta, P.A. Nikrityuk. *Experimental and numerical study of volt-ampere characteristics of a packed tube heated by Joule heating.* Journal of Energy Resources Technology (ASME), Vol. 144(5), pp. 052105 (12 pages), 2022. DOI: 10.1115/1.4053303

Nomenclature

A	area
r_p	radius of particle
r_c	radius of contact
r_{glass}	outer radius of the glass tube
x, y, z	coordinates of particles
ρ	density
c_p	specific heat capacity
T_g	gas temperature
T_s	particle surface temperature
T_p	particle temperature
T_c	cylinder wall temperature
T_∞	ambient temperature
d_p	particle diameter
k_p	particle thermal conductivity
k_g	gas thermal conductivity
h	convection coefficient
R_σ	electrical resistance
U	electrical potential
I	electrical current
Q_e	Joule heating power for a single particle
D	diameter of the bed
ε	void fraction
H	height of fixed bed
N_d	number of particles in the disk element
N_n	number of neighboring particles
N_c	number of particles in contact with the cylinder wall
$\mathbf{\Delta}$	thickness
$\vec{P}$	Position of particle
$\vec{F}$	Force acting on particle
E	Young's modulus
ν	Poisson ratio

5.1 Introduction

The use of Joule heating to sustain endothermic reactions in chemical reactors is a promising key technology to promote the use of renewable sources[1]. The primary application of Joule heating in the chemical industry is to convert electrical current into chemical energy [2, 3]. Direct current (DC) is commonly used in chemical processes as a versatile means of heating. A common use of Joule heating generated from DC is to produce the heat of reactions needed for endothermic chemical reactions [1, 4].

In particular, Lavoie and co-workers [1] developed a new iron bed consisting of steel wool (playing the role of the heater and catalyst) heated by the electrical current. This catalyst was used for the dry reforming of methane (DRM). Rieks et al. [4] reported an electrically heated mini-reactor for the steam methane reforming (SMR) and DRM. Heating elements made of $FeCrAl$ alloy have a wavy shape. Experimental and numerical studies on an annular four-layer fixed bed methane steam reformer with electrically heated catalysts were done by Zhang et al. [5]. A methane conversion of 83% at 1250 K has been achieved experimentally for the electrically heated reformer. It was shown that the placement of the catalyst layers has a significant influence on the performances of the reformer.

Despite the importance of subjects related energy storage related subjects in the field of heat transfer engineering, relatively few works have been published on multi-scale numerical techniques and scale-bridging models describing electrical fields, heat and mass transfer in electrically driven fixed-bed reactors. Recently, Lu and Nikrityuk [3] developed a new discrete-particle model for the heat transfer and electric fields in a fixed bed, especially for one heated by the Joule heating effect. The new feature of the said reactor is the application of electrically conductive particles, which carry the current to heat the reactor internally, and non-conductive catalyst particles, which provide active sites for the reacting gas. The concept of an electrically heated fixed bed was first studied by Glaser and Thodos [6]. In their experiments, the authors heated electrically conductive spherical particles using the Joule heating effect. One of the challenges for accurately modeling the Joule heating effect in fixed beds heated by electrical current lies in adequate predicting the contact area between particles. With significant progress in Discrete Element Modeling (DEM) of the heat and mass transfer in fixed and fluidized beds, it has become possible to make accurate predictions of different applications regarding moving dense beds [7]. Zhou et al. [8] developed a new approach using combined discrete particle simulation (DPS) and computational fluid dynamics (CFD) to model heat transfer in packed and bubbling fluidized beds. To calculate the heat conduction between two particles in stable contact, the authors used a modified form [9] of equations proposed by Batchelor & O'Brien [10], who adopted Hertzian theory for the contact radius between two particles. This equation takes the form [8] $Q_{ij} = \frac{4r_c(T_j - Ti)}{\frac{1}{k_{pi}} + \frac{1}{k_{pj}}}$, where r_c is the contact radius between spheres i and j, which are at temperatures T_i and T_j, respectively. Morris et al. [11] developed a soft-sphere contact

model for thermal heat conduction in granular flows, examining how different contact models (linear-spring dashpot (LSD) and Hertzian-spring dashpot (HSD) contact models) affect the conduction between particles in contact (or particles and a wall). Correction terms have been developed to minimize the impact that artificial softening has on the simulated heat transfer. Oschmann & Kruggel-Emden [12] developed a novel method calculating particle heat conduction and particle-wall heat transfer for the particle-unresolved Computational Fluid Dynamics/Discrete Element Method. The heat transfer approach used a non-linear contact model proposed by Tsuji et al. [13] which is based on Hertzian theory. The temperature inside each particle was calculated by solving the 3D heat conduction equation in spherical coordinates for each particle. Excellent agreement with experimental data was achieved.

Although numerous particle-unresolved DEM studies of heat transfer in different packed beds have been conducted, detailed in the review [7], there have been few particle-resolved simulations of fixed beds heated by direct electrical current going through metal particles. This fact can be explained by the high computational costs caused by the need to use fine meshes to adequately resolve a contact area between particles conducting electrical current. To solve this problem, a new model was developed in this work to compute electrical fields based on particle contact. This model enables the prediction of the distribution of Joule heating and the electrical fields inside a packed bed. To validate our model, an experiment has been conducted, which consists of passing DC through a packed bed of steel sphere and measuring the volt-ampere characteristics and temperature. The novelty of this work includes the development and the validation of a new particle-unresolved DEM model, enabling researchers to predict volt-ampere characteristics of electrically heated fixed beds. This new model can be used to model new energy conversion and energy storage reactors, that utilize direct current (DC) to sustain endothermic reactions.

5.2 Experiment

The main objective of the experimental study is to obtain the volt-ampere characteristics of a fixed bed heated by Joule heating. The fixed bed consists of 86 steel spheres packed in a glass cylinder with a diameter of $D = 0.048$ m and a height of $H = 0.11$ m, see Fig. 5.1. The glass wall thickness is $\delta_w = 1.7$ mm.

Two electrodes made of steel with a thickness of $\delta_e = 1$ mm are placed on the bottom and on the top of cylinder, closing the cylinder to any gas inflow or outflow. The bottom electrode lies on the ceramic plate (the thickness $\delta = 4$ mm) and the top electrode is covered by a ceramic plate. A 2 kg stainless steel weight was placed on the upper ceramic plate to improve the static contact between the steel spheres, allowing electrical current to flow through the bed. The mass of the weight was determined experimentally. With a 1 kg mass, the contact was not good enough to get a stable current for $U = 1$V. The schematic representation of the experimental setup is shown in

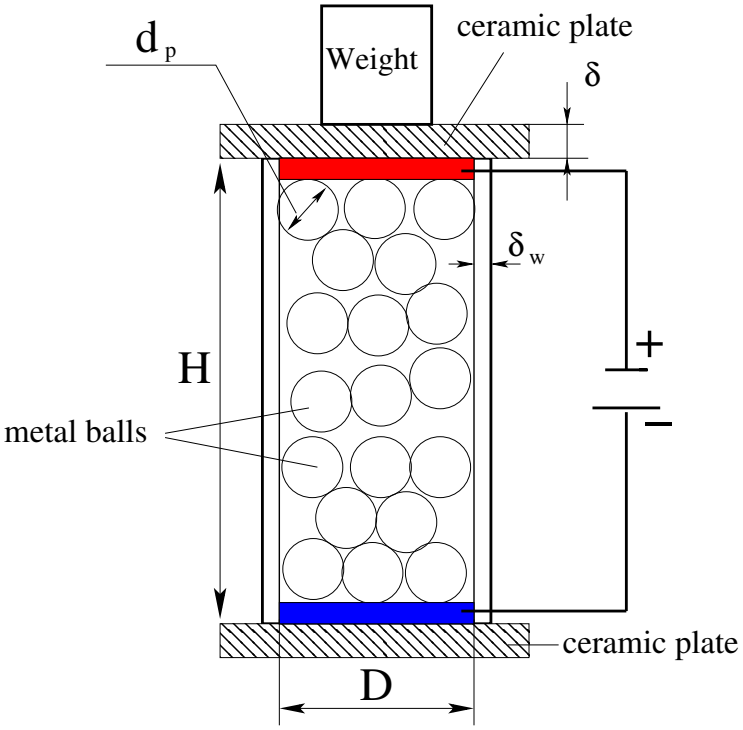

a

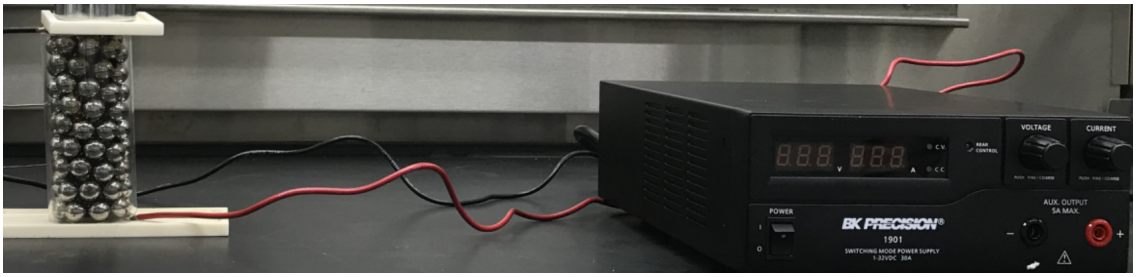

b

Figure 5.1: Experimental setup of the electrically heated steel particles packed in a glass cylinder: a - schematic representation of the experiment; b - photo of experimental setup.

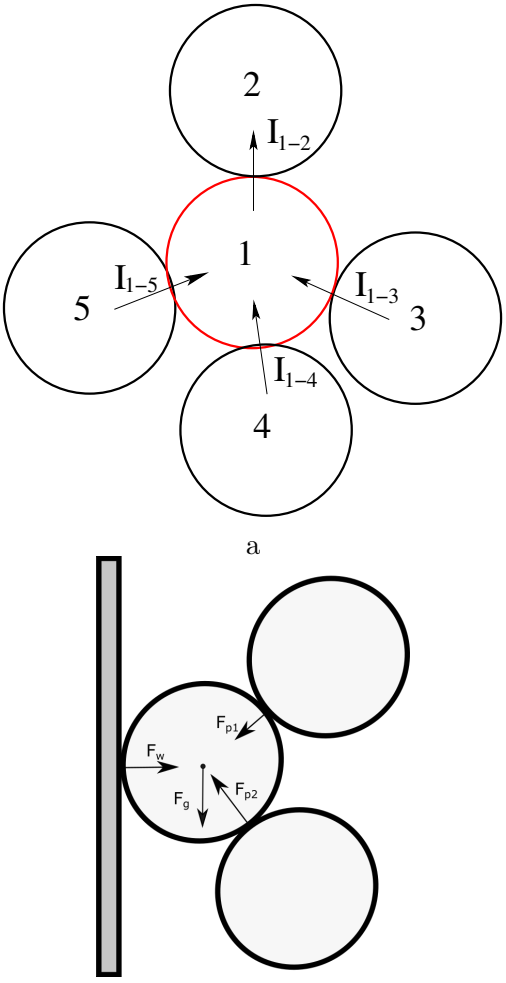

Figure 5.2: Illustration of electrical current density balance (a) and forces balance (b).

d_p	steel sphere diameter	0.0127 m (1/2-inch)
H	cylinder height between electrodes	0.11 m
D	glass cylinder internal diameter	0.048m
δ_w	glass wall thickness	0.0017 m
P	pressure	1 atm
T_∞	ambient temperature	296 K

Table 5.1: Operating conditions and input parameters used in the experiment

ρ_p	density of steel	7800 kg/m^3
σ	electrical conductivity of steel	$(4.28 - 0.00542\,(T - 273)) \cdot 10^6$ 1/Ohm
k_p	thermal conductivity of steel particles	43 W/m K
c_p	specific heat capacity of steel particles	448 J/kg K
ε_p	emissivity of steel particles	0.8
E	Young's modulus	190 GPa
ν_E	Poisson ratio	0.27
ρ_g	density of air	ideal gas law
k_g	thermal conductivity of air	0.0404 W/m K
c_g	specific heat capacity of air	1063 J/kg K
μ	viscosity of air	1.85 $\times 10^{-5}$ Pa s
ρ_c	density of glass	2500 kg/m^3
k_c	thermal conductivity of glass	0.8 W/m K

Table 5.2: Properties of steel particles [14, 15], air [14, 16] and glass cylinder.

Fig. 5.1. The instrument used to provide the voltage source "BK PRECISION 1901", (1-32V DC), which can supply current and voltage up to $I = 31.5$ A and $U = 32$ V. The accuracy of the I and U measurements was 0.1 A and 0.1 V, respectively. The electrodes were connected to the DC power using copper wires with the diameter of 1 mm. The geometric sizes and properties of the materials used are given in Table 5.1 and in Table 5.2, respectively. While measuring the volt-ampere characteristics, the voltage between the electrodes was increased slowly until electrical current start flowing through the bed. In this experiment, the minimum voltage required to have electrical current flowing through the bed was 0.75 V. For each specific voltage increase, we waited up to 20 minutes until the current value stabilized due to the corresponding increase in the temperature of the spheres and the corresponding change in electrical conductivity of the spheres. After the maximum electrical current was reached, the experiment was stopped.

5.3 Model Description

5.3.1 Electric field

In this work, we develop a new particle-unresolved (PUR) DEM-based model to calculate electric field distribution in fixed beds heated by the electrical current flowing through electrically conducting particles. The coordinates of the particles are calculated using the open-source Discrete Element Model (DEM) software YADE [17, 18], which employs the soft-sphere collision model. The composition of the fixed bed is simulated utilizing the gravity-driven settling of 86 steel particles in a tube. After the particles have reached the position of rest and the additinal weight of 2kg was set on the top, particles coordinates are used to obtain the contact area between particles. Thus, using the calculated area between them the electrical resistance between each pair of particles, $R_{\sigma,ij}$, can be calculated.

Before we introduce the electromagnetic field equations, we assume that when electrical current flows through the bed, each particle is characterized by the particle-averaged electric field potential ϕ_i, and the contact between the particles is treated like a resistor. Next, we use the electrical current conservation equation:

$$\nabla \cdot \vec{j} = 0 \tag{5.1}$$

Using Ohm's law we can write:

$$\vec{j} = \sigma \cdot \vec{E}; \implies \vec{j} = -\sigma \nabla \phi \tag{5.2}$$

Using Eq. 5.2, Eq. 5.1 and can be written for each particle i in the bed as follows:

$$\sum_{j=1}^{N_{nb}} \vec{j}_{ij} = 0 \implies \sum_{j=1}^{N_{nb}} \sigma_i \frac{\phi_i - \phi_j}{d_{ij}} = 0 \tag{5.3}$$

where N_{nb} is the number of particles i that are in contact with the particle i, ϕ_i represents the particle-averaged electric field potential, nad d_{ij} is the distance between centers of the two neighboring particles. An illustration of eq. (5.3) is shown in Fig. 5.2.

In analogy to the heat conduction between two particles with a static contact, Eq. 5.3 takes the form:

$$\sum_{j=1}^{N_{nb}} \frac{\phi_i - \phi_j}{R_{\sigma,ij}} = 0 \tag{5.4}$$

For a bed of N_p particles, a system of N_p equations needs to be solved. The ϕ of each particle is solved in an N_p by N_p matrix, with non-zero terms visualized in Fig. 5.3.

To solve the system of linear equations, the following boundary conditions are used:

$$\phi_i = 0 \; for \; z = 0; \; and \;\; \phi_j = \phi_c \; for \; z = H \tag{5.5}$$

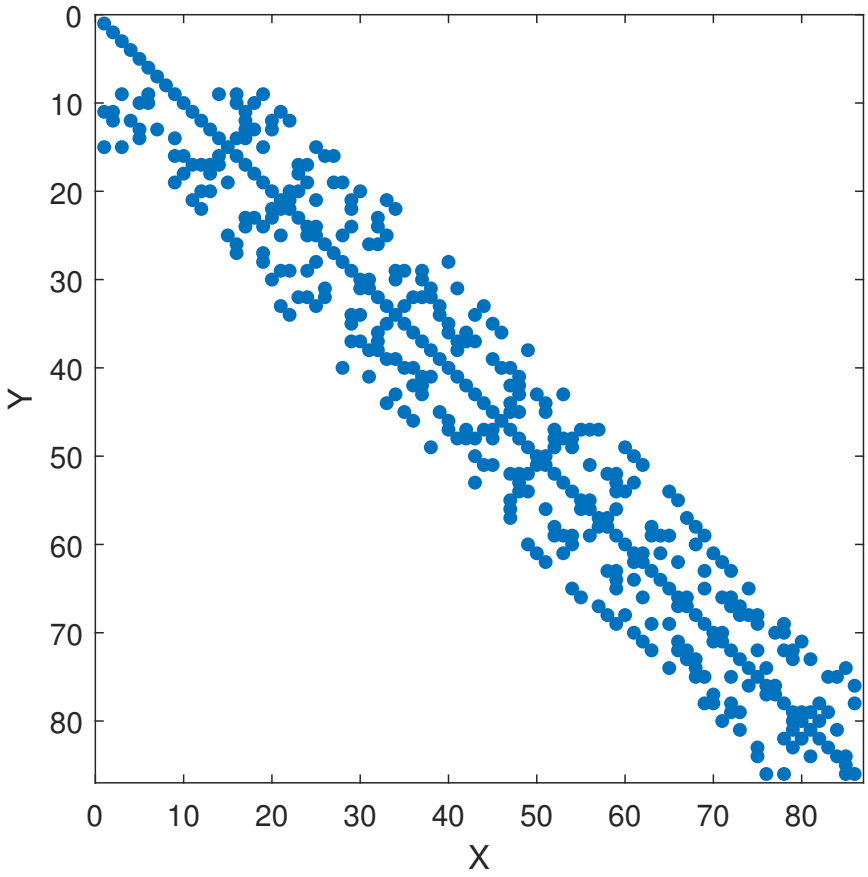

Figure 5.3: Final matrix structure used to calculate the distribution of the voltage between particles in the bed. Here axis X and Y correspond to number of particles, and change from 1 to $N_p = 86$.

This boundary conditions define the electric field potentials at the cathode and the anode, as specified by the current source.

To get a diagonally dominant band matrix, the particles are indexed based on the order of axial position. In the case of the simulation with 86 particles, the matrix is a sparse 15-diagonal matrix. If a particle i has only one contact with neighboring particles, this particle does not complete a circuit or have Joule heating. Thus the said particle has the same electrical potential as its single neighbor and can be excluded from the iteration of the voltage matrix. The matrix is solved using the Gaussian elimination method. The use of the band matrix speeds up calculations significantly. This fact might be computationally important when calculations involving large-scale endothermic reactors heated by the Joule heating or in fluidized beds heated by electrical discharge.

Since the electrical resistance of the steel spheres is temperature-dependent, the voltage distribution is coupled with temperature distribution and solved iteratively. A simple model for temperature is detailed in the following sections.

Finally, after the electric field potential is solved for each particle, the overall electric current is calculated at the cathode or the anode using the following formulas, respectively:

$$I_c = \pi \sum_{i=1}^{N_{pC}} r_{c,i}^2 \sigma_i \frac{\phi_i - 0}{\Delta z} \tag{5.6}$$

where $\Delta z = 0.5 d_p$, N_{pA} is the number of particles in contact with the cathode.

$$I_a = \pi \sum_{i=1}^{N_{pA}} r_{c,i}^2 \sigma_i \frac{\phi_c - \phi_i}{\Delta z} \tag{5.7}$$

where N_{pC} is the number of particles in contact with the anode. The values of I_c and I_a must be equal due to charge conservation, and they are used to check the numerical convergence of the system of linear equations.

5.3.2 Resistance

The heat transfer between a pair of particles that are in contact, is calculated as follows [7]:

$$Q_{cond} = \frac{T_i - T_j}{R_{th}} \tag{5.8}$$

where the thermal resistance due to the inter-particle conduction R_{th}, Q_{cond} is the conductive heat rate between two particles.

In analogy to heat transfer, the electrical current between the two particles i and j that are in contact, is calculated as follows:

$$I_{ij} = \frac{\phi_i - \phi_j}{R_{\sigma,ij}} \tag{5.9}$$

The Joule heating effect on particle i is described as the summation of Joule heating from all of its contact points.

$$Q_e = \frac{1}{2}\sum_{j=1}^{N_{nb}} \frac{(\phi_i - \phi_j)^2}{R_{\sigma,ij}} \tag{5.10}$$

The Joule heat at the contact point is split equally by the two particles, thus resulting in the coefficient $\frac{1}{2}$. Q_e is heat generation of each particle and the summation of all Q_e is equal to the total rate of Joule heating, $I \cdot U$.

In analogy to the thermal resistance between two contacting particles [7], the electrical resistance of the contact area takes the form:

$$\frac{1}{R_{th}} = \frac{4r_c}{\frac{1}{k_{p,i}} + \frac{1}{k_{p,j}}}; \implies \frac{1}{R_{\sigma,ij}} = \frac{4r_c}{\frac{1}{\sigma_{p,i}} + \frac{1}{\sigma_{p,j}}} \tag{5.11}$$

where r_c is the contact radius, and $\sigma_{p,j}$ and $\sigma_{p,i}$ are the electrical conductivity of particles j and i, respectively. If $\sigma_{p,j} = \sigma_{p,i}$, the electrical resistance $R_{\sigma,ij}$ takes the form:

$$R_{\sigma,ij} = \frac{1}{2\, r_c\, \sigma_p} \tag{5.12}$$

The contact radius r_c between two touching elastic particles i and j which are locally spherical with radii r_i and r_j can be calculated based on Hertzian theory[10, 19]. Since the fixed bed is modeled using DEM with a soft-sphere collision model (see Yade[18]), each particle reaches its state of the rest when the force balance for each particle is satisfied within a given numerical accuracy:

$$\Big|\sum_{i=1}^{N_p} \vec{F}_{pn,i} + \delta_w \vec{F}_w + \vec{F}_g\Big| \leq \delta_F \tag{5.13}$$

where $\vec{F}_{pn,i}$ and $\vec{F}_w$ are the compression forces acting on a particle normal to the common tangent plane at the point of contact with another particle or with the tube wall, respectively. $\vec{F}_g$ is the gravity force. In this work, we set $\delta_F = 10^{-2}$.

The force acting on a particle at position P_i from the particle at P_j is expressed as follows [19]:

$$\vec{F}_{pn} = \frac{4}{3} K R_m^{1/2} d^{3/2} \vec{n}; \text{ or } \vec{F}_{pn} = \frac{4}{3}\frac{K}{R_m} r_c^3 \vec{n} \tag{5.14}$$

where $\vec{n}$ is the unit vector indicating the direction of the force.

$$\vec{n} = \frac{\vec{P}_i - \vec{P}_j}{|\vec{P}_i - \vec{P}_j|} \tag{5.15}$$

The constant K is the effective stiffness and represents the elastic properties of the particle:

$$\frac{1}{K} = \frac{1-\nu_i^2}{E_i} + \frac{1-\nu_j^2}{E_j} \tag{5.16}$$

where E_i and E_j are the Young's moduli and ν_i, ν_j are the Poisson's ratios of particles i and j, respectively. The effective radius of curvature R_m of the particles i and j is given as follows:

$$\frac{1}{R_m} = \frac{1}{r_{p,i}} + \frac{1}{r_{p,j}} \tag{5.17}$$

Finally, the depth of indentation can be calculated using the following equation:

$$d = r_{p,i} + r_{p,j} - \left|\vec{P}_i - \vec{P}_j\right| \tag{5.18}$$

At the same time, d can be defined using the contact radius[19]:

$$d = \frac{r_c^2}{R_m}; \text{ or } r_c = \sqrt{R_m\, d} \tag{5.19}$$

To calculate $\vec{F}_w$, the same methodology can be used, albeit using a radius of curvature for the wall, i.e. $1/r_w = 0$, leading to $R_m = r_p$. Since the Young's modulus E of the wall is higher than that of the particle in contact with the wall, $\frac{1}{K} = \frac{1-\nu_i^2}{E_i}$. The same calculation is done for the electrodes. The solid particles have the mechanical properties of carbon steel, shown in Table 5.2. For a fixed bed with static particles, Eq. (5.13) has to be satisfied. Then Eq. (5.19) is used to calculated r_c.

The validation of our model for the contact area is shown in Fig. 5.4, which depicts the case used by Govender et al. [20] to investigate the effect of particle shape on the effective thermal conductivity of a packed bed. The conditions in the case were repeated using the model in this work. A bed of spherical particles ($N_p = 80323$) was generated in a 25 cm by 25 cm rectangular container with a height of 50 cm. After the bed is allowed to pack under gravity(g=9.81m/s^2), it is cut at 30cm, above which height any particles are removed. The particles have a density of 2700 kg/m^3 and a diameter of 0.6204cm. The friction coefficient of the particle surface is 0.4. The elastic coefficient used is 200kPa, converted from a linear stiffness of 1000 N/m. Poisson's ratio is 0.45. The restitution coefficient used is 0.45. Analysis of Fig.5.4a shows that the contact area is very close to the findings reported in the work [20] up to a contact area of 0.01 cm^2. There is some difference due to the models used in each case. In the validation case, a linear stiffness model is used based on intersection volume to accommodate different particle shapes. In this work, the simulation of the forces acting on the particles is based on the Hertz model. In reality, the contact area between spheres is not linearly proportional to the force applied, especially for the particles at the bottom of the bed where the applied load is large. The Hertz model is a more realistic representation of contact mechanics in the bed. We can conclude based on the agreement in low-stress conditions that the model is

validated.

In summary, a brief algorithm to calculate electric field and Joule heat distribution for a fixed bed is given below:

- After fixed bed composition is calculated using DEM, solving Eqs. (5.13) - (5.19) we define the contact radius r_c for each contact point between particles. One particle can have up to several neighbors resulting in several contact radii.
- Calculate electrical resistance for each contact point using Eq. 5.11.
- Establish a system of linear equations given by Eq. 5.4, setup boundary values for ϕ on electrodes, Eq. (5.5) and solve the final matrix equation using Gauss elimination method. Check the condition $I_a = I_c$ using Eqs. (5.6) - (5.7).
- Calculate the Joule heating term for each particle using Eq. 5.10.

5.3.3 Simple heat transfer model to define $\sigma = f(T_p)$

To account for the temperature dependency of the steel electrical conductivity with different values for the electrical power, we derive a simple steady-state heat transfer model using thermal resistance theory [14]. Fig. 5.5 contains a schematic representation of this resistance-based heat transfer model. Heat is generated in the particles and lost through the cylinder wall. The temperature difference between particle and air produces natural convection as temperature of particle rises. However, the heat transfer coefficient between cylinder wall and particle bed has not been reported in published studies. Since the cylinder in the experiment has a tube-to-particle ratio less than 4, we assume that all particles have the same temperature T_p,and neglect the thermal resistance between the particle and the internal surface of the glass cylinder, i.e. $T_p = T_{s,in}$. The glass wall is transparent, so the particles are assumed to have full radiative heat exchange with the surroundings. Thus, the heat balance is written in the form:

$$I \cdot U - A_{\sum}\sigma_{rad}\epsilon_s \left(T_p^4 - T_\infty^4\right) = \frac{T_p - T_\infty}{\frac{ln(r_{glass}/r)}{2\pi\, H\, k_{glass}} + \frac{1}{2\pi H r_{glass} h_\infty}} \tag{5.20}$$

where $A_{\sum} = N_p \cdot 4\pi r_p^2$, $r_{glass} = r + \delta_w$, where $r = D/2$ is the internal radius of the fixed bed, see Fig. 5.1, r_p is the radius of the steel particle, r_{glass} is the external radius of the glass tube, N_p is the number of particles in the fixed bed, ϵ_s is the emissivity of the steel particles, $T_\infty = 296$ K is the ambient air temperature, σ_{rad} is the Stefan-Boltzmann constant. It should be noted that in Eq. 5.20 it was assumed that the glass wall of the cylinder is transparent for the radiation.

The convective heat transfer coefficient between the volume-averaged gas phase and the particle

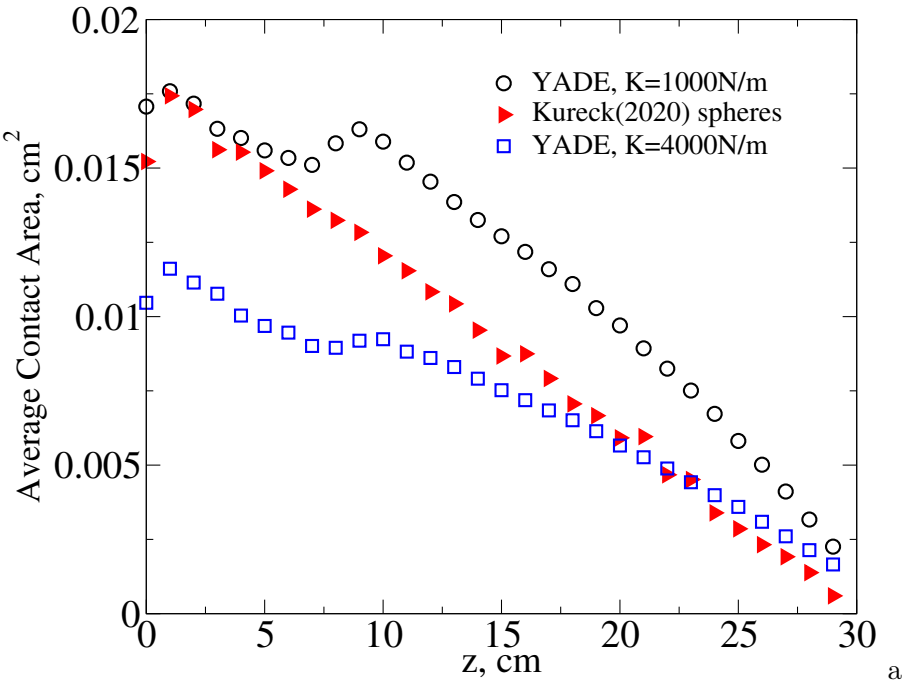

a

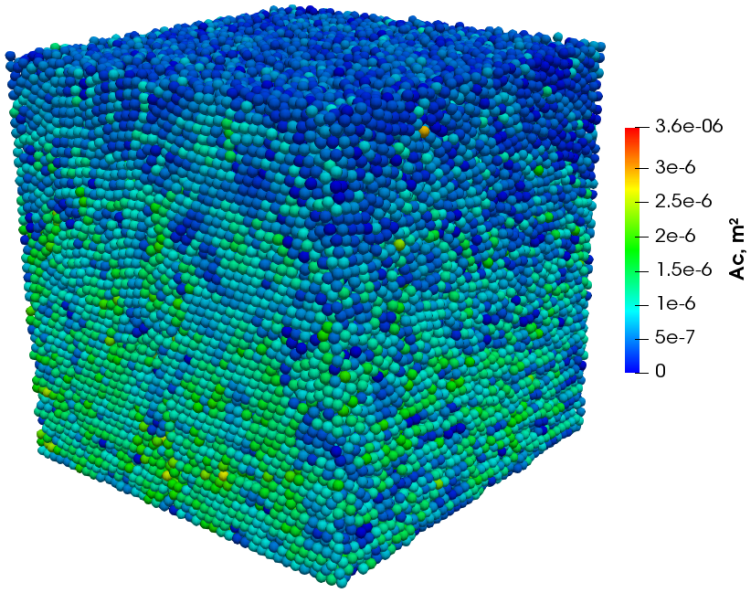

b

Figure 5.4: Code validation for the contact area calculation: a - axial profile of the averaged contact area calculated using our model and data taken from the literature; b - 3D plot of the contact area predicted numerically according to conditions from the work [20]. Here Kureck 2020 refers to the work [20].

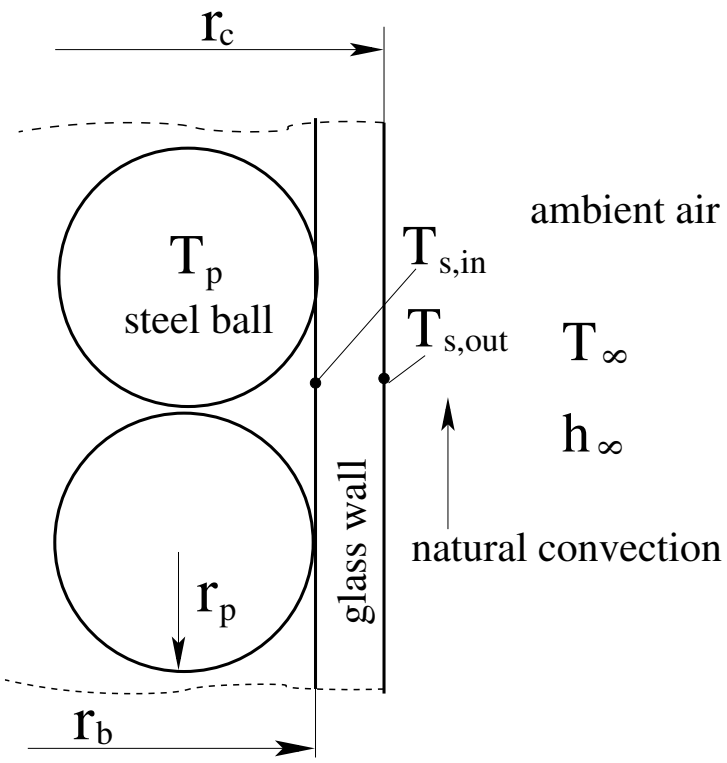

Figure 5.5: A schematic representation of the simple heat transfer model.

surface h_∞ is calculated as follows:

$$Nu_{nc} = \frac{h_\infty H}{k_\infty};\ \Longrightarrow h_\infty = \frac{Nu_{nc} k_\infty}{H} \tag{5.21}$$

The Nusselt number describing the heat transfer between the vertical wall and ambient air is taken from the work [21] with an additional correction term as in the work [22] due to the cylindrical shape of the vertical tube. The correction term is added to account for the closely packed particles, as the distance from interstitial gas to particle surface is much thinner than fully developed boundary.

$$Nu_{nc} = \left(0.825 + \frac{0.387 Ra^{1/6}}{[1 + 0.492/Pr)^{9/16}]^{8/27}}\right)^2 + \frac{0.97H}{r_{glass}} \tag{5.22}$$

where the Rayleigh number is calculated as follows:

$$Ra = \frac{g\beta(T_{s,out} - T_\infty)H^3}{\alpha\nu} \tag{5.23}$$

where $T_{s,out}$ is the temperature of the tube outer surface. Here, the thermal expansion coefficient is $\beta = \frac{1}{0.5(T_{s,out}+T_\infty)}$. The temperature of the outer surface of the glass cylinder can be defined using

the following equation:

$$2\pi H r_{glass} h_\infty \left(T_{s,out} - T_\infty\right) = \frac{2\pi\, H\, k_{glass}}{ln(r_{glass}/r)}(T_p - T_{s,out}) \tag{5.24}$$

The nonlinear Eq. (5.20) was solved numerically using Newton's method.

5.4 Validations

5.4.1 Comparison against particle resolved simulations

Before we contrast the measurements of volt-ampere characteristics of the bed and the results of calculations, we attempt to verify our particle-unresolved DEM-based model for the electrical field against particle-resolved simulations. The resistance equation is validated using the numerical solution of Eqs. 5.1 and 5.2 adopting a Finite Volume method.

Fig. 5.6a shows the principal scheme of the computational domain (cylindrical coordinates) consisting of two spherical particles with a radius $r_p = 0.5d_p$. The two particles share a contact radius of $r_c = 0.01r_p$. The particle surface is insulated except for the left and right areas with a radius r_c serving as the cathode and anode. Between the cathode and the anode, an electric field potential difference $\Delta\phi = 0.1$ V is applied leading to the Dirichlet boundary conditions on the left and right sides of the domain, see Fig. 5.6. On the particles surface we use the Neumann boundary condition, $\frac{\partial\phi}{\partial n} = 0$, where n is normal to the surface. The final equation solved takes the following form:

$$\nabla \cdot (\sigma \nabla \phi) = 0 \tag{5.25}$$

The axisymmetric computational domain was meshed using $0.25 \cdot 10^6$ control volumes (CVs). A mesh this fine is needed in order to resolve the contact area between two particles. Grid studies showed that this mesh resolution is sufficient to reproduce grid-independent results. Eq. 5.1 was solved numerically using the commercial software ANSYS-Fluent 19.2 [23]. The three-point central difference scheme (2nd order accuracy) was utilized to discretize Eq. 5.25. A system of discretized equations was solved using the Gauss-Seidel method. Numerical iterations were stopped when the residual reached the value 10^{-17}.

The results of the simulations are shown in Figs. 5.6b and 5.6c, depicting the contour plot of the magnitude of the electric current density and the contour plot of the Joule heating per volume, respectively. Both figures show that the magnitude of the electrical current density and the Joule heating reach a maximum at the contact point between two particles. Fig. 5.7 shows the comparison between the 2D particle-resolved simulations and the resistance model for different values of the contact radius from $0.001r_p$ to $0.1r_p$. To apply Eq. 5.9 and Eq. 5.10 using results of

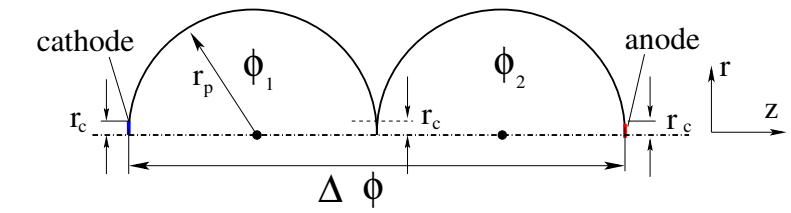

a

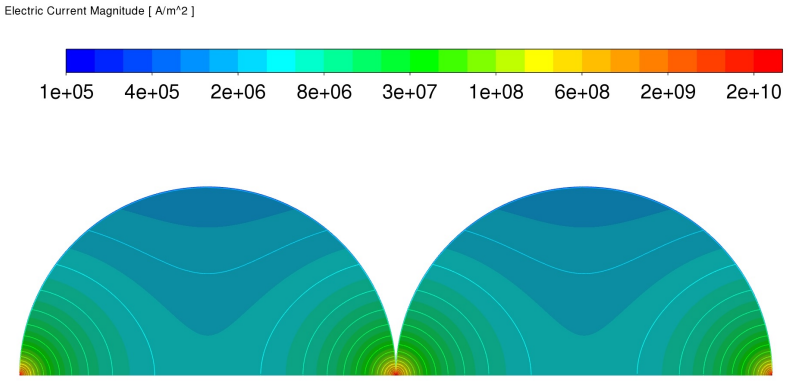

b

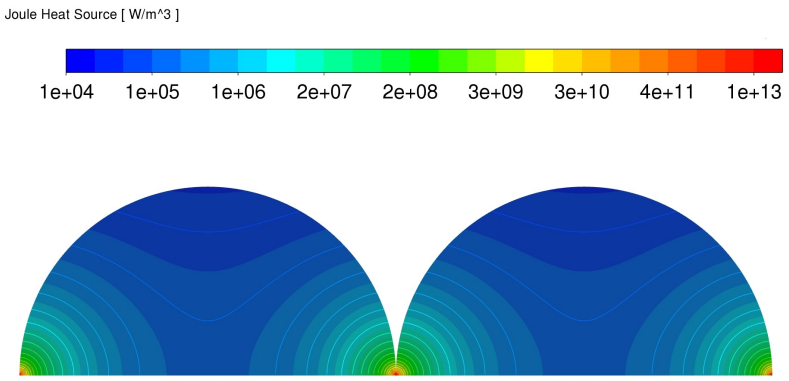

c

Figure 5.6: Results of particle resolved simulations for the verification of a new DEM-based resistance model: a - principal scheme, b - contour plot of the electric current density magnitude, c- contour plot of the Joule heat per volume, predicted for two steel balls for $\Delta\phi = 0.1$ V, $r_p = 0.00635$ m and $\frac{r_c}{r_p} = 0.01$. Mesh size is $0.25 \cdot 10^6$ CV.

the 2D axisymmetric simulations, we calculated the particle-averaged values of ϕ_1 and ϕ_2 as follows:

$$\phi_i = \int_V \phi(r,z) dV \tag{5.26}$$

where V is the volume of a single particle.

For example, for the contact radius $r_c = 0.001 r_p$ the 2D axisymmetric simulations revealed the following values of the particle-averaged ϕ: $\phi_1 = 0.02506$ V and $\phi_2 = 0.07502$ V. From Fig. 5.7 it can be seen that the electric current and the Joule heat predicted using Eq. 5.9 and Eq. 5.10, respectively, agree well with the results of particle-resolved simulations. Due to there being only one contact point between two particles, we used the following relation $Q_e = \frac{(\phi_2 - \phi_1)^2}{R_\sigma}$, which defines the Joule heat of one contact point.

5.4.2 Comparison against experimental data

The main validation result against experiments is plotted in Fig. 5.8a, which shows the so-called volt-ampere characteristics of the fixed bed with electrical current flowing through steel balls. To ensure repeatability of experimental results, the experiments have been repeated with the current stepping down to 0.4V after reaching maximum current at 3.3V. Slightly different packing of particles have also been used to check its influence. The effect of packing and persistent effect of heating on the overall volt-ampere characteristics are negligible and below the detection limit. The numerical simulations are shown to agree well with experiments. If the resistivity is constant, a directly proportional voltage-current response should be observed. A deviation between experiments and modeling ($\sigma = f(T_p)$) is observed for $I \cdot U > 30$ W. This input power corresponds to the case when T_p reaches 100 ^{o}C, as seen in Fig. 5.9, where the steady-state average temperature T_p predicted using simple heat transfer model are plotted against the input power. The experimental results for I increase slightly upwards in comparison to the predictions. We attribute this increase in the current detected in experiments to a probable increase in the contact area between the steel spheres. This increase in contact area could be caused by the thermal expansion of steel balls. The sintering effect of the contact area under high current density is also a contributing factor. Additionally, wire resistance causes a small difference between voltage measurements at the current source versus the voltage at the cathode and anode plates. These effects need to be studied separately in an temperature control environment. A detailed heat transfer model fully coupled with electrical current changes is needed to simulate the temperature changes. To quantify the influence of the thermal radiation on the particle temperature, we solved Eq.(5.20) without the thermal radiation term. The results are plotted in Fig. 5.9. It can be seen that the particle temperature predicted without thermal radiation increases significantly. In particular at $I \cdot U = 100$ W, the deviation in T_p reaches 60%. To show the effects of Joule heating with a different electrically conductive material,

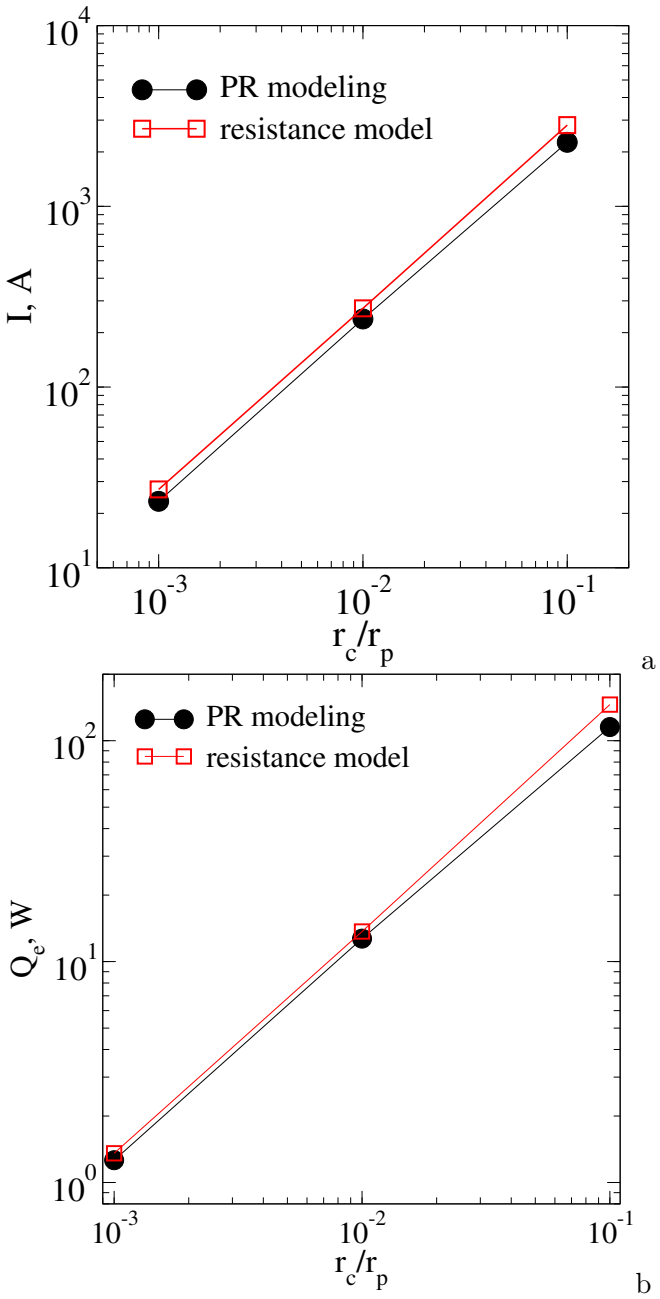

Figure 5.7: Results of the thermal resistance model verification against particle resolved simulations: a - electric current vs the dimensionless contact radius; b - the Joule heating rate vs the dimensionless contact radius

we present results of simulations performed under the same ambient conditions for the fixed bed consisting of the same size balls made of ZrB_2-B_4C. This material is the electrically conductive, wear- and corrosion-resistant ceramic composite described in the work [24]. The material properties used in the simulations are taken from the experimental data reported in the works [24] and [25]: $\sigma = 10^5$ 1/Ohm m, $\rho_p = 4370$ kg/m^3, $k = 60$ W/m K and $E = 498$ GPa. Fig. 5.8b shows the volt-ampere characteristics of the fixed bed calculated for up to $U = 22$ V and $I = 4.58$. Due to the higher electrical resistivity of ceramic balls and the smaller contact area, the electrical current is much smaller for the same voltage compared to the material used in the experiment, as results show in Fig. 5.8b.

Figs. 5.10a and 5.10b depict the 3D distribution of the contact area and electrical current pathways predicted numerically for $U = 3.3$ V and $I = 31.5$ A. Additionally, Fig. 5.10c shows steel particles after the experiment for the same I and U values. From Fig. 5.10a it can be seen that the contact radius changes in the range from $6 \cdot 10^{-5}$ to 10^{-3} in terms of the ratio r_c/r_p. There are two reasons for the current being constricted in the top part of the fixed bed. First, the contact area between the particles decreases with the height due to the impact of gravity. Secondly, the particles do not form a plane on the top of the fixed bed unlike the bottom, which aligns naturally due to gravity. To mitigate the problem, we recommend using flexible conductive wires at the top instead of plate electrodes. Fig. 5.10b shows that the electrical current is well distributed for the lower part of the fixed bed because of the good contact between particles due to gravity. At the same time, however, some particles do not conduct electrical current due to the absence of contact with neighbors. Although there are many points of contact as the bottom layer of particles is level on the plate, the current tends to be directed through one or two particles at the top. As a result, most of the Joule heat will be concentrated near the top end of the fixed bed leading to high temperatures of the particles on the top of the bed, see Fig. 5.10c. From the experiment shown in Fig. 5.10c it can be seen that the steel particles located on the top connecting anode plate changed color. This effect is attributed to the high temperature resulted from Joule heating. Based on the color of the steel, it was evident that the particles carrying the most current have reached temperatures near 570K to 600K, at which the steel turns violet and blue. For details about the change in the color of steel caused by the temperature increase, we refer to the work [26].

5.5 Conclusions

In this work, we presented a new particle-unresolved model based on Discrete Element method (DEM), enabling calculations of volt-ampere characteristics of a fixed bed heated by Joule heating. The results from the new model for the electrical field showed acceptable agreement with experimental data with some deviations when the bed temperature exceeds 500K. Experimental data revealed a non-linear correlation between electrical current and electric field potential difference between the

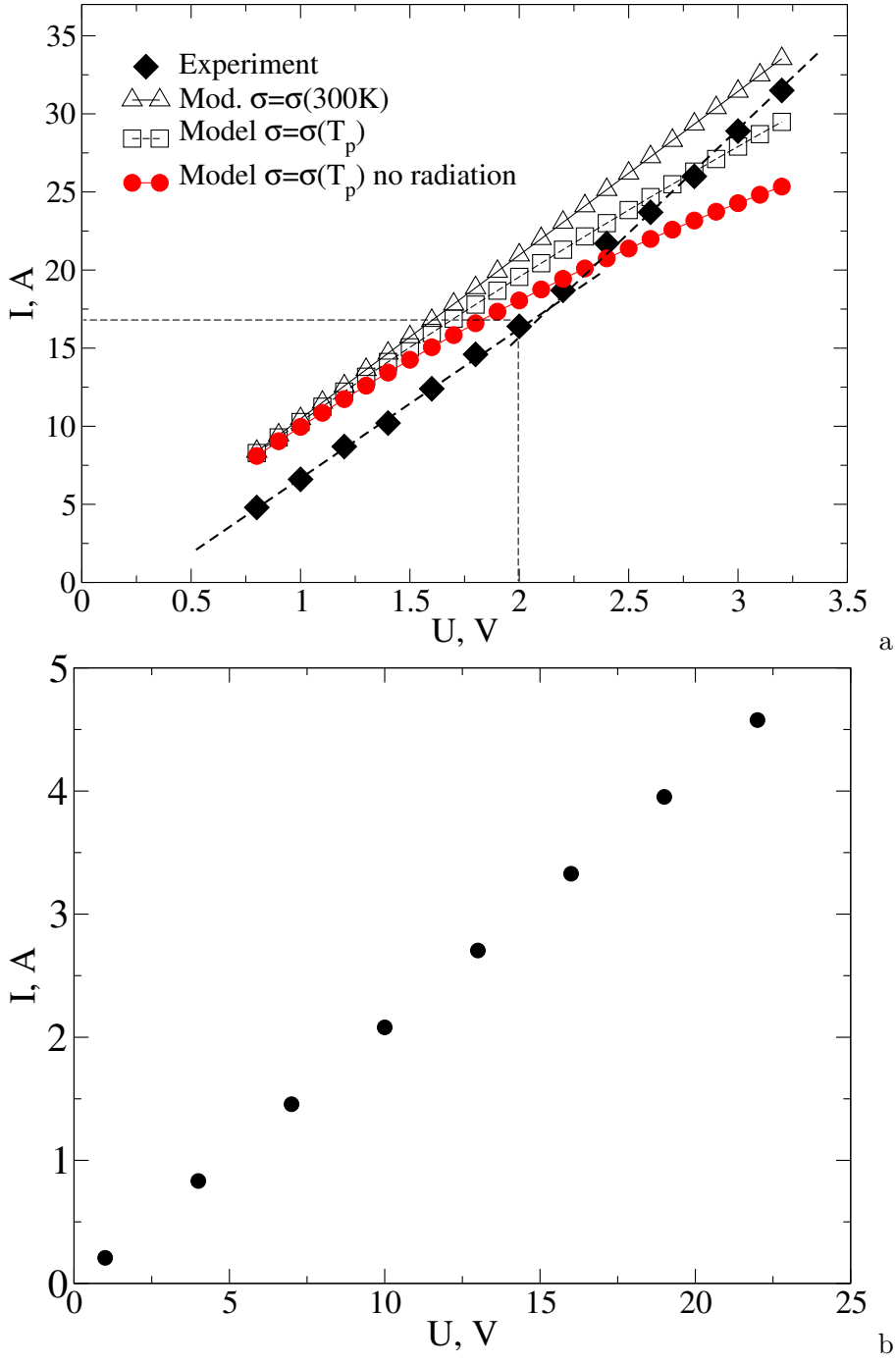

Figure 5.8: Volt-ampere characteristic of the fixed bed measured in the experiment and predicted numerically (a); volt-ampere characteristic of the fixed bed filled with electrically conducting ceramic particles (the same number of balls).

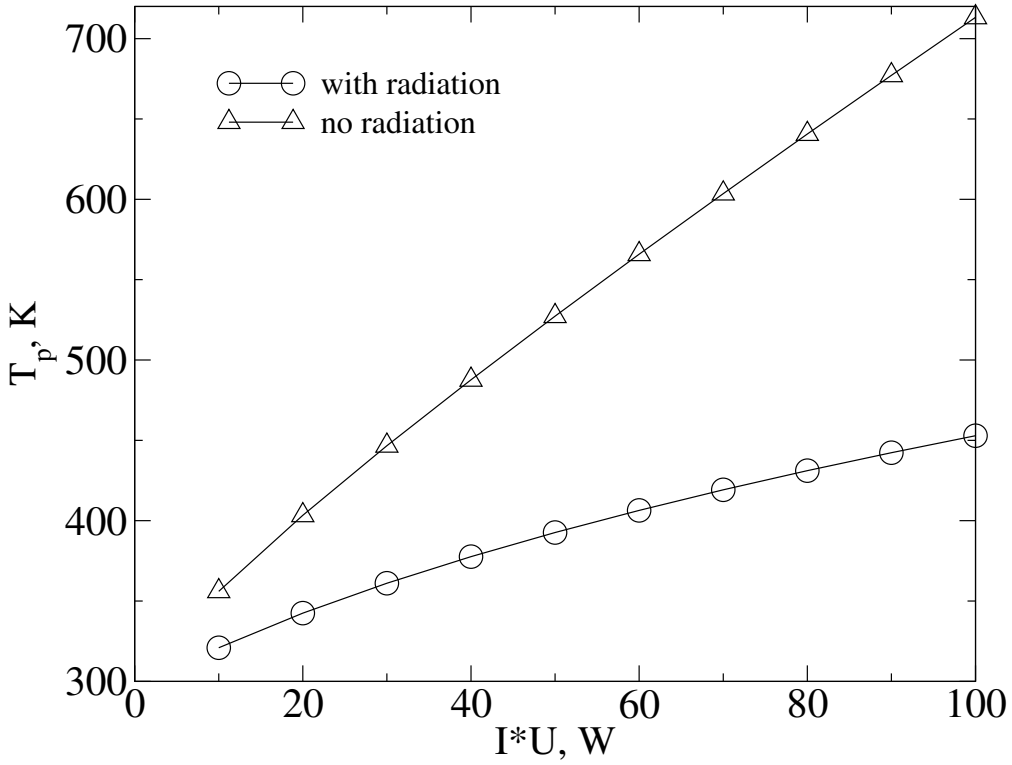

Figure 5.9: Steady state temperature of steal particles T_p in dependence on the input power predicted using simple heat transfer model (0D) (Sec. 5.3.3).

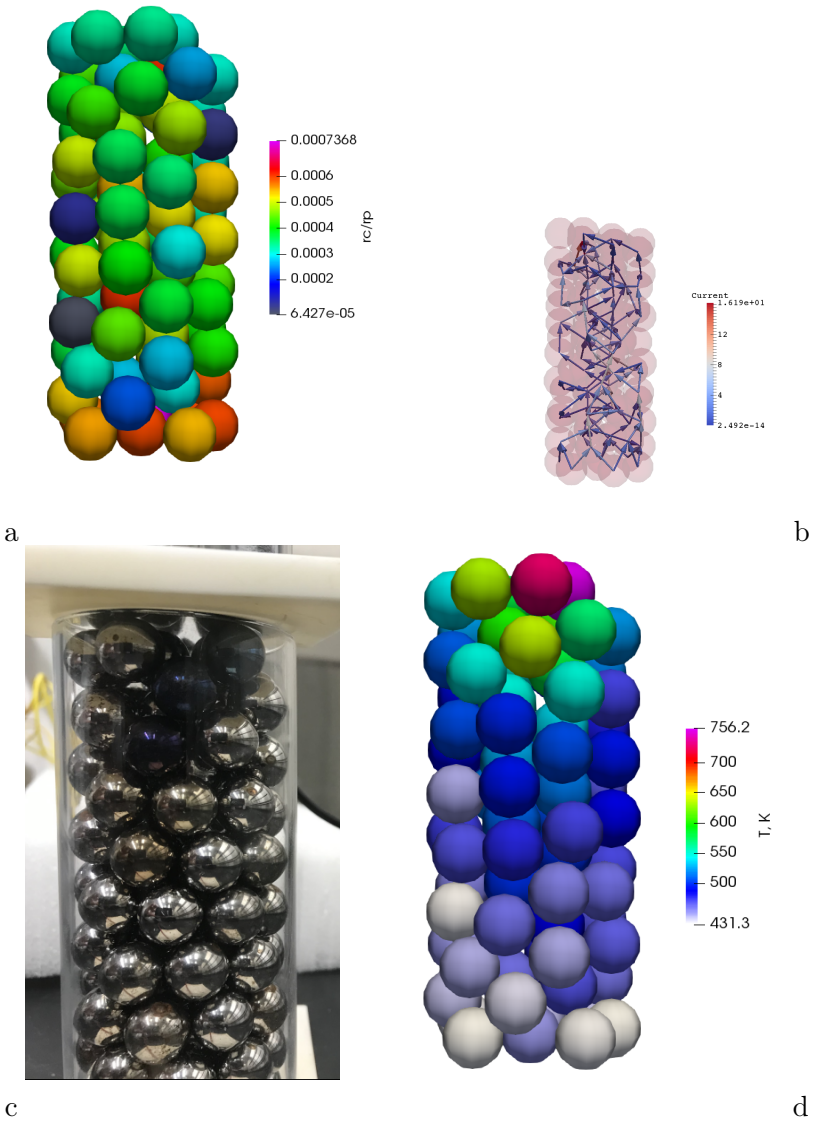

Figure 5.10: Results of simulations using DEM-based heat transfer model and electric field model: a - the contact area between particles under 2 kg external weight on the top; b - electrical current distribution in the bed for $U = 3.3$ V and $I = 31.5$ A; c - black/blue steel particles illustrating the area with high temperatures for the regime $U = 3.3$ V and $I = 31.5$ A; particles temperature T_p calculated using particle unresolved DEM-based heat transfer model for $U = 3.3$ V and $I = 31.5$ A

electrodes. The voltage-ampere curve is slight concave up despite an increase in temperature with higher current. This effect might be attributed to the thermal expansion of metal spheres and the corresponding increase in the contact area between particles. Additionally, the DEM-based resistance model was validated against particle resolved simulations in terms of the Joule heating and electrical current. Excellent agreement was demonstrated. The distinguishing feature of this model lies in the use of the volume-averaged electric field potential for each particle. This new DEM-based model can be used for predictions when employing Joule heating in endothermic chemical reactors, for converting electrical energy into chemicals.

Acknowledgment

The financial support by the Natural Sciences and Engineering Research Council (NSERC) Canada under Discovery Grants is appreciated.

Bibliography

[1] Raynald Labrecque and Jean Michel Lavoie. Dry reforming of methane with CO2 on an electron-activated iron catalytic bed. *Bioresource Technology*, 102:11244–11248, 2011.

[2] J.D. Holladay, J. Hu, D.L. King, and Y. Wang. An overview of hydrogen production technologies. *Catalysis Today*, 139:244–260, 2009.

[3] Yi Ran Lu and Petr A. Nikrityuk. A fixed-bed reactor for energy storage in chemicals (E2C): Proof of concept. *Applied Energy*, 228:593–607, 2018.

[4] M. Rieks, R. Bellinghausen, N. Kockmann, and L. Mleczko. Experimental study of methane dry reforming in an electrically heated reactor. *Int. J. Hydrogen Energy*, 40:15940–15951, 2015.

[5] Qi Zhang, Makoto Nakaya, Tetsuya Ootani, Hiroshi Takahashi, Makoto Sakurai, and Hideo Kameyama. Simulation and experimental analysis on the development of a co-axial cylindrical methane steam reformer using an electrically heated alumite catalyst. *International Journal of Hydrogen Energy*, 32:3870 – 3879, 2007.

[6] Marvin B Glaser and George Thodos. Heat and momentum transfer in the flow of gases through packed beds. *AIChE Journal*, 4(1):63–68, 1958.

[7] Zhengbiao Peng, Elham Doroodchi, and Behdad Moghtaderi. Heat transfer modelling in Discrete Element Method (DEM)-based simulations of thermal processes: Theory and model development. *Progress in Energy and Combustion Science*, 79:100847, 2020.

[8] Z.Y. Zhou, A.B. Yu, and P. Zulli. Particle scale study of heat transfer in packed and bubbling fluidized beds. *AIChE Journal*, 55:868–884, 2009.

[9] Cheng. G.J., Yu A.B., and P. Zulli. Evaluation of effective thermal conductivity from the structure of packed bed. *Chem Eng Sci*, 54:4199–4209, 1999.

[10] G.K. Batchelor and R.W. O'Brien. Thermal or electrical conduction through a granular material. *Proc. R. Soc. Lond. A*, 355:313–333, 1977.

[11] A. B. Morris, S. Pannala, Z. Ma, and C. M. Hrenya. Development of soft-sphere contact models for thermal heat conduction in granular flows. *AIChE Journal*, 62:4526–4535, 2016.

[12] Tobias Oschmann and Harald Kruggel-Emden. A novel method for the calculation of particle heat conduction and resolved 3d wall heat transfer for the CFD/DEM approach. *Powder Technology*, 338:289-303, 2018.

[13] Y. Tsuji, T. Tanaka, and T. Ishida. Lagrangian numerical simulation of plug flow of cohesionless particles in a horizontal pipe. *Powder Technol*, 71:239–250, 1992.

[14] T.L. Bergman, A.S. Lavine, F.P. Incropera, and D.P. Dewitt. *Fundamentals of Heat and Mass Transfer*. John Wiley & Sons, 7 edition, 2011.

[15] Jacek Senkara and Hongyan Zhang. *Resistance welding: fundamentals and applications*. CRC Press, 2011.

[16] K.A. Kobe and R. Emerson Lynn. The critcal properties of elements and compounds. *Chem. Rev.*, 52:117–236, 1953.

[17] J. Kozicki and F. Donzé. Yade-open DEM: an open-source software using a discrete element method to simulate granular material. *Engineering Computations*, 26(7):786–805, 2009.

[18] Yade - Open source software for DEM. https://yade-dem.org/doc/, 2009.

[19] E. Dintwa, E. Tijskens, and H. Ramon. On the accuracy of the hertz model to describe the normal contact of soft elastic spheres. *Granular Matter*, 10:209–221, 2008.

[20] N. Govender, P.W. Cleary, M. Kiani-Oshtorjani, D.N. Wilke, C.Y. Wu, and H. Kureck. The effect of particle shape on the packed bed effective thermal conductivity based on DEM with polyhedral particles on the GPU. *Chemical Engineering Science*, 219:115584, 2020.

[21] S.W. Churchill and Chu H.H.S. Correlating equations for laminar and turbulent free convection from a vertical plate. *Int. J. Heat Mass Transfer*, 18:1323–1329, 1975.

[22] Fujii Tetsu and Uehara Haruo. Laminar natural-convective heat transfer from the outer surface of a vertical cylinder. *International Journal of Heat and Mass Transfer*, 13(3):607 – 615, 1970.

[23] Inc. ANSYS. ANSYS-FLUENT™ V 19.2 – Commercially available CFD software package based on the Finite Volume method. Southpointe, 275 Technology Drive, Canonsburg, PA 15317, U.S.A., www.ansys.com, 2020.

[24] Gianpietro van de Goor, Peter Saegesser, and Karl Berroth. Electrically conductive ceramic composites. *Solid State Ionics*, 101-103:1163–1170, 1997.

[25] J.F. Guria, A. Bansal, and V. Kumar. Effect of additives on the thermal conductivity of zirconium diboride based composites - A review. *Journal of the European Ceramic Society*, 41: 1–23, 2021.

[26] Hubertus Colpaert. *Metallography of Steels - Interpretation of Structure and the Effects of Processing*. ASM International, 2018.

Chapter 6

Steam Methane Reforming driven by the Joule Heating[1]

Abstract

The main objective of this work is to present a new particle unresolved 3D-1D DEM-CFD-based model enabling predictions of a new steam methane reforming (SMR) driven by the direct electrical current. The main feature of this technology is the use of metal particles heated by the Joule heat resulting from direct electrical current flowing through metal particles in order to heat the gas phase and catalyst particles (Ni/α-Al_2O) to sustain endothermic chemical reactions. The model uses six gaseous chemical species (CH_4, CO_2, CO, H_2O, H_2, N_2) in the gas phase inside the catalyst. The Langmuir-Hinshelwood-Hougen-Watson (LHHW) kinetics is used. The distinguishing feature and the novelty of the model presented in this work consist in the calculation of the 3D distribution of the electric field inside non mono-disperse fixed beds. The electric field distribution is used to calculate the Joule heating term for each electrically conducting particle participating in the electrical current flow. Additionally, the new model predictions are compared with alternative models based on the chemical equilibrium principles. The models have been numerically solved using MATLAB. To illustrate the performance of the models and to check the feasibility of a new electrical steam methane reforming concept, we consider a cylindrical electrically insulated tube with a diameter of 0.1 m and a height of 0.5 m, which is filled with metal particles and catalyst particles with diameters of 5 mm and 2 mm, respectively. Parametric runs for different flow rates from 0.0025 kg/s to 0.01 kg/s and electrical power from 6.9 kW to 39 kW have been carried out. Results of simulations showed that an increase in the flow rate value ($\dot{m}$) by keeping constant input electrical power leads to a decrease in the conversion of CH_4 proportionally to $\dot{m}^{-1/2}$. A linear increase in the flow rate

[1]This chapter is based on the work: Y. R. Lu, P.A. Nikrityuk. *Steam methane reforming driven by Joule heating.* Chemical Engineering Science, Vol. 251, pp. 117446, 2022. DOI: 10.1016/j.ces.2022.117446

and input power leads to a decrease in methane conversion. When the input electrical power is increased, the difference between catalyst particle temperature and gas temperature decreases.

Nomenclature

A_p	surface area of the catalyst particle
A_{pm}	surface area of the metal particle
A_c	cross section area of the tube
c_p	constant-pressure heat capacity
D	internal diameter of the reactor
D_{eff}	effective diffusivity
d_{mean}	mean particle diameter
d_p	diameter of the catalyst particle
d_{pm}	diameter of the metal particle
k	thermal conductivity
h	thermal convection coefficient
ΔH_r	the enthalpy of r reaction
h_{pg}	thermal convection coefficient between the catalyst-particle and gas phase
h_{pmg}	thermal convection coefficient between the metal particle and gas phase
$(hA)_{in}$	heat transfer coefficient inside the catalyst particle
$(hA)_{inm}$	heat transfer coefficient inside the metal particle
$(\beta A)_{in}$	mass transfer coefficient inside the catalyst particle
I	electrical current
U	electrical field potential difference between anode and cathode
M	molar mass
m	mass
$\dot{m}$	mass flow rate
N	number of reactions
N_p	number of catalyst particles in a control volume
N_{pm}	number of metal particles in a control volume
r_c	contact area between particles
Q_e	Joule heating source term inside each metal particle
Q_{IU}	input electrical power for the reactor
$R_{r,s}$	reaction rate on particles surface
$R_{r,V}$	intrinsic reaction rate for the catalyst-particle
R_g	the universal gas constant
R_{th}	thermal resistance between particles

R_σ	electrical resistance between particles
T_g	temperature of the gas phase
T_{sm}	surface-averaged temperature of the metal particle
T_{pm}	volume-averaged temperature of the metal particle
T_s	surface-averaged temperature of the catalyst particle
T_p	volume-averaged temperature of the catalyst particle
V	volume
Y_i	mass fraction of species i
$Y_{i,g}$	mass fraction of i species in the gas phase
$Y_{i,s}$	surface-averaged mass fraction of i species on the catalyst-particle surface
$Y_{i,p}$	particle-averaged mass fraction of i species in the catalyst particle
$Y_{i,sm}$	surface-averaged mass fraction of i species on the metal particle surface
z	axial coordinate
Δz or dz	size of a control volume

Greek letters

α	stoichiometric coefficient
β	mass transfer coefficient
ϵ_p	catalyst particle emissivity
ϵ_{pm}	metal particle emissivity
ε	void fraction
ρ	density
σ	Stefan-Boltzmann constant
σ_{pm}	electrical conductivity of metal particles
τ	catalyst particle tortuosity
ξ	non-dimensional variable

Subscripts

$aver$	averaged
s	catalyst particle surface
p	catalyst particle
pm	metal particle
sm	metal particle surface
g	gas
w	wall
nb	adjacent particle
i	species i
V	volumetric

pg	particle-gas
inl	inlet
out	outlet
in	catalyst particle internal
inm	inside metal particle internal

6.1 Introduction

The demand on the use of renewable sources in energy production requires novel and cost-effective energy storage/conversion technologies. For example, to compensate for the disparity between the energy needs and the supply of renewable sources (such as wind and sun), it is necessary to store the energy during times when electricity is overproduced. One of the promising energy storage technology is the conversion of electrical current into chemical energy [1] in the form of chemicals obtained using endothermic reactions. One of the ways to store electrical energy in chemicals (E2C) is to use so-called electrically driven steam methane reforming (SMR) and/or the dry reforming of methane (DRM) [2, 3, 4]. Another well-known example of E2C is plasma-driven SMR and DRM [5, 6]. Alternatively to plasma-driven SMR/DRM, solar-driven SMR is being considered [7] as a means of directly converting renewable energy into chemical energy. A detailed review of different SMR/DRM reactor concepts can be found in the work [8].

An analysis of works devoted to electrically driven SMR and DRM shows that most of works use experimental studies to investigate the characteristics of endothermic lab-scale reactors heated by direct electrical current (DC). For example, Lavoie and co-workers developed a new iron bed consisting of steel wool (playing the roles of the heater and catalyst) heated by electrical current going through the bed. This was used for the dry reforming of methane with CO_2 [3]. Recently, the second generation of the electricity-activated DRM reactor was presented in the works [5, 9].

Oshima et al. [10] published experimental data on catalytic steam reforming of methane in an electric field applied through a catalyst. The electric field was generated by a DC high-voltage power supply. The authors demonstrated 40.6% conversion of CH_4 at 535.1 K. When the DC supply was interrupted, the reforming was stopped immediately, showing that the electrical current is the driving force behind the catalytic reforming and not Joule heat.

Che and co-workers [11] reported on theoretical and experimental studies on the use of Ni foam as a heater (through electrical current) and catalyst for SMR. The authors showed that a positive electric field enhances the methane conversion in comparison to the case with no electric field. Additionally, it was demonstrated experimentally that a positive electric field reduces the formation of coke.

In the works analyzed above, the distinguishing feature of electrically driven DRM and SMR is the use of electro-catalysts, where a catalyst plays the role of the heater and catalyst simultaneously.

One of the problems in modeling of electrically driven reforming is that the kinetics of endothermic reactions are virtually unknown. An alternative to electro-catalysts is the use of electrically heated surfaces covered with a catalyst which does not conduct electrical current itself. For example, Zhang et al. [2] reported on experimental and numerical studies on a co-axial cylindrical four-layer catalyst bed methane steam reformer where the catalyst layers were heated electrically from electrically conducting plates. Another example of an electrically heated catalyst being used for SMR is the work by Wismann and co-workers [4]. The authors used an electrically heated tube coated by a catalyst to drive SMR. It was shown that utilizing a close contact between the Joule heat source and the reaction site drives the reaction close to thermal equilibrium and makes the reactor smaller in comparison to a standard approach. Recently, Lu and Nikrityuk [12] presented a hybrid electro-reforming scheme using standard catalyst particles (Ni/α-Al_2O) packed randomly with nickel balls in a cylindrical tube made of an electrically non-conducting material. When a DC current is supplied through Ni particles, they serve as local heaters and at the same time as a non-porous catalyst in addition to the porous catalyst Ni/α-Al_2O packed randomly between the Ni particles. Such arrangements of electrically conducting particles and catalyst particles makes the reformer compact and prevents temperature drops in the center of the tube in comparison to standard reformers.

While numerous experimental works are available on electrically driven SMR, relatively few works have been published on multi-scale numerical and scale-bridging models describing heat and mass transfer in electrically driven reformers of methane. Existing simulations of classical reformers use permeability-based CFD models, for example see the work [13], where a fixed bed is treated as a permeable porous media, adding the Darcy-Forchheimer term to momentum conservation equations. It should be noted that this approach is not straightforward to use in an adaptation for electrically heated fixed beds consisting of poly-disperse particles. The second approach is Euler-Lagrange CFD-based models using particle-resolved (PR) or particle-unresolved (PUR) formulations. In the case of SMR, the particle-resolved CFD-based simulations, known as PR-DEM-CFD [14, 15], are used only to gain a fundamental understanding of transport processes inside the bed, similarly to experiments. Such simulations are computationally expensive [16]. The computational cost limits the use of PR for large-scale reactors or packed tubes. As significant progress is being made in multi-scale numerical simulations of packed beds using DEM-CFD-based model, e.g. see the review [17, 18], particle-unresolved DEM-CFD-based models are becoming increasingly adopted tools for simulations of chemically reacting large-scale particulate systems, see the work [19] for example of DEM-based simulations of SMR for a 10-m-long packed tube. For a more detailed analysis of existing CFD-based models for SMR, see the works [20, 19].

Finally, although there are numerous successful studies on classical SMR in different packed beds, there are few numerical studies on bi-dispersed or poly-dispersed fixed beds heated by DC going through particles. In particular, when applied to DC heated beds, the fine mesh generation that is required to properly resolve the contact area between electrically conductive particles comes

at high computational costs. Such fine meshes are needed to adequately model the flow of electrical current through conductive particles. The so-called caps and bridges are two ways to work around the problem[21]. However, both methods would lose accuracy, which can be significant when the particle-particle contact matters. To overcome this problem and reduce the computational costs, this work presents a new methodology for accurate predictions of the heat transfer and mass transfer (methane conversion rate) inside a new reactor, presented in Fig. 6.1. This reactor consists of two sorts of spherical particles: electrically conductive metal particles and electrically non-conductive catalyst particles. The use of catalysts enables enhancing the conversion rate of methane. The main feature of this reactor is the application of the Joule heating inside the electrically conductive particles. At the same time such particles heat the catalysts and gas phase inside the fixed bed. The main purpose of this reactor is to store electricity produced from renewable sources in chemicals such as syngas (CO and H_2).

The novelty of this work consists in the development of a new multi-scale DEM-based particle-unresolved 1D-Euler-3D-Lagrange model describing transport processes (heat and mass transfer) during SMR occurring in poly-disperse fixed beds heated by a direct current flowing through electrically conductive particles. The basic challenge in developing a new methodology for the calculation of a new reactor, shown in Fig. 6.1, lies in coupling electric field (EF) equations formulated for discrete media with energy conservation equations for solid particles. The methodology presented in [12] entails significant simplifications which reduce the overall accuracy of the model. A new EF model presented in this work makes it possible to calculate the 3D distribution of the electrical field inside the fixed bed, consisting in two kinds of particles: electrically conductive particles, e.g. Ni, and electrically non-conductive catalyst particles. Additionally, this work reports the influence of the gas flow rate and input electrical power on the heat and mass transfer processes inside the new SMR fixed bed reactor heated volumetrically by Joule heating.

6.2 Problem formulation

A new reactor consists of two different kinds of spherical particles: electrically conductive particles made of a metal and electrically non-conductive catalyst particles (any standard catalyst can be used). Between the top and bottom of the reactor, a DC is applied. The metal particles are heated by Joule heating due to the electrical current passing through metal particles. Fig. 6.1a shows a schematic of the proposed reactor. To simplify the calculations, we consider the geometry depicted in Fig. 6.1b. A random packed bed consists of $N_p = 2.3 \cdot 10^4$ spherical metal and catalyst particles packed randomly in a thermally and electrically insulated tube with a height of $H = 0.5$ m and diameter of $D = 0.1$ m. The diameters of metal particles and catalyst particles are $d_{pm} = 5$ mm and $d_p = 2$ mm, respectively. The volume fraction of the catalyst particle is $\varepsilon_{cat} = 25\%$. This optimal value is determined by finding the maximum possible number of electrically non-conducting

P, Pa	T, K	Y_{g,CH_4}	Y_{g,H_2O}	$Y_{g,CO}$	Y_{g,CO_2}	Y_{g,H_2}	$Y_{g,N}$	$\dot{m}$, kg/s	Q_{IU}, kW
10^5	1000	0.3	0.6	0	0	0	0.1	$5 \cdot 10^{-3}$	19.3
10^5	1000	0.3	0.6	0	0	0	0.1	$5 \cdot 10^{-3}$	13.9

Table 6.1: Inflow conditions

	Metal particles	catalyst particles
density, kg/m^3	ρ_p =8900	ρ_{pm} =3900
thermal conductivity, W/m K	k_{pm} = 76.1	k_p = 6.0
heat capacity, J/kg K	c_{pm}=440	c_{pp}=600
particle porosity	N/A	ε_V=0.5
catalyst tortuosity	N/A	τ =4
σ_{pm}, 1/Ohm m	$2.61 \cdot 10^5$	N/A
particle emissivity	ϵ_{pm}=0.8	ϵ_p=0.8
particle diameter, m	$d_{pm} = 5 \cdot 10^{-3}$	$d_p = 2 \cdot 10^{-3}$

Table 6.2: Properties of solid particles

particles mixed randomly among metal particles that allow electrical current to flow through the bed without hot spots; for the detailed methodology see the work [12]. In particular, it should be noted that increase in ε_{cat} value may lead to significant non-uniform distributions of electrically conductive (metal) and electrically non-conductive (catalyst) particles in the entire zone of the reactor. Thus, the arrangement of catalyst and metal particles is a critical issue in that type of reactor. The scheme of the reactor is shown in Fig. 6.2.

The gas flow rate is $\dot{m} = 5 \cdot 10^{-3}$ kg/s. The inflow gas conditions are shown in Table 6.1. Due to the thermally insulated side wall of the tube the total electrical power, Q_{IU}, needed to heat the bed can be estimated using the following balance equation:

$$\underbrace{I \cdot U}_{Q_{IU}} = \dot{m} c_p (T_{g,out} - T_{g,inl}) + \dot{m} \Delta H_{aver} \tag{6.1}$$

where I is the electrical current and U is the electrical field potential difference between the anode and cathode. ΔH_{aver} is the averaged enthalpy of chemical reactions. If $T_{g,out} = T_{g,inl}$, Eq. (6.1) can be simplified as follows: $Q_{IU} = \dot{m} \Delta H_{aver}$. To estimate Q_{IU} for a given $\dot{m}$ we assume that $\Delta H_{aver} = |\Delta H_1|$. The chemical reactions between methane and steam are described by the following semi-global reactions [20]:

$$CH_4 + H_2O \Leftrightarrow CO + 3H_2 \tag{6.2}$$

$$CO + H_2O \Leftrightarrow CO_2 + H_2 \tag{6.3}$$

$$CH_4 + 2H_2O \Leftrightarrow CO_2 + 4H_2 \tag{6.4}$$

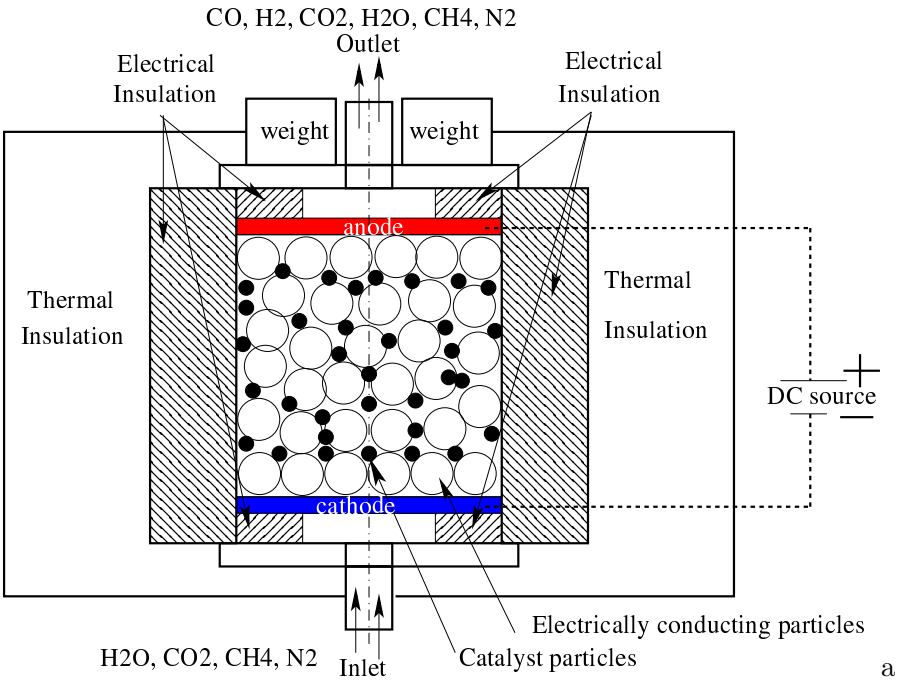

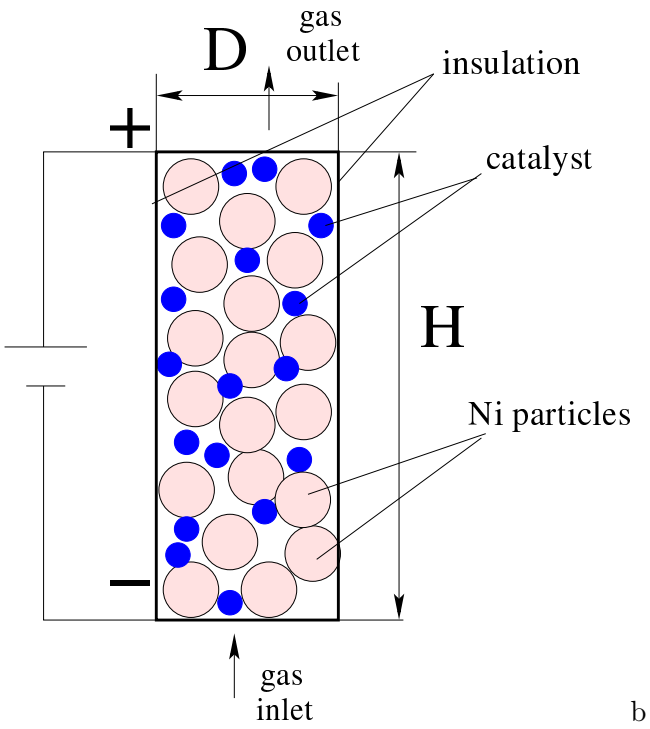

Figure 6.1: Principal schemes: a) - of a possible reactor for SMR and DRM for experimental studies. The 'weight' is used to control the contact area between particles. Cathode and anode are porous electrically conducting materials with melting temperature above 1500 K; b - reactor under investigation.

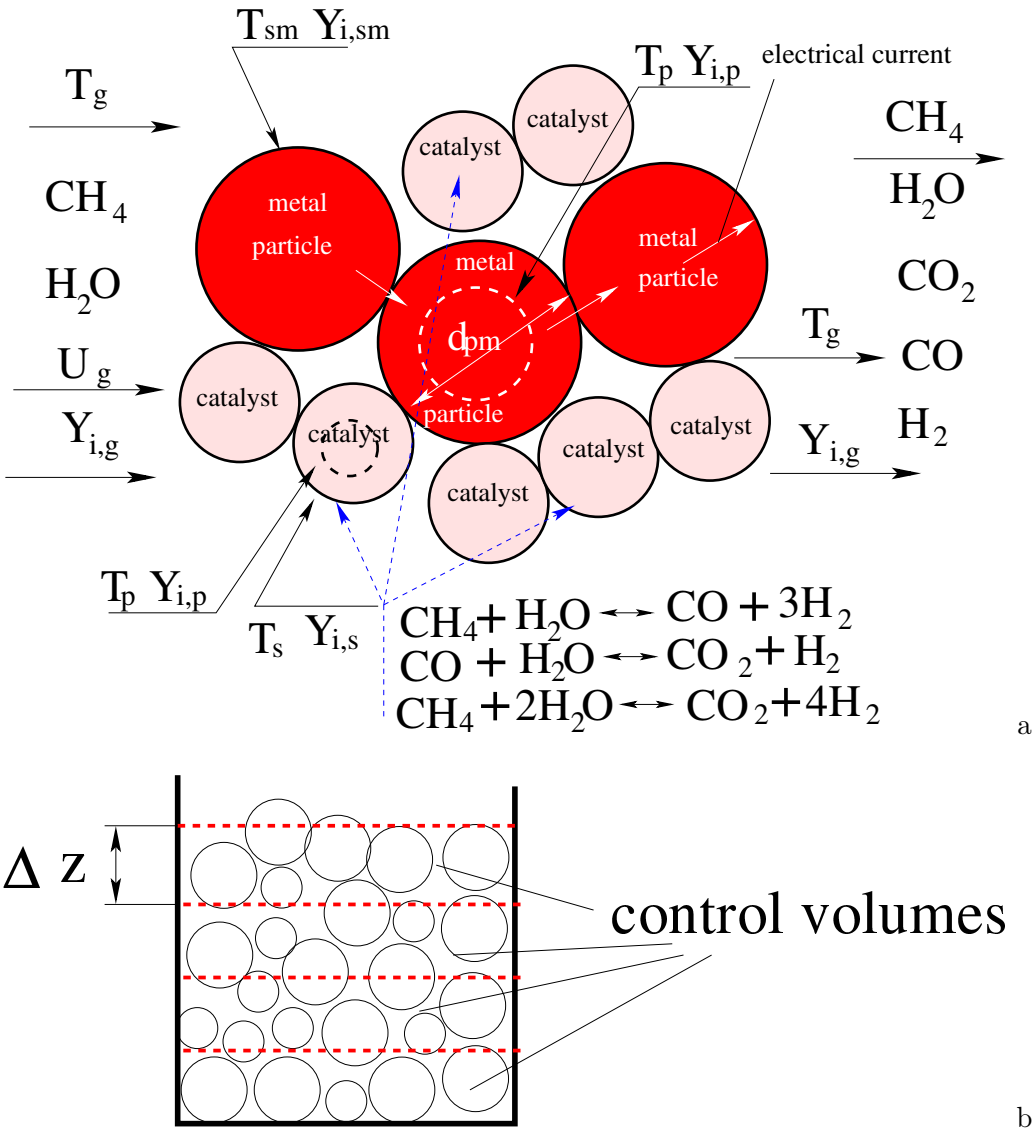

Figure 6.2: Diagram of catalyst and metal particles with its neighbors in a fixed bed to illustrate arrangement in the system of equations (a) and principal scheme of the domain discretization using control volumes (b).

The enthalpy for reactions in Eq. (6.2), Eq. (6.3) and Eq. (6.4) are $-\Delta H_1 = -206.1$ kJ/mol, $-\Delta H_2 = 41.2$ kJ/mol and $-\Delta H_3 = -165.0$ kJ/mol, respectively according to the work [16].

Finally, the composition of the fixed bed is simulated utilizing the gravity-driven settling of $2.3 \cdot 10^4$ spherical particles in a tube. The transport properties of the particles are given in Table 6.2. Catalyst particles comprise 25vol.% of all particles. To guarantee that there was sufficient contact between electrically conducting particles, an additional mass of 10 kg on the top was used, for details see[22]. The coordinates of the particles are calculated using the open-source DEM software YADE [23, 24], which uses the soft-sphere collision model.

6.3 Momentum, heat and mass transfer models

6.3.1 Full kinetic model (KM)

Before we formulate the heat and mass transfer model, we introduce the basic phenomena occurring inside the tube after the electrical current flows through the metal particles. Due to Joule heating, metal particles conducting electrical current are heated up. Consequently, heat transfer is initiated between the metal particles and the gas flow inside the tube and catalyst particles. The side walls of the tube are thermally and electrically insulated.

Due to the very small contact area between metal particles, it is not feasible to use a particle-contact-resolved numerical simulation of the packed tube. In this work, we adopt a particle-unresolved DEM-based heat transfer model from the work [19], with the temperature of the gas phase and chemical species in the gas phase being calculated using 1D heat transfer and species balance equations written for the gas phase in Eulerian space, and the temperature of each particle and species inside each catalyst being calculated utilizing 0D balance equations in 3D Lagrangian space. The following assumptions are made in the 1D-3D model:

- the fixed bed is one-dimensional and there are no radial gradients for the gas phase species mass fractions or gas temperature,
- the gas flow is one-dimensional,
- the solid particles temperature and species mass fractions inside the catalyst particles are calculated using 0D model [20, 19],
- the system is in a steady state with unsteady forms of the original balance equations shown to illustrate the derivation of the final equations,
- the catalyst particle porosity does not influence the overall pressure drop in the tube,
- the gas flow is treated as an ideal gas,

- buoyancy effects are neglected,
- the tube side walls are thermally insulated
- transport properties of catalyst and metal particles are constant, including the electrical conductivity of metal particles,
- transport properties of the gas phase are temperature dependent

Using these assumptions, the final governing equations take the following form:

- Mass conservation equation:

$$\frac{d}{dz}\left(\rho_g\, u_z\right) = 0; \qquad \rho_g = \frac{P}{R_g\, T_g} \tag{6.5}$$

The Ergun equation [25] is used to calculate P:

$$\frac{\Delta P}{H} = \frac{150\mu_g}{d_{mean}^2}\frac{(1-\varepsilon)^2}{\varepsilon^3}v + \frac{1.75\rho_g}{d_{mean}}\frac{(1-\varepsilon)}{\varepsilon^3}v^2 \tag{6.6}$$

where v is the superficial gas velocity. The mean particle diameter, d_{mean}, is calculated as follows [26]:

$$d_{mean} = \sqrt{\frac{1}{N_{pp}}\sum_{i=1}^{N_{pp}} d_{pi}^2} \tag{6.7}$$

where d_{pi} is the diameter of particle i inside a control volume and N_{pp} is the number of all sorts of particles inside a control volume $A_c\Delta z$. The use of 6.7 is attributed to the multi-dispersity of the fixed bed.

After the integration of Eq. (6.5) we have the following equation:

$$u_z = \frac{\dot{m}}{\rho_g \varepsilon \pi (0.5D)^2} \tag{6.8}$$

where D is the diameter of the reactor. This equation is used to calculate the flow velocity along the reactor height for each segment control volume of the cylinder.

- The energy conservation equation for the gas phase is formulated for a control volume of $A_c\Delta z$:

$$c_{pg}\rho_g\left(\varepsilon A_c\Delta z\right)\frac{\partial T_g}{\partial t}+\dot{m}c_{pg}\Delta z\frac{\partial T_g}{\partial z}=\varepsilon A_c\Delta z\frac{\partial}{\partial z}\left(k_g\frac{\partial T_g}{\partial z}\right)+\underbrace{\sum_{j=1}^{N_p}\left(h_{pg}A_p\left(T_{s,j}-T_g\right)\right)}_{Catalyst\,particles}+ \tag{6.9}$$

$$+\underbrace{\sum_{j=1}^{N_p}\left(\epsilon_p\sigma A_p\left(T_{s,j}^4-{T_g}^4\right)\right)}_{Catalyst\,particles}+\underbrace{\sum_{j=1}^{N_{pm}}\left(h_{pmg}A_{pm}\left(T_{sm,j}-T_g\right)\right)+\sum_{j=1}^{N_{pm}}\left(\epsilon_{pm}\sigma A_{pm}\left(T_{sm,j}^4-{T_g}^4\right)\right)}_{Metal\,particles}$$

  where $A_c=\pi\frac{D^2}{4}$, N_p is the number of particles inside the control volume $A_c\Delta z$ and D is the tube diameter. N_{pm} is the number of metal particles in the control volume and N_p is the number of catalyst particles in the control volume. It should be noted that all balance equations for the gas phase are written for a control volume using Control Volume method. The derivatives in each equation represent the control volume averaged quantities.

- The energy conservation equation for the catalyst surface [19] is

$$(hA)_{in}(T_s-T_p)=h_{pg}\cdot A_p(T_g-T_s)+\cancelto{0}{A_p\sum_{r}^{N_r}\left(-\Delta H_r\right)R_{r,s}}+\epsilon_p\sigma A_p\left(T_g^4-{T_s}^4\right) \tag{6.10}$$

  where T_s and T_p represent the catalyst surface temperature and particle-averaged temperature, respectively.

- The energy conservation equation for the catalyst-particle is:

$$m_pc_p\frac{dT_p}{dt}=\underbrace{(hA)_{in}(T_s-T_p)}_{internal\,conduction}+\underbrace{V_p\sum_{r}^{N_r}\left(\left(-\Delta H_r\right)R_{r,V}\right)}_{reactions}+\underbrace{\sum_{j=1}^{N_{nb}}\left(\frac{T_{p,j}-T_p}{R_{th}}\right)}_{catalyst-catalyst\,conduction}+\underbrace{\sum_{i=1}^{N_{nbm}}\left(\frac{T_{pm,i}-T_p}{R_{th,pm}}\right)}_{catalyst-metal\,conduction} \tag{6.11}$$

  where N_{nb} is the number of catalyst neighbors for each catalyst particle and N_{nbm} is the number of metal particles neighbors for each catalyst particle, R_{th} and $R_{th,pm}$ represents the thermal resistance for the contact catalyst-catalyst particles and catalyst-metal particles, respectively.

- The energy conservation equation for the metal particle is:

$$m_{pm}c_p\frac{dT_{pm}}{dt}=\underbrace{(hA)_{inm}(T_{sm}-T_{pm})}_{internal\,conduction}+\underbrace{\frac{1}{2}\sum_{j=1}^{N_{nb}}\frac{\left(\phi_i-\phi_j\right)^2}{R_{\sigma,ij}}}_{Q_e}-\underbrace{\sum_{j=1}^{N_{nb}}\left(\frac{T_{p,j}+T_{pm}}{R_{th,pm}}\right)}_{metal-catalyst\,conduction}+\underbrace{\sum_{i=1}^{N_{nbm}}\left(\frac{T_{pm,i}-T_{pm}}{R_{th,mm}}\right)}_{metal-metal\,conduction} \tag{6.12}$$

where Q_e is the Joule heating term described as the summation of Joule heating from all of each particle contact points, $R_{th,mm}$ is the thermal resistance for the contact between metal particles. It should be noted that the relation for Q_e was validated against numerical and experimental data in the work [22].

- The energy conservation equation for the surface of metal particle is:

$$\underbrace{(hA)_{inm}(T_{sm}-T_{pm})}_{internal\,conduction}=\underbrace{h_{pmg}\cdot A_{pm}(T_g-T_{sm})}_{convection-conduction}+\underbrace{A_{pm}\sum_{r}^{N_r}(-\Delta H_r)\,R_{r,s}}_{surface\,reactions}+\underbrace{\epsilon_{pm}\sigma A_{pm}\left(T_g^4-T_{sm}^4\right)}_{radiation} \tag{6.13}$$

- The balance equation for i species CH_4, CO_2, CO, H_2O and H_2 in the gas [19] is:

$$\varepsilon\rho_g A_c\Delta z\frac{\partial Y_{i,g}}{\partial t}+\dot{m}\Delta z\frac{\partial Y_{i,g}}{\partial z}=\varepsilon\cdot\rho_g A_c\Delta z\frac{\partial}{\partial z}\left(D_{gas}\frac{\partial Y_{i,g}}{\partial z}\right)+\underbrace{\sum_{j=1}^{N_{nb}}\left[\beta_{pg}\cdot\rho_g A_p\left(Y_{i,s,j}-Y_{i,g}\right)\right]}_{Catalyst\,particles} \tag{6.14}$$
$$+\underbrace{\sum_{j=1}^{N_{nbm}}\left[\beta_{pmg}\cdot\rho_g A_{pm}\left(Y_{i,sm,j}-Y_{i,g}\right)\right]}_{Metal\,particles}$$

- The balance equation for i species CH_4, CO_2, CO, H_2O and H_2 on the surface of catalyst-particle [19] is:

$$\beta_{pg}A_p\rho_{g,s}(Y_{i,g}-Y_{i,s})+\cancelto{0}{M_iA_p\sum_{r}^{N_r}\alpha_{r,i}\,R_{r,s}}=(\beta A)_{in}\rho_{g,p}(Y_{i,s}-Y_{i,p}) \tag{6.15}$$

Due to the fact that the ratio between the particle surface and overall particle surface participating in the reactions is approximately $10^{-2}\%$ for d_p, we neglect chemical reactions on the catalyst-particle surface in Eq. (6.15 and Eq. (6.10). It should be note that the total surface area (BET, m^2/g) of the catalyst is 14.3 m^2/g according to the data [27].

- The balance equation for i species CH_4, CO_2, CO, H_2O and H_2 inside the catalyst-particle:

$$V_p\varepsilon_V\rho_{g,p}\frac{dY_{i,p}}{dt}=\underbrace{(\beta A)_{in}\rho_{g,p}(Y_{i,s}-Y_{i,p})}_{internal\,diffusion}+\underbrace{M_iV_p\sum_{r}^{N_r}\alpha_{r,i}R_{r,V}}_{reactions} \tag{6.16}$$

It should be noted that the diffusive mass transfer between connected catalyst particles was neglect.

- The balance equation for i species CH_4, CO_2, CO, H_2O and H_2 on the metal particle surface:

$$\beta_{pmg} A_{pm} \rho_{g,s} (Y_{i,g} - Y_{i,sm}) + M_i A_{pm} \sum_r^{N_r} \alpha_{r,i} \; R_{r,s} = 0 \tag{6.17}$$

In this equation, we neglect the diffusive mass transfer between connected catalyst particles.

The chemical source terms in species balance equations take the following form:

$$CH_4 : \; \sum_r^{N_r} (\alpha_{r,i} R_{V,r}) = - (R_{V,1} + R_{V,3}) \tag{6.18}$$

$$H_2O : \; \sum_r^{N_r} (\alpha_{r,i} R_{V,r}) = - (R_{V,1} + R_{V,2} + 2R_{V,3}) \tag{6.19}$$

$$CO : \; \sum_r^{N_r} (\alpha_{r,i} R_{V,r}) = R_{V,1} - R_{V,2}; \; CO_2 : \; \sum_r^{N_r} (\alpha_{r,i} R_{V,r}) = R_{V,2} + R_{V,3} \tag{6.20}$$

$$H_2 : \; \sum_r^{N_r} (\alpha_{r,i} R_{V,r}) = 3R_{V,1} + R_{V,2} + 4R_{V,3} \tag{6.21}$$

The partial pressure relates to mass fractions as follows:

$$p_i = \frac{Y_i P \, M}{M_i}; \; M = \frac{1}{\sum_i^N \frac{Y_i}{M_i}} \tag{6.22}$$

6.3.2 LHHW kinetics

The reaction rates $R_{V,r}$ for chemical reactions are defined using the data from the work [27], where the reaction kinetics for steam reforming is given in units of [mol/m^3·s].

$$R_{V,1} = \frac{k_1 \left(p_{\mathrm{CH_4}} p_{\mathrm{H_2O}}^{0.5} - \frac{p_{\mathrm{H_2}}^3 \, p_{\mathrm{CO}}}{K_1 \, p_{\mathrm{H_2O}}^{0.5}} \right)}{p_{\mathrm{H2}}^{1.25} \, \xi^2}; \quad R_{V,2} = \frac{k_2 \left(p_{\mathrm{CO}} \, p_{\mathrm{H_2O}}^{0.5} - \frac{p_{\mathrm{H_2}} \, p_{\mathrm{CO_2}}}{K_2 \, p_{\mathrm{H_2O}}^{0.5}} \right)}{p_{\mathrm{H2}}^{0.5} \, \xi^2} \tag{6.23}$$

$$R_{V,3} = \frac{k_3 \left(p_{\mathrm{CH_4}} \, p_{\mathrm{H_2O}} - \frac{{p_{\mathrm{H_2}}}^4 \, p_{\mathrm{CO_2}}}{K_3 \, p_{\mathrm{H_2O}}} \right)}{{p_{\mathrm{H_2}}}^{3.5} \, \xi^2} \tag{6.24}$$

where

$$\xi = 1 + K_{\mathrm{CO}} \, p_{\mathrm{CO}} + K_{\mathrm{H}} \, p_{\mathrm{H_2}}^{0.5} + K_{\mathrm{H_2O}} \frac{p_{\mathrm{H_2O}}}{p_{\mathrm{H_2}}} \tag{6.25}$$

According to the work [27], the rate coefficients are

$$k_1 = 5.922 \cdot 10^8 \exp\left(\frac{-209200}{R_g\, T}\right) \text{ [kmol/s/kg/kPa}^{0.25}\text{]} \tag{6.26}$$

$$k_2 = 6.028 \cdot 10^{-4} \exp\left(\frac{-15400}{R_g\, T}\right) \text{ [kmol/s/kg/kPa]} \tag{6.27}$$

$$k_3 = 1.093 \cdot 10^3 \exp\left(\frac{-109400}{R_g\, T}\right) \text{[kmol/s/kg/kPa}^{0.25}\text{]} \tag{6.28}$$

The adsorption coefficients take the following forms [27]:

$$K_{\mathrm{H_2O}} = 9.251 \cdot \exp\left(\frac{-15900}{R_g\, T}\right) ; K_{\mathrm{H}} = 5.68 \cdot 10^{-10} \exp\left(\frac{93400}{R_g\, T}\right) \text{[kPa}^{-0.5}\text{]} \tag{6.29}$$

$$K_{\mathrm{CO}} = 5.127 \times 10^{-13} \exp\left(\frac{140000}{R_g\, T}\right) \text{[kPa}^{-1}\text{]} \tag{6.30}$$

In this work, we used the following expressions for the equilibrium coefficients:

$$K_1 = 1.198 \cdot 10^{17} \exp\left(\frac{-26830}{T}\right) \text{[kPa}^2\text{]};\ \mathrm{K_2} = 1.767 \cdot 10^{-2} \exp\left(\frac{4400}{\mathrm{T}}\right) \text{[kPa]} \tag{6.31}$$

$$K_3 = 2.117 \cdot 10^{15} \exp\left(\frac{-22430}{T}\right) \text{ [kPa}^2\text{]} \tag{6.32}$$

6.3.3 Closure relations

Mass transfer coefficients β_{pg} and β_{pmg}, and heat transfer coefficients between the catalyst-particle and gas phase, and between the metal particle and gas, respectively, are calculated from the correlations:

$$Sh = \frac{\beta_{pg} \cdot 2r_p}{D_{gas}};\quad Sh = \frac{\beta_{pmg} \cdot 2r_{pm}}{D_{gas}} \tag{6.33}$$

$$Nu = \frac{h_{pg} \cdot 2r_p}{k_g};\quad Nu = \frac{h_{pmg} \cdot 2r_{pm}}{k_g} \tag{6.34}$$

The non-dimensional numbers Sh and Nu are calculated using the Gunn relation [28]:

$$Nu = (7 - 10\varepsilon + 5\varepsilon^2)(1 + 0.7Re_i^{0.2}Pr^{0.33}) + (1.33 - 2.4\varepsilon + 1.2\varepsilon^2)Re_i^{0.7}Pr^{0.33} \tag{6.35}$$

$$Sh = (7 - 10\varepsilon + 5\varepsilon^2)(1 + 0.7Re_i^{0.2}Sc^{0.33}) + (1.33 - 2.4\varepsilon + 1.2\varepsilon^2)Re_i^{0.7}Sc^{0.33} \tag{6.36}$$

It should be noted that the Gunn relation was used here because it has been verified against 3D DNS [29] (for lower Re_p values). In this work, we assume that $Le = 1$ according to [30, 31], leading

to the condition $Nu = Sh$. In Eq. (6.35), ε is the void fraction of the bed:

$$\varepsilon = \frac{\frac{16}{3}\sum_{i=1}^{N_p} \pi r_i^3}{\pi D^2 H} \tag{6.37}$$

where H is the height of the tube, $r_i = r_{p,i}, r_{pm,i}$.

The particle Reynolds number is calculated using

$$Re_i = \frac{\rho_g u_z \cdot 2r_i}{\mu_g} \tag{6.38}$$

where $r_i = r_p, r_{pm}$.

The diffusion and intra-particle mass transfer coefficients of the gas take the forms [32]:

$$Le = \frac{k_g}{D_{gas} c_p \rho_g} = 1; \;\; D_{gas} = \frac{k_g}{c_p \, \rho_g} \tag{6.39}$$

$$(\beta A)_{in} = 4\pi D_{\text{eff}} \left(\frac{1}{a_1 r_p} - \frac{1}{r_p} \right)^{-1} \tag{6.40}$$

$$(hA)_{in} = 4\pi k_p \left(\frac{1}{a_1 r_p} - \frac{1}{r_p} \right)^{-1}; \quad (hA)_{inm} = 4\pi k_{pm} \left(\frac{1}{a_1 r_{pm}} - \frac{1}{r_{pm}} \right)^{-1} \tag{6.41}$$

where $a_1 = 0.85$ [32]. This coefficient represents a non-dimensional radius of a sphere referring to the location of the volume-averaged temperature T_p or T_{pm} in terms of the thermal resistance formula for a sphere. The variables $(hA)_{in}$ and $(hA)_{inm}$ are the intraparticle heat transfer coefficients for the catalyst particle and for the metal particle, respectively. $(\beta A)_{in}$ is the intraparticle mass transfer coefficient for the catalyst particle.

The effective diffusion inside the catalyst particle D_{eff} is calculated as follows [19]:

$$D_{\text{eff}} = \frac{\varepsilon_p}{\tau_p} D_{gas} \tag{6.42}$$

where $\varepsilon_p = 0.44$ is the catalyst particle porosity and $\tau_p = 3.54$ is the particle tortuosity [16].

The heat rate and the thermal resistance between the two particles due to their static contact can be calculated as follows [17]:

$$Q_{cond} = \frac{T_i - T_j}{R_{th}}; \quad \frac{1}{R_{th}} = \frac{4r_c}{\frac{1}{k_{p,i}} + \frac{1}{k_{p,j}}} \tag{6.43}$$

where r_c is the contact radius, and $k_{p,j}$ and $k_{p,i}$ are the thermal conductivity of particles j and i, respectively. The thermal resistance due to the contact between catalyst and metal particles, $R_{th,pm}$,

takes the form:

$$\frac{1}{R_{th,pm}} = \frac{4r_c}{\frac{1}{k_{p,i}} + \frac{1}{k_{pm,j}}} \tag{6.44}$$

If $k_{p,j} = k_{p,i}$, the thermal resistance between catalyst particles, R_{th}, and between metals particles, $R_{th,mm}$, take the form:

$$R_{th} = \frac{1}{2\,r_c\,k_p}; \quad R_{th,mm} = \frac{1}{2\,r_c\,k_{pm}} \tag{6.45}$$

The algorithm for calculating the contact radius r_c between two touching particles can be found in the work [19]. DEM uses real contact physics to find the contact area between particles through force balance. To calculate r_c for all particles we used the following mechanical properties: the Young's modulus for metal and catalyst particles was set to 200 GPa, the Poisson ratio was 0.31. A load of 200N was applied by the top plate to the fixed bed.

The convective and diffusion terms in Eqs. (6.9) and (6.14) were discretized using the 2^{nd}-order upwind scheme and central difference scheme, respectively. The discretized Eqs. (6.9) and (6.14) were solved using a Gauss-Seidel matrix solver with the overrelaxation technique. Eqs. (6.10), (6.11), (6.12), (6.13), (6.15), (6.16) and (6.17) were solved using the Newton method with underrelaxation of all dependent variables. Finally, the system of equations comprising Eqs. (6.5) - (6.17) has been solved implicitly (the code was programmed in MATLAB). The size of CV was used as follows $\Delta z = 2d_{pm}$. The outer iterations were stopped when the estimated relative error (ERE) for each dependent variable (T_s, T_p, $Y_{i,s}$, $Y_{i,p}$) was less than 10^{-6}.

6.3.4 Equilibrium models (EM and EM cat)

The main idea of the equilibrium-based models adopted in this work is based on the condition that gas composition inside the catalyst particle and on the surface of the metal particle corresponds to equilibrium values according to local temperatures [19]. To compare predictions of the KM model we consider two models: the equilibrium model (EM) taken from the work [19] and the equilibrium model inside catalyst only (EM cat). The species concentrations on the catalyst-particle surface and in the gas phase are calculated using balance equations. And the heat transfer equations are the same as for KM just the rates of reactions are defined using the rates of species mass transfer, for details see the work [19]. In particular, instead of solving species conservation equations for CH_4, CO_2, CO, H_2O and H_2 on the metal particle surface we define $Y_{i,p}$ using equilibrium values utilizing T_s and pressure values:

$$Y_{i,sm} = f(T_s, P, Y_{g,i}) \tag{6.46}$$

And instead of solving species conservation equations for CH_4, CO_2, CO, H_2O and H_2 inside the catalyst particle we we calculate $Y_{i,p}$ using equilibrium values utilizing T_p and pressure values:

$$Y_{i,p} = f(T_p, P, Y_{g,i}) \tag{6.47}$$

Our system has 5 species and 3 atom to be balanced. Eq. (6.2) and Eq. (6.3) are the two independent chemical reactions that are used to find the chemical composition inside the catalyst particle. Eq. (6.16) can be used to derive the source term in mass transfer equations:

$$M_i V_p \sum_{r}^{N_r} \alpha_{r,i} R_{r,V} = -(\beta A)_{in} \rho_{g,p} (Y_{i,s} - Y_{i,p}) \tag{6.48}$$

The reaction rate can be expressed as the rate of mass transfer for CH_4 and CO_2 as follows:

$$-M_{CH_4} V_p R_{1,V} = -(\beta A)_{in} \rho_{g,p} (Y_{CH_4,s} - Y_{CH_4,p}) = -\beta_{pg} \rho_g A_p (Y_{\mathrm{CH_4,g}} - Y_{\mathrm{CH_4,s}}) \tag{6.49}$$

$$M_{CO_2} V_p R_{2,V} = -(\beta A)_{in} \rho_{g,p} (Y_{CO_2,s} - Y_{CO_2,p}) = -\beta_{pg} \rho_g A_p (Y_{\mathrm{CO_2,g}} - Y_{\mathrm{CO_2,s}}) \tag{6.50}$$

Finally, the chemical source term in Eq. (6.11) takes the form:

$$\begin{aligned} V_p \sum_{r}^{N_r} (-\Delta H_r) R_{r,V} = \frac{(-\Delta H_1)}{M_{CH_4}} (\beta A)_{in} \rho_{g,p} (Y_{CH_4,s} - Y_{CH_4,p}) - \\ - \frac{(-\Delta H_2)}{M_{CO_2}} (\beta A)_{in} \rho_{g,p} (Y_{CO_2,s} - Y_{CO_2,p}) \end{aligned} \tag{6.51}$$

The equations for equilibrium constants take the form in Eqs. 6.31. The equilibrium constants were approximated based on Gibbs free energy from 1000K to 1100K, taken from NIST WebBook [33]. Details on calculation of Eq. (6.47) can be found in the work [19].

The equilibrium model inside catalyst only (EM cat) is similar to EM, the only difference is that Eq. 6.17 is used to calculate the species conservation equation for species CH_4, CO_2, CO, H_2O and H_2 on the surface of the metal particle, instead of utilizing Eq. (6.46).

Finally, the equilibrium-based models can be used in diffusion-limited regimes since the rate of reaction is determined by the mass transfer between the bulk flow and particles. Combined with the heat balance equation, the gas composition inside the particle is solved using equilibrium conditions. The main advantage of such class of models is no needs to know the kinetics of SMR and significant speed up of calculations due to the absence of exponential source terms in the species balance equations.

6.4 Electric field and contact resistance models

To calculate the Joule heating for each metal particle, we have to predict electric field distribution in the fixed bed. In this work we utilize the model developed and validated in the work[22]. In

particular, the electric field distribution in fixed beds is predicted numerically using a new particle-unresolved (PUR) DEM-based model. The coordinates of the particles are calculated using the open-source DEM software YADE [23, 24].

Before we introduce the electromagnetic field equations, we assume that when electrical current flows through the bed, each metal particle is characterized by the particle-averaged electric field potential ϕ_i and the contact between particles is treated like a resistor. Next, we use the electrical current conservation equation:

$$\nabla \cdot \vec{j} = 0 \tag{6.52}$$

Using Ohm's law we can write:

$$\vec{j} = \sigma \cdot \vec{E}; \implies \vec{j} = -\sigma \nabla \phi \tag{6.53}$$

Using Eq. 6.53, Eq. 6.52 and can be written for each particle i in the bed as follows:

$$\sum_{j=1}^{N_{nb}} \vec{j}_{ij} = 0 \implies \sum_{j=1}^{N_{nb}} \sigma_{pm,i} \frac{\phi_i - \phi_j}{d_{ij}} = 0 \tag{6.54}$$

where N_{nb} is the number of metal particle neighbours for the metal particle i that have a static contact with the particle i, ϕ_i represents the particle-averaged electric field potential, d_{ij} is the distance between centers of two metal particles that have a static contact.

By the analogy with the heat conduction between two particles with a static contact, Eq. 6.54 takes the form:

$$\sum_{j=1}^{N_{nb}} \frac{\phi_i - \phi_j}{R_{\sigma,ij}} = 0 \tag{6.55}$$

For a bed of N_{pm} particles, a system of N_{pm} equations needs to be solved. The ϕ of each particle is solved in an N_{pm} by N_{pm} matrix. To solve the system of linear equations, Eq. (6.55), only the metal particles were included since catalyst particle do not conduct electricity. This method allows the computational time to be significantly reduced.

To solve a system of linear equations the following boundary conditions are used:

$$\phi_i = 0 \; for \; z = 0; \; and \;\; \phi_j = \phi_c \; for \; z = H \tag{6.56}$$

This condition implies that the electric field potentials at the cathode and the anode are constant.

To establish a diagonally dominant sparse matrix, the particles are indexed based on the order of the axial position. The matrix is solved using the Gaussian elimination method. Finally, it should be emphasized that if a particle i only has contact with one neighboring particle, this particle does not conduct the current and its electrical potential is equal to the electric potential of its single touching particle.

Finally, after the electric field potential is known for each particle, the electric current is calculated at the cathode or anode, respectively using the formulas:

$$I = \pi \sum_{i=1}^{N_{pC}} r_{c,i}^2 \sigma_{pm,i} \frac{\phi_i - 0}{\Delta z} \tag{6.57}$$

where $\Delta z = 0.5 d_p$ and N_{pA} is the number of particles in contact with the cathode.

$$I = \pi \sum_{i=1}^{N_{pA}} r_{c,i}^2 \sigma_{pm,i} \frac{\phi_c - \phi_i}{\Delta z} \tag{6.58}$$

N_{pC} is the number of particles contacting the anode.

By analogy to the heat transfer, the electrical current between the two particles i and j, which have a stationary connection, is calculated as follows [22]:

$$I_{ij} = \frac{\phi_i - \phi_j}{R_{\sigma,ij}} \tag{6.59}$$

The electrical resistance of the contact area takes the form [22]:

$$\frac{1}{R_{th}} = \frac{4 r_c}{\frac{1}{k_{p,i}} + \frac{1}{k_{p,j}}}; \implies \frac{1}{R_{\sigma,ij}} = \frac{4 r_c}{\frac{1}{\sigma_{pm,i}} + \frac{1}{\sigma_{pm,j}}} \tag{6.60}$$

where r_c is the contact radius, and $\sigma_{p,j}$ and $\sigma_{p,i}$ are the electrical conductivity of particles j and i, respectively. If $\sigma_{p,j} = \sigma_{p,i}$, the electrical resistance $R_{\sigma,ij}$ takes the form:

$$R_{\sigma,ij} = \frac{1}{2\, r_c\, \sigma_{pm}} \tag{6.61}$$

The contact radius r_c between two touching elastic particles i and j which are locally spherical with radii r_i and r_j can be calculated according to Hertz theory[34, 35]. Details on r_c calculation can be found in the work [22]. Finally, the MATLAB code of the developed EF model including input files with 3D coordinates of each particle can be found in supplementary materials of this article.

6.5 Validations

To proceed with the validations of the EF model, and the heat and mass transfer model, the validation of our model for the contact area is presented. Fig. 6.3 depicts the case used by Govender et al. [36]. The conditions in the case were repeated using the model described in this work. A bed of spherical particles ($N_p = 80323$) was generated in a 25 cm by 25 cm rectangular container with a height of 50 cm. After the bed is allowed to pack under gravity(g=9.81m/s^2), it is cut at 30cm, above which height any particles are removed. The particles have a density of 2700 kg/m^3 and a

diameter of 0.6204cm. The friction coefficient of the particle surface is 0.4. The elastic coefficient used is 200kPa, converted from a linear stiffness of 1000 N/m. Poisson's ratio is 0.45. The restitution coefficient used is 0.45. Analysis of Fig.6.3a shows that the contact area is very close to the findings reported in the work [36], up to a contact area of 0.01 cm^2. There is some difference due to the slightly different stiffness model used. In the validation case, Govender et al. [36] used a linear stiffness model based on intersection volume to accommodate different particle shapes. In this work, the simulation of the contact area between particles is based on the Hertz model [34, 35].

To validate our EF model, represented by Eqs. (6.55) - (6.60), we use experiments published in the work [22]. In experiment [22], the fixed bed consisted of 86 steel balls packed in a glass cylinder with a diameter of 0.047 m and a height of 0.11 m. Two electrodes made of steel with a thickness of 1 mm were placed on the bottom and on the top of cylinder, closing the cylinder to any gas inflow or outflow. A 2 kg stainless steel weight was placed on the upper ceramic plate to improve the static contact between the steel balls, allowing electrical current to flow through the balls. The geometric sizes and properties of the materials used are given in the work [22]. Fig. 6.4a shows the voltage-ampere characteristics of the fixed bed, predicted numerically for a constant electrical conductivity of steel calculated for $T = 400K$ as follows: $(4.28 - 0.00542\,(T - 273)) \cdot 10^7$ 1/Ohm. The voltage calculated from 3D DEM-based model was compared to the experimental data [22]. Relatively good agreement can be observed. The experimental curve is concave upward and has a non-zero x-intercept. The difference is likely due to wire resistance between the voltmeter and the electrical plates. To illustrate the influence of r_c on $I = f(U)$ profile we carried out a sensitivity study multiplying all r_c predicted using our model by 0.9 and 1.1 coefficients. It can be seen that $\pm 10\%$ change in r_c leads to $\pm 4\%$ change in I for $U = 3$ V.

To validate the heat and mass transfer model for SMR, we repeat the simulations reported in the work [37]. Authors presented a numerical study of an industrial-scale reformer using a multi-scale axisymmetric model [37]. Parameters used in our validation can be found in the works [37, 19]. Figs. 6.4b and 6.4c compares the axial profiles of chemical species mole fractions predicted using the kinetic model (KM) ($\Delta z = 2d_p$) with profiles takes from the literature [37]. Good agreement (within 4%) can be observed for the outlet values of CH_4, H_2 and CO_2 mole fraction. For the CO, the deviation comprises about 8 %. Additionally, we carried out a sensitivity study for the influence of the grid size Δz on axial profiles of species mole fractions. It can be seen that the difference between results obtained using $\Delta z = 2d_p$ and $\Delta z = 4d_p$ is below 1%.

6.6 Results and Discussion

Before we proceed with the analysis of numerical simulations, we would like to highlight the main physical processes inside the reactor after the electric field potential is applied between the top and bottom of the reactor. The electrically conductive metal particles allow current to pass through the

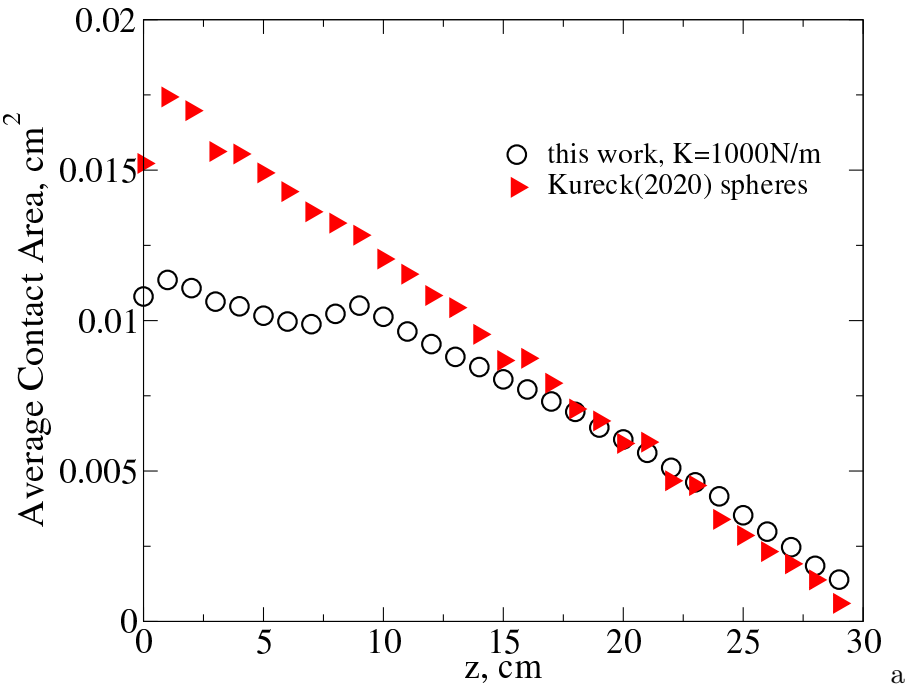

a

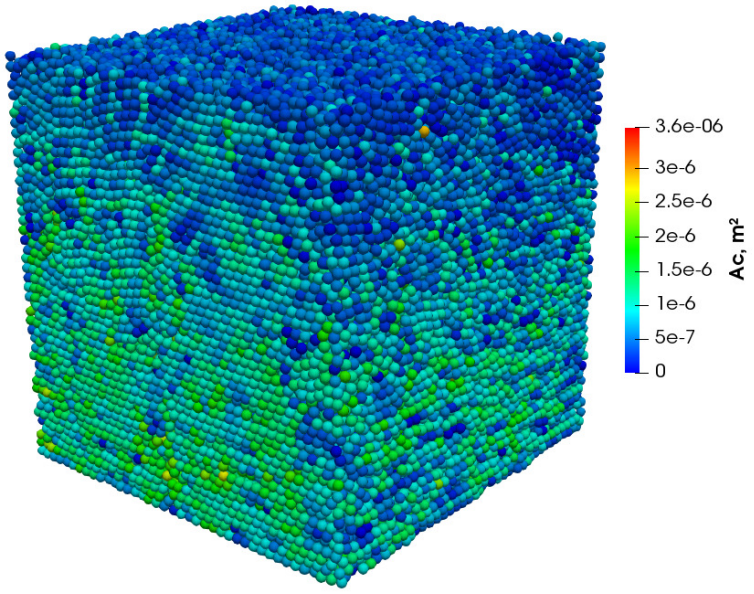

b

Figure 6.3: Code validation for the contact area calculation: a - axial profile of the averaged contact area calculated using our model and data taken from the literature; b - 3D plot of the contact area predicted numerically according to conditions from the work [36]. Here Kureck 2020 refers to the work [36].

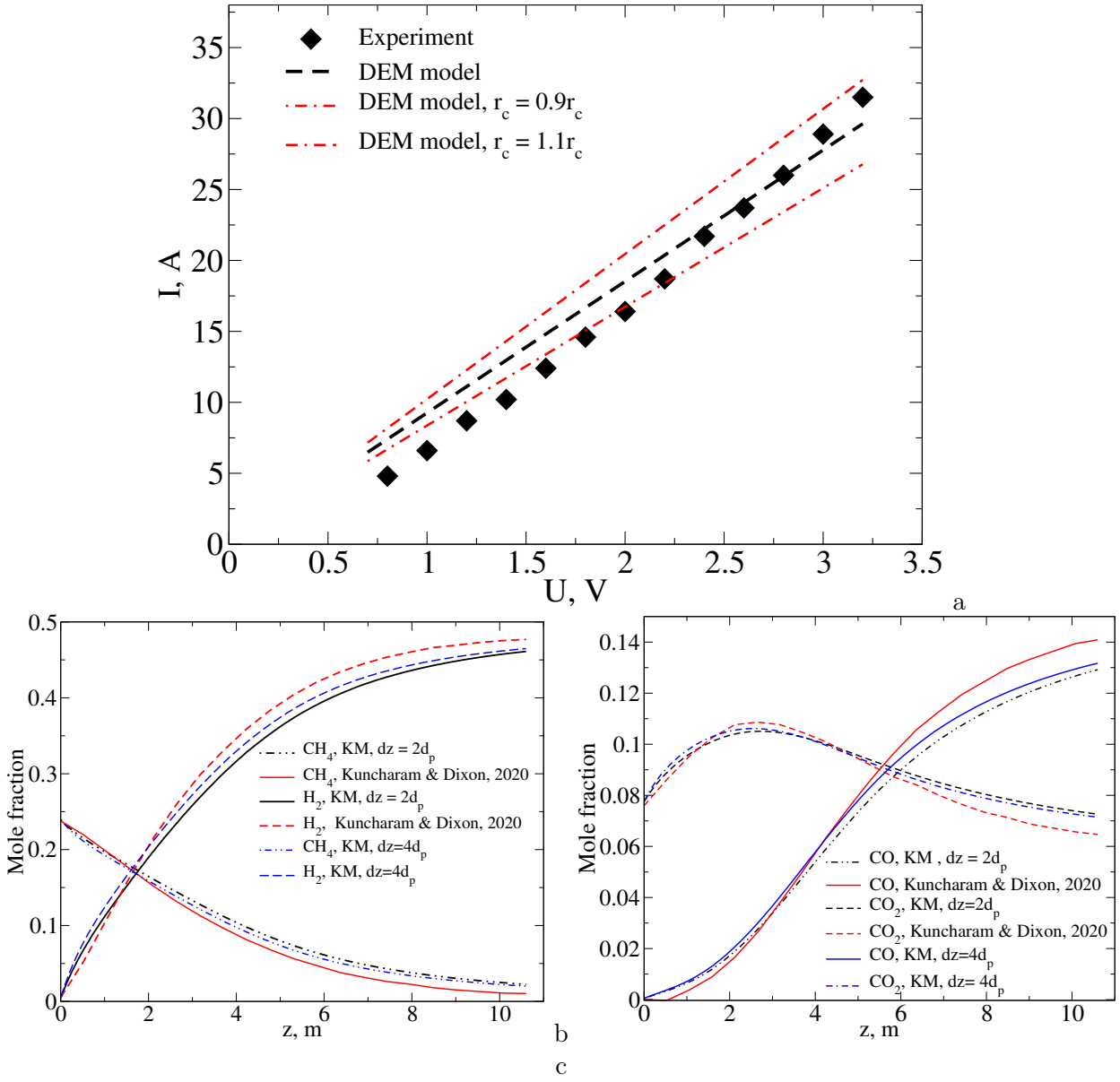

Figure 6.4: Volt-ampere characteristic of the fixed bed measured in the experiment[22] and predicted numerically (a), b and c - axial profile of species mole fractions predicted numerically using 3D DEM based KM model and calculations taken from the literature [37].

fixed bed and provide the heat of reaction by Joule heating. Fig. 6.5 shows the contact area, voltage distribution between metal particles and 3D distribution of the electrical current. The contact area between particles determines the resistance of the fixed bed and corresponding values of the electrical current flowing between the metal particles. From Fig. 6.5a it can be seen that due to the effect of gravity, the contact area is largest near the bottom of the fixed bed and gradually decreases towards the top, where the contact radius has the lowest values. The maximum contact area between the particles is $5 \cdot 10^{-7}$ m^2, equivalent to the ratio of $r_c/r_p \approx 10\%$ for the metal particles. The minimum value of the contact radius is about $r_c = 0.0002 r_p$. Fig. 6.5b shows the electrical potential for each particle. The voltage is roughly linearly dependent on the axial position of metal particles. It should be noted that with the amount of electrically non-conductive catalyst in the mix, 3.5% of the electrically conductive particles are not connected to the circuit; thus, they do not produce any Joule heat. These particles are more likely to be located near the side wall, as near-wall particles have naturally fewer contacting neighbors. Therefore, with a larger-diameter bed, the heat distribution is likely better than this study suggests. The current distribution is shown in Fig. 6.5c. Electricity in the fixed bed is sparsely distributed and widespread, but most of the current goes through a few particles with the largest contact area within each axial section, as electricity follows the least-resistance path. Despite the unequal distribution of current, the heat in each section of the fixed bed is relatively uniform and the distribution of heating is approximately equal in each axial section. However, it should be noted that increase in the ratio of catalyst particles will lead to a non-homogeneous distribution of the temperature over the reactor height [12].

The uniformity of conduction, and thus heating, is determined not only by the proportion of particles, but also the random packing of particles. DEM simulation is especially important because the local stacking conditions of the bi-disperse fixed bed can only be known through detailed simulation using real material properties. A sizable sample of particles is needed, not only to negate the wall effects, but also statistically, to encompass the various possibilities of the particle packing. Ultimately, the metal-to-catalyst ratio of 1:6 is decided on as a good balance between the maximum catalyst and uniform current distribution.

Fig. 6.6 shows a 3D visualization of the particle-averaged temperature of metal and catalyst particles, T_{pm} and T_p, respectively, predicted using KM, EM cat and EM. It can be seen that the equilibrium model (EM) produces the lowest temperature in comparison to KM and EM cat models. This is in good agreement with the findings in the work [19]. The values of T_{pm} and T_p calculated using the kinetic model (KM) are close to the data obtained utilizing the catalyst-equilibrium model(EM cat). For all three models, although there are a few particles which are significantly hotter than others, the estimated temperature is still safely below the melting temperature of the nickel metal at 1700K, shown in Fig. 6.6. The temperature changes significantly along the axis of the cylinder because of the reaction and heating, but the radial distribution of heating and temperature is quite uniform, as evident from the cross-sectional snapshot in Fig. 6.6. The temperature profile

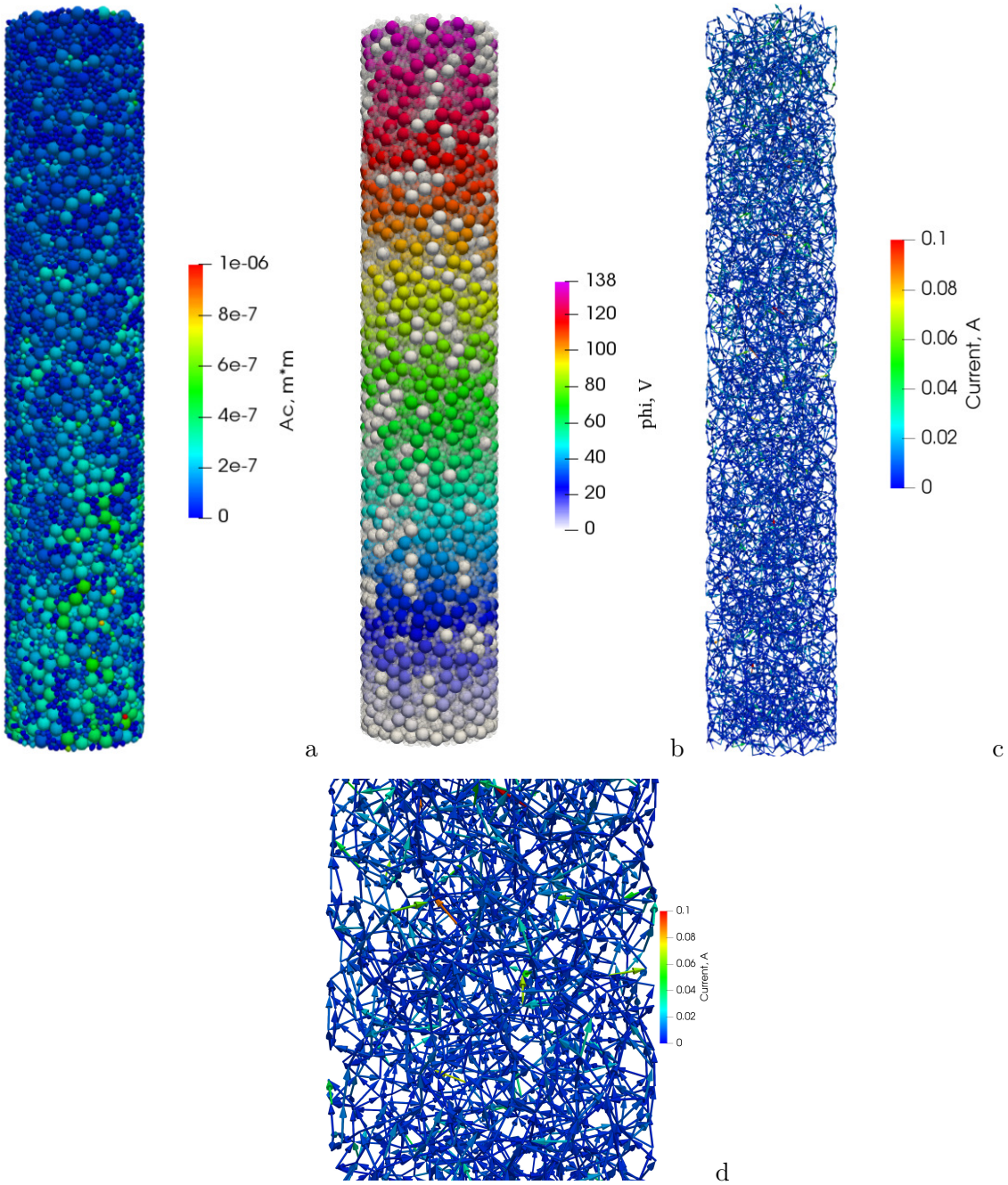

Figure 6.5: 3D visualization of (a) contact area between particles, (b) particle voltage, (c) and (d) electrical current distribution inside the fixed bed predicted numerically for for $Q_{IU} = 20$ kW, U=138.19 V.

in the radial direction is one of the key advantages of this type of reactor over conventional steam reformers, where the heat generation occurs from outside the walls of a reactor heated by methane combustion. A uniform cross-sectional temperature means the reactor can be enlarged to any radial diameter, reducing the area-to-volume ratio and thereby improving efficiency. The source of energy is a mixture of electrical energy and natural gas. As the energy economy shifts towards renewables, the technology has the potential to become commercially viable. However, the configuration requires development of technology and optimization of design to realize the high efficiency.

The 3D temperature distribution for a case with a total heating power of 14kW ($Q_{IU} \ll \dot{m}\Delta H_{aver}$) is shown in Fig. 6.7 for comparison. The temperature in the case of 14KW is much lower, as expected. At a lower temperature, the reactions are slower and further away from equilibrium. As a result, the difference in T between the KM and EM models is more pronounced in the case of 14kW compared to the case of 20kW. The flow rate value for both Q_{IU} are given in Table 6.3.

To compare temperature profiles along the reactor height qualitatively, Fig. 6.8 shows the axial distribution of the particle-averaged temperature of the metal particles T_{pm} and catalyst particles T_p predicted using KM and EM models. In the case of 20kW, the gas temperature in the fixed bed dips quickly down to around 900K before recovers and the outlet temperature reaches 1200K in kinetic model. In the case of 20kW, the heating power is adjusted to match the maximum possible rate of reaction for R_1, so the temperature is expected to exceed the inlet temperature as R_2 is an exothermic reaction. However, compared to the equilibrium model in Fig. 6.8, the temperature is significantly higher. In EM simulation, where the reaction nears completion at the outlet, the outlet temperature is only 50K above inlet. Additionally, we depict axial profiles of the gas phase temperature T_g a control-volume averaged T_{pm} and T_p calculated as follows:

$$T = \frac{1}{N_p} \sum_{j=1}^{N_p} T_{i,j} \tag{6.62}$$

where T_i refers to T_{pm} and T_p and the control-volume is $\Delta V = \frac{\pi}{4} D^2 \Delta z$.

The analysis of Fig. 6.8c shows that all temperature drops after the inlet and increase linearly after $z = 0.1$ m for the case of 20 kW. In the outlet zone T_g asymptotically approaches T_p while T_{pm} exceeds T_p by 30 K, because the heat of reaction has decreased.

Fig. 6.9 shows axial profiles of the control volume averaged temperature of metal particles T_{pm}, catalyst particles T_p and gas temperature T_g predicted using KM, EM cat and EM models for $Q_{IU} = 20$ kW (left column) and for $Q_{IU} = 14$ kW (right column). In Fig. 6.9, we see that the KM and the EM cat have very close results in the beginning, but the temperature begin to differ after 0.2 m. The difference between KM and EM means the reaction is not close to equilibrium.

We observe a significant increase in the reaction rate when by using equilibrium conditions on

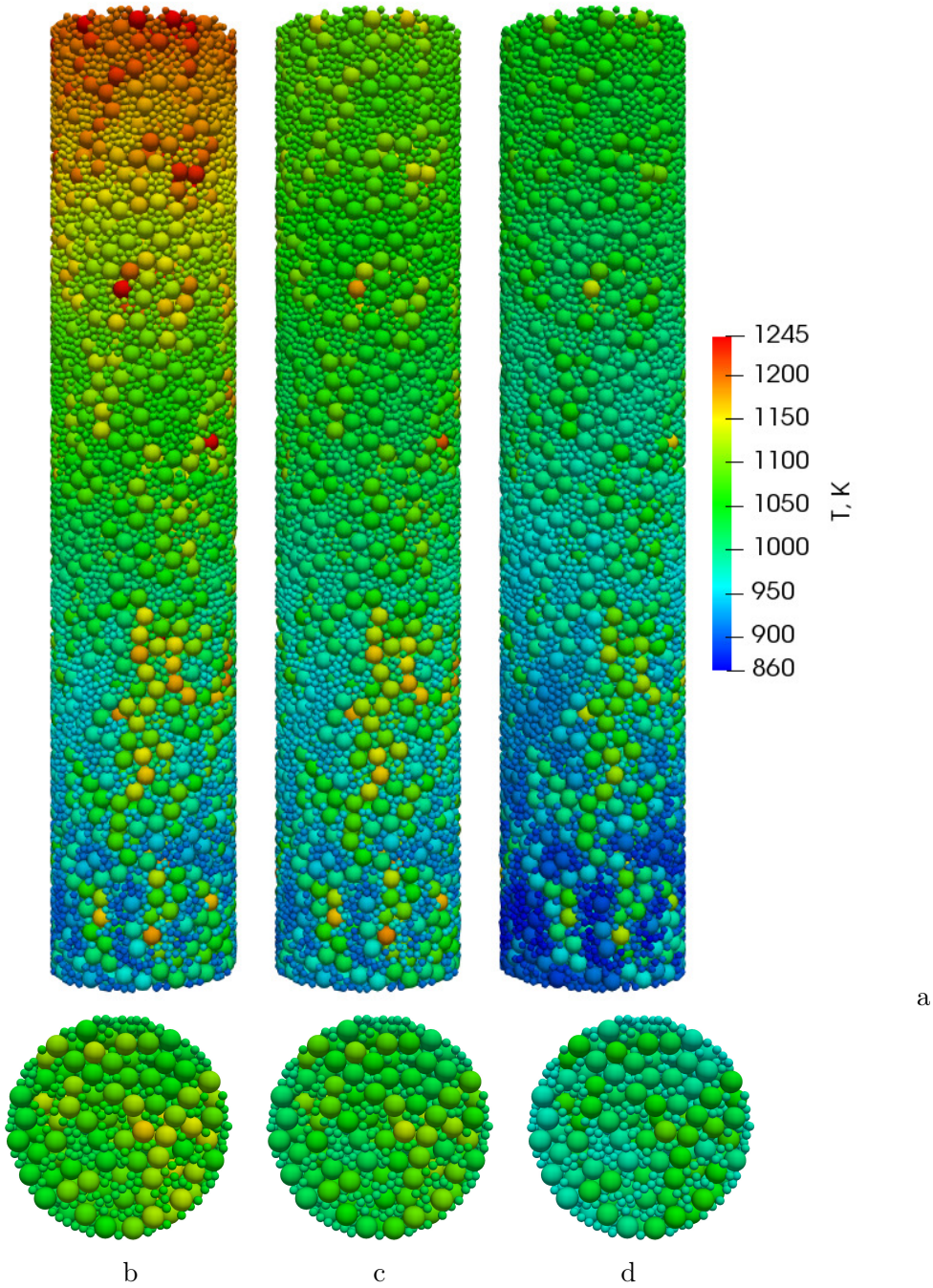

Figure 6.6: 3D distribution of the particle temperature T_p and T_{pm} predicted using three different models (a) - left: KM, middle: EM cat, right: EM, a), c) and d) T_p and T_{pm} distributions predicted using KM, EM cat and EM model, respectively, at the cross-section at $z = H/2$. Here $Q_{IU} \approx 20$ kW.

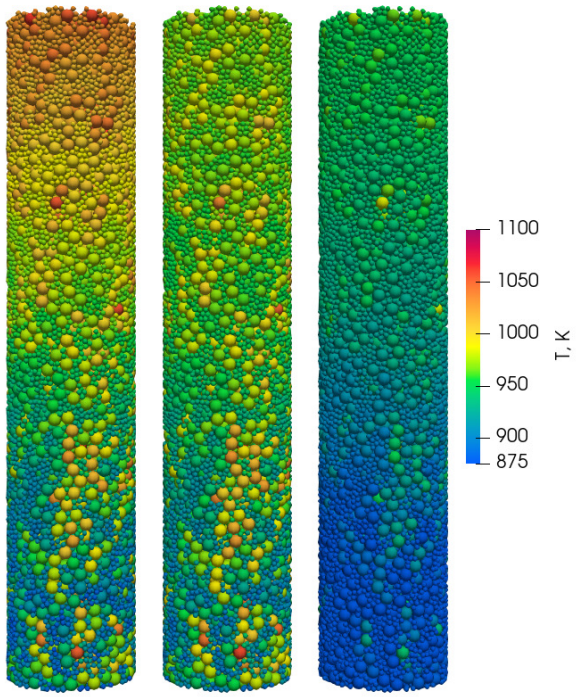

Figure 6.7: 3D distribution of the particle temperature T_p and T_{pm} predicted using three different models left: KM, middle: PEM, right: EM. Here $Q_{IU} \approx 14$ kW.

the metal surface. Since metal particles are the heat source and have very high conductivity, the surface and internal temperatures of the metal particles are nearly the same. There is very little heat transfer limitation for the reaction rate on metal. Conversely, metal particles do not have much active surface area compared to the porous catalyst particles. Even though the metal surface at above-bulk conditions, the reaction does not contribute much to the overall reaction occurring in the reactor. Therefore, the rate on the metal surface are always reaction-limited in the reactor.

The rate limiters for catalyst particles are seen by comparing the profiles obtained using KM and EMcat. Initially, the profiles of KM and EMcat are almost identical. The similarity is due to the heat transfer limitations experienced when the gas initially enters the reactor. The gas temperature decreases as a result of the endothermic reaction. As the reactions proceeds towards equilibrium, the net reaction rate decreases and the temperature begins to recover. Up to about 0.2 m, the temperature and conversion profiles are also very close between KM and EMcat. At this stage, the reactions are diffusion-limited and the inside of the catalyst particles are at near-equilibrium conditions. Therefore, the results for EMcat and KM are nearly equivalent. However, nearing the end of the reactor, the KM and EMcat models begin to reveal differences. The difference means that the equilibrium conditions inside the catalyst particles are no longer a valid assumption.

Fig. 6.10 depicts the 3D distribution of the species mass fractions Y_{p,CH_4}, $Y_{p,CO}$ and Y_{p,H_2}

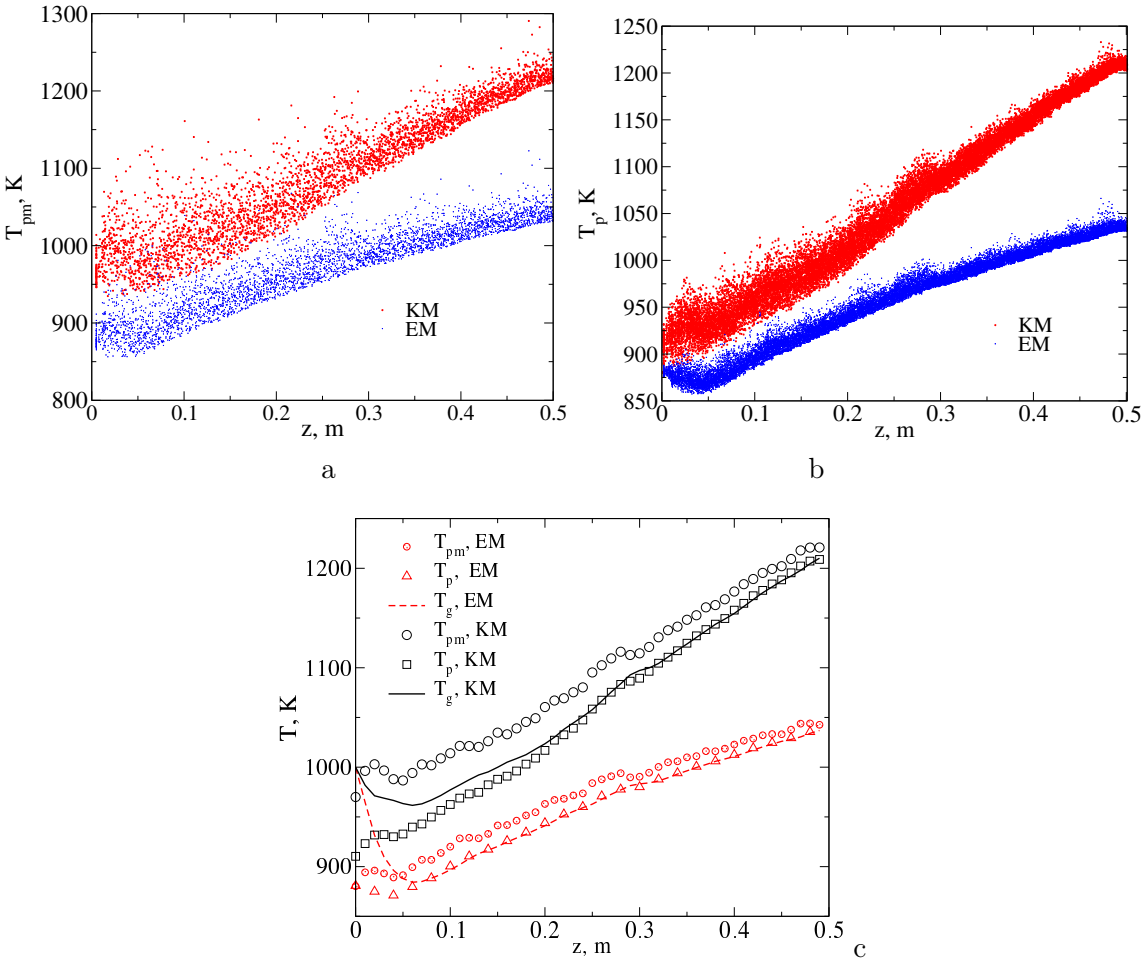

Figure 6.8: Axial distributions of the temperature of metal particles T_{pm} (a) and catalyst particles T_p (b) predicted using KM and EM models for $Q_{IU} \approx 20$kW (red color corresponds to KM and blue color shows EM results) and c) axial profiles of the control-volume averaged temperatures of T_{pm}, T_p and T_g calculated using different models for $Q_{IU} \approx 20$kW.

inside the catalyst particles and on the surface of the metal particles Y_{ms,CH_4}, $Y_{ms,CO}$ and Y_{ms,H_2}, respectively, predicted using three different models. The characteristics of each model is evident in both cases, with 20kW resulting in higher conversion of CH_4 and much higher CO formation.

To characterize the species mass transfer in the bed qualitatively, we use the mass fractions of all species, which are plotted in Figs. 6.11 and 6.12 for $Q_{IU} = 20$ kW and $Q_{IU} = 14$ kW, respectively. The main difference between KM and EM cat is the amount of CO at the outlet of the reactor. Figs. 6.11 and 6.12 confirm the conclusion from the temperature plots that equilibrium is not reached either in the gas phase or inside the catalyst. The reason for this effect is that equilibrium is not reached for water-gas shifting in the reactor. Comparing the KM results and the EM cat results in Fig. 6.11, almost no difference is found in the conversion of CH_4. Although Reaction 6.2 reaches the equilibrium, the water-gas shift reaction 6.3 is a slower reaction, that limits the gas composition at the outlet of the reactor. In the outlet part of the reactor, the reaction is diffusion-limited, as the composition inside the particle is close to equilibrium. From Figs. 6.11 and 6.12 it can be seen that close similarity is observed between KM and EM cat in the outlet part of the reactor.

In the middle of the reactor, the difference between the predictions of KM and EMcat for species in the gas phase is the highest. This effect can be explained by examining the three reaction rates. Fig. 6.13 shows the control-volume averaged reaction rate of all three reactions 6.2-6.4 predicted for $Q_{IU} = 20$ kW and $Q_{IU} = 14$ kW, respectively. The reaction rate in the catalyst particles decreases over distance as the reactant is depleted. From Fig. 6.13 it is obvious that reaction 6.2 governs reactions 6.3 and 6.4. The water-gas shift reaction moves in a forward direction in the inlet part of the reactor until z reaches $\approx 0.4H$. From Fig. 6.13, we can see that after $\approx 0.5H$, the water-gas shifting reaction is backwards and consistently around 10^{-4} mol/s. The methane conversion reaches equilibrium about halfway through the reactor.

While methane steam reforming is not limited by kinetics, the nickel based catalyst has limited active sites for water-gas shifting. Therefore, we see much closer CH_4 conversion in Fig. 6.11 than CO formation when comparing the KM and EM cat results. Hence the CH_4 conversion rates for both KM and EM cat are nearly identical, but the lack of heat absorption from water-gas shifting causes the temperature to be higher than with EM cat. Since the water-gas shifting does not reach equilibrium in the reactor, we can exploit this fact to control the CO_2-to-CO selectivity in the product. A syngas with higher CO has a higher heat value, but if pure hydrogen is the desired final product, a higher CO_2 ratio is good for the pressure/temperature swing adsorption process. Although the length of the reactor can be adjusted to give the desired CO composition, it is not efficient to carry out water-gas shifting using the Ni/Al_2O catalyst. Hence in commercial reactors, a secondary reactor is usually required to control the hydrogen-to-CO ratio, using a much faster iron-based catalyst at a lower temperature [38].

The axial profiles of the control-volume averaged mass fraction of each species in the catalyst particles and on the metal particles predicted using KM and EM models are plotted in Fig. 6.14 and

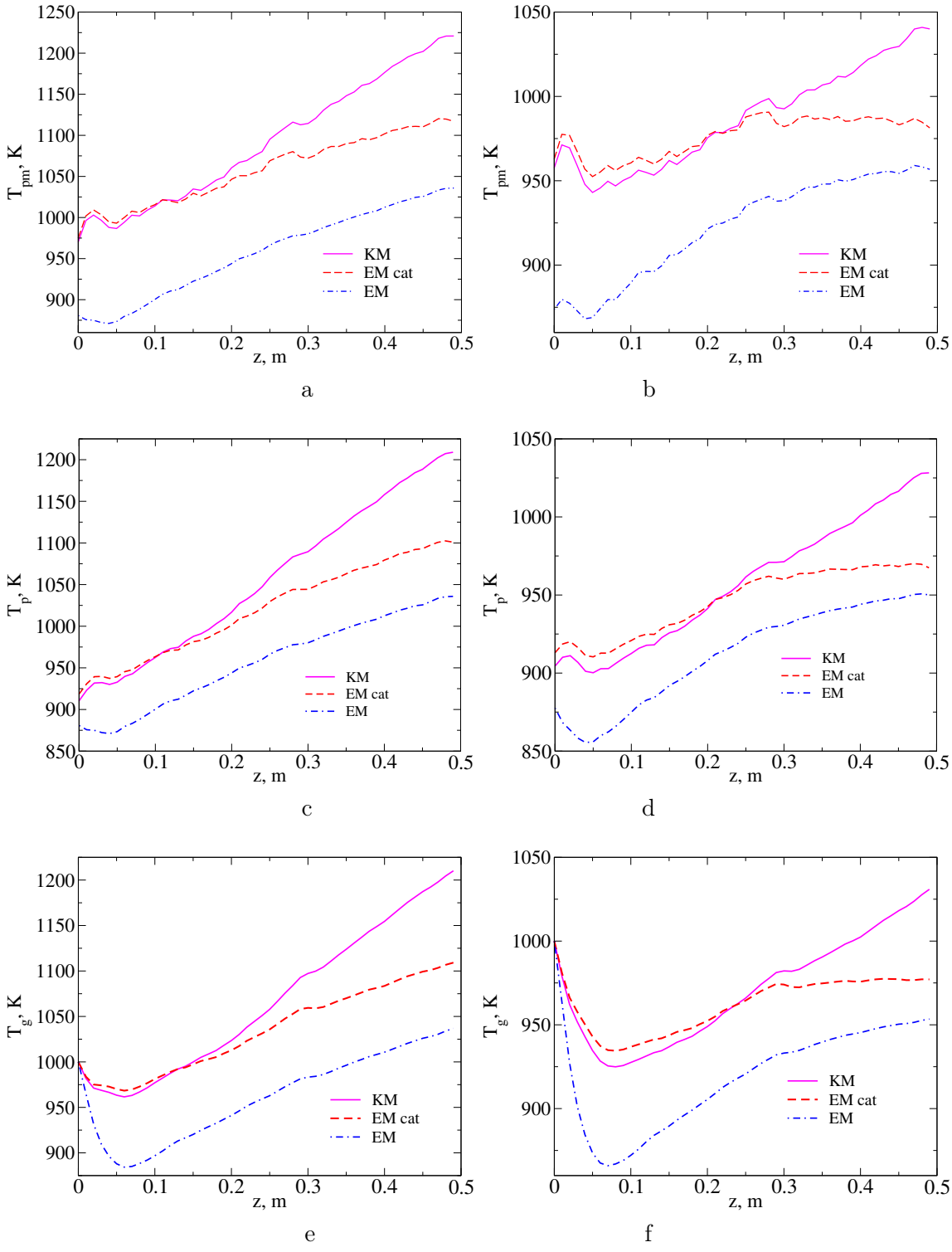

Figure 6.9: Axial profiles of the control-volume averaged temperature of metal particles T_{pm} (a), catalyst particles T_p (b) and gas temperature T_g (c) predicted using KM, EM cat and EM models for $Q_{IU} \approx 20$ kW (left column - a, c, e) and for $Q_{IU} \approx 14$ kW (right column - b, d, f).

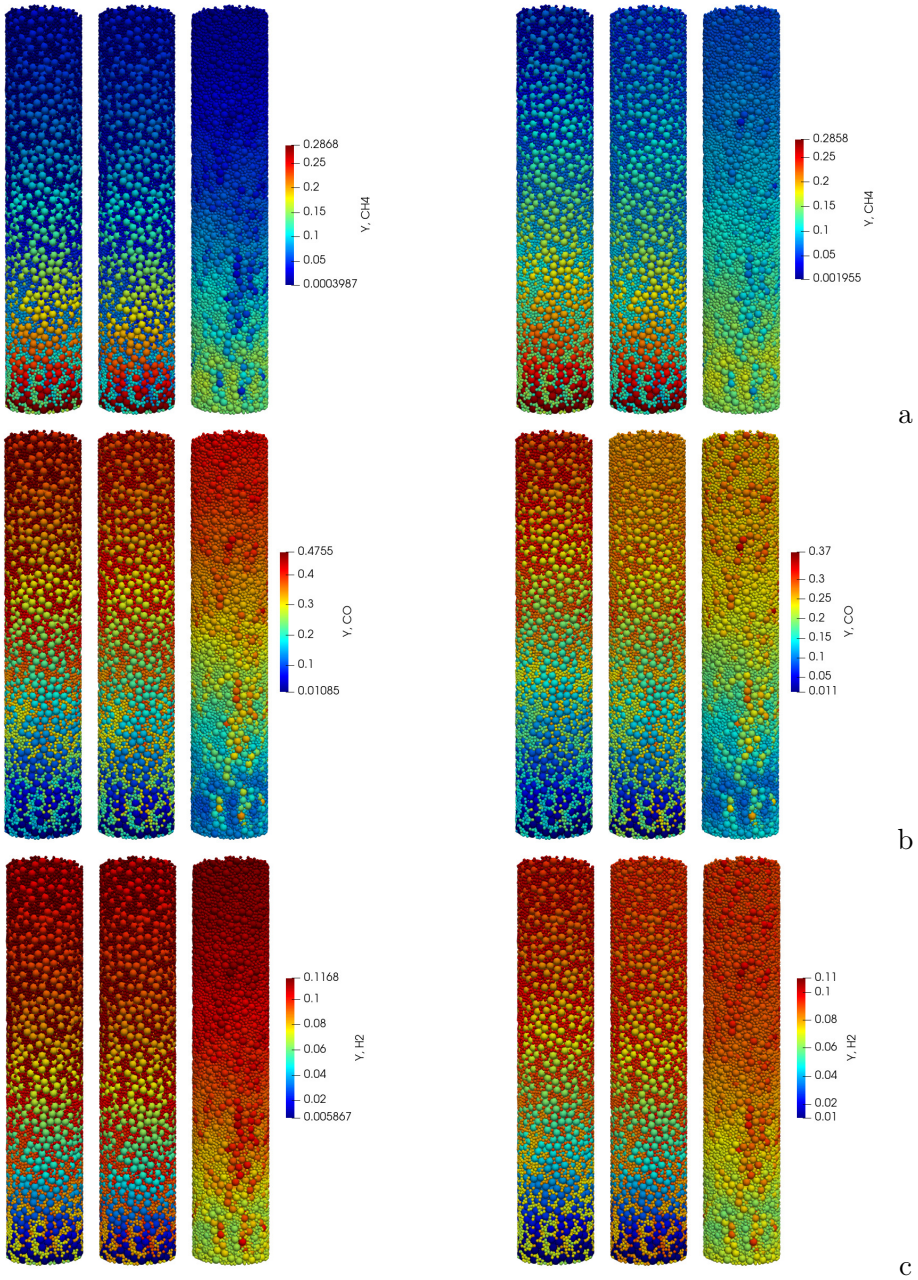

Figure 6.10: 3D distribution of the species mass fractions $Y_{p,i}$ inside the catalyst particles and on the metal particles surface $Y_{ms,i}$ predicted using three different models left: KM, middle: EM cat, right: EM, (a) CH_4, (b) CO and (c) H_2. Here $Q_{IU} \approx 20$ kW (left column) and $Q_{IU} \approx 14$ kW (right column).

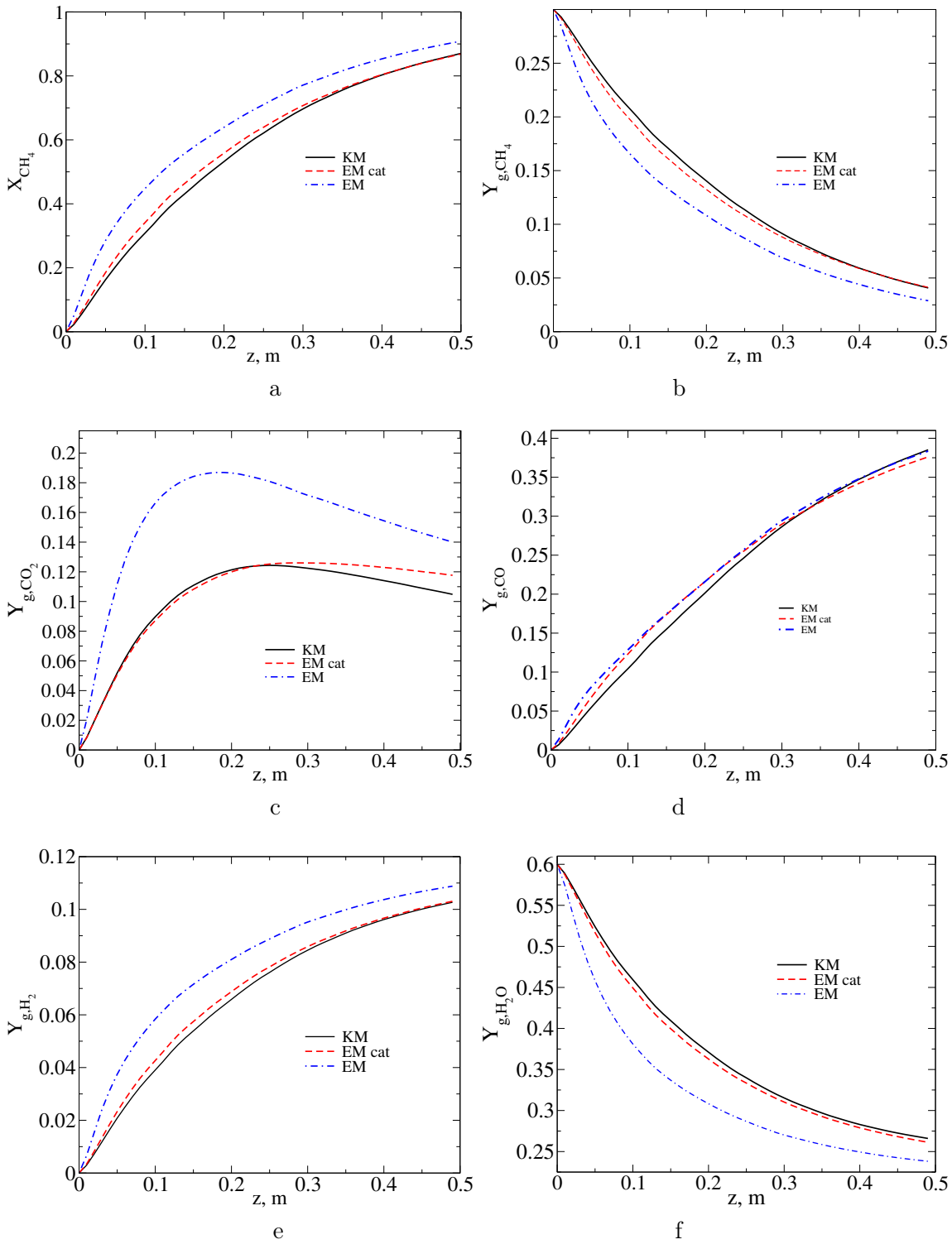

Figure 6.11: Axial profiles of the mass fractions of different species in the gas phase predicted using KM, EM cat and EM models for $Q_{IU} \approx 20$ kW: a - conversion of CH_4 (X_{CH_4}) ; b - Y_{g,CH_4}; c - Y_{g,CO_2}; d - $Y_{g,CO}$; e - Y_{g,H_2}; f - Y_{g,H_2O};

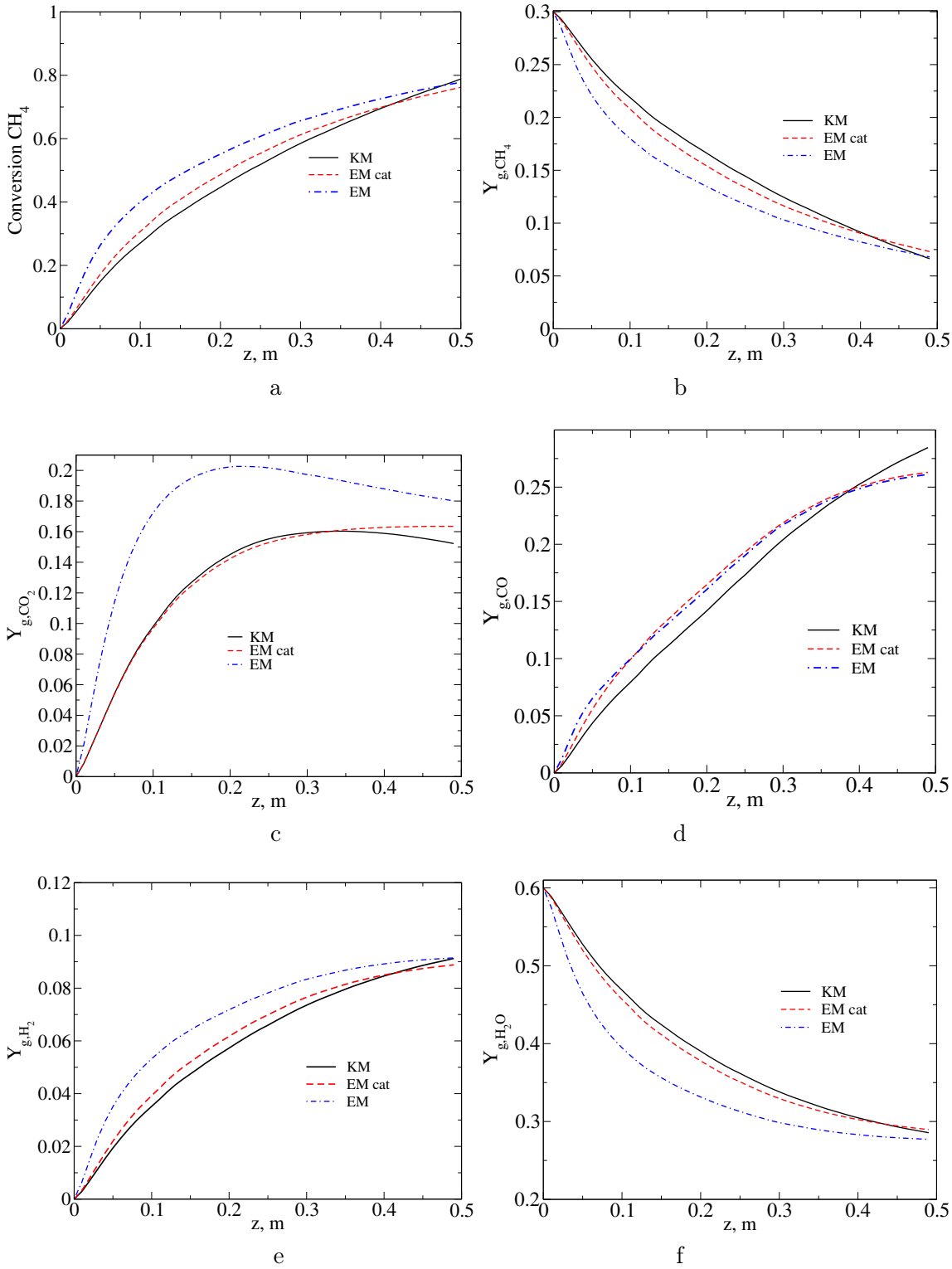

Figure 6.12: Axial profiles of the mass fractions of different species in the gas phase predicted using KM, EM cat and EM models for $Q_{IU} \approx 14$ kW: a - conversion of CH_4 (X_{CH_4}) ; b - Y_{g,CH_4}; c - Y_{g,CO_2}; d - $Y_{g,CO}$; e - Y_{g,H_2}; f - Y_{g,H_2O};

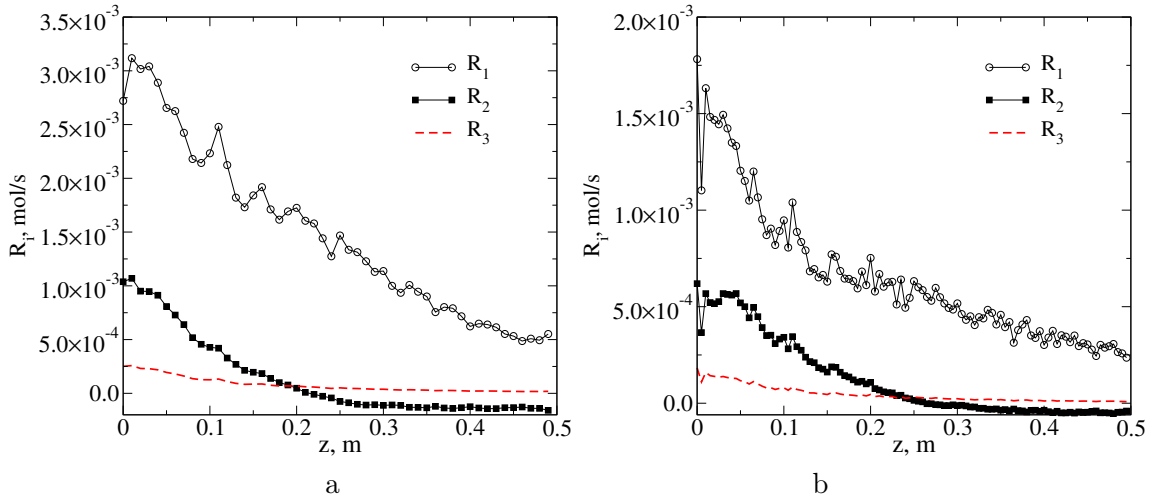

Figure 6.13: Axial profiles of the control-volume averaged values of reaction rates $R_{r,V}$ in the catalyst particles predicted for $Q_{IU} \approx 20$ kW (a) and $Q_{IU} \approx 14$ kW (b).

in Fig. 6.15 for $Q_{IU} = 20$ kW and $Q_{IU} = 14$ kW, respectively. In the kinetic model, the catalyst particles have conversions much higher than the gas phase because of diffusion limitations. The comparison between KM and EM shows that the difference is indeed quite large. This is because in EM, the surface of the metal particles are at equilibrium, which far exceeds the rate of internal mass transfer for the catalyst particles. EM predicts much higher conversion in the gas phase despite lower reaction rate inside the catalysts. Since this is clearly not the case as seen in Fig. 6.13, EM is not a reliable model and cannot sufficiently model for the reactor.

Comparing mass fractions in Figs. 6.14 and 6.15, we see that the conversion of CH_4 is improved by the higher power input. However, the H_2 production is increased by around 10% despite a 35% increase in the power input. This is because the supplied heat in the case of 20 kW went into reverse water-gas shifting and sensible heat due to the temperature rising over that of 14 kW.

In this study, the particle size is deliberately chosen in the millimeter range to illustrate the difference between the reaction-limited regime and the kinetic-limited regime. In a typical industrial operation, the catalysts usually range from 1 cm to 5 cm in diameter [37]. The large catalyst size leads to more diffusion limitations and EM cat should be able to predict more similar results to KM, for details we refer to the work [39].

To illustrate the influence of the flow rate $\dot{m}$ on the reactor performances for a constant Q_{IU}, Fig. 6.16 depicts the conversion of CH_4 predicted numerically using KM model for $Q_{IU} = 13.9\,kW$ and different values of $\dot{m}$. It can be seen that increase in $\dot{m}$ leads to the decrease in the conversion of CH_4 proportionally to $\dot{m}^{-1/2}$. The decreased conversion rate is attributed to the decrease in T_{pm} and slower reaction rate due to increase in the gas velocity by constant Q_{IU}.

Finally, Fig. 6.17 presents the influence of the gas flow rate and input power on the methane

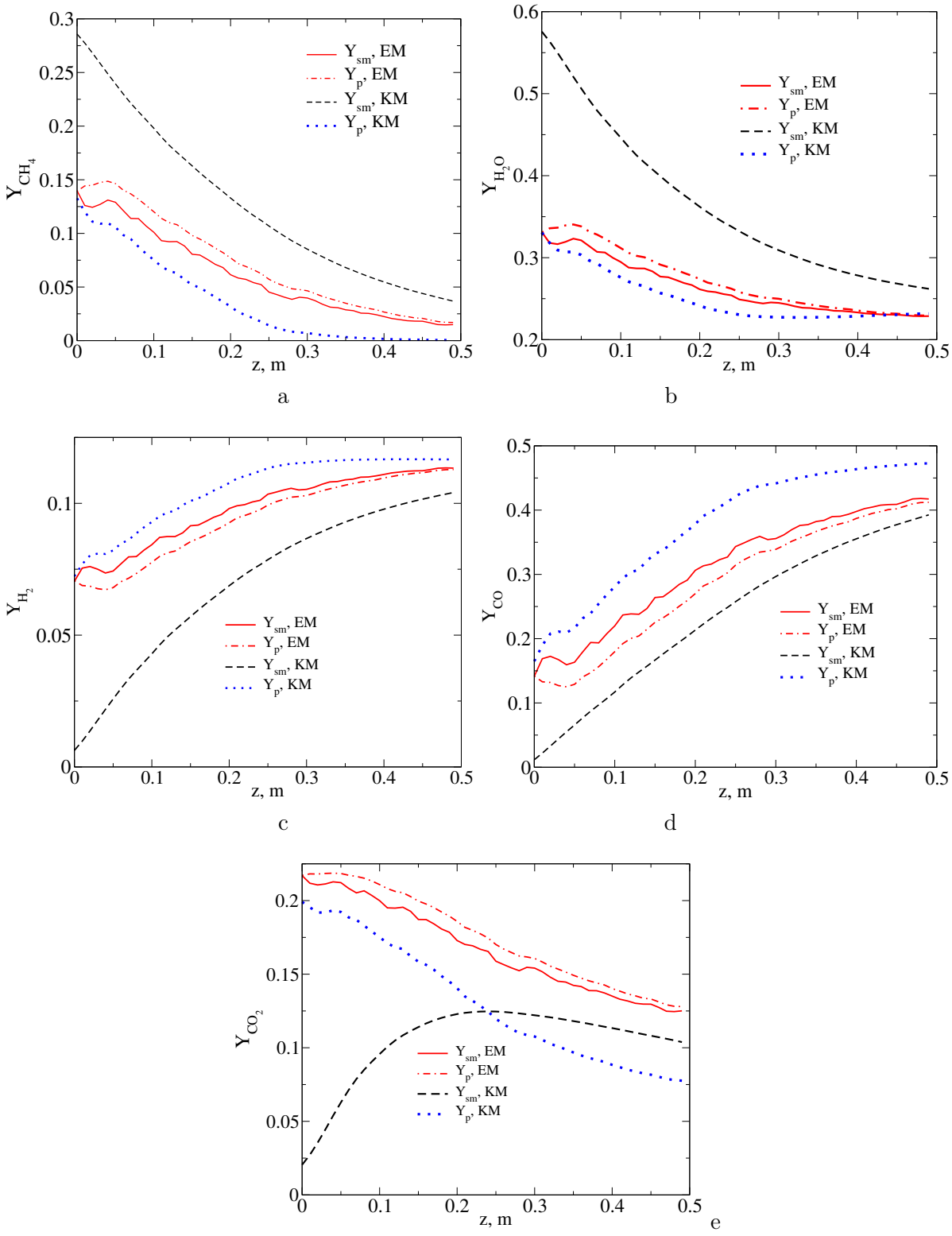

Figure 6.14: Axial profiles of the control-volume averaged mass fractions of different species inside catalyst particles Y_p and on the metal particles surface Y_{sm} predicted for $Q_{IU} \approx 20$ kW using KM and EM models: a - Y_{CH_4}; b - Y_{H_2O}; c - Y_{H_2}; d - Y_{CO}; e - Y_{CO_2};

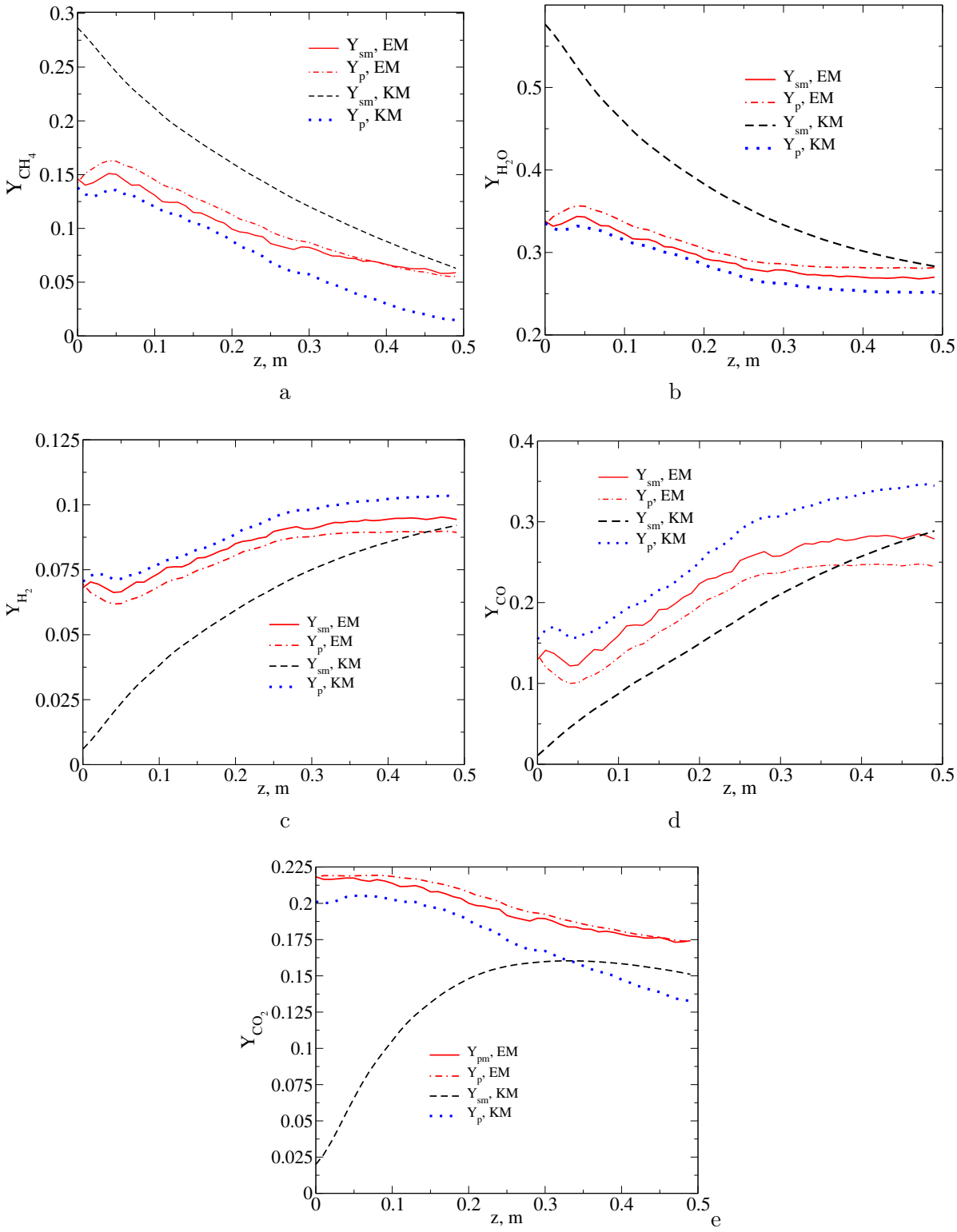

Figure 6.15: Axial profiles of the control-volume averaged mass fractions of different species inside catalyst particles Y_p and on the metal particles surface Y_{sm} predicted for $Q_{IU} \approx 14$ kW using KM and EM models: a - Y_{CH_4}; b - Y_{H_2O}; c - Y_{H_2}; d - Y_{CO}; e - Y_{CO_2};

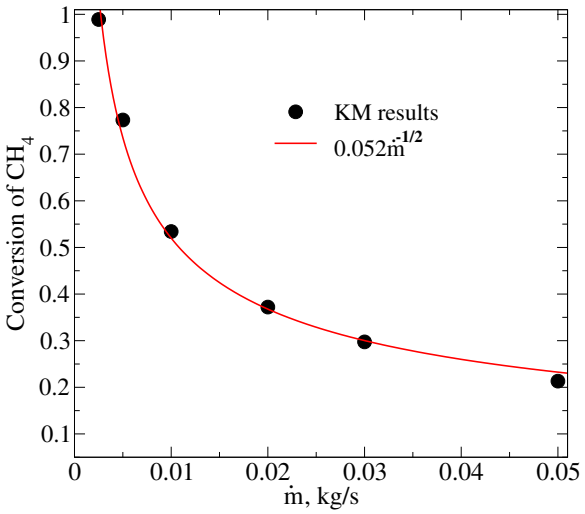

Figure 6.16: The influence of the gas flow rate $\dot{m}$ on the conversion of CH_4 predicted numerically using KM model for $Q_{IU} = 13.9kW$

conversion and the maximum temperature of the metal particles. The heat power is set proportional to the mass flowrate. When the flowrate is increased, the conversion of CH_4 goes down as the mean residence time is shorter. The maximum particle temperature also increases with flowrate due to the increase in heating power . Conversion and maximum temperature are the two important limiting factors that determine the production capacity of the reactor. Finally, Table 6.3 details all flow rates and corresponding power consumption used to generate results in Fig. 6.17.

$\dot{m}$, kg/s	Q_{IU}, kW	U, V
0.0025	9631	97.71
0.0025	6935	82.92
0.005	19262	138.19
0.005	13870	117.26
0.01	38524	195.43
0.01	27740	165.84

Table 6.3: Input parameters using in simulations for Fig. 6.17

To investigate the start up time and to understand the reaction inside the reactor, an unsteady study is conducted. In the unsteady study, the reactor starts with a temperature at 300K and inlet composition with an inlet gas flow temperature of 1000 K. The boundary conditions are the same as the steady-state case. The heating power of 20 kW is held constant during the unsteady simulation. The initial timestep used is 10^{-6} s. The timestep is gradually increased until it reaches 1s. For each timestep, the iteration is stopped when the estimated relative error reaches below 10^{-4} for temperature and 10^{-2} for species. The inlet composition represents an extreme case with the

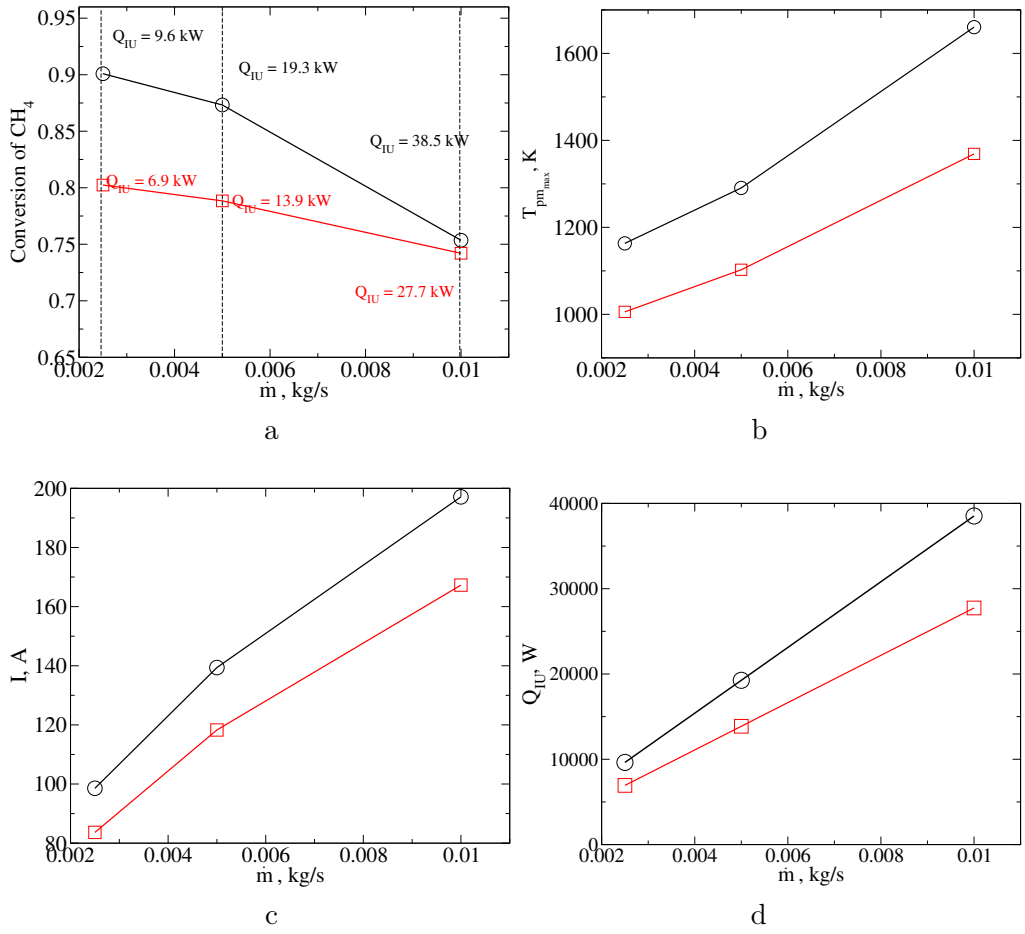

Figure 6.17: Conversion of CH_4 (a) and maximum temperature of metal particles T_{pm} (b) electrical current, I, (c) and total inputelectrical power, Q_{IU}, (d) predicted and used for different flow rates and Q_{IU} given in Table 6.3.

maximum reaction rate. Since the reaction is mostly endothermic, the start-up time should be less in any other scenario than the predicted case.

To analyze the start-up time we use the reactor-averaged temperatures T_p, T_{pm} and T_g and the reactor-averaged mass fraction of CH_4 in the gas phase Y_g calculated as follows:

$$T_g = \frac{1}{H}\int_0^H T_g\, dz;\;\; Y_{CH_4} = \frac{1}{H}\int_0^H Y_{CH_4,g}\, dz \tag{6.63}$$

$$T_p = \frac{1}{H}\int_0^H \left(\frac{1}{N_p}\sum_{j=1}^{N_p} T_{p,j}\right) dz;\;\; T_{pm} = \frac{1}{H}\int_0^H \left(\frac{1}{N_{pm}}\sum_{j=1}^{N_{pm}} T_{pm,j}\right) dz \tag{6.64}$$

The time history of the reactor-averaged temperatures and the reactor-averaged mass fraction of CH_4 is shown in Fig. 6.18a and Fig. 6.18b, respectively.

The 3D visualization of the temperature at different points of the unsteady study is shown in Fig. 6.18c-f. The unsteady study shows the system reaches steady state about 800s after heating begins. It can be seen that most of the start-up time is due to the slow propagation of the flow of reactant through the fixed-bed reactor. Since the inlet is at 1000K and the initial temperature is 300K, we see the flow front move up the reactor. At least 300s is needed for the flow to completely purge out the cold gas inside. Once the hot inlet gas reaches the outlet, the conversion of CH_4 is almost 20% higher than the steady state value. If we can adjust the thermal conditions in the fixed bed, there are ways to decrease the start-up time. The methods to initiate a fast start-up include reducing the initial flowrate or amplifying the heating power. Storing sensible heat using excess energy in the fixed bed will also improve response time and operating efficiency.

6.7 Conclusions

In this work, we have presented the new 3D DEM-based (Euler-Lagrange) model for the electrically driven steam reforming of methane using the Joule heat resulting from direct electrical current flowing through metal particles. The distinguishing features of the model are its ability to calculate the 3D distribution of the electric field inside the bed and to take into account the intraparticle heat and mass transfer for each individual particle (including particles different sizes) coupled with the heat and mass transfer between the particles and the bulk flow. Predictions of the new model are carefully compared with equilibrium models which utilize the chemical equilibrium inside the catalyst particles taking into account the species mass transfer rates on particle surfaces. Comparisons of these models showed that there were significant differences in their predictions with an increase in the input electrical energy used to heat the reactor. To evaluate the performance of each model and to investigate the feasibility of a new electrical steam methane reforming concept, we have simulated a cylindrical electrically insulated tube with a diameter of 0.1 m and a height of 0.5 m, which is

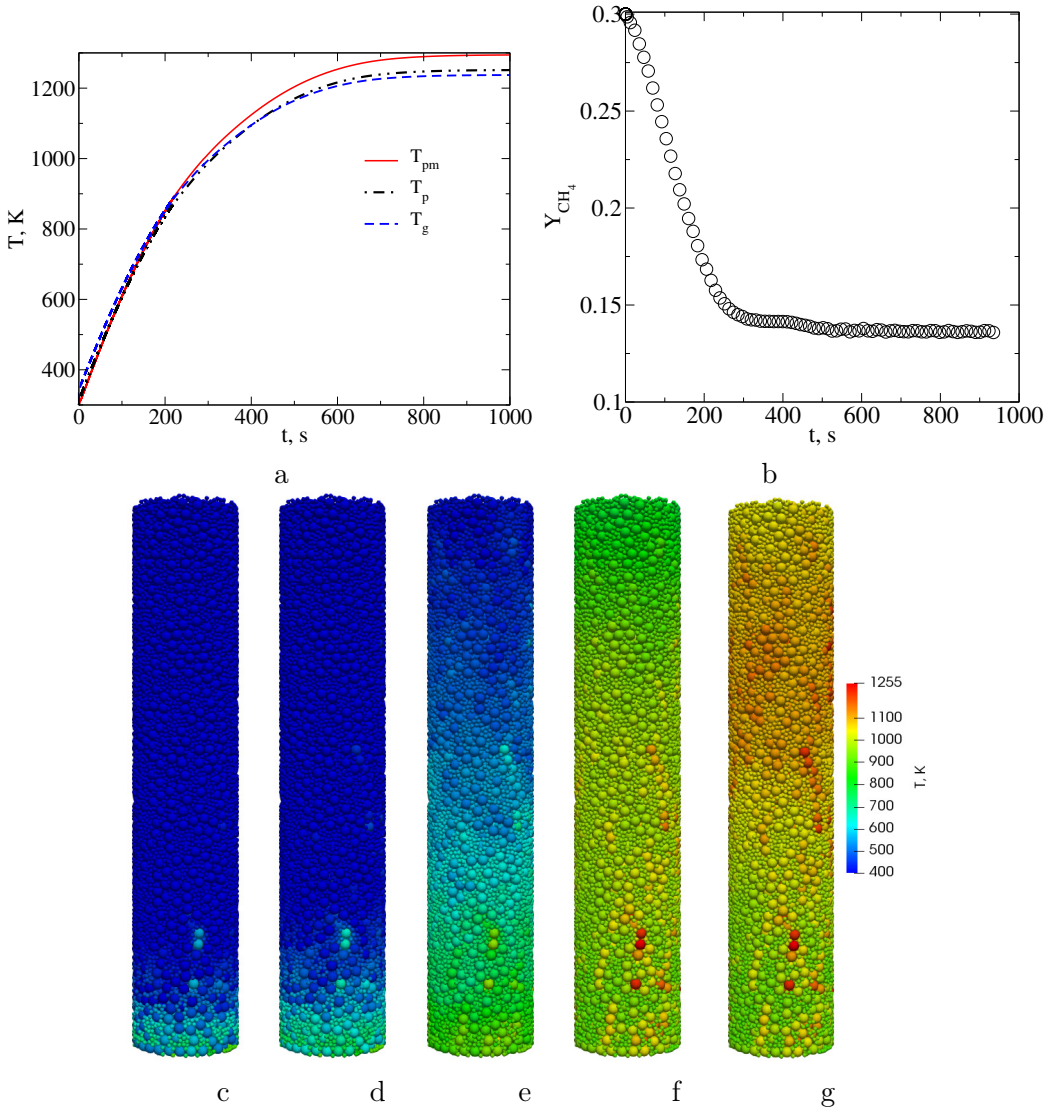

Figure 6.18: Time history of the control volume-averaged temperatures (a) and CH_4 mass fraction (b) in the gas phase. Snapshots of 3D distribution of the particles temperature T_{pm} and T_p predicted numerically using unsteady KM model at 10 s (c), 100 s (d), 300 s (e), 600 s (f), 1000 s (g).

filled with metal particles and catalyst particles with diameters of 5 mm and 2 mm, respectively. Parametric runs were carried out for different flow rates from 0.0025 kg/s to 0.01 kg/s with electrical power levels from 6.9 kW to 39 kW. Analysis of the results showed that equilibrium-based models predicts the species mass fractions at the outlet of the reactor well, but underestimates outlet gas temperature in comparison to the kinetic model (KM). When the input electrical power is increased, the difference between catalyst particle temperature and gas temperature decreases. The increase in $\dot{m}$ by keeping constant input electrical power leads to the decrease in the conversion of CH_4 proportionally to $\dot{m}^{-1/2}$. Finally, it was shown that a linear increase in the flow rate and input power leads to a decrease in methane conversion. The highest conversion rate for the geometry under investigation was achieved for the flow rate of 0.0025 kg/s and an input power of 9.6 kW.

6.8 Acknowledgment

The authors tank the Natural Sciences and Engineering Research Council (NSERC) Canada for the financial support under the Discovery Grant *Energy to Chemicals (E2C) using direct electrical current flowing through dense beds.*

Bibliography

[1] M. Aneke and M. Wang. Energy storage technologies and real life applications – a state of the art review. *Applied Energy*, 179:350–377, 2016.

[2] Q. Zhang, M. Nakaya, T. Ootani, H. Takahashi, M. Sakurai, and H. Kameyama. Simulation and experimental analysis on the development of a co-axial cylindrical methane steam reformer using an electrically heated alumite catalyst. *International Journal of Hydrogen Energy*, 32: 3870 – 3879, 2007.

[3] R. Labrecque and J.M. Lavoie. Dry reforming of methane with CO2 on an electron-activated iron catalytic bed. *Bioresource Technology*, 102:11244–11248, 2011.

[4] S.T. Wismann, J.S. Engbak, A.B.Vendelbo, F.B. Bendixen, W.L. Eriksen, K. Aasberg-Petersen, C. Frandsen, I. Chorkendorf, and P.M. Mortensen. Electreified methane reforming: A compact approach to greener industrial hydorgen production. *Science*, 364:756–759, 2019.

[5] M. Banville, R. Labrecque, and M.J. Lavoie. Dry reforming of methane under an electro-catalytic bed: Effect of electrical current and catalyst composition. *Energy and Sustainability V*, 186:603–611, 2014.

[6] K. Yamada, S. Ogo, R. Yamano, T. Higo, and Y. Sekine. Low-temperature conversion of carbon dioxide to methane in an electric field. *Chem Lett*, 49:303–306, 2020.

[7] E.J. Sheu, E.M.A. Mokheimer, and A.F. Ghoniem. A review of solar methane reforming systems. *Int. J. Hydrogen Energy*, 40:12929–12955, 2015.

[8] M. Rieks, R. Bellinghausen, N. Kockmann, and L. Mleczko. Experimental study of methane dry reforming in an electrically heated reactor. *Int. J. Hydrogen Energy*, 40:15940–15951, 2015.

[9] B.R. De Vasconcelos and J.M. Lavoie. Is dry reforming the solution to reduce natural gas carbon foorptint? *Int. J. Energy Prod. Mgmt*, 3:44–56, 2018.

[10] K. Oshima, T. Shinagawa, M. Haraguchi, and Y. Sekine. Low temperature hydrogen production by catalytic steam reforming of methane in an electric field. *Int J. Hydrogen Energy*, 38:3003–3011, 2013.

[11] F. Che, J.T. Gray, S. Ha, and J.S. McEwen. Reducing reaction temperature, steam requirements, and coke formation during methane steam reforming using electric fields: A microkinetic modeling and experimental study. *ACS Catal*, 7:6957–6968, 2017.

[12] Y.R. Lu and P.A. Nikrityuk. A new fixed bed reactor for electrical energy storage into chemicals: Proof of concept. *Applied Energy*, 228:593–607, 2018.

[13] D. Pashchenko. Effect of the geometric dimensionality of computational domain on the results of CFD-modeling of steam methane reforming. *International Journal of Hydrogen Energy*, 43 (18):8662–8673, 2018.

[14] N.G. Deen, E.A.J.F. Peters, J.T. Padding, and J.A.M.Kuipers. Review of direct numerical simulation of fluid-particle mass, momentum and heat transfer in dense gas-solid flows. *Chem. Eng. Sci.*, 116:710–724, 2014.

[15] V. Chandra, E.A.J.F. Peters, and J.A.M. Kuipers. Direct numerical simulation of a non-isothermal non-adiabatic packed bed reactor. *Chem. Eng. Journal*, 385:123641, 2020.

[16] A.G. Dixon. Local transport and reaction rates in a fixed bed reactor tube: Endothermic steam methane reforming. *Chemical Engineering Science*, 168:156–177, 2017.

[17] Z. Peng, E. Doroodchi, and B. Moghtaderi. Heat transfer modelling in Discrete Element Method (DEM)-based simulations of thermal processes: Theory and model development. *Progress in Energy and Combustion Science*, 79:100847, 2020.

[18] S. Golshan, R. Sotudeh-Gharebagh, R. Zarghami, N. Mostoufi, B. Blais, and J.A.M. Kuipers. Review and implementation of CFD-DEM applied to chemical process systems. *Chemical Engineering Science*, 221:115646, 2020.

[19] Y.R. Lu and P.A. Nikrityuk. DEM-based model for a steam methane reforming. *Chemical Engineering Science*, 247:116903, 2022.

[20] Y.R. Lu, D. Pashchenko, and P.A. Nikrityuk. A new semiempirical model for the heat and mass transfer inside a spherical catalyst in a stream of hot CH_4/H_2O gases. *Chemical Engineering Science*, 238:116565, 2021.

[21] M. Nijemeisland, A.G. Dixon, and E. Stitt. Catalyst design by CFD for heat transfer and reaction in steam reforming. *Chemical Engineering Science*, 59:5185–5191, 2004.

[22] Y.R. Lu, D. Pudasainee, Md. Khan, R. Gupta, and P.A. Nikrityuk. Experimental and numerical study of volt-ampere characteristics of a packed tube heated by joule heating. *Journal of Energy Resources Technology*, online, 2021.

[23] J. Kozicki and F. Donzé. Yade-open DEM: an open-source software using a discrete element method to simulate granular material. *Engineering Computations*, 26(7):786–805, 2009.

[24] Yade - Open source software for DEM. https://yade-dem.org/doc/, 2009.

[25] S. Ergun. Fluid flow through packed columns. *Chem. Eng. Prog.*, 48:89–94, 1952.

[26] P.N. Dwivedi and S.N. Upadhyay. Particle-fluid mass transfer in fixed and fluidized beds. *Ind. Eng. Chem., Process Des. Dev.*, 16:157–165, 1977.

[27] K. Hou and R. Hughes. The kinetics of methane steam reforming over a Ni/α-Al_2O catalyst. *Chem. Eng. J.*, 82:311–328, 2001.

[28] D. J. Gunn. Transfer of heat or mass to particles in fixed and fluidized beds. *International Journal of Heat and Mass Transfer*, 21(467-476), 1978.

[29] M.W. Baltussen, K.A. Buist, E.A.J.F. Peters, and J.A.M. Kuipers. Multiscale modelling of dense gas-particle flows. *Advances in Chemical Engineering*, 53:1–52, 2018.

[30] S. Schulze, M. Kestel, D. Safronov, and P. Nikrityuk. From detailed description of chemical reacting coal particles to subgrid models for CFD: model development and validation. *Oil & Gas Science and Technology*, 68:1007–1026, 2013.

[31] S. Schulze, A. Richter, M. Vascellari, A. Gupta, B. Meyer, and P. Nikrityuk. Novel intrinsic-based submodel for char particle gasification in entrained-flow gasifiers: Model development, validation and illustration. *Applied Energy*, 164:805–814, 2016.

[32] R. Schmidt, K. Wittig, and P. Nikrityuk. Single particle heating and drying. In P. Nikrityuk and B. Meyer, editors, *Gasification Processes: Modeling and Simulation*, pages 105–142. Willey-VCH Verlag GmbH & Co, Weinheim, Germany, 2014.

[33] National Institute of Standarts and Technology, Chemistry WebBook, USA. https://webbook.nist.gov/chemistry, 2018.

[34] G.K. Batchelor and R.W. Brien. Thermal or electrical conduction through a granular material. *Pro. Roy. Soc. Lond. A Math. Phys. Sci.*, 355:313–333, 1977.

[35] E. Dintwa, E. Tijskens, and H. Ramon. On the accuracy of the hertz model to describe the normal contact of soft elastic spheres. *Granular Matter*, 10:209–221, 2008.

[36] N. Govender, P.W. Cleary, M. Kiani-Oshtorjani, D.N. Wilke, C.Y. Wu, and H. Kureck. The effect of particle shape on the packed bed effective thermal conductivity based on DEM with polyhedral particles on the GPU. *Chemical Engineering Science*, 219:115584, 2020.

[37] B.V.R. Kuncharam and A.G. Dixon. Multi-scale two-dimensional packed bed reactor model for industrial steam methane reforming. *Fuel Processing Technology*, 200:106314, 2020.

[38] A. Iulianelli, C. Pirola, A. Comazzi, F. Galli, F. Manenti, and A. Basile. 1 - water gas shift membrane reactors. In Angelo Basile, Luisa Di Paola, Faisal l. Hai, and Vincenzo Piemonte, editors, *Membrane Reactors for Energy Applications and Basic Chemical Production*, Woodhead Publishing Series in Energy, pages 3–29. Woodhead Publishing, 2015.

[39] Y.R. Lu and P.A. Nikrityuk. Scale-up studies on electrically driven steam methane reforming. *Fuel*, page submitted, 2021.

Chapter 7

Scale-up Studies on Electrically Driven Steam Methane Reforming[1]

Abstract

This work is devoted to scale-up parametric studies of a new reactor for the steam reforming of methane driven by electrical current. The main distinguishing feature of this type of reactor is the use of direct electrical current flowing through metal particles to heat the whole reactor volume using Joule heating. The heat and mass transfer model uses six gaseous chemical species (CH_4, CO_2, CO, H_2O, H_2, N_2) in the gas phase inside the catalyst. Reaction rate expressions are taken from the literature (Langmuir-Hinshelwood-Hougen-Watson (LHHW) kinetics). The distinguishing feature of the model is its ability to calculate the 3D distribution of the electric field inside the bed and account for the intraparticle heat and mass transfer for each individual particle, coupled with the heat and mass transfer between the particles and the bulk flow. In this work we consider a cylindrical electrically insulated tube with a diameter of 0.5 m and a height of 0.88 m, which is filled with metal particles and catalyst particles with diameters of 10 mm and 4 mm, respectively. Parametric runs have been carried out for different flow rates from 0.04 kg/s to 0.1 kg/s and electrical power from 185 kW to 462 kW. The results are discussed.

[1]This chapter is based on the work: *Scale-up studies on electrically driven steam methane reforming.* FUEL. Vol. 319, pp. 117446, 2022. DOI: 10.1016/j.fuel.2022.123596

Nomenclature

A_p	surface area of the catalyst particle
A_{pm}	surface area of the metal particle
A_c	cross section area of the tube
c_p	constant-pressure heat capacity
D	internal diameter of the reactor
D_{eff}	effective diffusivity
d_{mean}	mean particle diameter
d_p	diameter of the catalyst particle
d_{pm}	diameter of the metal particle
k	thermal conductivity
h	thermal convection coefficient
ΔH_r	the enthalpy of r reaction
h_{pg}	thermal convection coefficient between the catalyst-particle and gas phase
h_{pmg}	thermal convection coefficient between the metal particle and gas phase
$(hA)_{in}$	heat transfer coefficient inside the catalyst particle
$(hA)_{inm}$	heat transfer coefficient inside the metal particle
$(\beta A)_{in}$	mass transfer coefficient inside the catalyst particle
I	electrical current
U	electrical field potential difference between anode and cathode
M	molar mass
$\dot{m}$	mass flow rate
N	number of reactions
N_p	number of catalyst particles in a control volume
N_{pm}	number of metal particles in a control volume
r_c	contact area between particles
Q_e	Joule heating source term inside each metal particle
Q_{IU}	input electrical power for the reactor
$R_{r,s}$	reaction rate on particles surface
$R_{r,V}$	intrinsic reaction rate for the catalyst-particle
R_g	the universal gas constant
R_{th}	thermal resistance between particles
R_σ	electrical resistance between particles
T_g	temperature of the gas phase
T_{sm}	surface-averaged temperature of the metal particle
T_{pm}	volume-averaged temperature of the metal particle

T_s	surface-averaged temperature of the catalyst particle
T_p	volume-averaged temperature of the catalyst particle
V	volume
Y_i	mass fraction of species i
$Y_{i,g}$	mass fraction of i species in the gas phase
$Y_{i,s}$	surface-averaged mass fraction of i species on the catalyst-particle surface
$Y_{i,p}$	particle-averaged mass fraction of i species in the catalyst particle
$Y_{i,sm}$	surface-averaged mass fraction of i species on the metal particle surface
z	axial coordinate
Δz or dz	size of a control volume

Greek letters

α	stoichiometric coefficient
β	mass transfer coefficient
ϵ_p	catalyst particle emissivity
ϵ_{pm}	metal particle emissivity
ε	void fraction
ρ	density
σ	Stefan-Boltzmann constant
σ_{pm}	electrical conductivity of metal particles
τ	catalyst particle tortuosity
ξ	non-dimensional variable

Subscripts

$aver$	averaged
s	catalyst particle surface
p	catalyst particle
pm	metal particle
sm	metal particle surface
g	gas
w	wall
nb	adjacent particle
i	species i
V	volumetric
pg	particle-gas
inl	inlet
out	outlet
in	catalyst particle internal
inm	inside metal particle internal

7.1 Introduction

Classical steam methane reforming reactors, where the endothermic reactions are driven by the heat supplied by methane combustion, are most widely used in industry to produce H_2 [1]. With the new climate protection restrictions, reducing CO_2 emissions and using sustainable energy sources in industry has become the main goal of many research works. In this view, the use of electrical current obtained from renewable energy in chemical processes, combined with energy storage, has recently received considerable attention in scientific literature [2]. One of the options to store electricity from renewable sources is the direct conversion of electrical current into chemical energy [2]. One way to store electrical energy in chemicals (E2C) is to use so-called electrically driven steam methane reforming (SMR) and/or the dry reforming of methane (DRM) [3], or electrically driven methane decomposition. Compared to electrolysis, the electrified reforming gets the majority of the energy from traditional fuel, providing a way to transition from fuel before renewable energy becomes vastly abundant. A detailed review of different electrically driven SMR/DRM reactor concepts can be found in the work [4]. An analysis of works devoted to electrically driven SMR and DRM shows that most use experimental studies to investigate the characteristics of endothermic lab-scale reactors heated by direct electrical current (DC), where electrical current simultaneously plays the role of the heat source and the catalyst [5, 6].

Recently, Che and co-workers [7] reported on theoretical and experimental studies on the use of Ni foam as a heater (through electrical current) and catalyst for SMR. The authors showed that a positive electric field enhances the methane conversion in comparison to the case with no electric field. Additionally, it was demonstrated experimentally that a positive electric field reduces the formation of coke.

One of the problems in modeling electrically driven reforming is that the kinetics of endothermic reactions supported by the electrical current are unknown. An alternative to electro-catalysts [5, 7] is the use of electrically heated surfaces covered with a catalyst which does not conduct electrical current itself. For example, Zhang et al. [3] reported on experimental and numerical studies on a co-axial cylindrical four-layer catalyst bed methane steam reformer where the catalyst layers were heated electrically with electrically conducting plates. Another example of an electrically heated catalyst being used for SMR is the work by Wismann and co-workers [8]. The authors used an electrically heated tube coated by a catalyst to drive SMR. It was shown that close contact between the Joule heat source and the reaction site drives the reaction close to thermal equilibrium and makes the reactor smaller in comparison to a standard approach.

Recently, Lu and Nikrityuk [9] presented a new numerical model for the hybrid electro-reforming reactor introduced in the work [10]. In this type of reformer, standard catalyst particles (Ni/α-Al_2O) packed randomly with nickel or metal balls in a cylindrical tube are used to speed up endothermic reactions. When a direct current (DC) current is supplied through metal particles, they serve as

local heaters and at the same time as a non-porous catalyst in addition to the porous catalyst Ni/α-Al_2O packed randomly between the Ni particles. Such arrangements of electrically conducting particles and catalyst particles make the reformer compact and prevent temperature drops in the center of the tube in comparison to standard reformers. The model presented in the work [9] has been validated against experimental data [11] and numerical simulations for a standard SMR tube [12]. One of the challenge in scale-up simulations is the fact that increasing the reactor and particles size leads to a change in the heat and mass transfer between particles due to the increased contact area. Thus, the volt-ampere characteristic of larger beds are also changed.

Keeping in mind classical steam methane reforming driven by the heat supplied from the combustion of methane, it should be noted that there are few modeling works devoted to predicting the heat and mass transfer inside industrial-scale tubes packed with catalysts. For example, [13] presented 3D CFD-based model of the transport and reaction phenomena inside an industrial-scale steam methane reformer comprising 336 reforming reactors, 96 burners and 8 flue gas tunnels. ANSYS-Fluent software was used, where the Langmuir-Hinshelwood kinetic mechanism was implemented using user-defined functions (UDF).

Bhanu Vardhan Reddy Kuncharam and Dixon [14] developed a multi-scale non-isothermal heterogeneous steady-state model for steam methane reforming in a packed bed tube. The model is based on two-dimensional transport equations describing the heat and mass transfer in the gas phase, directly coupled with the chemical reactions (including the heat and mass transfer) inside the catalyst particle. The results of a sensitivity analysis studying different closure relations (empirical equations) were discussed. The simulations were conducted on a 10 m long packed tube with a total heat rate to the wall of about 400 kW.

Wang and co. [15] carried out comprehensive transient CFD-based studies (using ANSYS-Fluent) on the transport phenomena in a single reforming tube (12.5 m long and internal diameter of 12.6 cm) in an industrial-scale methane steam reforming reactor. The authors showed numerically that near the tube wall, which heats the catalyst particles, the heat transfer resistance is significant. This effect leads to the large radial gradient of CH_4 conversion, with the maximum is located near the wall. A sensitivity analysis showed that the inlet mass flow rate is the governing parameter in comparison to the inlet fluid temperature, the inlet steam-to-carbon (S/C) ratio.

In spite of recent progress in the modeling of industrial-scale reformers, as highlighted above, no numerical works on the scale-up of electrically driven reformers have been published yet, to the best of our knowledge. Motivated by this fact, this work is devoted to scale-up investigation of the new type of reactor. In reactors of a larger size, the gas flow rate and input power are main parameters that we investigate in this work in order to illustrate industrial-scale usage of this type of reformer. The main difference between this work and work [9] is significant increase in the size of packed tube, the input power and the flow rate for the reactor. A scaled-up reactor consisting of 1 million particles is simulated in a cylinder that is 0.9 m tall and 0.5 m in diameter. Inlet gas passes through the fixed

bed, injected from the top at 1000K. The composition of the gas is 0.3 CH_4 by mass, 0.6 H_2O, and 0.1 inert gas. The parametric study includes altering the flow rate and power both simultaneously and independently to compare the conversion, maximum temperature, temperature distribution and axial profiles. In addition to the flow rate and power, the flow direction and the height-diameter aspect ratio are also investigated.

7.2 Problem and Model Formulation

A new reactor consists of two different kinds of spherical particles: electrically conductive particles made of a metal and electrically non-conductive catalyst particles (any standard catalyst can be used). Between the top and bottom of the reactor, a DC is applied. The metal particles are heated by Joule heating due to the electrical current passing through them. Fig. 7.1 shows a schematic of the proposed reformer adapted from the work [9]. The inlet was moved from the bottom to the top where the most of heating was found to happen.

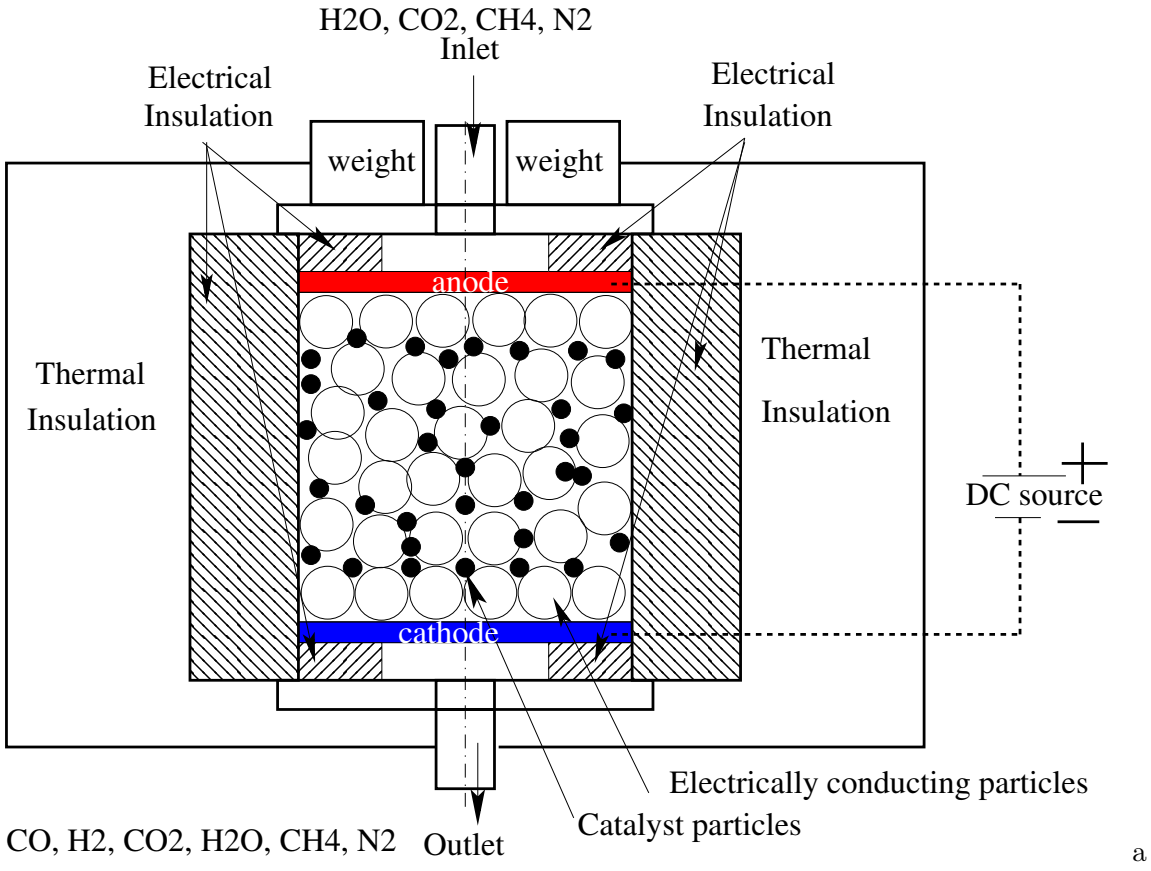

a

Figure 7.1: Schematic diagram of the reformer adapted from [9].

A random packed bed consists of $N_p = 1020912$ spherical metal and catalyst particles packed

randomly in a thermally and electrically insulated tube with a height of $H = 0.88$ m and diameter of $D = 0.5$ m. The diameters of the metal particles and catalyst particles are $d_{pm} = 10$ mm and $d_p = 4$ mm, respectively. This optimal value is determined by finding the maximum possible number of electrically non-conducting particles mixed randomly among metal particles that allow electrical current to flow through the bed without hot spots; for the detailed methodology see the work [9]. The gas flow rate ranges from $\dot{m} = 0.04$ kg/s to $\dot{m} = 0.1$kg/s. The inflow gas conditions are shown in Table 7.1. Due to the thermally insulated side wall of the tube, the total electrical power, Q_{IU}, needed to heat the bed can be estimated using the following balance equation:

$$\underbrace{I \cdot U}_{Q_{IU}} = \dot{m} c_p (T_{g,out} - T_{g,in}) + \dot{m} \Delta H_{aver} \tag{7.1}$$

where I is the electrical current and U is the electrical field potential difference between the anode and cathode. ΔH_{aver} is the averaged enthalpy of chemical reactions. If $T_{g,out} = T_{g,in}$, Eq. (7.1) can be simplified as follows: $Q_{IU} = \dot{m} \Delta H_{aver}$. To estimate Q_{IU} for a given $\dot{m}$ we assume that $\Delta H_{aver} = |\Delta H_1|$.

The chemical reactions between methane and steam are described by the following semi-global reactions [16]:

$$\mathrm{CH_4 + H_2O \Leftrightarrow CO + 3H_2} \tag{7.2}$$

$$\mathrm{CO + H_2O \Leftrightarrow CO_2 + H_2} \tag{7.3}$$

$$\mathrm{CH_4 + 2H_2O \Leftrightarrow CO_2 + 4H_2} \tag{7.4}$$

The enthalpy for reactions in Eq. (7.2), Eq. (7.3) and Eq. (7.4) are $-\Delta H_1 = -206.1$ kJ/mol, $-\Delta H_2 = 41.2$ kJ/mol and $-\Delta H_3 = -165.0$ kJ/mol, respectively according to the work [17].

Finally, the composition of the fixed bed is simulated utilizing the gravity-driven settling of 1.3 million spherical particles in a tube. The transport properties of the particles are given in Table 7.2. Catalyst particles comprise 24.3 vol.% of all the particles. To guarantee that there was sufficient contact between electrically conducting particles, an additional mass of 10 kg on the top was used; for details see[11]. The coordinates of the particles are calculated using the open-source DEM software YADE [18, 19], which uses the soft-sphere collision model.

7.2.1 Mathematical Model

In this work, we adopt a particle-unresolved DEM-based heat and mass transfer model from the work [9], with the temperature of the gas phase and chemical species in the gas phase being calculated using 1D for of the heat transfer and species balance equations written for the gas phase in Eulerian space, and the temperature of each particle and species inside each catalyst being calculated utilizing balance equations in 3D Lagrangian space. In order to illustrate basic equation, we introduce a

CH_4	0.3
H_2O	0.6
H_2	0
CO	0
CO_2	0
N_2	0.1
T_i	1000K
P	1 atm

Table 7.1: Inlet composition

Number of metal particles	N_{pm}		$1.7 \cdot 10^5$
Number of catalyst particles	N_p		$8.3 \cdot 10^5$
Metal particle diameter	d_{pm}	m	0.01
Catalyst particle diameter	d_p	m	0.04
Tube diameter	D	m	0.5
Tube length	H	m	0.85
Young's modulus	E	GPA	207
Thermal conductivity of metal particles	k_m	W/mK	60.7
Thermal conductivity of catalyst particles	k_p	W/mK	1.0
Electrical conductivity of metal particles	σ_e	S/m	1.44×10^7
Density of metal particles	ρ_{pm}	kg/m^3	8.9×10^3
Density of catalyst particles	ρ_p	kg/m^3	1.9×10^3
Poisson's Ratio	ν		0.31
Particle emissivity	ϵ_p,ϵ_{pm}		0.8
Packed bed void fraction	ε		0.3025

Table 7.2: Dimensions of the base case reactor and material properties [20, 21, 17].

system of equations solved for the steady state. Using similar assumptions as in the work [12], the final governing equations take the following form:

- Mass conservation equation:

$$\frac{d}{dz}\left(\varepsilon \rho_g u_z\right) = 0; \qquad \rho_g = \frac{P}{R_g T_g} \tag{7.5}$$

The Ergun equation [22] is used to calculate the change in P:

$$\frac{\Delta P}{H} = \frac{150\mu_g}{d_{mean}^2}\frac{(1-\varepsilon)^2}{\varepsilon^3}v + \frac{1.75\rho_g}{d_{mean}}\frac{(1-\varepsilon)}{\varepsilon^3}v^2 \tag{7.6}$$

where v is the superficial gas velocity, expressed as $v = \frac{\dot{m}}{\rho_g \pi (0.5D)^2}$

Flowrate	$\dot{m}$	kg/s	0.1	0.08	0.05	0.04
Reynolds number	Re_D		1193	955	597	477
Heating power	Q_{IU}	kW	462kW	370kW	231kW	185kW
Conversion at outlet	X_{conv}		96.7%	98.3%	99.5%	99.7%
Maximum T	T_{max}	K	1884	1640	1378	1328
Outlet T	T_o	K	1280	1285	1290	1294

Table 7.3: Flow rates and proportional power used in the parametric study of 1 million particles. Here $Re_D = \frac{\rho_g U_{in} D_{pm}}{\mu_g}$.

Flow rate	$\dot{m}$	kg/s	0.1	0.1
Heating power	Q_e	kW	462kW	308kW
Conversion	X_{conv}		96.7%	78.0%
Maximum T	T_{max}	K	1884	1591
Outlet T	T_o	K	1280	1068

Table 7.4: Parametric study of 1 million particles with identical flow rate and different powers

The mean particle diameter, d_{mean}, is calculated as follows [23]:

$$d_{mean} = \sqrt{\frac{1}{N_{pp}} \sum_{i=1}^{N_{pp}} d_{pi}^2} \tag{7.7}$$

where d_{pi} is the diameter of particle i inside a control volume and N_{pp} is the number of all sorts of particles inside a control volume $A_c \Delta z$. The use of 7.7 is attributed to the multi-dispersity of the fixed bed.

- The energy conservation equation for the gas phase is formulated for a control volume of $A_c \Delta z$:

$$\dot{m} c_{pg} \Delta z \frac{\partial T_g}{\partial z} = \varepsilon A_c \Delta z \frac{\partial}{\partial z} \left(k_g \frac{\partial T_g}{\partial z} \right) + \sum_{j=1}^{N_p} \left(h_{pg} A_p \left(T_{s,j} - T_g \right) \right) + \tag{7.8}$$

$$+ \sum_{j=1}^{N_p} \left(\epsilon_p \sigma A_p \left(T_{s,j}^4 - {T_g}^4 \right) \right) + \underbrace{\sum_{j=1}^{N_{pm}} \left(h_{pg} A_{pm} \left(T_{sm,j} - T_g \right) \right) + \sum_{j=1}^{N_{pm}} \left(\epsilon_{pm} \sigma A_{pm} \left(T_{sm,j}^4 - {T_g}^4 \right) \right)}_{Metal\ particles}$$

where $A_c = \pi \frac{D^2}{4}$, N_p is the number of particles inside the control volume $A_c \Delta z$ and D is the tube diameter. N_{pm} is the number of metal particles in the control volume and N_p is the number of catalyst particles in the control volume.

- The energy conservation equation for the catalyst surface [12] is

$$(hA)_{in}(T_s - T_p) = h_{pg} \cdot A_p(T_g - T_s) + +\epsilon_p \sigma A_p \left(T_g^4 - {T_s}^4\right) \tag{7.9}$$

where T_s and T_p represent the catalyst surface temperature and particle-averaged temperature, respectively.

- The energy conservation equation for the catalyst-particle is:

$$\underbrace{(hA)_{in}(T_s - T_p)}_{internal\ conduction} + \underbrace{V_p \sum_r^{N_r} \left((-\Delta H_r)\, R_{r,V}\right)}_{reactions} + \underbrace{\sum_{j=1}^{N_{nb}} \left(\frac{T_{p,j} - T_p}{R_{th}}\right)}_{catalyst-catalyst\ conduction} + \underbrace{\sum_{i=1}^{N_{nbm}} \left(\frac{T_{pm,i} - T_p}{R_{th,pm}}\right)}_{catalyst-metal\ conduction} = 0 \tag{7.10}$$

where N_{nb} is the number of catalyst neighbors for each catalyst particle and N_{nbm} is the number of metal particles neighbors for each catalyst particle, R_{th} and $R_{th,pm}$ represents the thermal resistance for the catalyst-catalyst particle and catalyst-metal particle contact, respectively.

- The energy conservation equation for the metal particle is:

$$\underbrace{(hA)_{inm}(T_{sm} - T_{pm})}_{internal\ conduction} + Q_e - \underbrace{\sum_{j=1}^{N_{nb}} \left(\frac{T_{p,j} + T_{pm}}{R_{th,pm}}\right)}_{metal-catalyst\ conduction} + \underbrace{\sum_{i=1}^{N_{nbm}} \left(\frac{T_{pm,i} - T_{pm}}{R_{th,mm}}\right)}_{metal-metal\ conduction} = 0 \tag{7.11}$$

where Q_e is the Joule heating term and $R_{th,mm}$ is the thermal resistance of the contact point between metal particles.

- The energy conservation equation for the surface of the metal particle is:

$$\underbrace{(hA)_{inm}(T_{sm} - T_{pm})}_{internal\ conduction} = \underbrace{h_{pgm} \cdot A_{pm}(T_g - T_{sm})}_{convection-conduction} + \underbrace{A_{pm} \sum_r^{N_r} (-\Delta H_r)\, R_{r,s}}_{surface\ reactions} + \underbrace{\epsilon_{pm} \sigma A_{pm} \left(T_g^4 - T_{sm}^4\right)}_{radiation} \tag{7.12}$$

- The balance equation for i species CH_4, CO_2, CO, H_2O and H_2 in the gas [12] is:

$$\dot{m} \Delta z \frac{\partial Y_{i,g}}{\partial z} = \varepsilon \cdot \rho_g A_c \Delta z \frac{\partial}{\partial z}\left(D_{gas} \frac{\partial Y_{i,g}}{\partial z}\right) + \underbrace{\sum_{j=1}^{N_{nb}} \left[\beta_{pg} \cdot \rho_g A_p \left(Y_{i,s,j} - Y_{i,g}\right)\right]}_{catalyst\ particles} + \underbrace{\sum_{j=1}^{N_{nbm}} \left[\beta_{pg} \cdot \rho_g A_{pm} \left(Y_{i,sm,j} - Y_{i,g}\right)\right]}_{metal\ particles} \tag{7.13}$$

- The balance equation for i species CH_4, CO_2, CO, H_2O and H_2 on the surface of the catalyst particle [12] is:

$$\beta_{pg} A_p \rho_{g,s} (Y_{i,g} - Y_{i,s}) = (\beta A)_{in} \rho_{g,p} (Y_{i,s} - Y_{i,p}) \tag{7.14}$$

  Due to the fact that the ratio between the particle surface and the overall particle surface participating in the reactions is approximately $10^{-2}\%$ for d_p, we neglect chemical reactions on the catalyst particle surface in Eq. (7.14) and Eq. (7.9). The total surface area (BET, m^2/g) of the catalyst is 14.3 m^2/g based on data provided in kinetics study [24].

- The balance equation for i species CH_4, CO_2, CO, H_2O and H_2 inside the catalyst particle:

$$\underbrace{(\beta A)_{in} \rho_{g,p} (Y_{i,s} - Y_{i,p})}_{internal\ diffusion} + \underbrace{M_i V_p \sum_r^{N_r} \alpha_{r,i} R_{r,V}}_{reactions} = 0 \tag{7.15}$$

  It should be noted that the diffusive mass transfer between connected catalyst particles was neglect.

- The balance equation for i species CH_4, CO_2, CO, H_2O and H_2 on the metal particle surface:

$$\beta_{pgm} A_{pm} \rho_{g,s} (Y_{i,g} - Y_{i,sm}) + M_i A_{pm} \sum_r^{N_r} \alpha_{r,i}\ R_{r,s} = 0 \tag{7.16}$$

  In this equation, we neglect the diffusive mass transfer between connected catalyst particles.

The chemical source terms in species balance equations take the following form:

$$CH_4 :\ \sum_r^{N_r} (\alpha_{r,i} R_{V,r}) = -\left(R_{V,1} + R_{V,3}\right) \tag{7.17}$$

$$H_2O :\ \sum_r^{N_r} (\alpha_{r,i} R_{V,r}) = -\left(R_{V,1} + R_{V,2} + 2R_{V,3}\right) \tag{7.18}$$

$$CO :\ \sum_r^{N_r} (\alpha_{r,i} R_{V,r}) = R_{V,1} - R_{V,2};\ CO_2 :\ \sum_r^{N_r} (\alpha_{r,i} R_{V,r}) = R_{V,2} + R_{V,3} \tag{7.19}$$

$$H_2 :\ \sum_r^{N_r} (\alpha_{r,i} R_{V,r}) = 3R_{V,1} + R_{V,2} + 4R_{V,3} \tag{7.20}$$

The enthalpies of reaction in Eq. (7.2), Eq. (7.3) and Eq. (7.4) are $-\Delta H_1 = -206.1$ kJ/mol, $-\Delta H_2 = 41.2$ kJ/mol and $-\Delta H_3 = -165.0$ kJ/mol, see the work [17]. The partial pressure relates

to mass fractions as follows:

$$p_i = \frac{Y_i P\, M}{M_i};\; M = \frac{1}{\sum_i^N \frac{Y_i}{M_i}} \tag{7.21}$$

The full setup of the equations including expressions for the LHHW kinetic [24] can be found in the work [9]. The code and models validation can be found in the works [12, 9, 11]. The partial pressure relates to mass fractions as follows:

$$p_i = \frac{Y_i P\, M}{M_i};\; M = \frac{1}{\sum_i^N \frac{Y_i}{M_i}} \tag{7.22}$$

7.2.2 Closure Relations

Mass transfer coefficients β_{pg} and β_{pmg}, and heat transfer coefficients between the catalyst particle and gas phase, and between the metal particle and gas, respectively, are calculated from the correlations:

$$Sh = \frac{\beta_{pg} \cdot 2r_p}{D_{gas}};\quad Sh = \frac{\beta_{pmg} \cdot 2r_{pm}}{D_{gas}} \tag{7.23}$$

$$Nu = \frac{h_{pg} \cdot 2r_p}{k_g};\quad Nu = \frac{h_{pgm} \cdot 2r_{pm}}{k_g} \tag{7.24}$$

The nondimensional numbers Sh and Nu are calculated using the Gunn relation [25]:

$$Nu = (7 - 10\varepsilon + 5\varepsilon^2)(1 + 0.7Re_i^{0.2}Pr^{0.33}) + (1.33 - 2.4\varepsilon + 1.2\varepsilon^2)Re_i^{0.7}Pr^{0.33} \tag{7.25}$$

$$Sh = (7 - 10\varepsilon + 5\varepsilon^2)(1 + 0.7Re_i^{0.2}Sc^{0.33}) + (1.33 - 2.4\varepsilon + 1.2\varepsilon^2)Re_i^{0.7}Sc^{0.33} \tag{7.26}$$

It should be noted that the Gunn relation was used here because it has been verified against 3D DNS [26] (for lower Re_p values). In this work, we assume that $Le = 1$ according to [27, 28], leading to the condition $Nu = Sh$. In Eq. (7.25), ε is the void fraction of the bed:

$$\varepsilon = \frac{\frac{16}{3}\sum_{i=1}^{N_p} \pi r_i^3}{\pi D^2 H} \tag{7.27}$$

where H is the height of the tube, $r_i = r_{p,i}, r_{pm,i}$.

The particle Reynolds number is calculated using

$$Re_i = \frac{\rho_g v \cdot 2r_i}{\mu_g} \tag{7.28}$$

where $r_i = r_p, r_{pm}$.

The diffusion and intra-particle mass transfer coefficients of the gas take the forms [29]:

$$Le = \frac{k_g}{D_{gas} c_p \rho_g} = 1; \;\; D_{gas} = \frac{k_g}{c_p \, \rho_g} \tag{7.29}$$

$$(\beta A)_{in} = 4\pi D_{\text{eff}} \left(\frac{1}{a_1 r_p} - \frac{1}{r_p} \right)^{-1} \tag{7.30}$$

$$(hA)_{in} = 4\pi k_p \left(\frac{1}{a_1 r_p} - \frac{1}{r_p} \right)^{-1}; \;\; (hA)_{inm} = 4\pi k_m \left(\frac{1}{a_1 r_{pm}} - \frac{1}{r_{pm}} \right)^{-1} \tag{7.31}$$

where $a_1 = 0.85$ [29], $(hA)_{in}$ is the intraparticle heat transfer coefficient for the catalyst particle and $(hA)_{inm}$ is the intraparticle heat transfer coefficient for the metal particle, $(\beta A)_{in}$ is the intraparticle mass transfer coefficient for the catalyst particle.

The effective diffusion inside the catalyst particle D_{eff} is calculated similarly to the work [12]. We used $r_{pore} = 10^{-7}$m, $\varepsilon_p = 0.44$ and $\tau_p = 3.54$ according to the works [24, 17].

The effective diffusion inside the porous particle D_{eff} is calculated based on the main mechanism of pore diffusion:

$$D_{\text{eff}} = \frac{\varepsilon_p}{\tau_p} D_{gas} \tag{7.32}$$

where $\varepsilon_p = 0.44$ is the catalyst particle porosity and $\tau_p = 3.54$ is the particle tortuosity [17].

The formulae for the heat rate and thermal resistance between particles due to their static contact can be found in the work [9].

7.2.3 Electric Field Model

To calculate the Joule heating for each metal particle, we have to predict the electric field distribution in the fixed bed. In this work we utilize the model developed and validated in the work[11]. In this work, we list only the basic equations used to calculate electric field distribution in bi-disperse packing, where small catalyst particles are not electrically conductive particles. The main distinguishing feature of that model is we treat each metal particle as a node characterized by the particle-averaged electric field potential ϕ_i when electrical current flows through the bed, and the contact between particles is treated as a resistor. The coordinates of the particles are calculated using the open-source DEM software YADE [18, 19].

Before we introduce the electromagnetic field equations, we assume that when electrical current flows through the bed, each metal particle is characterized by the particle-averaged electric field potential ϕ_i and the contact between particles is treated like a resistor. The equations finally used to calculate the electric field potential of each electrically conducting particle and the electric current

density between particles takes the following form[9]:

$$\sum_{j=1}^{N_{nb}} \vec{j}_{ij} = 0 \implies \sum_{j=1}^{N_{nb}} \sigma_{pm,i} \frac{\phi_i - \phi_j}{d_{ij}} = 0 \tag{7.33}$$

where N_{nb} is the number of metal particle in contact with the metal particle i that have a static contact with the particle i, ϕ_i represents the particle-averaged electric field potential and d_{ij} is the distance between centers of two metal particles that have a static contact.

For the conduction between two particles with static contact, Eq. 7.33 takes the form:

$$\sum_{j=1}^{N_{nb}} \frac{\phi_i - \phi_j}{R_{\sigma,ij}} = 0 \tag{7.34}$$

For a bed of N_{pm} particles, a system of N_{pm} equations needs to be solved. The ϕ of each particle is solved in an N_{pm} by N_{pm} matrix. It should be noted that to solve a system of linear equations, Eq. (7.34), we used a list of metal particles only, instead of utilizing all particles. This method allows the computational time to be significantly reduced.

To solve a system of linear equations, the following boundary conditions are used:

$$\phi_i = 0 \; for \; z = 0; \; and \;\; \phi_j = \phi_c \; for \; z = H \tag{7.35}$$

These conditions imply that the electric field potentials at the cathode and the anode are constant.

To establish a diagonally dominant sparse matrix, the particles are indexed based on the order of the axial position. The matrix is solved using the Gaussian elimination method. Finally, it should be emphasized that if a particle i only has contact with one neighboring particle, this particle does not conduct the current and its electrical potential is equal to the electric potential of its single touching particle.

Finally, after the electric field potential is known for each particle, the electric current is calculated at the cathode or anode, respectively using the formulae:

$$I_c = \pi \sum_{i=1}^{N_{pC}} r_{c,i}^2 \sigma_{pm,i} \frac{\phi_i - 0}{\Delta z} \tag{7.36}$$

where $\Delta z = 0.5 d_p$ and N_{pA} is the number of particles in contact with the cathode.

$$I_a = \pi \sum_{i=1}^{N_{pA}} r_{c,i}^2 \sigma_{pm,i} \frac{\phi_c - \phi_i}{\Delta z} \tag{7.37}$$

N_{pC} is the number of particles in contact with the anode. It should be noted that both values I_c

and I_a must be equal with a given numerical accuracy if the system of linear equations, Eq. (7.34), is solved correctly.

The electrical current between the two particles i and j, which have a stationary connection, is calculated as follows [11]:

$$I_{ij} = \frac{\phi_i - \phi_j}{R_{\sigma,ij}} \tag{7.38}$$

The Joule heating effect on particle i is described as the summation of Joule heating from all of its contact points.

$$Q_e = \frac{1}{2} \sum_{j=1}^{N_{nb}} \frac{(\phi_i - \phi_j)^2}{R_{\sigma,ij}} \tag{7.39}$$

The coefficient $\frac{1}{2}$ is explained by the fact that the Joule heat in the contact point goes into two particles. This relation was verified using energy conservation, as the summation of all Q_e must be equal to the overall Joule heat, $I \cdot U$.

The electrical resistance of the contact area takes the form [11]:

$$\frac{1}{R_{th}} = \frac{4r_c}{\frac{1}{k_{p,i}} + \frac{1}{k_{p,j}}}; \implies \frac{1}{R_{\sigma,ij}} = \frac{4r_c}{\frac{1}{\sigma_{pm,i}} + \frac{1}{\sigma_{pm,j}}} \tag{7.40}$$

where r_c is the contact radius, and $\sigma_{p,j}$ and $\sigma_{p,i}$ are the electrical conductivity of particles j and i, respectively. If $\sigma_{p,j} = \sigma_{p,i}$, the electrical resistance $R_{\sigma,ij}$ takes the form:

$$R_{\sigma,ij} = \frac{1}{2\, r_c\, \sigma_{pm}} \tag{7.41}$$

The contact radius r_c between two touching elastic particles i and j which are locally spherical with radii r_i and r_j can be calculated according to Hertz theory[30, 31]. Details on r_c calculation can be found in the work [11]. Finally, we offer a brief algorithm to calculate the electric field and Joule heat distribution for a given fixed bed:

- After fixed bed composition is calculated using DEM, solving force balance equations for each particle, we define the contact radius r_c for each contact point between particles. One particle can have one or several neighbors, resulting in several contact radii.
- Calculate the electrical resistance for each contact point using Eq. 7.40.
- Establish a system of linear equations given by Eq. 7.34, set up boundary values for ϕ on electrodes, Eq. (7.35), and solve the final matrix equation using Gauss elimination method. Check the condition $I_a = I_c$ using Eqs. (7.36) - (7.37).
- Calculate the Joule heating term for each particle, Q_e, using Eq. 7.39. This term can be used to calculate the heating of each electrically conducting particle.

7.2.4 Equilibrium Model

The main idea of the equilibrium-based model in this work is based on the condition that the gas composition inside the catalyst particle corresponds to equilibrium values depending on local temperatures [12]. The species concentrations on the catalyst particle surface and in the gas phase are calculated using balance equations. The heat transfer equations are the same as for the kinetic model, the exception being that the rates of reactions are defined using the rates of species mass transfer; for details see the work [12]. Instead of solving species conservation equations for CH_4, CO_2, CO, H_2O and H_2 inside the catalyst particle, we calculate $Y_{i,p}$ using equilibrium values employing T_p and pressure values:

$$Y_{i,p} = f(T_p, P, Y_{g,i}) \tag{7.42}$$

Eq. 7.16 is used to calculate the species conservation equation for species CH_4, CO_2, CO, H_2O and H_2 on the surface of the metal particle.

Our system has 5 species and 3 atom to be balanced. Eq. (7.2) and Eq. (7.3) are the two independent chemical reactions that are used to find the chemical composition inside the catalyst particle. Eq. (7.15) can be used to derive the source term in mass transfer equations:

$$M_i V_p \sum_{r}^{N_r} \alpha_{r,i} R_{r,V} = -(\beta A)_{in} \rho_{g,p} (Y_{i,s} - Y_{i,p}) \tag{7.43}$$

The reaction rate can be expressed as the rate of mass transfer for CH_4 and CO_2 as follows:

$$-M_{CH_4} V_p R_{1,V} = -(\beta A)_{in} \rho_{g,p} (Y_{CH_4,s} - Y_{CH_4,p}) = -\beta_{pg} \rho_g A_p (Y_{\mathrm{CH_4,g}} - Y_{\mathrm{CH_4,s}}) \tag{7.44}$$

$$M_{CO_2} V_p R_{2,V} = -(\beta A)_{in} \rho_{g,p} (Y_{CO_2,s} - Y_{CO_2,p}) = -\beta_{pg} \rho_g A_p (Y_{\mathrm{CO_2,g}} - Y_{\mathrm{CO_2,s}}) \tag{7.45}$$

Finally, the chemical source term in Eq. (7.10) takes the form:

$$\begin{aligned} V_p \sum_{r}^{N_r} (-\Delta H_r) R_{r,V} = \frac{(-\Delta H_1)}{M_{CH_4}} (\beta A)_{in} \rho_{g,p} (Y_{CH_4,s} - Y_{CH_4,p}) - \\ - \frac{(-\Delta H_2)}{M_{CO_2}} (\beta A)_{in} \rho_{g,p} (Y_{CO_2,s} - Y_{CO_2,p}) \end{aligned} \tag{7.46}$$

The equilibrium constants were approximated based on Gibbs free energy from 1000K to 1100K, taken from NIST WebBook [32]. The details on the calculation of Eq. (7.42) can be found in the work [12].

It should be noted that the equilibrium-based model can be used in diffusion-limited regimes since the rate of reaction is determined by the mass transfer between the bulk flow and particles.

Combined with the heat balance equation, the gas composition inside the particle is solved using equilibrium conditions. The main advantage of this class of models is that the kinetics of SMR need not be known and subsequently of the calculations are significantly faster due to the absence of exponential source terms in the species balance equations.

7.3 Results and Discussion

7.3.1 Analysis of Flow Rate and Input Power

Before we proceed with the analysis of the transport phenomena inside the electrically heated SMR packed tube, we present the results of the parametric study on the influence of flow rates and input power on the maximum temperature of particles and methane conversion. To investigate the influence of flow rates and power, 4 cases with flow rates ranging from 0.04 kg/s to 0.1 kg/s are computed with a total heating power proportionate to the flow rate according to Eq. 7.1. The heating power is equal to the mass flow rate of CH_4 in the inlet multiplied by the heat of Reaction 7.2, based on complete conversion. Because of the limited number of reaction sites in the reactor, as the flow rate increases, the conversion decreases as a result, along with a rise in the outlet temperature. Since the power of heating particles in the fixed bed is also amplified as the flow rate increases, heat transfer limitation also becomes a significant factor, as extreme temperatures will cause the particles to melt and the reactors to fail. In Table 7.3, the results of the parametric study are shown with maximum temperature, outlet temperature and conversion. Fig. 7.2 shows the maximum temperature of metal particles and methane conversion change with respect to the total power and flow rate. It can be seen that the increase in the input electrical power leads to the increase in $T_{p,max}$. However, the increase in Q_{IU} and corresponding increase in $\dot{m}$ causes the decrease in methane conversion.

7.3.2 3D Distributions

To make sense of the results of the temperature and species distribution, the distribution of the particle-averaged contact area along the bed height is presented. Fig. 7.3 shows the axial distribution of the particle-averaged contact area and control-volume-averaged particle-averaged contact area of the metal and catalyst particles, predicted numerically for the long reactor.As most particles have five to seven neighbors, the particle-averaged contact area was used. From Fig. 7.3, it can be seen that the particle-averaged contact area deviates by 50% from minimum and maximum values of the particle-averaged contact area for catalyst and metal particles. The control-volume-averaged contact area increases almost linearly from the top to the bottom by a factor of 9.

Fig. 7.4 shows the 3D visualization of the Joule heating Q_e, the particle-averaged electric field potential of metal particles ϕ_i, the particle-averaged temperature T_p and the particle-averaged mass

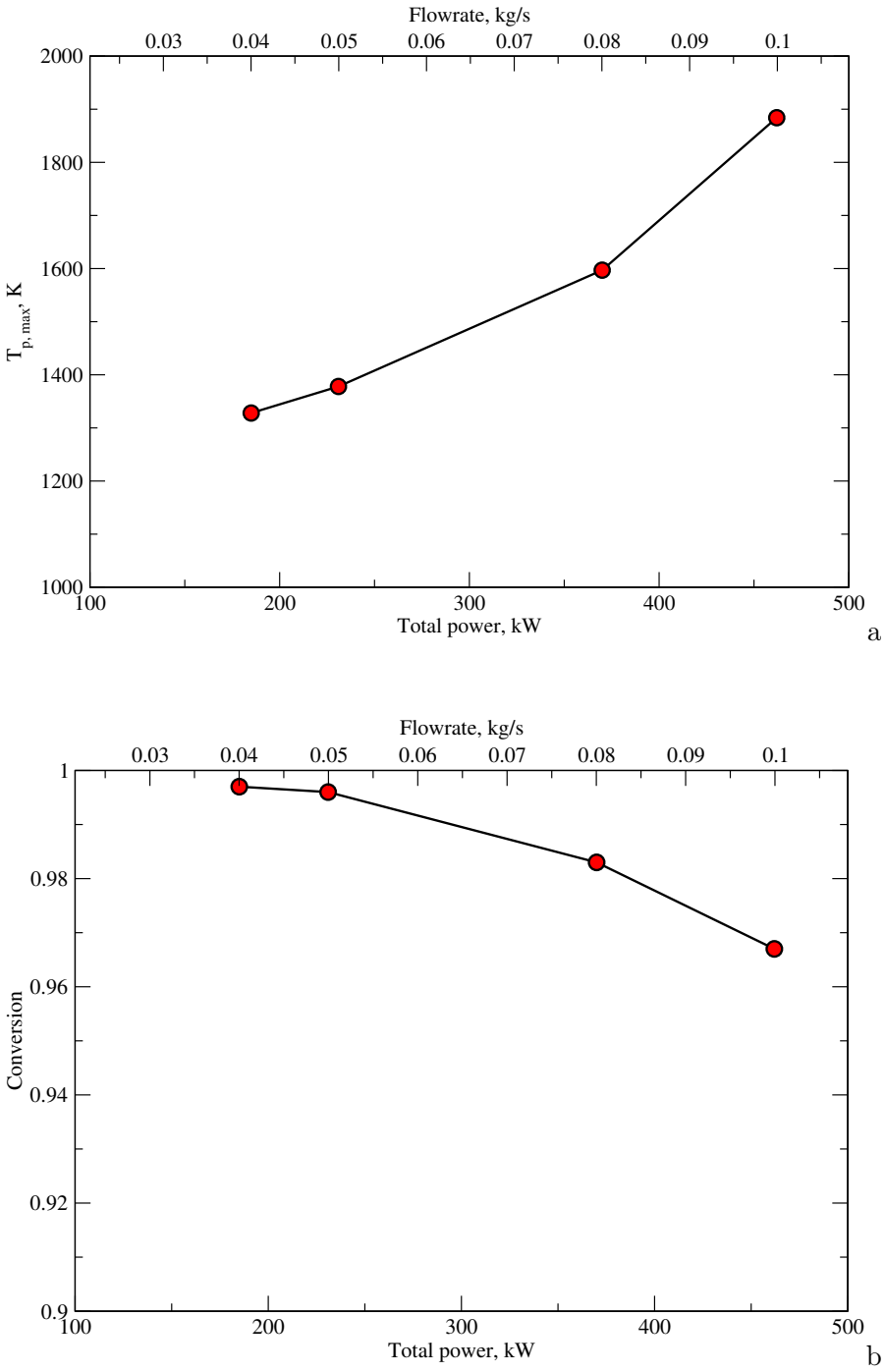

Figure 7.2: Comparison of maximum temperature (a) and conversion (b) with different flow rates and proportional power given in Table 7.3.

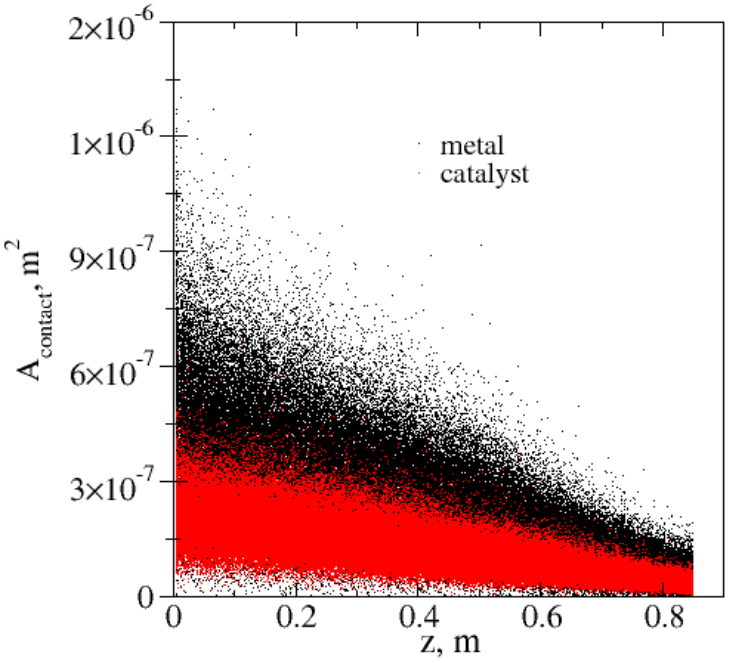

a

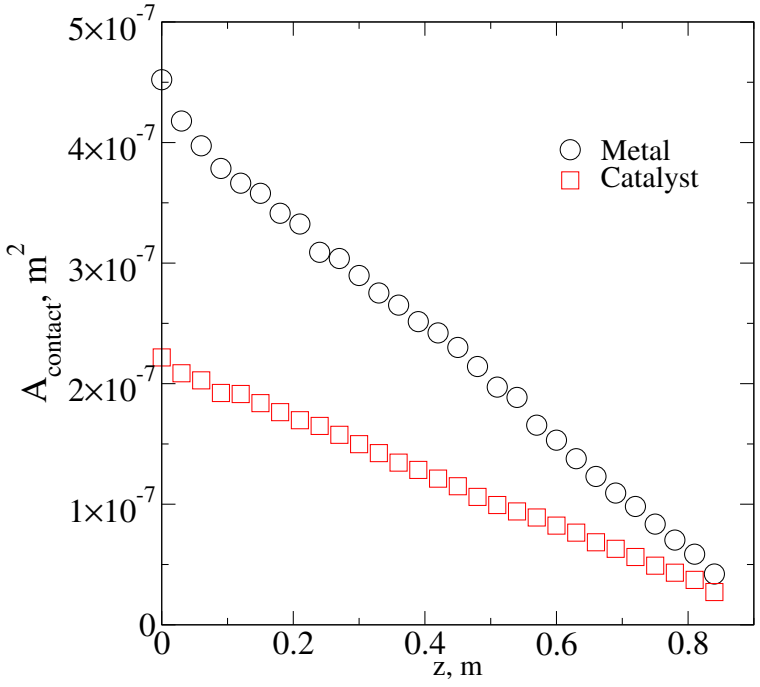

b

Figure 7.3: Axial distribution of the particle-averaged contact area for metal and catalyst particles (a) and control-volume-averaged particle contact area of particles (b) predicted numerically for the long reactor.

fraction of CH_4 predicted numerically for $Q_{IU} = 370$ kW and $\dot{m} = 0.08$ kg/s. The upper limit of power of an individual particle is about 20 W, resulting in a maximum T_{pm} temperature close to 1600 K. The hottest particles are found at the top, where the volume-averaged contact area is smallest, despite the fact the control-volume averaged-particle temperature is the lowest. This tells us that the uneven contact near the top has caused significantly non-uniform heating. In the voltage visualization, the particles are colored based on the average electrical field potential. The voltage predictions show that most of the particles are connected to the circuit. The few that have no voltage applied are colored white, meaning they are not connected to the circuit and they do not generate heat. The Joule heating distribution shows that most of the particles are generating some heat, but a number of particles are responsible for most of the Joule heating. The current path can be traced through the bed by finding the particles with the most Joule heating. As we approach the bottom, the contact improves and the heat is generated more homogeneously. Although not heated uniformly, the heating is sparsely distributed in all areas of the bed, which should result in a homogeneous radial temperature profile.

Fig. 7.5 visualizes the 3D distributions of the particle-averaged mass fractions predicted using the kinetic model (KM) for $Q_{IU} = 370$ kW and $\dot{m} = 0.08$ kg/s. As can be seen from Table 7.3, the conversion is lower for the 370kW case compared to the 185kW case, presumably due to the lower residence time with the same number of active sites. However, the 3D visualization reveals that despite the heat source being closely placed among the catalysts, interparticle heat transfer is still a significant limiting factor to the reaction rate. For the 3D species profiles, the surfaces of metal particles have concentration close to the bulk condition, indicating that they have a small impact on reaction rates, despite having a temperature higher than the gas phase. The metal surfaces do contribute to active sites, but only at a minor fraction of what the catalysts do. The catalysts, represented by their internal mass fraction, have a CH_4 conversion rate that is much higher than bulk at the top, but the temperature is much lower. Shown at the bottom left in Fig. 7.4, the temperature at the top inlet of the reactor has some particles near 900K as well as particles above 1200K. The majority of all the particles are well below 1300K except for the few hot spots. The temperature difference shows that the reactions occur quickly, but the heat is not sufficient to drive the conversion further in the catalyst particles. Fig. 7.5 shows that the catalysts closest to the hottest particles have a much higher H_2 concentration than the surrounding particles not in contact. The 3D images prove that the heat transfer is the main rate limiting factor in the initial part of the reactor, more so than the number of active sites. The 370kW is also at the limit of power for a reactor, as the 462kW case results in a maximum temperature that exceeds the operational limit. The power-to-catalyst ratio can be used as a reference for designing such reactors, and controlling the flow rate and power is crucial to the operation of the reactor.

To show the radial distribution of the particle temperature, Fig. 7.6 depicts the particle-averaged temperature T_p at 0.2m, 0.4m and 0.6m from the inlet, predicted numerically using the kinetic model

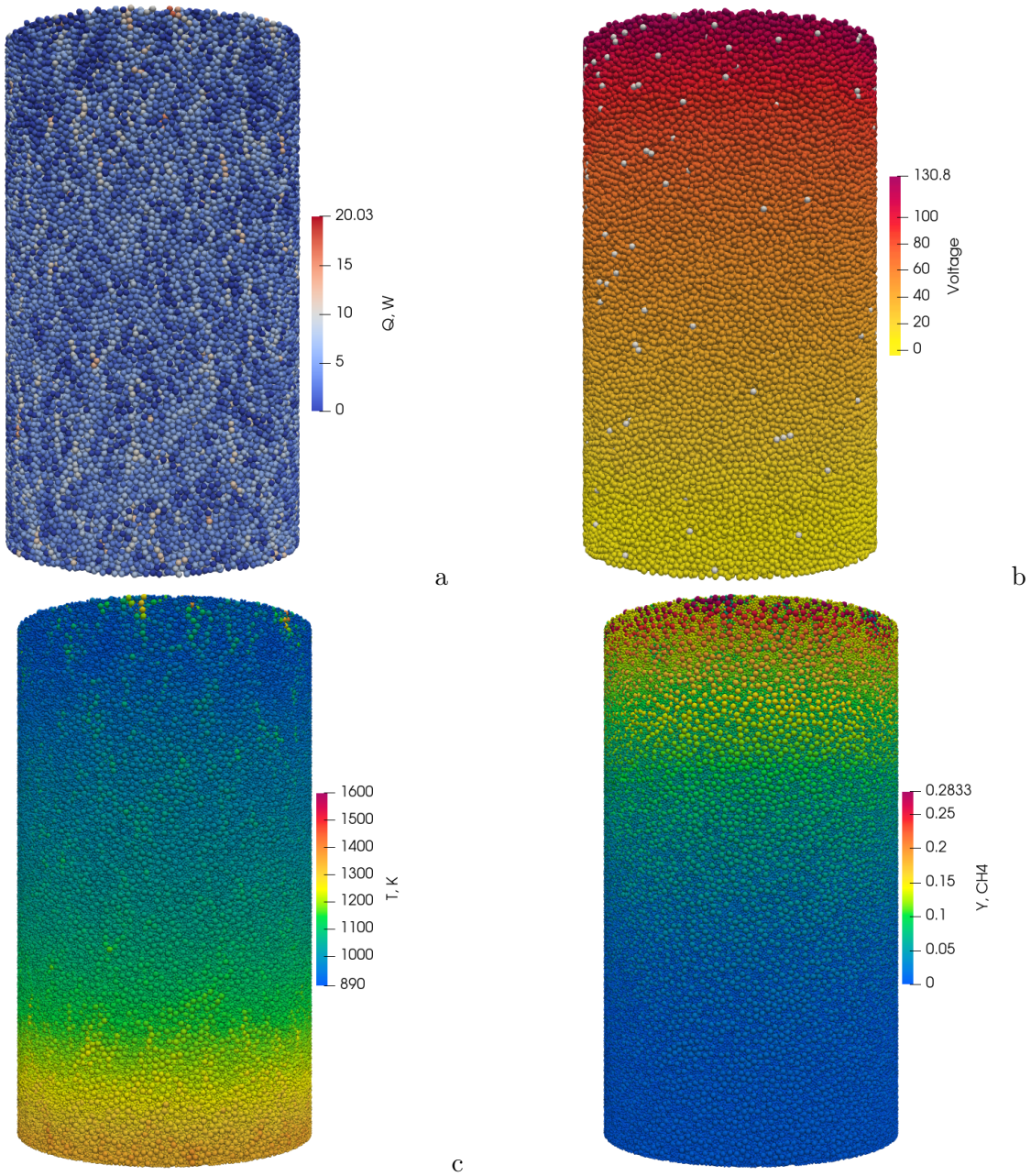

Figure 7.4: 3D visualization of the Joule heating Q_e (a); particle-averaged electric field potential of metal particles ϕ_i (b); particle-averaged temperature T_p (c) and particle-averaged mass fraction of CH_4 (d) predicted numerically for $Q_{IU} = 370$ kW and $\dot{m} = 0.08$ kg/s.

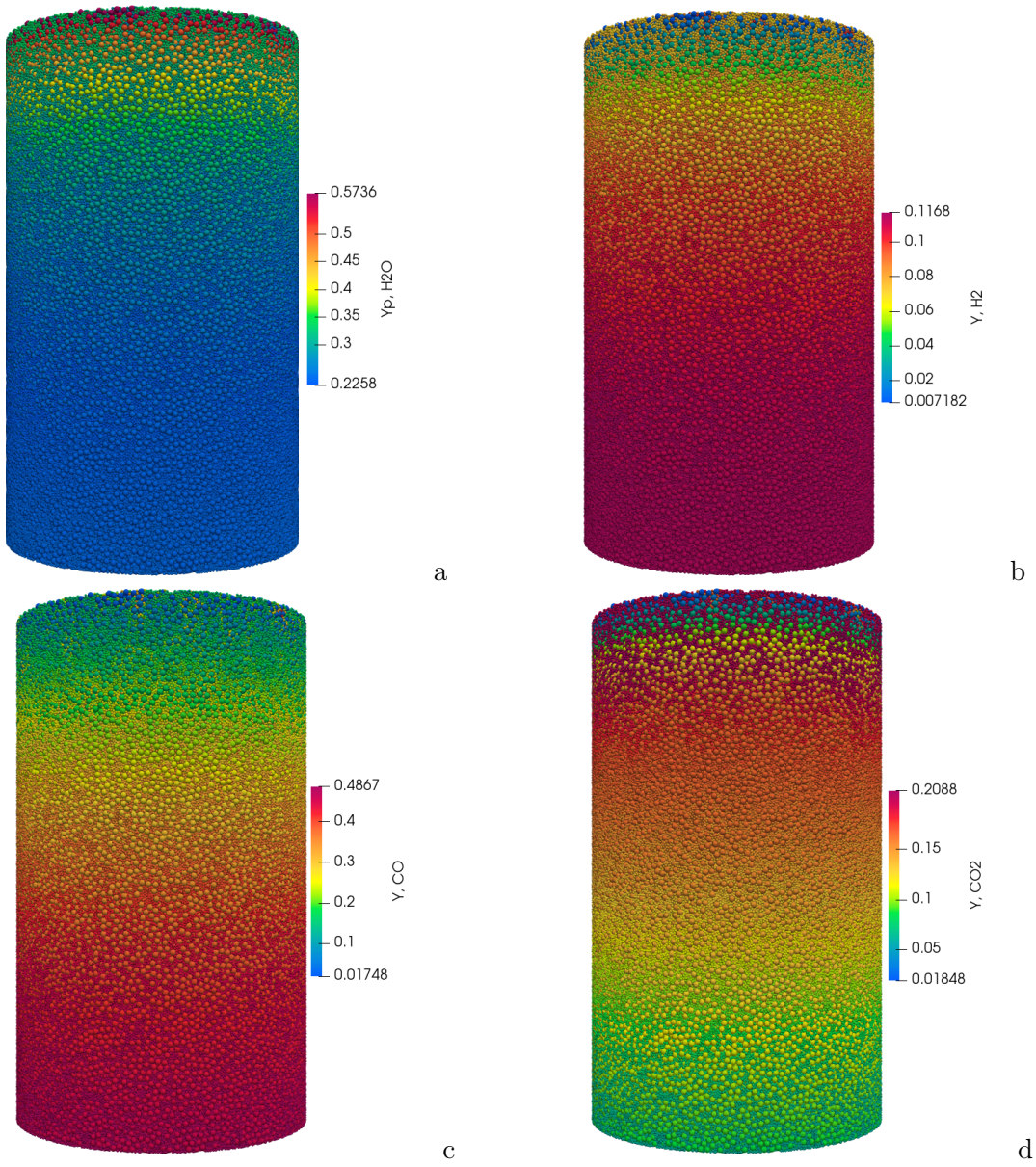

Figure 7.5: 3D visualization of the particle-averaged mass fraction: (a) Y_{p,H_2O}; (b) Y_{p,H_2}; (c) $Y_{p,CO}$; (d) Y_{p,CO_2} predicted numerically for $Q_{IU} = 370$ kW and $\dot{m} = 0.08$ kg/s.

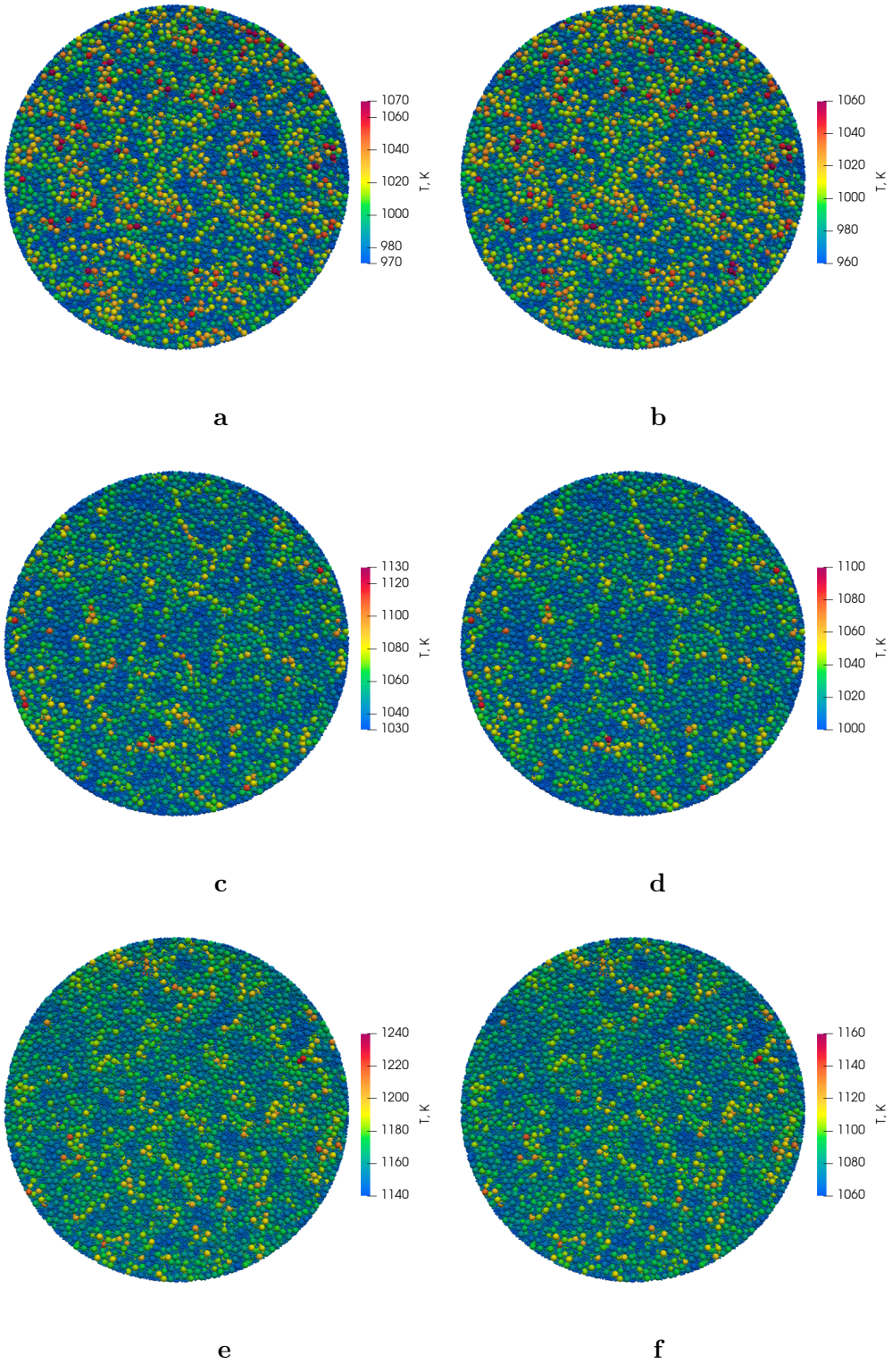

Figure 7.6: The particle-averaged temperature T_p predicted numerically using the kinetic model and equilibrium model for $Q_{IU} = 370$ kW. Upper row: a, b - z=0.2m; middle row: c, d - z=0.4m; bottom row: e, f - z=0.6m. Kinetic model - left column: a,c, e; equilibrium model - right column: b, d, f. $Q_{IU} = 370$ kW and $\dot{m} = 0.08$ kg/s.

and equilibrium model for the reactor with $Q_{IU} = 370$ kW. As the flow comes down from the inlet, it first decreases in temperature due to the heat of reaction. Because the reaction rate is higher in the initial part of the reactor, the temperature difference between metal particles and catalyst particles is much more significant, as seen in the temperature profile on the left. In all profiles, it can be seen that the particles temperature does not have any long-rage gradient in the radial direction. The metal particles have a higher temperature than the catalysts due to the Joule heating effect, but the Joule heating happens in many locations in the cross section, so the reactor maintains the degree of temperature homogeneity.

7.3.3 Axial profiles

In order to illustrate the influence of difference parameters on the heat and mass transfer inside the reactor qualitatively, we use the control-volume-averaged quantities of the particle-averaged temperature T_{pm} and T_p, and of the particle-surface-averaged temperature T_{sm} and T_s, calculated as follows:

$$T = \frac{1}{N_p} \sum_{j=1}^{N_p} T_{i,j} \tag{7.47}$$

where T_i refers to T_{pm}, T_p, T_{sm} and T_s and the control volume is $\Delta V = \frac{\pi}{4} D^2 \Delta z$. Similarly, the control-volume-averaged quantities of the catalyst particle-averaged mass fractions of species i $Y_{i,p}$ and of the particle surface-averaged mass fractions of species i $Y_{i,s}$ and $Y_{i,sm}$ are used, calculated as follows:

$$Y = \frac{1}{N_p} \sum_{j=1}^{N_p} Y_{i,j} \tag{7.48}$$

The first comparison of axial profiles is from the results between kinetic model and equilibrium model, shown in Figs. 7.7 and 7.8. If the reactions in the catalyst particles are rate-limited by heat and mass transfer, the interior of the particles can be assumed to be at equilibrium and the results should be reasonably close. The two cases of identical conditions are simulated using the kinetic model and the equilibrium model. The results generally agree well but there are some differences. The equilibrium model overpredicts the reaction rate in the initial part, as expected. However, the equilibrium model also reveals a larger difference close to the outlet. The difference is due to the prediction of the rate of Reaction 2. As CH_4 nears completion but still has not reached equilibrium, Reactions 1 and 3 have much lower rate as a result. Instead, the added heat causes Reaction 2 to shift towards water and CO. The rate of water-gas shifting cannot be predicted using the same equilibrium model, as it is slower than the steam-methane reforming on the nickel catalyst. Therefore, the accuracy of the equilibrium model begins to decline near the outlet of the reactor.

The next comparison is to show the influence of the flow direction, with results for the upward and downward flow in Figs. 7.9 and 7.10. The downward flow has a smoothly rising profile with a

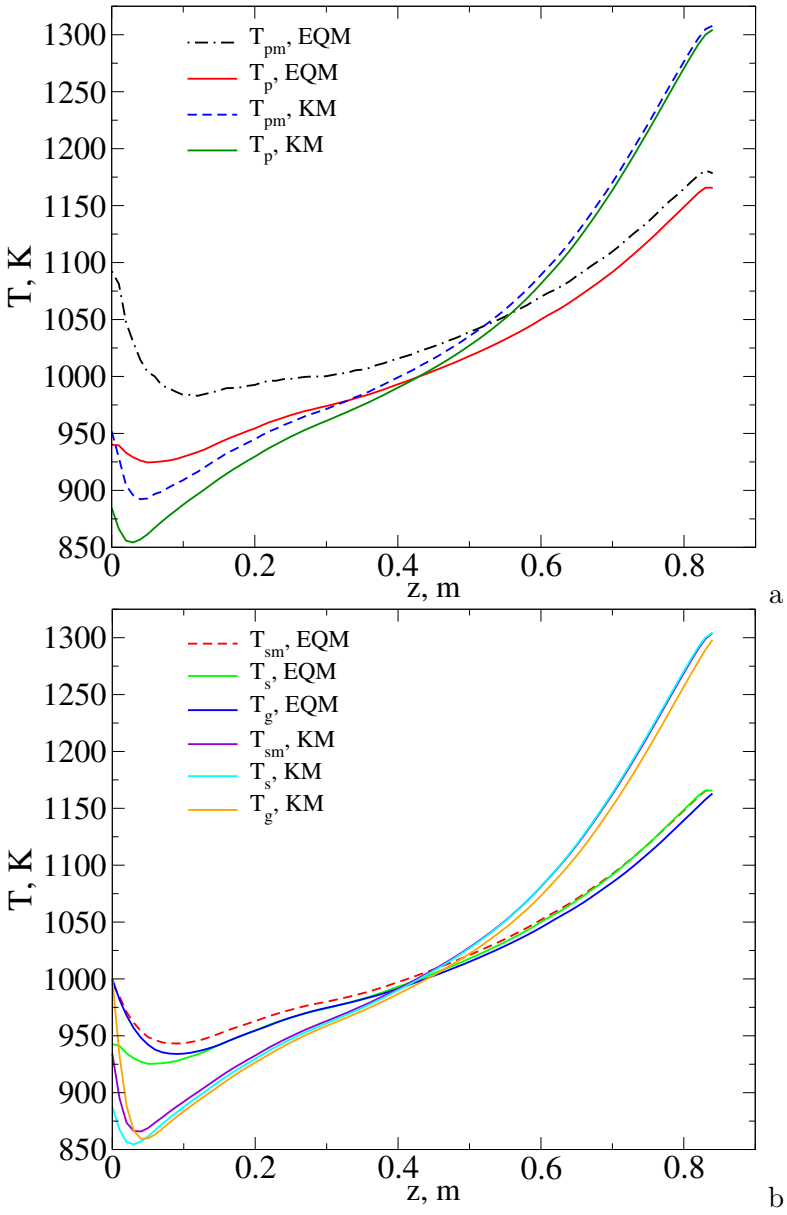

Figure 7.7: Axial profiles of the temperature (a) - control-volume averaged temperature of particles T_p and (b) - gas phase temperature T_g and control-volume-averaged temperature of particle surface T_s predicted numerically using the kinetic model (KM) and equilibrium model (Eq. model) for the reactor H=0.85 m and D=0.5 m operating at the input power $Q_{IU} = 370$ kW.

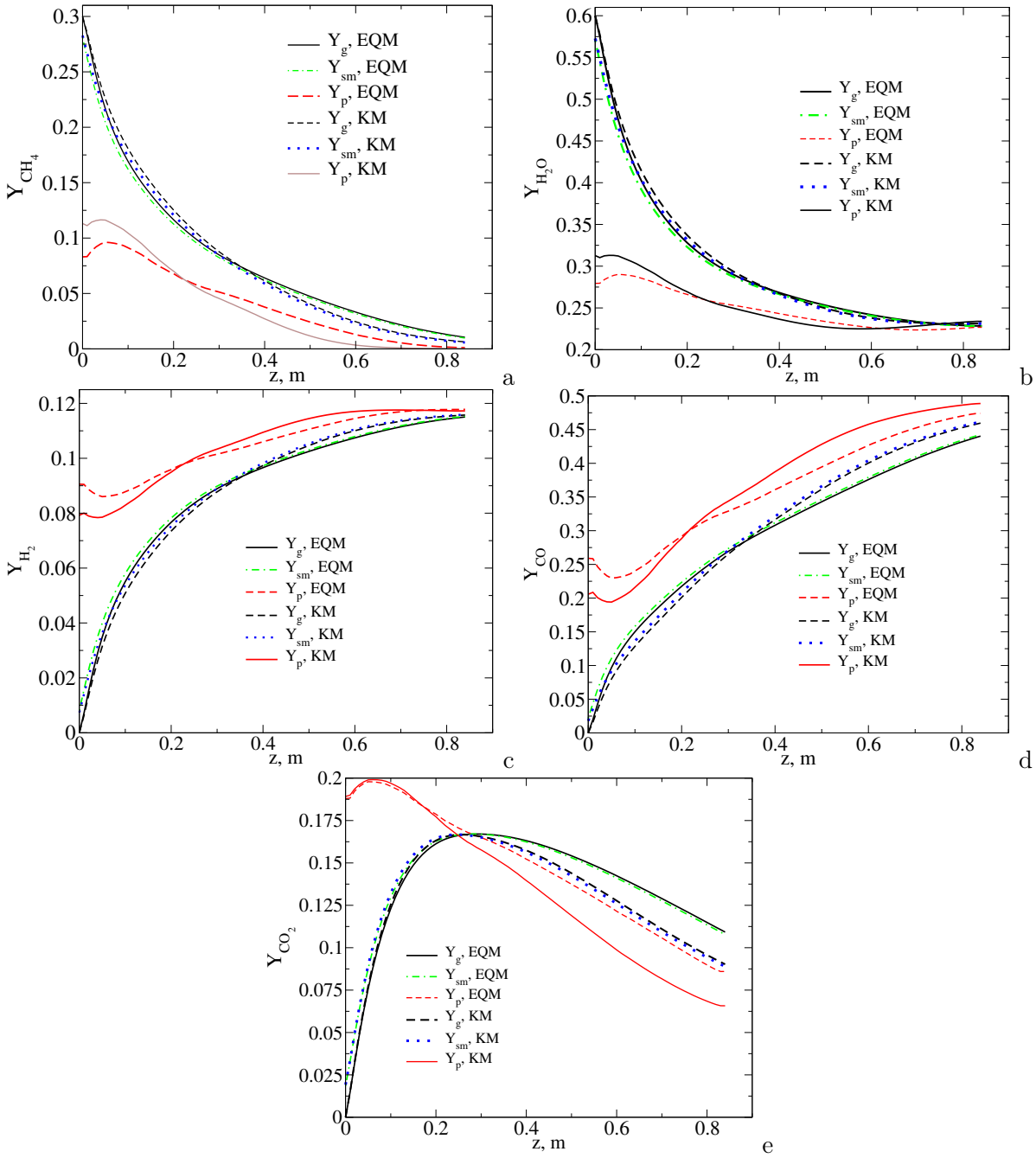

Figure 7.8: Axial profiles of the mass fractions of species (in the gas phase Y_g and in the solid phase Y_p, Y_s) predicted numerically using the kinetic model (KM) and equilibrium model (Eq. model) for the reactor H=0.85 m and D=0.5 m operating at the input power $Q_{IU} = 370$ kW. Here a - Y_{CH_4}; b - Y_{H_2}; c - Y_{H_2}; d - Y_{CO}; e - Y_{CO_2}.

lower temperature and higher conversion at the outlet of the reactor. The difference is not caused by the effect of gravity on the gas phase, but rather on the contact area and Joule heating. Because gravity causes the bottom particles to be in better contact than those at the top, the resistance at the top of the bed is higher and so is the Joule heating. As a result, the top-down injected gas has better heat transfer and takes a longer time to react. Bottom-up injection sees the temperature rising sharply at the end, but conversion failing to improve because it does not have enough time to react. Having more heat supplied closer at the inlet is the most efficient way of heating.

A comparison between 185kW and 370kW is plotted in Figs. 7.11 and 7.12. Although the flow rate and power are doubled, the difference between the two cases is only a few percents. In terms of CH_4 conversion, the difference is less than 1%. However, the similarity is because the chosen parameters provide excess heat that results in the almost depletion of methane in the gas. The outlet composition in both cases is quite close to equilibrium for Reaction 1. The outlet temperature increases with conversion, though not significantly. The increased temperature for the 370kW case is becasue there is less backwards shifting of the exothermic Reaction 2. Therefore, the main difference between the cases of different flow rate is the amount of CO_2 in the outlet. The temperature difference is about 30K and the 185kW case has about 30% less CO_2 formation. Based on the outlet composition and residence time, both cases would be acceptable as they both produce a similar amount of hydrogen. However, the gas phase results alone are not sufficient to determine the validity of the reactor. This is why particle-based simulation is important.

Lastly, the profiles for changing the power while keeping the flow rate constant are compared in Figs. 7.13 and 7.14. The outlet temperature is significantly lower as a result. Both the CH_4 conversion and H_2 yield are moreover significantly reduced. While the conversion of CH_4 is also reduced, energetically it is more efficient to run a lower heat rate as the H_2 per watt has been improved by almost 30%. If the target is to produce the most syngas for the least amount of energy, the lower power-to-flow ratio can be a worthwhile tradeoff. The power can be adjusted to optimize the total cost of material and energy. The changes in the output CO:CO_2 ratio are also noteworthy and can have an impact on the overall efficiency of the production process.

7.3.4 Comparison with a Long Tubular Reactor

The influence of geometry was investigated and the results are shown in Figs. 7.15 and 7.16. The two reactors have the same number of particles in them and roughly the same volume. The shorter reactor has a diameter of 0.5m and the longer reactor has a diameter of 0.3m. The total heating power and flow rate for both reactors are 385kW and 0.08kg/s, respectively. Due to the different aspect ratio, the shorter reactor has better contact between particles and slightly denser packing. The longer case has a higher velocity over a smaller cross section, which improves the mass transfer. The higher velocity also results in the pressure drop being about 9 times higher. The curves in the figures are similarly shaped and the outlet temperature and conversion are close in both cases.

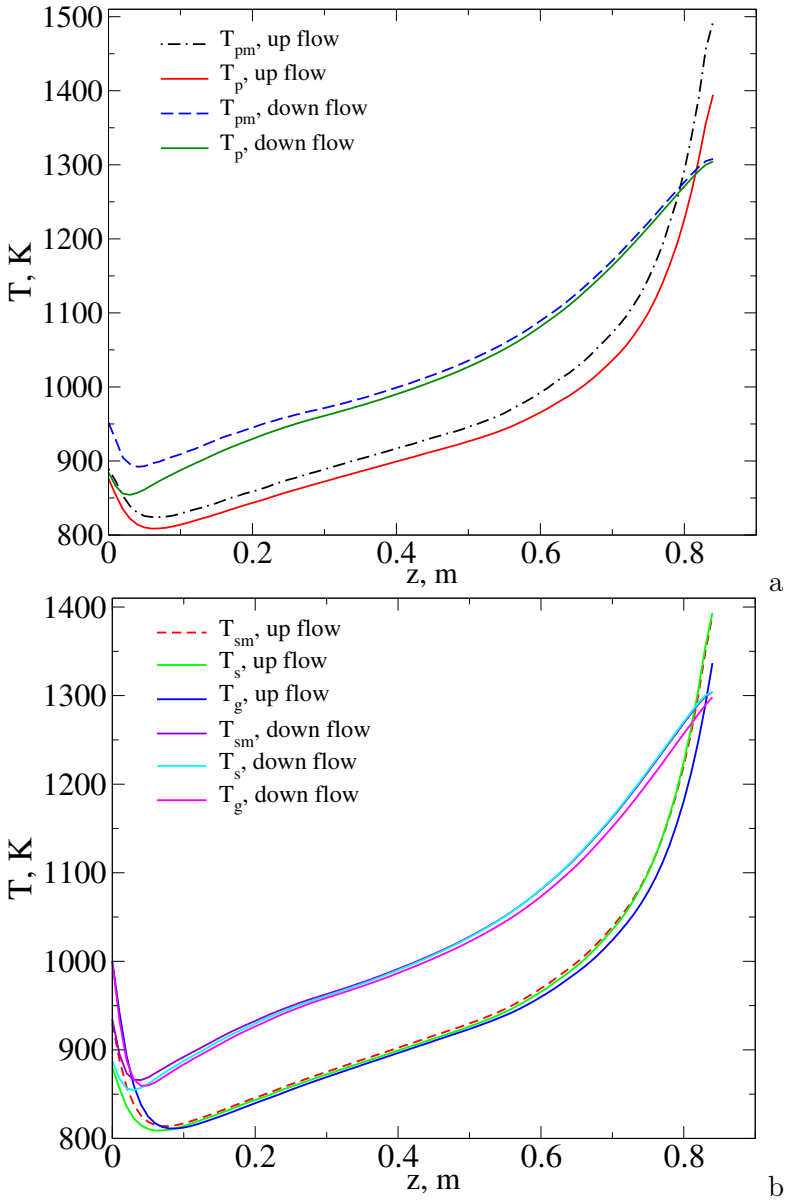

Figure 7.9: Axial profiles of the temperature (a) - control-volume averaged temperature of particles T_p and (b) - gas phase temperature T_g and control-volume-averaged temperature of particle surface T_s predicted numerically using the kinetic model (KM) for the different location of the gas inflow (top and bottom) for the reactor H=0.85 m and D=0.5 m operating at the input power $Q_{IU} = 370$ kW.

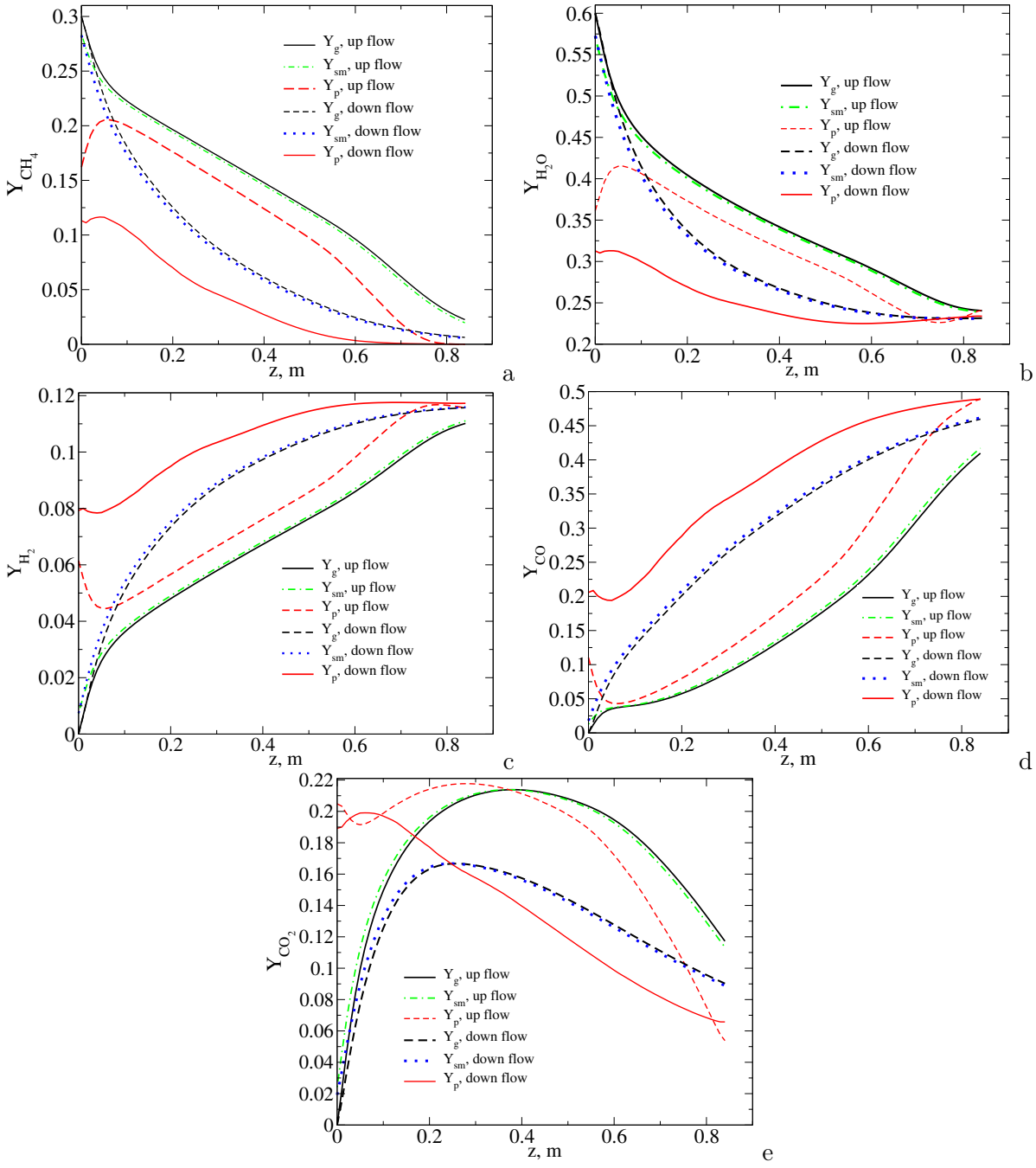

Figure 7.10: Axial profiles of the mass fractions of species (in the gas phase Y_g and in the solid phase Y_p, Y_s) predicted numerically using the kinetic model for the different location of the gas inflow (top and bottom) for the reactor H=0.85 m and D=0.5 m operating at the input power $Q_{IU} = 370$ kW. Species: a - Y_{CH_4}; b - Y_{H_2}; c - Y_{H_2}; d - Y_{CO}; e - Y_{CO_2}.

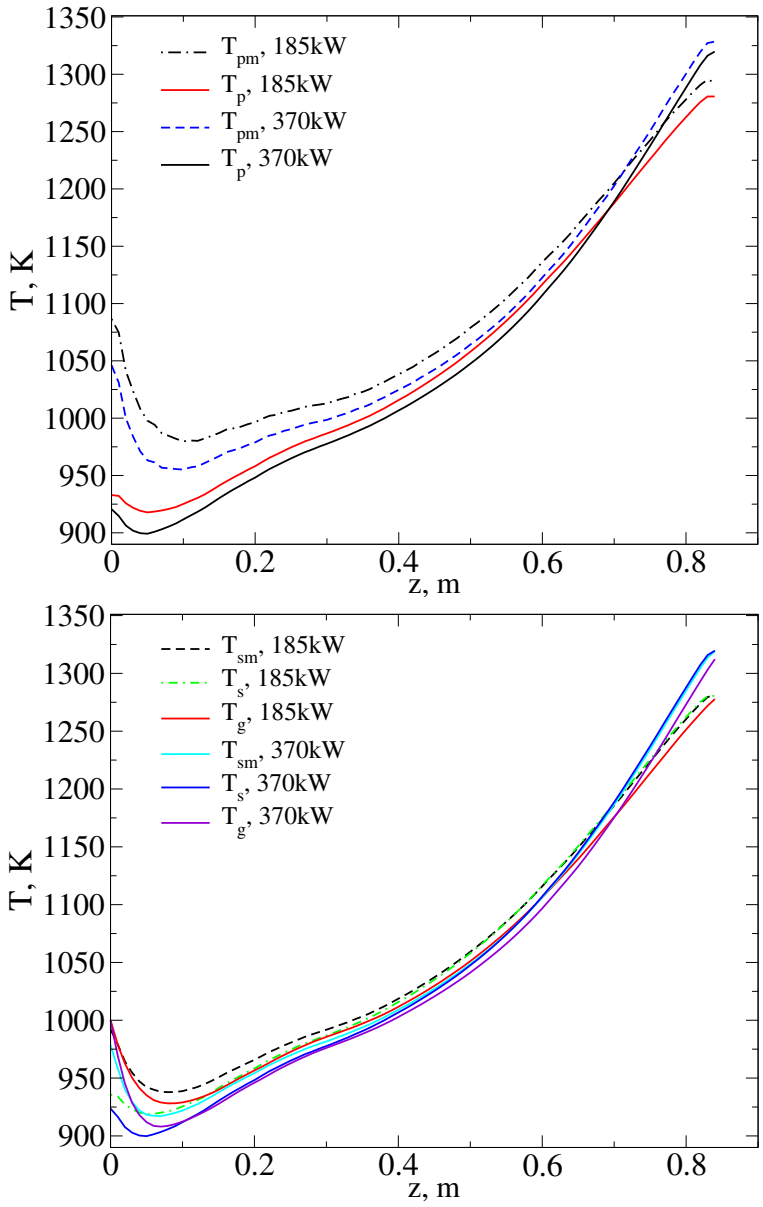

Figure 7.11: Axial profiles of the temperature (a) - control-volume-averaged temperature of particles T_p and (b) - gas phase temperature T_g and control-volume-averaged temperature of particle surface T_s predicted numerically for the reactor H=0.85 m and D=0.5 m operating at different input powers and corresponding flow rates, see Table 7.3.

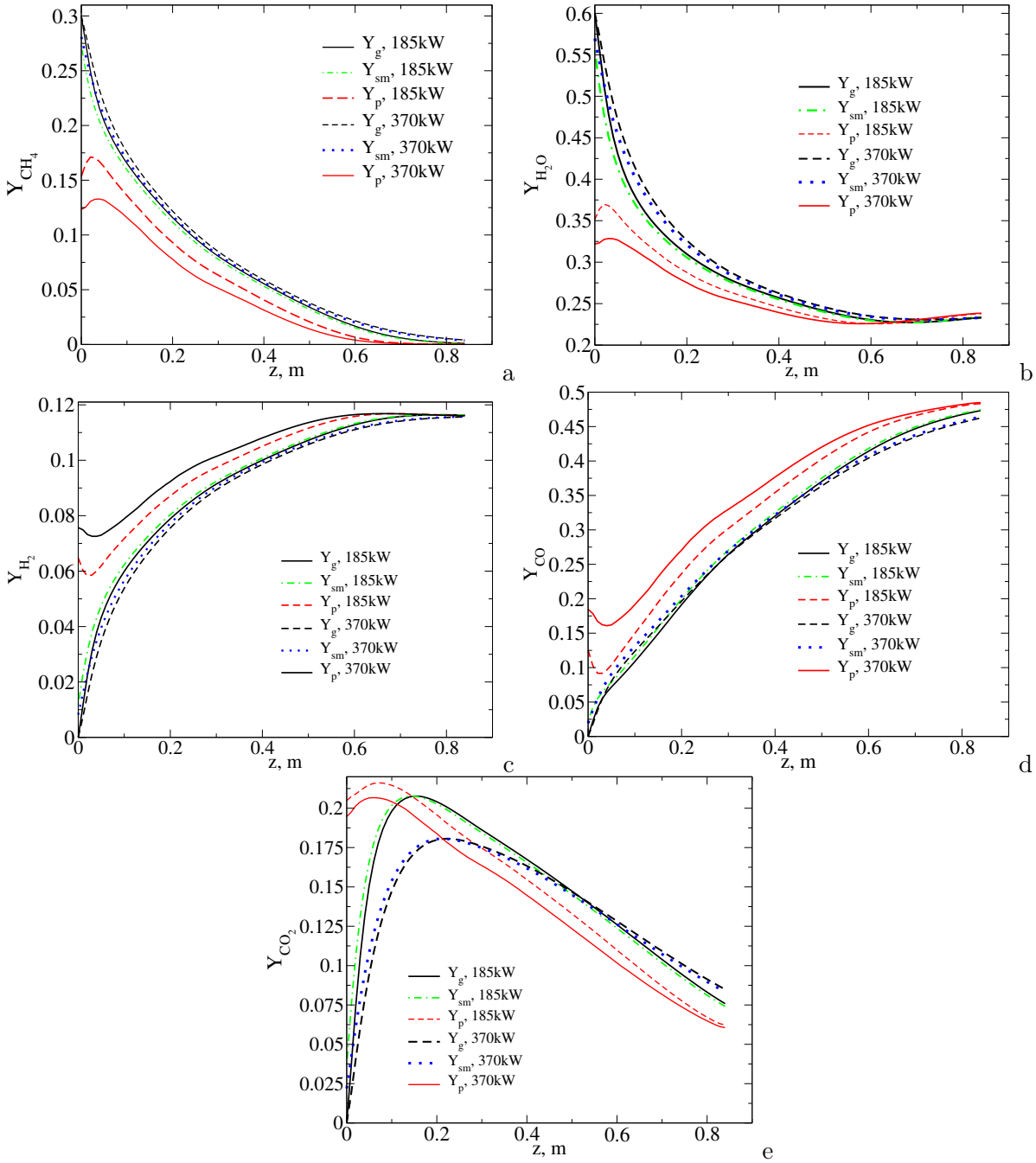

Figure 7.12: Axial profiles of the mass fractions of species (in the gas phase Y_g and in the solid phase Y_p, Y_s) predicted numerically for the reactor H=0.85 m and D=0.5 m operating at different input powers but at different flow rates, see Table 7.3. Here a - Y_{CH_4}; b - Y_{H_2}; c - Y_{H_2}; d - Y_{CO}; e - Y_{CO_2}.

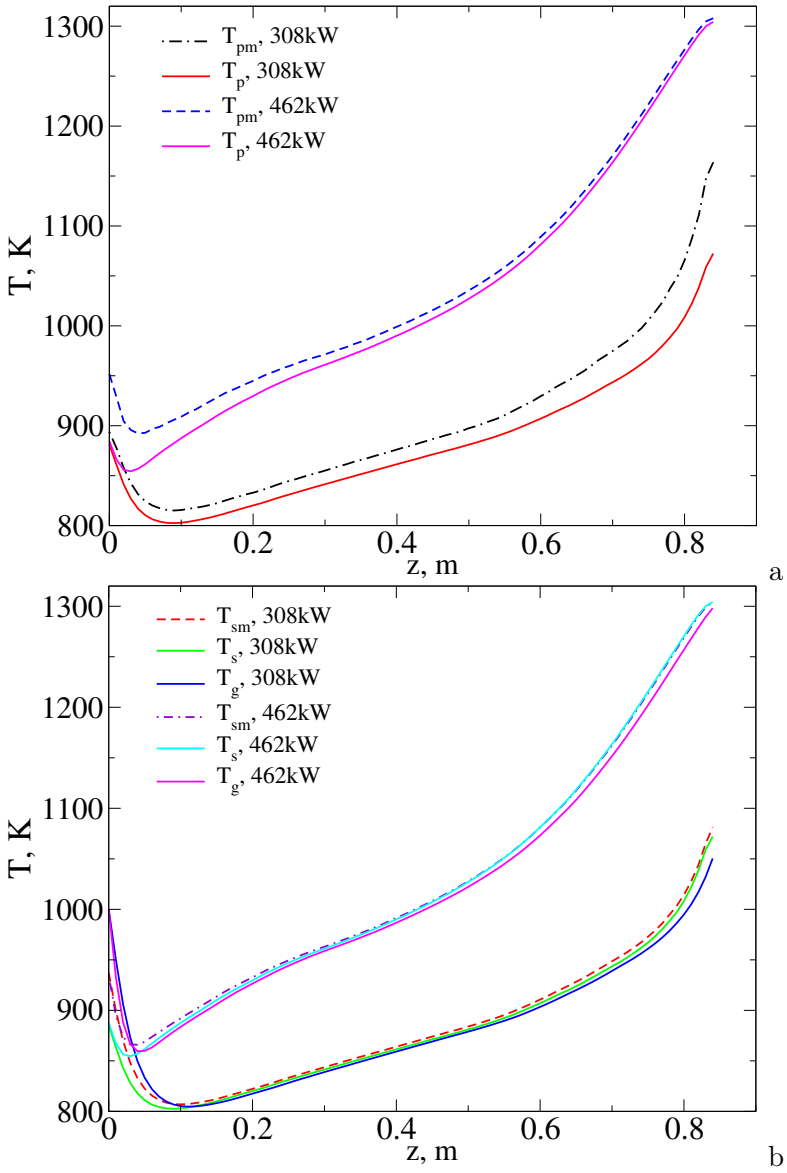

Figure 7.13: Axial profiles of the temperature (a) - control-volume-averaged temperature of particles T_p and (b) - gas phase temperature T_g and control-volume-averaged temperature of particle surface T_s predicted numerically for the reactor H=0.85 m and D=0.5 m operating at different input powers but at the same flow rate $\dot{m} = 0.1$ kg/s. For conditions, see Table 7.4.

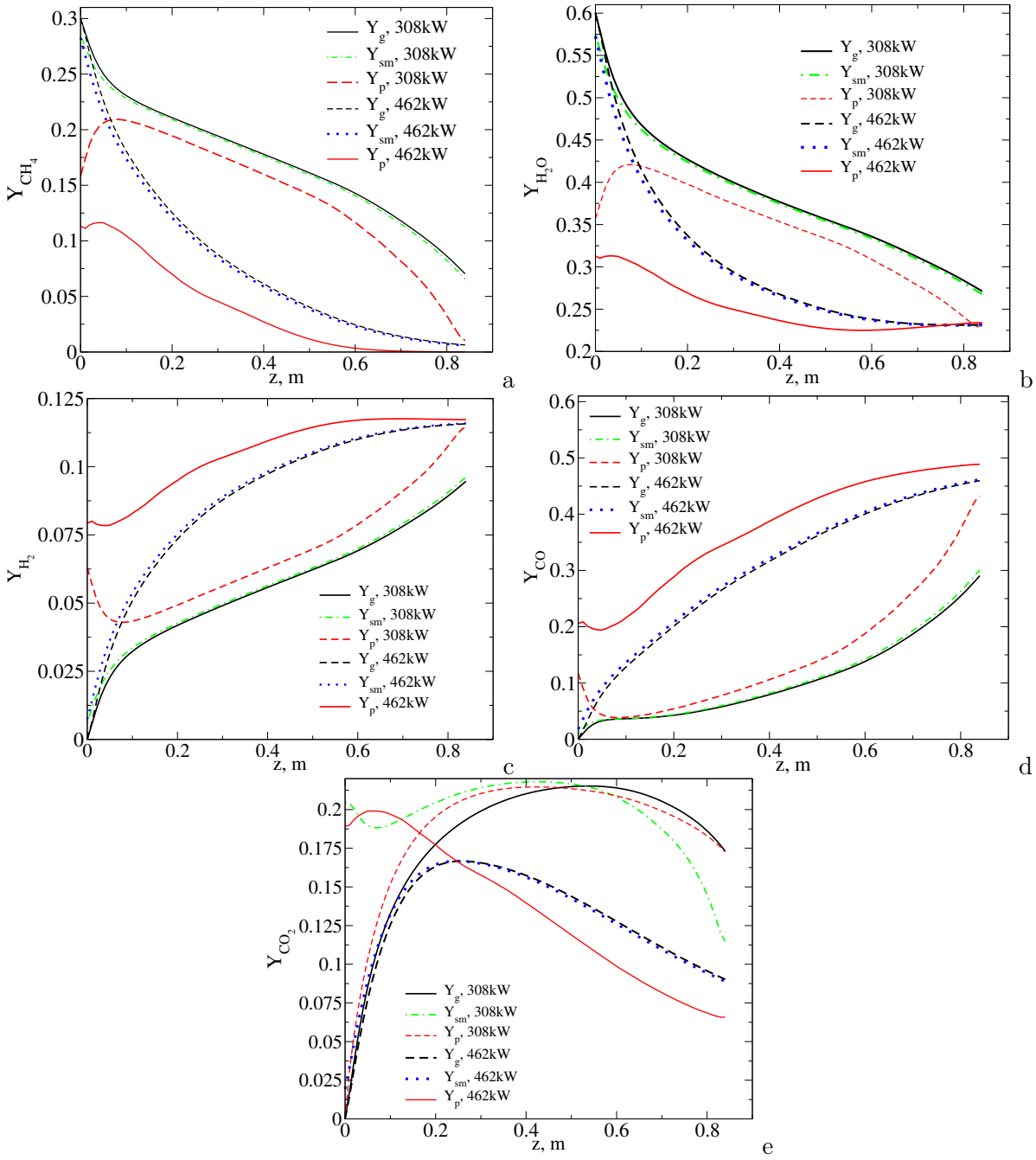

Figure 7.14: Axial profiles of the mass fractions of species (in the gas phase Y_g and in the solid phase Y_p, Y_s) predicted numerically for the reactor H=0.85 m and D=0.5 m operating at different input powers but at the same flow rate $\dot{m} = 0.1$ kg/s. For conditions, see Table 7.4. Here a - Y_{CH_4}; b - Y_{H_2}; c - Y_{H_2}; d - Y_{CO}; e - Y_{CO_2}.

The main difference is that near the inlet, longer reactor has a slower reaction inside the catalyst particles before it recovers and approaches the bulk value. This difference is because the heating in the shorter reactor is skewed more towards the inlet and the reaction is faster initially, resulting in a lower local minimum temperature in the profile. However, as both reactors have the same volume and residence time, the conversion in both reactors should be similar, and they are indeed almost identical, with the 0.85m case at 98.3% and the 2.35m case at 98.4% in the outlet, shown in Fig. 7.17. The shorter reactor has a lead in the conversion rate at the beginning because the distribution of the heating is concentrated near the inlet, where the contact is poor and the resistance is highest. One advantage the longer reactor has is the maximum temperature. With the longer tube, the contact between particles is improved due to gravity, and the heating is more uniform throughout the reactor. Additionally, the high velocity produces better particle-gas heat transfer, resulting in cooler metal particles and a lower temperature difference. In fact, the maximum temperature in the longer case occurs near the outlet rather than the inlet. The lower temperature differential between the gas and the particle is good for managing the thermal stress in the reactor.

7.4 Conclusion

In this study, the impact of the flow rate, flow direction, power input and aspect ratios of the electrically heated steam-methane reforming reactor was investigated through a parametric study. The equilibrium model was compared with the kinetic model to understand the degree of transport limitations in the reactor. When the flow rate is kept constant, increasing the power will increase conversion, but may not be the best for thermal efficiency. The ideal power-to-flow ratio should be equal to the heat of reaction, based on the conversion of steam methane reforming. A higher flow rate can increase production capacity while maintaining a similar conversion rate. However, a high flow rate also causes more severe heat transfer limitations, a higher maximum temperature, a higher temperature gradient and a higher pressure drop. The maximum temperature should be considered carefully in the design as it was shown to become the top restrictive factor, before the conversion rate. The recommended mass flow limit for a reactor that 0.88m tall and 0.5 in diameter is 0.05kg/s. In particular, we showed that the cross-sectional temperature profile of a scaled-up reactor is mostly uniform, with small hot spots but a temperature difference that is usually within 100K. More importantly, the temperature differential only exists from particle to particle and does not extend over a longer radial distance. Therefore, the scalability and the efficiency of the reactor present a significant advantage over conventional steam methane reformers in an energy market with abundant renewable energy in the future.

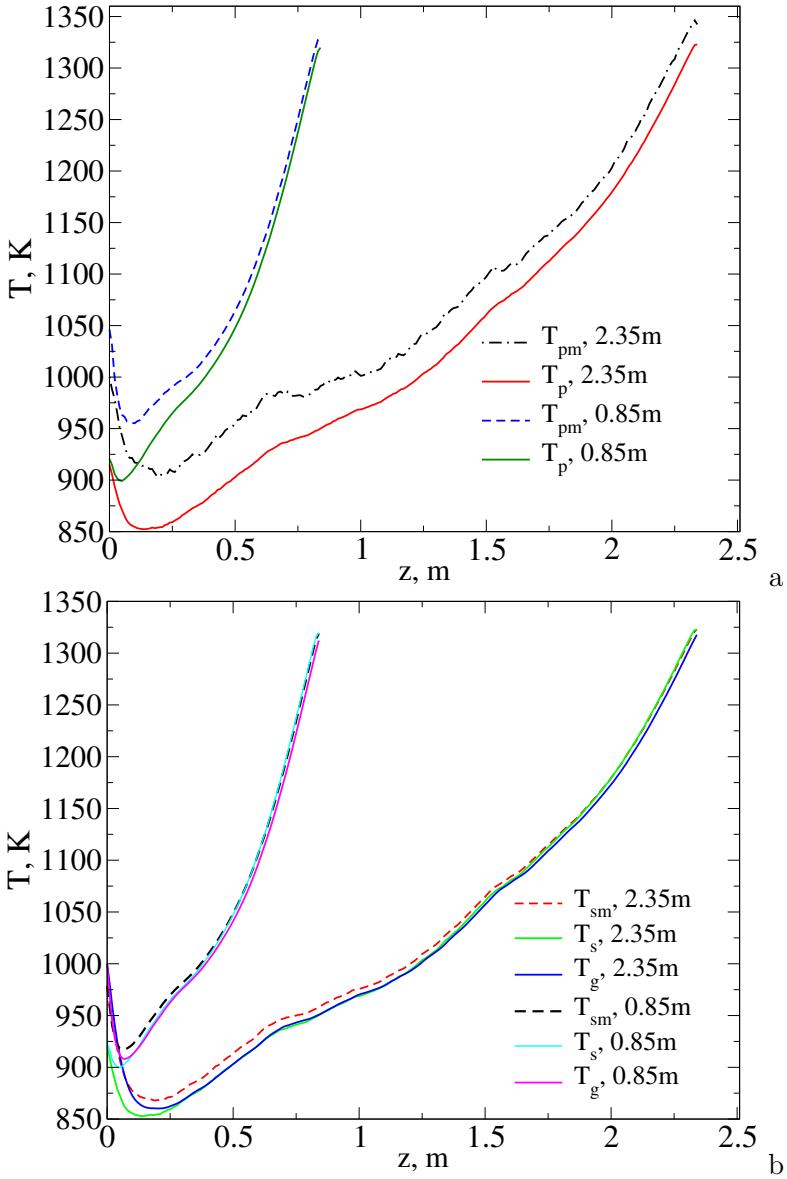

Figure 7.15: Axial profiles of the temperature (a) - control-volume averaged temperature of particles T_p and (b) - gas phase temperature T_g and control-volume-averaged temperature of particles surface T_s predicted numerically for different reactors (long reactor - H = 2.35 m and D = 0.3 m, short reactor H = 0.85 m, D = 0.5 m) for the same input power $Q_{IU} = 370$ kW.

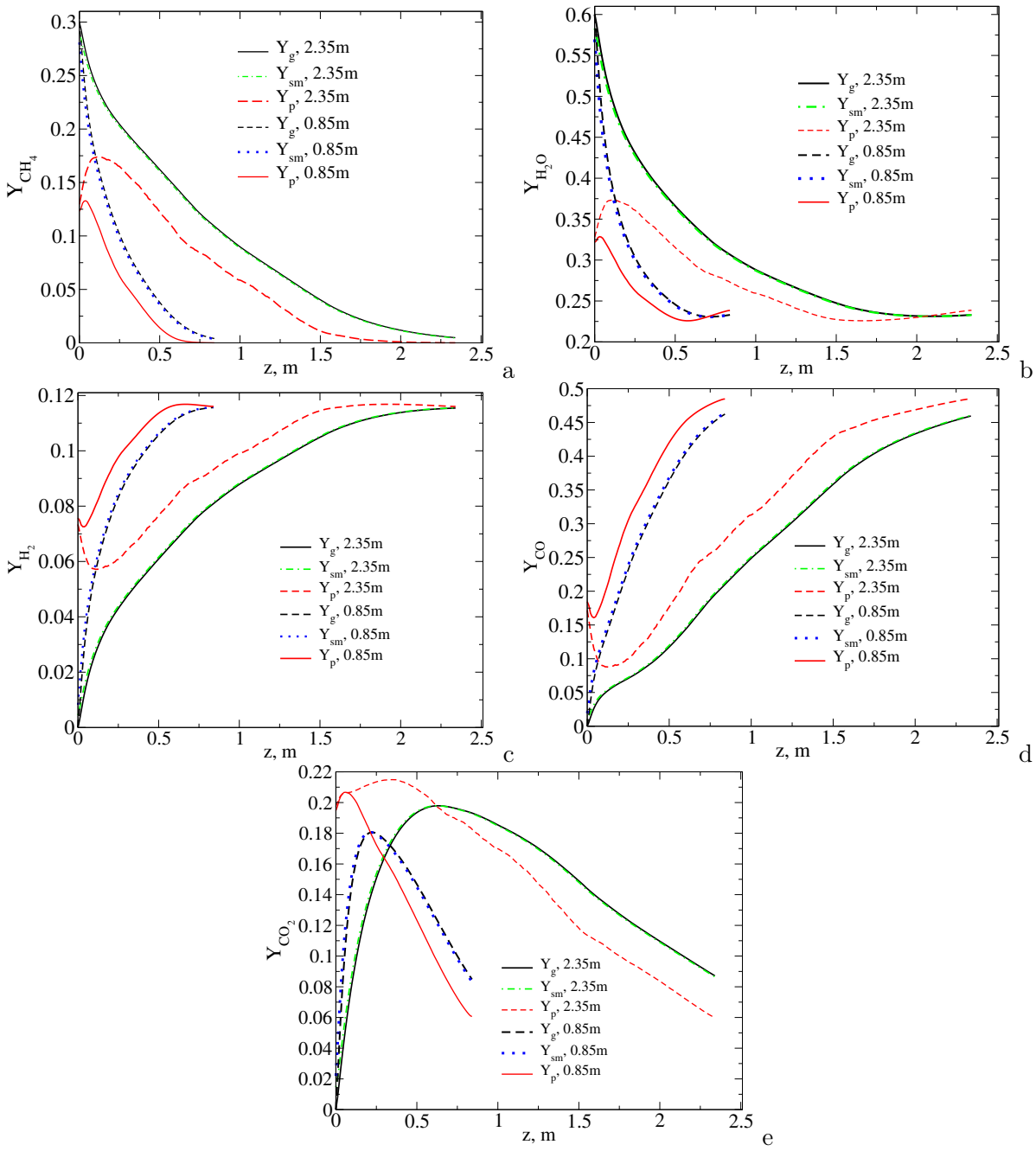

Figure 7.16: Axial profiles of the mass fractions of species (in the gas phase Y_g and in the solid phase Y_p, Y_s) predicted numerically for different reactors (long reactor - H = 2.35 m and D = 0.3 m, short reactor H = 0.85 m, D = 0.5 m) for the same input power $Q_{IU} = 370$ kW. Here a - Y_{CH_4}; b - Y_{H_2}; c - Y_{H_2}; d - Y_{CO}; e - Y_{CO_2}.

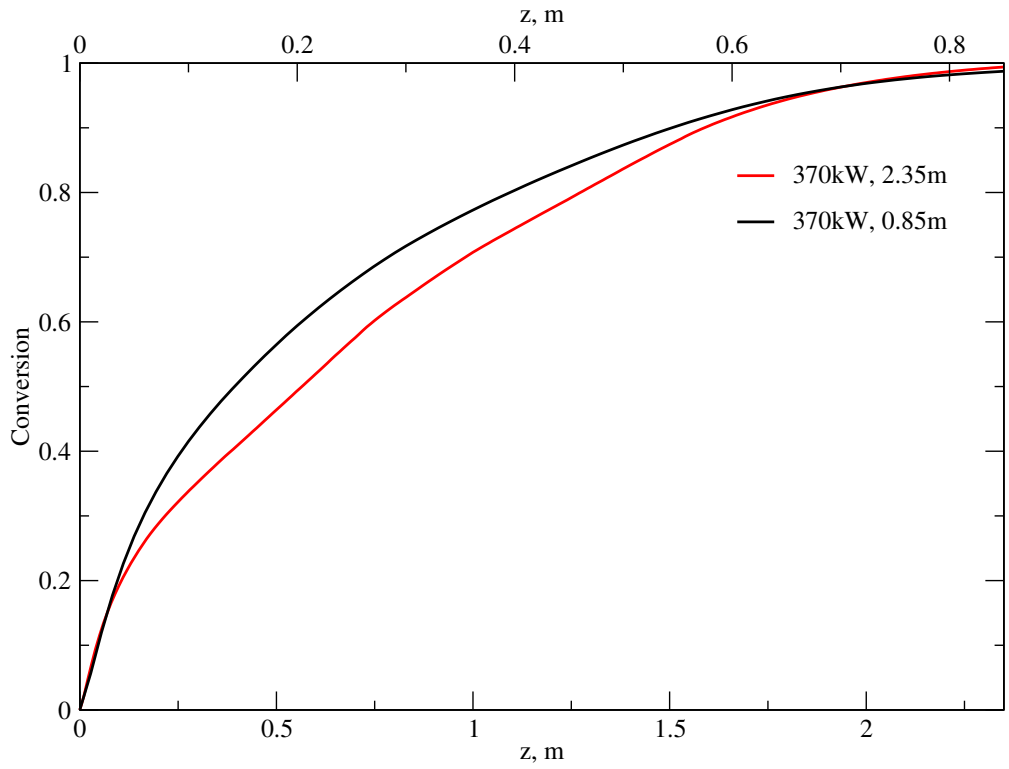

Figure 7.17: Axial profile of the methane conversion predicted numerically plotted against relative distance for the long reactor (H=2.35 m and D=0.3 m) and short reactor (H=0.85 m and D=0.5 m) with the same electrical power $Q_{IU} = 370$ kW and number of particles.

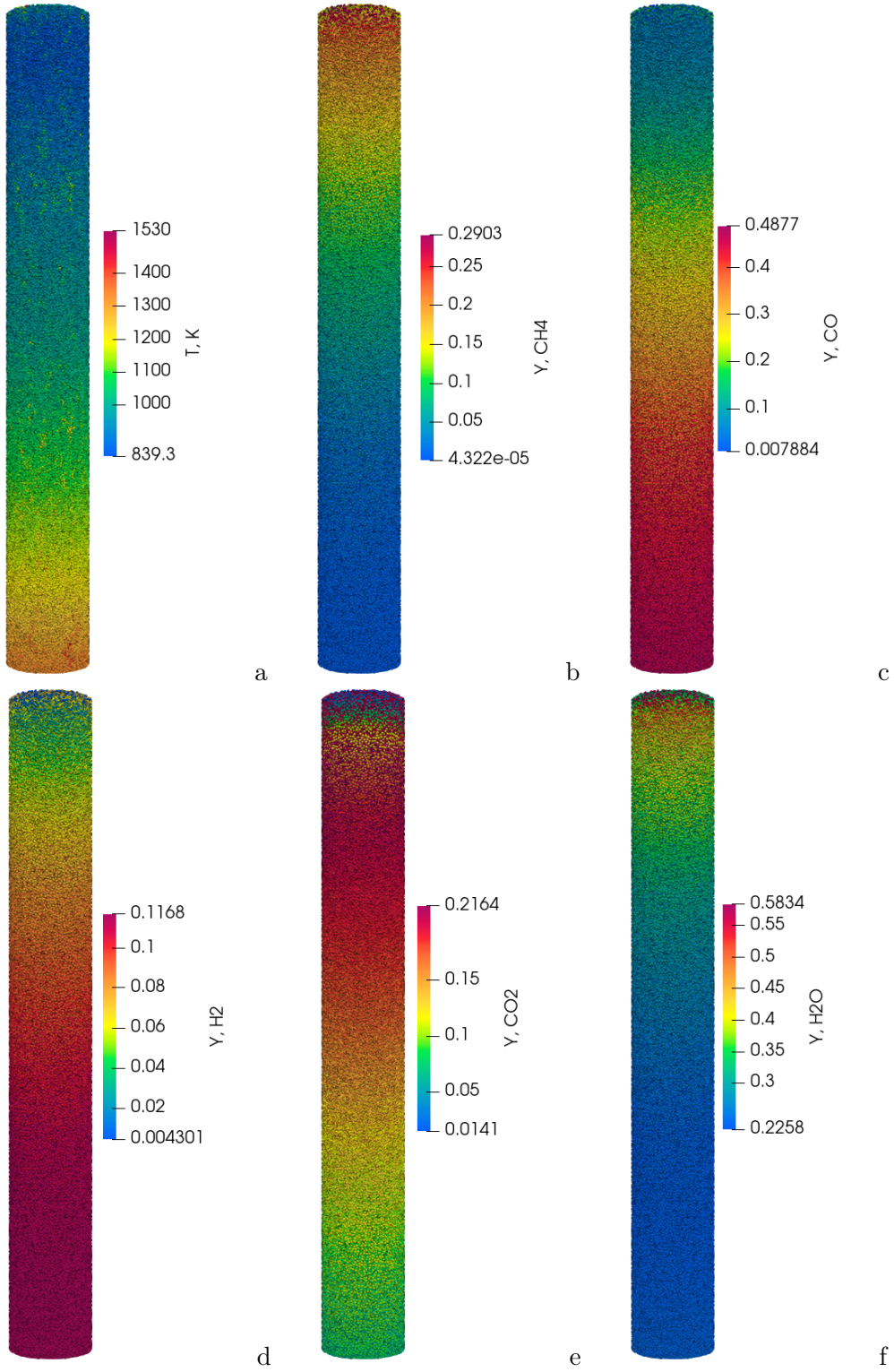

Figure 7.18: 3D visualization of the particle temperature T_p (a) and species mass fractions Y_{p,CH_4} (b), $Y_{p,CO}$ (c), Y_{p,H_2} (d), Y_{p,CO_2} (e) and Y_{p,H_2O} (f) predicted numerically for the reactor with H=2.35m and D=0.3m m reactor for $Q_{IU} = 370$ kW.

7.5 Acknowledgments

The authors acknowledge the financial support by the Natural Sciences and Engineering Research Council (NSERC) Canada under the Discovery Grant *Energy to Chemicals (E2C) using direct electrical current flowing through dense beds.*

Bibliography

[1] James G. Speight. *Handbook of Industrial Hydrocarbon Processes.* Gulf Professional Publishing, Oxford, UK, 2011.

[2] M. Aneke and M. Wang. Energy storage technologies and real life applications – a state of the art review. *Applied Energy*, 179:350–377, 2016.

[3] Qi Zhang, Makoto Nakaya, Tetsuya Ootani, Hiroshi Takahashi, Makoto Sakurai, and Hideo Kameyama. Simulation and experimental analysis on the development of a co-axial cylindrical methane steam reformer using an electrically heated alumite catalyst. *International Journal of Hydrogen Energy*, 32:3870 – 3879, 2007.

[4] M. Rieks, R. Bellinghausen, N. Kockmann, and L. Mleczko. Experimental study of methane dry reforming in an electrically heated reactor. *Int. J. Hydrogen Energy*, 40:15940–15951, 2015.

[5] Raynald Labrecque and Jean Michel Lavoie. Dry reforming of methane with CO2 on an electron-activated iron catalytic bed. *Bioresource Technology*, 102:11244–11248, 2011.

[6] B.R. De Vasconcelos and J.M. Lavoie. Is dry reforming the solution to reduce natural gas carbon foorptint? *Int. J. Energy Prod. Mgmt*, 3:44–56, 2018.

[7] F. Che, J.T. Gray, S. Ha, and J.S. McEwen. Reducing reaction temperature, steam requirements, and coke formation during methane steam reforming using electric fields: A microkinetic modeling and experimental study. *ACS Catal*, 7:6957–6968, 2017.

[8] S.T. Wismann, J.S. Engbak, A.B.Vendelbo, F.B. Bendixen, W.L. Eriksen, K. Aasberg-Petersen, C. Frandsen, I. Chorkendorf, and P.M. Mortensen. Electreified methane reforming: A compact approach to greener industrial hydorgen production. *Science*, 364:756–759, 2019.

[9] Y.R. Lu and P.A. Nikrityuk. Steam methane reforming driven by the joule heating. *CES*, page submitted, 2021.

[10] Yi Ran Lu and Petr Nikrityuk. A new fixed bed reactor for electrical energy storage into chemicals: Proof of concept. *Applied Energy*, 228:593–607, 2018.

[11] Y.R. Lu, D. Pudasainee, Md Khan, R. Gupta, and P.A. Nikrityuk. Experimental and numerical study of volt-ampere characteristics of a packed tube heated by the joule heating. *Int. J. Thermal Sciences*, page under 2nd review, 2021.

[12] Y.R. Lu and P.A. Nikrityuk. DEM-based model for a steam methane reforming. *Chemical Engineering Science*, 247:116903, 2022.

[13] A.Tran, A. Aguirre, H. Durand, M. Crose, and P.D. Christofides. CFD modeling of a industrial-scale steam methane reforming furnace. *Chemical Engineering Science*, 171:576–589, 2017.

[14] Bhanu Vardhan Reddy Kuncharam and Anthony G. Dixon. Multi-scale two-dimensional packed bed reactor model for industrial steam methane reforming. *Fuel Processing Technology*, 200: 106314, 2020.

[15] Jingyu Wang, Shangshang Wei, Qiuwang Wang, and Bengt Sunden. Transient numerical modeling and model predictive control of an industrial-scale steam methane reforming reactor. *International Journal of Hydrogen Energy*, 46:15241–15256, 2021.

[16] Y.R. Lu, D. Pashchenko, and P.A. Nikrityuk. A new semiempirical model for the heat and mass transfer inside a spherical catalyst in a stream of hot CH_4/H_2O gases. *Chem. Eng. Sci.*, 238:116565, 2021.

[17] Dixon A.G. Local transport and reaction rates in a fixed bed reactor tube: Endothermic steam methane reforming. *Chemical Engineering Science*, 168:156–177, 2017.

[18] J. Kozicki and F. Donzé. Yade-open DEM: an open-source software using a discrete element method to simulate granular material. *Engineering Computations*, 26(7):786–805, 2009.

[19] Yade - Open source software for DEM. https://yade-dem.org/doc/, 2009.

[20] Robert B. Ross. *Metallic materials specification handbook*. Chapman & Hall, 4. ed. edition. ISBN 0412369400. doi: 10.1007/978-1-4615-3482-2.

[21] F. Hardesty. Metals handbook (ninth ed.). volume 2, properties and selection: Nonferrous alloys and pure metals. 5(1-2):133–135. doi: 10.1016/0378-3804(81)90025-5.

[22] S. Ergun. Fluid flow through packed columns. *Chem. Eng. Prog.*, 48:89–94, 1952.

[23] P.N. Dwivedi and S.N. Upadhyay. Particle-fluid mass transfer in fixed and fluidized beds. *Ind. Eng. Chem., Process Des. Dev.*, 16:157–165, 1977.

[24] K. Hou and R. Hughes. The kinetics of methane steam reforming over a Ni/α-Al_2O catalyst. *Chem. Eng. J.*, 82:311–328, 2001.

[25] D. J. Gunn. Transfer of heat or mass to particles in fixed and fluidized beds. *International Journal of Heat and Mass Transfer*, 21(467-476), 1978.

[26] M.W. Baltussen, K.A. Buist, E.A.J.F. Peters, and J.A.M. Kuipers. Multiscale modelling of dense gas-particle flows. *Advances in Chemical Engineering*, 53:1–52, 2018.

[27] S. Schulze, M. Kestel, Safronov. D., and P. Nikrityuk. From detailed description of chemical reacting coal particles to subgrid models for CFD: model development and validation. *Oil & Gas Science and Technology*, 68:1007–1026, 2013.

[28] S. Schulze, A. Richter, M. Vascellari, A. Gupta, B. Meyer, and P. Nikrityuk. Novel intrinsic-based submodel for char particle gasification in entrained-flow gasifiers: Model development, validation and illustration. *Applied Energy*, 164:805–814, 2016.

[29] R. Schmidt, K. Wittig, and P. Nikrityuk. Single particle heating and drying. In P. Nikrityuk and B. Meyer, editors, *Gasification Processes: Modeling and Simulation*, pages 105–142. Willey-VCH Verlag GmbH & Co, Weinheim, Germany, 2014.

[30] G.K. Batchelor and R.W. Brien. Thermal or electrical conduction through a granular material. *Pro. Roy. Soc. Lond. A Math. Phys. Sci.*, 355:313–333, 1977.

[31] E. Dintwa, E. Tijskens, and H. Ramon. On the accuracy of the hertz model to describe the normal contact of soft elastic spheres. *Granular Matter*, 10:209–221, 2008.

[32] National Institute of Standards and Technology, Chemistry WebBook, USA. https://webbook.nist.gov/chemistry, 2018.

Chapter 8

Conclusion

The scarcity and the environmental impact of hydrocarbon based energy sources have prompted alternative ways to meet future energy demands and sustain economic growth. The recent advancement in technology and growing adaptation of renewable energy source creates a unprecedented demand for energy storage and utilization. Countries are looking for ways to reduce their carbon emissions and find new renewable energy sources. Hydrogen research has garnered attention from governments as an approach to store and use renewable energy source. However, most of the hydrogen today is produced using steam-methane reforming. The efficiency and carbon intensity of SMR makes the intention to use hydrogen as a fuel counterproductive in the current economy. In an effort to find improve efficiency and incorporate new renewable energy source in the production of hydrogen, a series of studies have been conducted to investigate the possibilities of a Joule heated steam methane reformer. The reformer uses DC current generated from renewable sources to provide endothermic heat of reaction. A multi-stage model was developed to calculate the reaction rate, conversion, and local temperature profiles inside the new steam-methane reformer.

A 0-D model was developed to calculate the chemical reactions inside a catalyst particle without resolving the particle in fine mesh. The 0-D model includes six gaseous chemical species (CH_4, CO_2, CO, H_2O, H_2, N_2) using a global mechanism of LHHW kinetics taken from the literature. This new model predicts the surface-averaged volume-averaged values of the temperature and the mass fractions for each species. The values are calculated by using internal heat transfer and mass transfer coefficients, which are in turn calculated from particle size, void fraction, tortuosity, thermal conductivity and mass diffusivity and external transport parameters. The 0-D model has been validated against a comprehensive 3D-CFD simulation, which resolves the interiors of the catalyst particle and its surroundings. Excellent agreement was achieved between the results of the new 0-D model and the 3D particle-resolved CFD model. The results of CFD simulations revealed considerable mass and heat transfer limitations inside the particle as the ambient temperature increased from 800 K to 1000 K.

Since the 0D model showed excellent agreement with the 3D simulation, and the profile inside the particle was mostly spherical symmetrical, with gradient concentrated near the surface boundary, the validity of the 0D model was further tested against 1D PDE solutions of the particles under different conditions. A grid of 120 mesh is found to be sufficient for achieve grid independence. The parametric variations include particle diameter from 0.002m to 0.04m, Reynolds number from 500 to 10000, emissivity from 0 to 0.9, freestream temperature from 700 to 1000K, and steam-to-carbon ratio from 2 to 3. The 0D model was found to work on most conditions except when the surface of the catalyst has high emissivity. Because the radiative heat transfer no longer scales linearly with the temperature, there exists significant error when the same 0D model was applied to a case where the external heat transfer is much higher at elevated temperature. To model the reactions inside, we used both kinetic model (KM) and the partial equilibrium model (PEM) which does not make use of the LHHW kinetics but rather assumes equilibrium condition inside the catalyst and calculates the reaction rate based on heat and mass transfer rate. Good agreement is found between both models for larger particles where the reaction rate is diffusion limited.

The 0D model for the steam reforming of methane, coupled with 3D DEM heat transfer model and 1D finite difference gaseous model, was used to calculate conditions inside a cylindrical packed bed filled with catalyst particles heated from the sidewall. Both models account for the intra-particle heat and mass transfer using surface-averaged and volume-averaged temperature and species concentrations predicted for each individual particle. The models incorporate interparticle heat transfer using the resistance model and particle-gas heat and mass transfer using closure relations. The model is used to reproduce results from a 3D CFD simulation of the packed bed. Despite of the lack of resolution of the transport processes in the radial direction, the model was able to reproduce axial profiles with good agreement. In particular, the deviation between our DEM-based model and 3D benchmark results comprised of 1% difference in the temperature of outflow gas phase and up to 3% differences in the composition of outflow gas. The basis for this agreement is the local variations in the temperature and mass fractions from particle to particle, as observed in CFD simulations but unaccounted for in traditional 1D and 2D effective medium models. Additionally, we found out that for the given inlet flow conditions, the reaction is strongly diffusion-limited and the inlet gas compositions is close to equilibrium values.

With good results shown against published CFD studies, we present results of the new particle-unresolved model based on Discrete Element method (DEM). The new DEM model predicts the volt-ampere characteristics of a fixed bed heated by direct Joule heating. The results from the new model for the electrical field showed acceptable agreement with experimental data with some deviations when the bed temperature exceeds 500K. Experimental data revealed a non-linear correlation between electrical current and electric field potential difference between the electrodes. The voltage-ampere curve is slight concave up despite an increase in temperature with higher current. This effect might be attributed to the thermal expansion of metal spheres and the corresponding

increase in the contact area between particles. Additionally, the DEM-based resistance model was validated against particle resolved simulations in terms of the Joule heating and electrical current. Excellent agreement was demonstrated. The distinguishing feature of this model lies in the use of the volume-averaged electric field potential for each particle. This new DEM-based model can be used for predictions when employing Joule heating in endothermic chemical reactors, for converting electrical energy into chemicals.

The various components of the DEM-based (Euler-Lagrange) model for the electrically driven steam reforming of methane have been validated separately. The new model is then used to simulate a SMR which uses metal particles inside the fixed bed to provide the heat of reaction. The new model uses a 0D sub-system model to account for chemical reaction inside catalyst, resistance model for 3D heat transfer between particles, and closure correlations to couple particles and the gas phase. The kinetic model(KM) and the equilibrium model are both used for modeling reactions inside the catalyst. To investigate the performance of the new methane reforming concept, we have simulated a cylindrical electrically insulated tube with a diameter of 0.1 m and a height of 0.5 m, which is filled with metal particles and catalyst particles with diameters of 5 mm and 2 mm, respectively. Parametric runs were carried out for different flow rates from 0.0025 kg/s to 0.01 kg/s with electrical power levels from 6.9 kW to 39 kW. Analysis of the results showed that equilibrium-based models predicts the species mass fractions at the outlet of the reactor well, but underestimates outlet gas temperature in comparison to the KM. When the input electrical power is increased, the difference between catalyst particle temperature and gas temperature decreases. Finally, it was shown that a linear increase in the flow rate and input power leads to a decrease in methane conversion. The results show that the reactor can adapt to changes in power by adjusting the flow rate to maintain a steady conversion in the output and stable temperature inside the reformer, up to a maximum of 0.0025 kg/s and an input power of 9.6 kW.

In the last chapter of this study, the impact of the flow rate, flow direction, power input and aspect ratios of the electrically heated steam-methane reforming reactor was investigated through a parametric study. The equilibrium model was compared with the kinetic model to understand the degree of transport limitations in the reactor. When the flow rate is kept constant, increasing the power will increase conversion, but may not be the best for thermal efficiency. The ideal power-to-flow ratio should be equal to the heat of reaction, based on the conversion of steam methane reforming. A higher flow rate can increase production capacity while maintaining a similar conversion rate. However, a high flow rate also causes more severe heat transfer limitations, a higher maximum temperature, a higher temperature gradient and a higher pressure drop. The maximum temperature should be considered carefully in the design as it was shown to become the top restrictive factor, before the conversion rate. The recommended mass flow limit for a reactor that 0.88m tall and 0.5 in diameter is 0.05kg/s. In particular, we showed that the cross-sectional temperature profile of a scaled-up reactor is mostly uniform, with small hot spots but a temperature difference that is usually

within 100K. More importantly, the temperature differential only exists from particle to particle and does not extend over a longer radial distance. Therefore, the scalability and the efficiency of the reactor present a significant advantage over conventional steam methane reformers in an energy market with abundant renewable energy in the future.

8.1 Future Steps and Recommendations

The fluid model used in this work is 1D axial. Although the solid phase is able to retain 3D features of the fixed bed, part of the details is lost due to the lack of temperature gradient in the cross-sectional plane. As a result, the temperature difference between particles in the fixed bed tends to be underpredicted due to the pooling effect of uniform gas phase temperature. To improve the accuracy of the model, a 3D meso-scale model is recommended for the gas phase, with pressure correction to solve the momentum change in the transverse direction for each element.

The objective for developing the electrically driven reformer is to take advantage of excess renewable energy. Therefore, the reformer's ability to adapt to the change in power is an important factor. The metal particles not only act as current carriers, but also heat capacitors that help buffer the temperature in reformer. The flow must be adjusted in real time to accommodate the change of power. For future work, more unsteady study with variable voltage supply should be carried out to test the response of the new reactor.

General Bibliography

Aasberg-Petersen, K., Bak Hansen, J., Christensen, T., Dybkjaer, I., Christensen, P., Stub Nielsen, C., Winter Madsen, S., and Rostrup-Nielsen, J. (2001). "Technologies for large-scale gas conversion". In: *Applied Catalysis A: General* 221.1-2, pp. 379–387.

Abbas, S., Dupont, V., and Mahmud, T. (2017). "Kinetics study and modelling of steam methane reforming process over a NiO/Al_2O_3 catalyst in an adiabatic packed bed reactor". In: *Int. J. Hydrogen Energy* 42, pp. 2889–2903.

Ajuwon, O. (2015). "Experimental and numerical study of particles heating using DC discharge". MSc thesis. Edmonton, AB, Canada: University of Alberta.

Aneke, M. and Wang, M. (2016). "Energy storage technologies and real life applications – A state of the art review". In: *Applied Energy* 179, pp. 350–377.

ANSYS (2011). "Ansys Fluent Theory Guide". In: *ANSYS, Inc. Southpointe 275 Technology Drive Canonsburg, PA 15317, USA* Release 14.0.

Automotive Engineers, S. of (1995). *SAE ferrous materials standards manual*. Warrendale,PA,USA: Society of Automotive Engineers.

Balakotaiah, V. (2008). "On the relationship between Aris and Sherwood numbers and friction and effectiveness factors". In: *Chemical Engineering Science* 63.24, pp. 5802–5812.

Baltussen, M., Buist, K., Peters, E., and Kuipers, J. (2018). "Multiscale Modelling of Dense Gas-Particle Flows". In: *Advances in Chemical Engineering* 53, pp. 1–52.

Bansal, H., Ghaemi, S., and Nikrityuk, P. (2017). "A scale-bridging model for ice particles melting in air". In: *Chem. Eng. Sci.* 172, pp. 66–78.

Bansal, H. and Nikrityuk, P. (2017a). "A submodel for spherical particles undergoing phase change under the influence of convection". In: *Can. J. Chem. Eng.* 95, pp. 150–156.

Bansal, H. and Nikrityuk, P. (2017b). "Arbitrary shaped ice particle melting under the influence of natural convection". In: *AIChE J.* 63, pp. 3158–3176.

Banville, M., Labrecque, R., and Lavoie, M. (2014). "Dry reforming of methane under an electrocatalytic bed: Effect of electrical current and catalyst composition". In: *Energy and Sustainability V* 186, pp. 603–611.

Barrington, A. (1956). "The fusing of wires with heavy surge currents". In: *British Journal of Applied Physics* 7.11, p. 408.

Batchelor, G. and Brien, R. (1977). "Thermal or electrical conduction through a granular material". In: *Pro. Roy. Soc. Lond. A Math. Phys. Sci.* 355, pp. 313–333.

Bergman, T., Lavine, A., Incropera, F., and Dewitt, D. (2011). *Fundamentals of Heat and Mass Transfer*. 7th ed. John Wiley & Sons.

Bhattacharyya, D. and Pei, D. (1975). "Heat transfer in fixed bed gas-solid systems". In: *Chemical Engineering Science* 30.3, pp. 293–300.

Bird, R., Stewart, W., and Lightfoot, E. (2007). *Transport Phenomena*. John Wiley & Sons.

Bluhm-Drenhaus, T., Simsek, E., Wirtz, S., and Scherer, V. (2010). "A coupled fluid dynamic-discrete element simulation of heat and mass transfer in a lime shaft kiln". In: *Chemical Engineering Science* 65, pp. 2821–2834.

Bride, B., Gordon, S., and Reno, M. (1993). "Coefficients for calculating Thermodynamic and Transport Properties of Individual Species." In: *Technical report, NASA*.

Centi, G., Quadrelli, E., and Perathoner, S. (2013). "Catalysis for CO_2 conversion: a key technology for rapid introduction of renewable energy in the value chain of chemical industries". In: *Energy Environ. Sci.* 6 (6), pp. 1711–1731.

Chandra, V., Peters, E., and Kuipers, J. (2020). "Direct numerical simulation of a non-isothermal non-adiabatic packed bed reactor". In: *Chem. Eng. Journal* 385, p. 123641.

Che, F., Gray, J., Ha, S., and McEwen, J. (2017). "Reducing Reaction Temperature, Steam Requirements, and Coke Formation During Methane Steam Reforming Using Electric Fields: A Microkinetic Modeling and Experimental Study". In: *ACS Caralysis* 7, pp. 6957–6968.

Chen, L., Wang, C., Moscardini, M., Kamlah, M., and Liu, S. (2019). "A DEM-based heat transfer model for the evaluation of effective thermal conductivity of packed beds filled with stagnant fluid: Thermal contact theory and numerical simulation". In: *Int. J. Heat Mass Transfer* 132, pp. 331–346.

Chen, W. (2014). "CO_2 conversion for syngas production in methane ctalytic particlal axidation". In: *Journal of CO2 Utilization* 5, p. 109.

Cheng, G., Yu, A., and Zulli, P. (1999). "Evaluation of effective thermal conductivity from the structure of packed bed". In: *Chem. Eng. Sci.* 54, pp. 4199–4209.

Churchill, S. W. (2002). "Free Convection Around Immersed Bodies". In: *Heat Exchanger Design Handbook*. Ed. by G. Hewitt. New York, USA: Begell House, Section 2.5.7.

Churchill, S. and Chu, H. (1975). "Correlating equations for laminar and turbulent free convection from a vertical plate". In: *Int. J. Heat Mass Transfer* 18, pp. 1323–1329.

Ciesielski, P., Pecha, M., Thornburg, N., Crowley, M., Gao, X., Oyedeji O. nd Sitaraman, H., and Brunhart-Lupo, N. (2021). "Bridging Scales in Bioenergy and Catalysis: A Review of Mesoscale Modeling Applications, Methods, and Future Directions". In: *Energy and Fuels* 35 (18), pp. 14382–14400.

Cocco, R., Fullmer, W., Liu, P., and Hrenya, C. (2017). "CFD-DEM: Modeling the Small to Understand the Large". In: *Chemical Eng. Progress* 113.9, pp. 38 –45.

Colpaert, H. (2018). *Metallography of Steels - Interpretation of Structure and the Effects of Processing*. ASM International.

Cornejo, I., Nikrityuk, P., and Hayes, R. (2018). "Multiscale RANS-based modeling of turbulence decay in an automotive catalytic converter". In: *Chem. Eng. Sci.* 175, pp. 377–386.

Crabtee, G., Dresselhaus, M., and Buchanan, M. (2004). "The Hydrogen Economy". In: *Physics Today*, pp. 39–44.

Cui, Z., Shao, W., Chen, Z., and Cheng, L. (2017). "Mathematical model and numerical solutions for the coupled gas-solid heat transfer process in moving packed beds". In: *Applied Energy* 206, pp. 1297–1308.

Cunha, A., Mahata, N., Orafo, J., and Figueiredo, J. (2009). "Methane Decomposition on La2O3-Promoted Raney-Type Fe Catalysts". In: *Energy & Fuels* 23.8, pp. 4047–4050.

Dahl, J., Barocas, V., Clough, D., and Weimer, A. (2002). "Intrinsic kinetics for rapid decomposition of methane in an aerosol flow reactor". In: *International Journal of Hydrogen Energy* 27.4, pp. 377–386. ISSN: 0360-3199.

De Vasconcelos, B. and Lavoie, J. (2018). "Is dry reforming the solution to reduce natural gas carbon foorptint?" In: *Int. J. Energy Prod. Mgmt* 3, pp. 44–56.

Deen, N., Peters, E., Padding, J., and Kuipers, J. (2014). "Review of direct numerical simulation of fluid-particle mass, momentum and heat transfer in dense gas-solid flows". In: *Chem. Eng. Sci.* 116, pp. 710–724.

Dierich, F., Richter, A., and Nikrityuk, P. (2018). "A fixed-grid model to track the interface and porosity of a chemically reacting moving char particle". In: *Chemical Engineering Science* 175, pp. 296–305.

Diglioa, G., Hanak, D., Bareschino, P., Pepe, F., Montagnaro, F., and Manovic, V. (2018). "Modelling of sorption-enhanced steam methane reforming in a fixed bed reactor network integrated with fuel cell". In: *Applied Energy* 210, pp. 1–15.

Dincer, I. and Zamfirescu, C. (2016). *Sustainable Hydrogen Production*. Amsterdam, Netherlands: Elsevier Inc.

Dintwa, E., Tijskens, E., and Ramon, H. (2008). "On the accuracy of the Hertz model to describe the normal contact of soft elastic spheres". In: *Granular Matter* 10, pp. 209–221.

Dixon, A. (2014). "CFD study of effect of inclination angle on transport and reaction in hollow cylinder catalysts". In: *Chemical Engineering Research and Design* 92, pp. 1279–1295.

Dixon, A. (2017). "Local transport and reaction rates in a fixed bed reactor tube: Endothermic steam methane reforming". In: *Chemical Engineering Science* 168, pp. 156–177.

Dixon, A., Nijemeisland, M., and E.H., S. (2006). "Packed tubular reactor modeling and catalyst design using computational fluid dynamics". In: *Advances in Chemical Engineering* 31, pp. 307–389.

Dixon, A., Taskin, M., Nijemeisland, M., and Stitt, E. (2010). "CFD Method To Couple Three-Dimensional Transport and Reaction inside Catalyst Particles to the Fixed Bed Flow Field". In: *Ind. Eng. Chem. Res.* 49, pp. 9012–9025.

Dwivedi, P. and Upadhyay, S. (1977). "Particle-Fluid Mass Transfer in Fixed and Fluidized Beds". In: *Ind. Eng. Chem., Process Des. Dev.* 16, pp. 157–165.

Eisfeld, B. and Schnitzlein, K. (2001). "The influence of confining walls on the pressure drop in packed beds". In: *Chem. Eng. Sci.* 56, pp. 4321–4329.

Eppinger, T., Wehinger, G., and Kraume, M. (2014). "Parameter optimization for the oxidative coupling of methane in a fixed bed reactor by combination of response surface methodology and computational fluid dynamics". In: *Chem. Eng. Res. Des.* 92, pp. 1693–1703.

Ergun, S. (1952). "Fluid Flow through packed columns". In: *Chem. Eng. Prog.* 48, pp. 89–94.

Esence, T., Bruch, A., Molina, S., Stutz, B., and Fourmigue, J. (2017). "A review on experience feedback and numerical modeling of packed-bed thermal energy storage systems". In: *Solar Energy* 153, pp. 628–654.

Freiwald, M. and Paterson, W. (1992). "Accuracy of model predictions and reliability of experimental data for heat transfer in packed beds". In: *Chemical engineering science* 47.7, pp. 1545–1560.

Gan, J., Zhou, Z., and Yu, A. (2016). "Particle scale study of heat transfer in packed and fluidized beds of ellipsoidal particles". In: *Chemical Engineering Science* 144, pp. 201–215.

Gao, B., Wang, I., Ren, L., Haines, T., and Hu, J (2018). "Catalytic Performance and Reproducibility of Ni/Al_2O_3 and Co/Al_2O_3 Mesoporous Aerogel Catalysts for Methane Decomposition". In: *Industrial & Engineering Chemistry Research* 58.2, pp. 798–807.

Geng, S., Han, Z., Hu, Y., Cui, Y., Yue, Y., Yu, J., and Xu, G. (2018). "Methane Decomposition Kinetics over Fe_2O_3 Catalyst in Micro Fluidized Bed Reaction Analyzer". In: *Industrial & Engineering Chemistry Research* 57.25, pp. 8413–8423.

Gimez, M., Porteiro, J., Patino, D., and Miguez, J. (2015). "Fast-solving thermally thick model of biomass particles embedded in a CFD code for the simulation of fixed-bed burners". In: *Energy Conversion and Management* 105, pp. 30–44.

Glaser, M. and Thodos, G. (1958). "Heat and momentum transfer in the flow of gases through packed beds". In: *AIChE Journal* 4.1, pp. 63–68.

Golshan, S., Sotudeh-Gharebagh, R., Zarghami, R., Mostoufi, N., Blais, B., and J.A.M., K. (2020). "Review and implementation of CFD-DEM applied to chemical process systems". In: *Chemical Engineering Science* 221, p. 115646.

Govender, N., Cleary, P., Kiani-Oshtorjani, M., Wilke, D., Wu, C., and Kureck, H. (2020). "The effect of particle shape on the packed bed effective thermal conductivity based on DEM with polyhedral particles on the GPU". In: *Chemical Engineering Science* 219, p. 115584.

Granta Design Limited (2018). *CES EduPack software.*

Greenwood, J. (1966). "Constriction resistance and the real area of contact". In: *British Journal of Applied Physics* 17.12, p. 1621.

Gunn, D. (1978). "Transfer of Heat or Mass to Particles in Fixed and Fluidized Beds". In: *International Journal of Heat and Mass Transfer* 21.467-476.

Guria, J., Bansal, A., and Kumar, V. (2021). "Effect of additives on the thermal conductivity of zirconium diboride based composites - A review". In: *Journal of the European Ceramic Society* 41, pp. 1–23.

Hardesty, F. (n.d.). "Metals handbook (Ninth Ed.). Volume 2, properties and selection: Nonferrous alloys and pure metals". In: *Journal of Mechanical Working Technology* 5.1-2 (), pp. 133–135.

Hayes, R. E. and Mmbaga, J. P. (2012). *Introduction to chemical reactor analysis*. CRC Press/Taylor & Francis Group. ISBN: 9781466580534.

Heating, R. American Society of and Engineers, Air-Conditioning (1972). *ASHRAE handbook of fundamentals; an instrument of service prepared for the profession containing reference material pertaining to fundamental theory and basic data*. USA: American Society of Heating, Refrigerating and Air-Conditioning Engineers.

Herron, J., Kim, J., Upadhye, A., Huber, G., and Maravelias, C. (2015). "A general framework for the assessment of solar fuel technologies". In: *Energy Environ. Sci.* 8 (1), pp. 126–157.

Hirsch, D. and Steinfeld, A. (2004). "Solar hydrogen production by thermal decomposition of natural gas using a vortex-flow reactor". In: *International Journal of Hydrogen Energy* 29.1, pp. 47–55. ISSN: 0360-3199.

Holladay, J., Hu, J., King, D., and Wang, Y. (2009). "An overview of hydrogen production technologies". In: *Catalysis Today* 139, pp. 244–260.

Hou, B., Ye, R., Huang, Y, Wang, X., and Zhang, T. (2018). "A CFD model for predicting the heat transfer in the industrial scale packed bed". In: *Chinese Journal of Chemical Engineering* 26, pp. 228–237.

Hou, K. and Hughes, R. (2001). "The kinetics of methane steam reforming over a Ni/α-Al_2O catalyst". In: *Chem. Eng. J.* 82, pp. 311–328.

IEA (2019). *The Future of Hydrogen*. Tech. rep. G20.

Iulianelli, A., Pirola, C., Comazzi, A., Galli, F., Manenti, F., and Basile, A. (2015). "1 - Water gas shift membrane reactors". In: *Membrane Reactors for Energy Applications and Basic Chemical Production*. Ed. by A. Basile, L. Di Paola, F. l. Hai, and V. Piemonte. Woodhead Publishing Series in Energy. Woodhead Publishing, pp. 3–29. ISBN: 978-1-78242-223-5.

Jiang, B., Dou, B., Wang, K., C., Z., Song, Y., Chen, H., and Xu, Y. (2016). "Hydrogen production by chemical looping steam reforming of ethanol using NiO/montmorillonite oxygen carriers in a fixed-bed reactor". In: *Chemical Engineering Journal* 298, pp. 96–106.

Jo, S., Kim, T., Lee, D., Kang, W., and Song, Y. (2014). "Effect of the Electric Conductivity of a Catalyst on Methane Activation in a Dielectric Barrier Discharge Reactor". In: *Plasma Chem. Plasma Process* 34, pp. 175–186.

Johnson, T. and Patel, V. (1999). "Flow past a sphere up to a Reynolds number of 300". In: *Journal of Fluid Mechanics* 378, pp. 19–70.

Joshi, S. Y., Harold, M. P., and Balakotaiah, V. (2009). "On the use of internal mass transfer coefficients in modeling of diffusion and reaction in catalytic monoliths". In: *Chemical Engineering Science* 64.23, pp. 4976–4991.

Juncu, G. (2002). "The influence of the henry number on the conjugate mass transfer from a sphere: II - Mass transfer accompanied by a first-order chemical reaction". In: *Heat Mass Transfer* 38, pp. 523–534.

Kang, W., Kim, H., Teramoto, Y., Ogata, A., Lee, J., Kim, D., Hur, M., and Song, Y. (2018). "Surface streamer propagations on an alumina bead: experimental observation and numerical modeling". In: *Plasma Sources Science and Technology* 27, p. 015018.

Karim Aramouni, N., Touma, J., Tarboush, B., Zeaiter, J., and Ahmad, M. (2018). "Catalyst design for dry reforming of methane: Analysis review". In: *Renewable and Sustainable Energy Reviews* 82, pp. 2570–2585.

Khajeh, S., Aboosadi, Z., and Honarvar, B. (2014). "A comparative study between operability of fluidized-bed and fixed-bed reactors to produce synthesis gas through tri-reforming". In: *Journal of Natural Gas Science and Engineering* 19, pp. 152 –160.

Kim, J., Johnson, T., Miller, J., Stechel, E., and Maravelias, C. (2012). "Fuel production from CO_2 using solar-thermal energy: system level analysis". In: *Energy Environ. Sci.* 5 (9), pp. 8417–8429.

Kim, T. W., Park, J. C., Lim, T.-H., Jung, H., Chun, D. H., Lee, H. T., Hong, S., and Yang, J.-I. (2015). "The kinetics of steam methane reforming over a Ni/γ-Al_2O_3 catalyst for the development of small stationary reformers". In: *Int. J. Hydrogen Energy* 40, pp. 4512–4518.

Kobe, K. and Lynn, R. (1953). "The Critcal Properties of Elements and Compounds". In: *Chem. Rev.* 52, pp. 117–236.

Kondratenko, E., Mul, G., Baltrusaitis, J., Larrazabal, G., and Perez-Ramirez, J. (2013). "Status and perspectives of CO_2 conversion into fuels and chemicals by catalytic, photocatalytic and electrocatalytic processes". In: *Energy Environ. Sci.* 6 (11), pp. 3112–3135.

Kozicki, J. and Donzé, F. (2009). "Yade-open DEM: an open-source software using a discrete element method to simulate granular material". In: *Engineering Computations* 26.7, pp. 786–805.

Kruyt, N. (2016). "On weak and strong contact force networks in granular materials". In: *International Journal of Solids and Structures* 92-93, pp. 135 –140.

Kucharski, T., Tian, Y., Akbulatov, S., and Boulatov, R. (2011). "Chemical solutions for the closed-cycle storage of solar energy". In: *Energy Environ. Sci.* 4 (11), pp. 4449–4472.

Kuncharam, B. and Dixon, A. (2020). "Multi-scale two-dimensional packed bed reactor model for industrial steam methane reforming". In: *Fuel Processing Technology* 200, p. 106314.

Labrecque, R. and Lavoie, J. (2011). "Dry reforming of methane with CO2 on an electron-activated iron catalytic bed". In: *Bioresource Technology* 102, pp. 11244–11248.

Landau, L. and Lifshitz, E. (1959). *Theory of elasticity*. Pergam on Press.

Lapidus, N. and Amundson, N. (1977). *Chemical reactor theory: A Review*. New Jersey, USA: Prentice-Hall, Inc. Englewood Cliffs.

Lavoie, J. (2014). "Review on dry reforming of methane, a potentially more environmentally-friendly approach to the increasing natural gas exploitation". In: *Frontiers in Chemistry* 2, p. 81.

Lázaro, M., Pinilla, J., Utrilla, R., Suelves, I., Moliner, R., Moreno, F., and M. Muñoz, M. (2010). "$H_2 - CH_4$ Mixtures Produced by Carbon-Catalyzed Methane Decomposition as a Fuel for Internal Combustion Engines". In: *Energy & Fuels* 24.6, pp. 3340–3345.

Lee, D., Chae, M., and Chung, B. (2017). "Natural convective heat transfer of heated packed beds". In: *International Communications in Heat and Mass Transfer* 88, pp. 54–62.

Lee, J., Yun, T., and Choi, S. (2015). "The Effect of Particle Size on Thermal Conduction in Granular Mixtures". In: *Materials* 8, pp. 3975–3991.

LeValley, T., Richard, A., and Fan, M. (2014). "The progress in water gas shift and steam reforming hydrogen production technologies - A review". In: *Int. J. Hydrogen Energy* 39, pp. 16983–17000.

Li, C. and Finlayson, B. (1977). "Heat transfer in packed beds–a reevaluation". In: *Chemical Engineering Science* 32.9, pp. 1055–1066.

Lu, J., Chen, Y., Ding, J., and Wang, W. (2016). "High temperature energy storage performances of methane reforming with carbon dioxide in a tabular packed reactor". In: *Applied Energy* 162, pp. 1473–1482.

Lu Y.R.and Nikrityuk, P. (2021). "Scale-up Studies on Electrically Driven Steam Methane Reforming". In: *Fuel*, submitted.

Lu L. ad Gao, X., Shahnam, M., and Rogers, W. (2020). "Bridging particle and reactor scales in the simulation of biomass fast pyrolysis by coupling particle resolved simulation and coarse grained CFD-DEM". In: *Chemical Engineering Science* 216, p. 115471.

Lu, Y. and Nikrityuk, P. (2018). "A fixed-bed reactor for energy storage in chemicals (E2C): Proof of concept". In: *Applied Energy* 228, pp. 593–607.

Lu, Y. and Nikrityuk, P. (2022a). "DEM-based Model for a Steam Methane Reforming". In: *Chemical Engineering Science* 247, p. 116903.

Lu, Y. and Nikrityuk, P. (2022b). "Steam Methane Reforming driven by the Joule Heating". In: *Chemical Engineering Science*.

Lu, Y., Pashchenko, D., and Nikrityuk, P. (2021). "A New Semiempirical Model for the Heat and Mass Transfer Inside a Spherical Catalyst in a Stream of Hot CH_4/H_2O gases". In: *Chem. Eng. Sci.* 238, p. 116565.

Lu, Y., Pudasainee, D., Khan, M., Gupta, R., and Nikrityuk, P. (2022). "Experimental and Numerical Study of Volt-Ampere Characteristics of a Packed Tube Heated by Joule heating". In: *J. Energy Resources Technology* 144, p. 052105.

Luckos, A. and Bunt, J. (2011). "Pressure-drop predictions in a fixed-bed coal gasifier". In: *Fuel* 90.3, pp. 917 –921.

Maag, G., Rodat, S., Flamant, G., and Steinfeld, A. (2010). "Heat transfer model and scale-up of an entrained-flow solar reactor for the thermal decomposition of methane". In: *International*

Journal of Hydrogen Energy 35.24. 3rd Asian Bio Hydrogen Symposium, pp. 13232–13241. ISSN: 0360-3199.

Mahmoudi, A., Donkers, P., Walayat, K., Peters, B., and Shahi, M. (2021). "A thorough investigation of thermochemical heat storage system from particle to bed scale". In: *Chemical Engineering Science* 246, p. 116877.

Maqbool, F., Abbas, S., Ramirez-Solis, S., Dupont, V., and Mahmud, T. (2021). "Modelling of one-dimensional heterogeneous catalytic steam methane reforming over various catalysts in an adiabatic packed bed reactor". In: *Int. J. Hydrogen Energy* 46, pp. 5112–5130.

McKenna, R., Bchini, Q., Weinand, J., Michaelis, J., König, S., Köppel, W., and Fichtner, W. (2018). "The future role of Power-to-Gas in the energy transition: Regional and local techno-economic analyses in Baden-Württemberg". In: *Applied Energy* 212, pp. 386–400.

Morris, A., Pannala, S., Ma, Z., and Hrenya, C. (2016). "Development of Soft-Sphere Contact Models for Thermal Heat Conduction in Granular Flows". In: *AIChE Journal* 62, pp. 4526–4535.

Mott, N. (1934). "The Resistance of Liquid Metals". In: *Proceedings of the Royal Society of London. Series A, Containing Papers of a Mathematical and Physical Character* 146.857, pp. 465–472.

Mueller, G. (1992). "Radial void fraction distributions in randomly packed tied beds of uniformly sized spheres in cylindrical containers". In: *Powder Technology* 72, pp. 269–275.

Newinger, C., Geyer, C., and Kellberg, S. (2017). *Energy Transitions as Chance and Challenge in Our Time*. Munich, Germany: Oekom Verlag.

Ngo, S., Lim, Y., Kim, W., Seo, D., and Yoon, W. (2019). "Computational fluid dynamics and experimental validation of a compact steam methane reformer for hydrogen production from natural gas". In: *Applied Energy* 236, pp. 340–353.

Ni, M. (2013). "2D heat and mass transfer modeling of methane steam reforming for hydrogen production in a compact reformer". In: *Energy Conversion and Management* 65, pp. 155–163.

Nijemeisland, M., Dixon, A., and Stitt, E. (2004). "Catalyst design by CFD for heat transfer and reaction in steam reforming". In: *Chemical Engineering Science* 59, pp. 5185–5191.

NIST (2018). *National Institute of Standarts and Technology, Chemistry WebBook, USA*.

Oschmann, T. and Kruggel-Emden, H. (2018). "A novel method for the calculation of particle heat conduction and resolved 3D wall heat transfer for the CFD/DEM approach". In: *Powder Technology* 338, pp. 289–303.

Oschmann, T., Schiemann, M., and Kruggel-Emden, H. (2016). "Development and verification of a resolved 3D inner particle heat transfer model for the Discrete Element Method (DEM)". In: *Powder Technology* 291, pp. 392–407.

Oshima, K., Shinagawa, T., Haraguchi, M., and Sekine, Y. (2013). "Low temperature hydrogen production by catalytic steam reforming of methane in an electric field". In: *Int J. Hydrogen Energy* 38, pp. 3003–3011.

Pashchenko, D. (2018). "Effect of the geometric dimensionality of computational domain on the results of CFD-modeling of steam methane reforming". In: *International Journal of Hydrogen Energy* 43.18, pp. 8662–8673.

Pashchenko, D. (2019a). "Combined methane reforming with a mixture of methane combustion products and steam over a Ni-based catalyst: An experimental and thermodynamic study". In: *Energy* 185, pp. 573–584.

Pashchenko, D. (2019b). "Experimental investigation of reforming and flow characteristics of a steam methane reformer filled with nickel catalyst of various shapes". In: *Energy Conversion and Management* 185, pp. 465–472.

Pashchenko, D. (2020). "Thermodynamic equilibrium analysis of steam methane reforming based on a conjugate solution of material balance and law action mass equations with the detailed energy balance". In: *International Journal of Energy Research* 44.1, pp. 438–447.

Pashchenko, D. and Eremin, A. (2021). "Heat flow inside a catalyst particle for steam methane reforming: CFD-modeling and analytical solution". In: *International Journal of Heat and Mass Transfer* 165, p. 120617.

Paxman, D., Trottier, S., Flynn, M., Kostiuk, L., and Secanell, M. (2017). "Experimental and numerical analysis of a methane thermal decomposition reactor". In: *International Journal of Hydrogen Energy* 42.40, pp. 25166–25184.

Peng, Z., Doroodchi, E., and Moghtaderi, B. (2020). "Heat transfer modelling in Discrete Element Method (DEM)-based simulations of thermal processes: Theory and model development". In: *Progress in Energy and Combustion Science* 79, p. 100847.

Peters, B., Baniasadi, M., Baniasadi, M., Besseron, X., Donoso, A., Mohseni, M., and Pozzetti, G. (2019). "XDEM multi-physics and multi-scale simulation technology: Review of DEM-CFD coupling, methodology and engineering applications". In: *Particuology* 44, pp. 176–193.

Ping, C. (1964). "Two-dimensional radiating gas flow by a moment method". In: *AIAA journal* 2.9, pp. 1662–1664.

Ranz, W. and Marshall, W. (1952). "Evaporation from drops". In: *Chem. Eng. Prog* 48.3, pp. 141–146.

Ray, N., Kempf, B., Mützel, T., Froyen, L., Vanmeensel, K., and Vleugels, J. (2015). "Effect of WC particle size and Ag volume fraction on electrical contact resistance and thermal conductivity of Ag-WC contact materials". In: *Materials & Design* 85, pp. 412 –422.

Richter, A. and Nikrityuk, P. (2012). "Drag forces and heat transfer coefficients for spherical, cuboidal and ellipsoidal particles in cross flow at sub-critical Reynolds numbers". In: *Int. J. Heat Mass Transfer* 55, pp. 1343–1354.

Rieks, M., Bellinghausen, R., Mleczko, L., and Kockmann, N. (2015). "Experimental study of methane dry reforming in an electrically heated reactor". In: *International Journal of Hydrogen Energy* 40.46, pp. 15940–15951.

Roh, H., Koo, K., Jung, U., and Yoon, W. (2010a). "Hydrogen production from natural gas steam reforming over Ni catalysts supported on metal substrates". In: *Current Applied Physics* 10.2, S37 –S39.

Roh, H., Lee, D., Koo, K., Jung, U., and Yoon, W. (2010b). "Natural gas steam reforming for hydrogen production over metal monolith catalyst with efficient heat-transfer". In: *International Journal of Hydrogen Energy* 35.4, pp. 1613–1619.

Ross, R. (1992). *Metallic Materials Specification Handbook*. 4th. Chapman & Hall, London.

Rostrup-Nielsen, J. and Christiansen, L. (2011). *Concepts in syngas manufacture*. Imperial College Press, London.

Ryu, J., Lee, K., La, H., Kim, H., Yang, J., and Jung, H (2007). "Ni catalyst wash-coated on metal monolith with enhanced heat-transfer capability for steam reforming". In: *Journal of Power Sources* 171.2, pp. 499 –505.

Said, S., Waseeuddin, M., and Simakov, D. (2016). "A review on solar reforming systems". In: *Renewable and Sustainable Energy Reviews* 59, pp. 149–159.

Schmidt, R., Wittig, K., and Nikrityuk, P. (2014). "Single Particle Heating and Drying". In: *Gasification Processes: Modeling and Simulation*. Ed. by P. Nikrityuk and B. Meyer. Weinheim, Germany: Willey-VCH Verlag GmbH & Co, pp. 105–142.

Schulze, S., Kestel, M., D., S., and Nikrityuk, P. (2013). "From detailed description of chemical reacting coal particles to subgrid models for CFD: model development and validation". In: *Oil & Gas Science and Technology* 68, pp. 1007–1026.

Schulze, S. and Nikrityuk, P. (2016). "A New Subgrid Model for the Heat and Mass Transfer Between a Hot Gas and Char Particles in Dense-Bed Reactors". In: *Journal of Energy Resources Technology* 138, p. 042206.

Schulze, S., Nikrityuk, P., and Meyer, B. (2015). "The porosity distribution in monodisperse and polydisperse fixed beds and its impact on the fluid flow". In: *Particulate Science and Technology* 33, pp. 23–33.

Schulze, S., Richter, A., Vascellari, M., Gupta, A., Meyer, B., and Nikrityuk, P. (2016). "Novel intrinsic-based submodel for char particle gasification in entrained-flow gasifiers: Model development, validation and illustration". In: *Applied Energy* 164, pp. 805–814.

Schulze, S., Schmidt, R., and Nikrityuk, P. (2014). "Subgrid models for particle devolatilization-combustion-gasification". In: *Gasification Processes: Modeling and Simulation*. Ed. by P. Nikrityuk and B. Meyer. Weinheim, Germany: Willey-VCH Verlag GmbH & Co, pp. 271–304.

Schwarz, R., S., D., and Spliethoff, H. (2021). "Numerical simulation of gasification with a one-dimensional particle submodel for char structure evolution". In: *Fuel* 293, p. 120492.

Scipioni, A., Manzardo, A., and Jingzheng, R. (2017). *Hydrogen economy: supply chain, life cycle analysis and energy transition for sustainability*. Academic Press.

Sener, A., Günay, M., Leba, A., and Yildirim, R. (2018). "Statistical review of dry reforming of methane literature using decision tree and artificial neural network analysis". In: *Catalysis Today* 299, pp. 289–302.

Senkara, J. and Zhang, H. (2011). *Resistance welding: fundamentals and applications*. CRC Press.

Sharif Zein, S. and Mohamed, A. (2004). "Mn/Ni/TiO2 Catalyst for the Production of Hydrogen and Carbon Nanotubes from Methane Decomposition". In: *Energy & Fuels* 18, pp. 1336–1345.

Sheu, E., Mokheimer, E., and Ghoniem, A. (2015). "A review of solar methane reforming systems". In: *Int. J. Hydrogen Energy* 40, pp. 12929–12955.

Shigarov, A. (2020). "Modeling of low temperature steam reforming of flare gas to methane-rich fuel gas on Ni catalyst in different types of reactors". In: *Chemical Engineering Journal* 397, p. 125313.

Siegel, R. and Howell, J. (1992). *Thermal radiation heat transfer*. Hemisphere Pub. Corp., Washingtin DC.

Slade, P. (1999). *Electrical Contacts: Principles and Applications*. CRC Press.

Speight, J. (2011). *Handbook of Industrial Hydrocarbon Processes*. Oxford, UK: Gulf Professional Publishing.

Steinberg, M. and Cheng, H. (1989). "Modern and prospective technologies for hydrogen production from fossil fuels". In: *Int. J. Hydrog. Energy* 14, pp. 797–820.

Ström, H. and Thunman, H. (2013). "A computationally efficient particle submodel for CFD-simulations of fixed-bed conversion". In: *Applied Energy* 112, pp. 808–817.

Ström, H. and Thunman, H. (2013). "CFD simulations of biofuel bed conversion: A submodel for the drying and devolatilization of thermally thick wood particles". In: *Combustion and Flame*, pp. 417–431.

Sulaiman, M., Climent, E., Hammouti, A., and Wachs, A. (2019). "Mass transfer towards a reactive particle in a fluid flow: Numerical simulations and modeling". In: *Chemical Engineering Science* 199, pp. 496–507.

Takenaka, S., Shigeta, Y., Tanabe, E., and Otsuka, K. (2004). "Methane decomposition into hydrogen and carbon nanofibers over supported pd-ni catalysts: characterization of the catalysts during the reaction". In: *The Journal of Physical Chemistry B* 108.23, pp. 7656–7664.

Taner, T. (2021). "The novel and innovative design with using H2 fuel of PEM fuel cell: Efficiency of thermodynamic analyze". In: *FUEL* 302, p. 121109.

Taskin, M., Dixon, A., and Stitt, E. (2007). "CFD study of fluid flow and heat transfer in a fixed bed of cylinders". In: *Numerical Heat Transfer, Part A: Applications* 52.3, pp. 203–218.

Tetsu, F. and Haruo, U. (1970). "Laminar natural-convective heat transfer from the outer surface of a vertical cylinder". In: *International Journal of Heat and Mass Transfer* 13.3, pp. 607 –615.

Tran, A., Aguirre, A., Durand, H., Crose, M., and Christofides, P. (2017). "CFD modeling of a industrial-scale steam methane reforming furnace". In: *Chemical Engineering Science* 171, pp. 576–589.

Tsuji, Y., Tanaka, T., and Ishida, T. (1992). "Lagrangian numerical simulation of plug flow of cohesionless particles in a horizontal pipe". In: *Powder Technol* 71, pp. 239–250.

Van de Goor, G., Saegesser, P., and Berroth, K. (1997). "Electrically conductive ceramic composites". In: *Solid State Ionics* 101-103, pp. 1163–1170.

van der Hoef, M., A.M., v., Deen, N., and Kuipers, J. (2008). "Numerical simulation of dense gas-solid fluidized beds: a multiscale modeling strategy". In: *Annu. Rev. Fluid Mech.* 40, pp. 47–70.

Vortmeyer, D. and Haidegger, E. (1991). "Discrimination of three approaches to evaluate heat fluxes for wall-cooled fixed bed chemical reactors". In: *Chemical engineering science* 46.10, pp. 2651–2660.

Wakao, N. and Smith, J. (1962). "Diffusion in catalyst pellets". In: *Chem. Eng. Sci.* 17, pp. 825–834.

Wang, J., Wei, S., Wang, Q., and Sunden, B. (2021). "Transient numerical modeling and model predictive control of an industrial-scale steam methane reforming reactor". In: *International Journal of Hydrogen Energy* 46, pp. 15241–15256.

Wang, Y., Chen, J., and Larachi, F. (2013). "Modelling and simulation of trickle-bed reactors using computational fluid dynamics" a state of the art review". In: *Can. J. Chem. Eng.* 91, pp. 136–180.

Watanabe, R., Yamauchi, M., Sadakiyo, M., Abe, R., and Takeguchi, T. (2015). "CO_2-free electric power circulation via direct charge and discharge using the glycolic acid/oxalic acid redox couple". In: *Energy Environ. Sci.* 8 (5), pp. 1456–1462.

Wehinger, G., Eppinger, T., and Kraume, M. (2015). "Detailed numerical simulations of catalytic fixed-bed reactors: Heterogeneous dry reforming of methane". In: *Chemical Engineering Science* 122, pp. 197–209.

Wehinger, G., Klippel, F., and Kraume, M. (2017). "Modeling pore processes for particle-resolved CFD simulations of catalytic fixed-bed reactors". In: *Comput. Chem. Eng.* 101, pp. 11–22.

Wen, D. and Ding, Y. (2006). "Heat transfer of gas flow through a packed bed". In: *Chemical Engineering Science* 61.11, pp. 3532 –3542.

Whitaker, S. (1972). "Forced convection heat transfer correlations for flow in pipes, past flat plates, single cylinders, single spheres, and flow in packed beds and tube bundles". In: *American Institute of Chemical Engineers Journal* 18, p. 361.

Wismann, S., Engbak, J., Vendelbo, A., Bendixen, F., Eriksen, W., Aasberg-Petersen, K., Frandsen, C., Chorkendorf, I., and Mortensen, P. (2019). "Electreified methane reforming: A compact approach to greener industrial hydorgen production". In: *Science* 364, pp. 756–759.

Wittig, K., Nikrityuk, P., and Richter, A. (2017). "Drag coeffcient and Nusselt number for porous particles under laminar flow conditions". In: *Int. J. Heat Mass Transfer* 112, pp. 1005–1016.

Wittig, K., Golia, A., and Nikrityuk, P. (2012). "3D Numerical study of the influence of particle porosity on the heat and fluid flow". In: *Progress in Computational Fluid Dynamics* 12, pp. 207–219.

Xu, J. and Froment, G. (1989a). "Methane Steam Reforming: II. Diffusional Limitations and Reactor Simulation". In: *AIChE Journal* 35, pp. 97–103.

Xu, J. and Froment, G. (1989b). "Methane Steam Reforming, Methanation and Water-Gas Shift: 1. Intrinsic Kinetics". In: *AIChE Journal* 35, pp. 88–96.

Yagi, S. and Wakao, N. (1959). "Heat and mass transfer from wall to fluid in packed beds". In: *AIChE J* 1, pp. 79–85.

Yamada, K., Ogo, S., Yamano, R., Higo, T., and Sekine, Y. (2020). "Low-temperature conversion of carbon dioxide to methane in an electric field". In: *Chem. Lett.* 49, pp. 303–306.

Yang, X., Wang, S., Li, B., He, Y., and Liu, H. (2020). "Performance of ethanol steam reforming in a membrane-assisted packed bed reactor using multiscale modelling". In: *Fuel* 274, p. 117829.

Yuan, Q., Gu, R., Ding, J., and Lu, J. (2017). "Heat transfer and energy storage performance of steam methane reforming in a tubular reactor". In: *Applied Thermal Engineering* 125, pp. 633–643.

Zhang, Q., Nakaya, M., Ootani, T., Takahashi, H., Sakurai, M., and Kameyama, H. (2007). "Simulation and experimental analysis on the development of a co-axial cylindrical methane steam reformer using an electrically heated alumite catalyst". In: *International Journal of Hydrogen Energy* 32, pp. 3870 –3879.

Zhou, Z., Yu, A., and Zulli, P. (2009). "Particle Scale Study of Heat Transfer in Packed and Bubbling Fluidized Beds". In: *AIChE Journal* 55, pp. 868–884.